Climate in Svalbard 2100

– a knowledge base for climate adaptation

Photo: Ketil Isaksen, MET Norway

Editors

I.Hanssen-Bauer, E.J.Førland, H.Hisdal, S.Mayer, A.B.Sandø, A.Sorteberg

Commissioned by

MILJØ-
DIREKTORATET

The Norwegian Centre for Climate Services [NCCS] is collaboration between the Norwegian Meteorological In-
stitute, the Norwegian Water Resources and Energy Directorate, Norwegian Research Centre and the Bjerknes
Centre for Climate Research. The main purpose of NCCS is to provide decision makers in Norway with relevant
information regarding climate change adaptation. In addition to the partners, the Norwegian Environment
Agency is represented on the Board.

The NCCS report series includes reports where one or more authors are affiliated to the Centre, as well as
reports initiated by the Centre. All reports in the series have undergone a professional assessment by at least
one expert associated with the Centre. They may also be included in report series from the institutions to
which the authors are affiliated.

Norwegian
Meteorological
Institute

NORCE

NVE

Bjerknes Centre
for Climate Research

CLIMATE IN SVALBARD 2100

Authors

Editors: I.Hanssen-Bauer[1,12], E.J.Førland[1,12], H.Hisdal[2,12], S.Mayer[3,12,13], A.B.Sandø[5,13], A.Sorteberg[4,13]

Authors: M.Adakudlu[3,13], J.Andresen[2], J.Bakke[4,13], S.Beldring[2,12], R.Benestad[1], W.G.M. van der Bilt[4,13], J.Bogen[2], C.Borstad[6], K.Breili[9], Ø.Breivik[1,4], K.Y.Børsheim[5,13], H.H.Christiansen[6], A.Dobler[1], R.Engeset[2], R.Frauenfelder[7], S.Gerland[10], H.M.Gjelten[1], J.Gundersen[2], K.Isaksen[1,12], C.Jaedicke[7], H.Kierulf[9], J.Kohler[10], H.Li[2,12], J.Lutz[1,12], K.Melvold[2,12], A.Mezghani[1,12], F.Nilsen[4,6], I.B.Nilsen[2,12], J.E.Ø.Nilsen[5,8,13], O. Pavlova[10], O.Ravndal[9], B.Risebrobakken[3,13], T.Saloranta[2], S.Sandven[6,8,13], T.V.Schuler[6,11], M.J.R.Simpson[9], M.Skogen[5,13], L.H.Smedsrud[4,6,13], M.Sund[2], D. Vikhamar-Schuler[1,2,12], S.Westermann[11], W.K.Wong[2,12]

Affiliations: See Acknowledgements!

Abstract

This report was commissioned by the Norwegian Environment Agency in order to provide basic information for use in climate change adaptation in Svalbard. It includes descriptions of historical, as well as projections for the future climate development in the atmosphere, hydrosphere, cryosphere and ocean, and it includes effects on the physical nature e.g. on permafrost and various types of landslides and avalanches. The projections for the future climate are based on results in the IPCCs fifth assessment report. The report is to a large degree an assessment of existing literature and model results. New results from atmosphere, ocean and hydrological models are, however, also presented. The report may be downloaded from the Norwegian Centre for Climate Service's web portal www.klimaservicesenter.no.

Keywords

Climate in Svalbard, projections, temperature, precipitation, wind, runoff, floods, sediment transport, snow, glaciers, permafrost, landslides and avalanches, ocean climate, sea ice, sea level

Disciplinary signature   Responsible signature

Contents

Acknowledgements

Inger Hanssen-Bauer

Summary

Main findings

Under medium to high scenarios for future climate gas emissions, the following changes are projected for Svalbard from 1971–2000 to 2071–2100:
- Increased annual air temperature (ensemble median about 10 °C for high and 7 °C for medium emissions)
- Increased annual precipitation (ensemble median about 65% for high and 45% for medium emissions)
- Events with heavy rainfall will be more intense and occur more frequently
- River flow will increase, but the magnitude will strongly depend on the precipitation and temperature increase and contribution of glacier meltwater
- In regions where the maximum annual snow storage will decrease, snowmelt floods will become smaller
- Increased precipitation, and increasing fraction as rain, will lead to increased rain-floods and increased combined snowmelt-, glacier melt- and rain-floods
- The snow season will become shorter
- Erosion and sediment transport will increase
- Near-surface permafrost is projected to thaw in coastal and low altitude areas for the high emission scenario
- Many types of avalanches and landslides will become more frequent
- The glacier area and net mass balance will be severely reduced during the 21st century
- The loss of glacier mass and area will change the landscape and contribute to global sea-level rise
- Because of large land uplift and reduced gravitational pull, the mean sea level around Spitsbergen will probably decrease

A climate projection for the ocean areas (for medium emissions) gives from 2010–2019 to 2060–69:
- An average warming of surface waters around Svalbard of about 1°C
- A substantially decreased sea ice concentration in the northern Barents Sea

Inadequate knowledge of the climate system's sensitivity and of future natural climate variations, as well as limitations in the climate models, lead to large uncertainties in the projections even under a given emission scenario. It is still clear that reduced greenhouse gas emissions will lead to reduced changes in the physical climate.

Background

This report was commissioned by the Norwegian Environment Agency in order to provide basic information for climate change effect studies and climate change adaptation in Svalbard. It includes descriptions of historical, as well as projections for future climate development in the atmosphere, hydrosphere, cryosphere and ocean, and it includes effects on the physical nature, e.g. risks associated with landslides and avalanches. The projections for future climate are based on the global climate models used in the IPCCs fifth assessment report (IPCC, 2013). Dependent on availability of model data, three scenarios for emissions of greenhouse gases are used: "RCP8.5" ("business as usual"; "high emissions"), "RCP4.5" (reductions after 2040; "medium emissions") and "RCP2.6" (drastic cuts from 2020; "low emissions"). Climate change in the atmosphere and land surface are projected up to the year 2100 and in the ocean up to the year 2070.

The report is to a large degree an assessment of existing literature and model results, e.g. the Arctic CORDEX regional climate models. In addition, a fine scale atmospheric regional climate model (COSMO-CLM) has been run, and the results were applied for estimating changes in e.g. heavy rainfall, frost days, snow, permafrost and glaciers. Further, a hydrological model has been run for Svalbard for present and projected future climate, based on input data from Arctic CORDEX. Also for the ocean, new analyses have been performed, based on the best available model data. Below follows a summary based on a combination of the assessment and results from new analyses.

Atmospheric variables

Air temperature and derived variables. The mean observed annual temperature (1971-2000) for the manned weather stations in Svalbard varies from -1.7°C (Bjørnøya) to -5.9°C (Svalbard Airport). The estimated average temperature for Svalbard land areas is -8.7 °C. The difference between this average and the station values may be explained by all stations being situated at low altitudes and in western, coastal environments. From 1971 to 2017, a warming of 3 – 5°C has been observed (less in the south, more in the inner fjords), with the largest increase in winter and the smallest in summer. For RCP8.5, the ensemble median projections from regional models and statistical downscaling indicate an increase in annual mean temperature for Svalbard of almost 10 °C from 1971-2000 to 2071-2100. The projected increase is highest in the northeast and lowest in southwest. The uncertainty is large, and the fine scale simulation projects a 7 °C increase under RCP8.5. Under emission scenario RCP4.5 the projected ensemble median temperature increase is 6 – 7 °C and for RCP2.6 about 4 °C.

The temperature projections imply a considerable increase in the number of growing days for grass and a decrease in the number of frost days. Only a moderate change is projected in the annual number of days with maximum temperature above and minimum temperature below 0°C. However, a decrease in such zero-crossings is projected in summer and an increase in winter.

Precipitation. Mean annual precipitation (1971-2000) measured at the weather stations in Svalbard varied from 196 mm (Svalbard Airport) to 581 mm (Barentsburg). The estimated average annual precipitation for the Svalbard land areas is about 720 mm. Some of the difference between measured and estimated values is due to increasing precipitation with altitude, and that models often overestimate precipitation in this area. However, it is also known that precipitation gauges, especially during snowfall and strong winds, do not capture all precipitation. Historical and projected future changes are given in percent of the 1971-2000 values. On Bjørnøya and Hopen, significant positive trends in annual precipitation (20 – 30%) occur from 1971 to 2017, mainly because of increased precipitation in winter and spring. On Spitsbergen, few trends are significant for this period, but trends tend to be positive in autumn and winter and negative in spring and summer. For emission scenario RCP8.5, the ensemble median projections from regional models show an increase in annual precipitation for Svalbard of about 65% from 1971-2000 to 2071-2100. The uncertainty is large, and the fine scale simulation projects a 35% increase for RCP8.5. For RCP4.5 the projected ensemble median precipitation increase is 45%.

On Spitsbergen, episodes with heavy rainfall may occur even midwinter. At Svalbard Airport and Ny-Ålesund, the highest daily rainfalls of 43 and 98 mm respectively make up around 25% of the average annual rainfall. In the latest decades the frequency of heavy rainfalls has increased, and towards the end of the century an increase is projected for frequency as well as intensity of heavy rainfalls. For the fine scale simulations under emission scenario RCP8.5, the increase in heavy daily rainfall is projected to be about 20%, i.e. lower than for the total annual precipitation for this model.

Wind. Svalbard lies in the transit zone between cold Arctic air in the north and mild maritime air in the south. Thus the cyclonic activity is high, especially in winter. The area is dominated by northeasterly winds, though the local wind direction will be affected by topographic effects. The fine scale simulation projects

increased average wind speeds northeast of Spitsbergen, slightly reduced wind speeds west of Spitsbergen, and only minor changes in the fjord areas.

Hydrological variables

Runoff. Because runoff observation records are few and short, the runoff development in recent years is based on model calculations with re-analysis data (precipitation and temperature: Sval-Imp data) as input to a hydrological model. During the period 1980-2015, the annual runoff has increased by more than 35%. The increased runoff is mainly caused by enhanced glacier melt.

The average annual runoff for Svalbard in the reference period 1971–2000 is estimated to be 600 mm. The projections show a rapid and large increase towards the end of this century. Runoff using the two emission scenarios RCP4.5 and RCP8.5 is quite similar until the middle of the century (2031-2060) with more than 100% increase relative to the reference period. The increase is partly due to increased precipitation, but the main contribution is glacier melt caused by increasing temperatures. Towards the end of the century (2071-2100), the projected runoff for RCP8.5 increases further. This is caused by a strong warming (and consequently an increase in glacier meltwater) and a large increase in precipitation.

The modelled changes in individual catchments may deviate considerably from the projected changes in runoff for the total Svabard land area, mainly depending on the expected changes in glacier melt. One example is Bayelva, close to Ny-Ålesund, where the fraction of glaciers is 50% and the altitude ranges from 4 to 742 m a.s.l. For this catchment, the median RCP8.5 projection shows a more moderate increase in runoff towards the middle of the century, and a slight decrease thereafter because the glacier area and volume are so reduced that the glacier meltwater decreases even if the temperature increases.

Floods. The flood estimates for Svalbard are highly uncertain, but changes in the frequency and magnitude of floods are strongly linked to changes in precipitation, snow storage and glacier regimes.

In regions where the annual maximum snow storage is expected to decrease, snowmelt floods will become smaller. Increased precipitation and a larger fraction as rain will increase the magnitude and frequency of rain floods and combined snowmelt, glacier melt and rain floods. For the high emission scenario towards the end of the century, the glacier area and volume in several catchments will be reduced to the extent that the contribution from glacier meltwater to floods will be negligible.

With continued warming and melting of glaciers, glacial lake outburst floods (GLOFs) may become more frequent, but such floods will not necessarily affect settlements.

Snow. The snow season duration for the Svalbard land areas has decreased over the period 1958–2017 with approximately 20 days. The future snow conditions up to 2071–2100 strongly depend on the emission scenario. The median simulation with RCP4.5 still shows areas with the same, or slightly more, snow storage, while the median simulation with RCP8.5 shows a reduction in maximum snow storage of 50% or more over most of Svalbard. The fine scale simulation gives increased maximum snow storage (up to 100% for certain areas) for large areas in the northeast and reduced amounts in western and southern areas. The number of days with snow cover will be reduced all over Svalbard for both RCP4.5 and RCP8.5. In some areas the snow cover duration is only slightly reduced, in other areas it is drastically reduced. With increasing winter temperatures, the snow line will increase and the timing of maximum snow storage will shift from June (1971–2000) to May (2071–2100) in the fine scale RCP8.5 simulation.

Sediment transport and erosion. A warmer climate will affect the erosion intensity and increase the water discharge and sediment supply to the rivers from both glaciers with moraines and from areas without glaciers. The increased sediment supply may increase channel splitting and lateral activity of channels and expose adjacent slopes to erosion. This accelerated erosion may affect the tributaries first, and after some time, the large sandurs in the main valleys

Glaciers

Following deglaciation under early Holocene, most local glaciers in Svalbard disappeared during the Early Holocene around 9700 years before present. Glaciers reformed during the Late Holocene and reached their historical maxima when the Little Ice Age culminated in the 19th century.

Presently the glaciers in Svalbard are losing more ice through melting and calving than they are accumulating through snowfall. All of the well-observed glaciers are shrinking, and models and satellite measurements confirm that Svalbard as a whole is losing glacier mass. An average glacier area reduction of 7% was estimated from the period 1961-1990 to the 2000s. The glacier area was reduced in all regions. This loss of glacier mass and area is changing the landscape and contributing to sea-level rise. Presently more than half of Svalbard's ice area terminates in the ocean and are subject to calving, but future warming will lead to a decline in the number of these "tidewater glaciers" around Svalbard.

Variability in the glacier mass balance in Svalbard is primarily driven by summertime melt variations. Lengthening of the melt season and warmer summers in coming decades are likely to continue driving increased glacier melt and glacier retreat. Given the temperature increase projected by the fine scale simulation for emission scenario RCP8.5, the modelled glacier net mass balance becomes progressively more negative during the 21st century. The winter balance does not have a clear trend; the strong negative trend in net balance is driven entirely by increasingly negative summer balance. Comparing the two time periods 1971-2000 and 2071-2100 shows that the equilibrium line altitude (ELA) rises by 400 m on average, and that there is a five-fold increase in glacier mass loss. There is considerable spatial variability in these changes, with more pronounced ELA increases in the northwest and south of Svalbard than in the northeastern region, but due to the larger glacier area in the latter region, the change in overall mass loss is strongest there. There are some suggestions that increased melt hastens the triggering effect on surges (rapid glacier advance) and a number of large-scale surge events have been reported in Svalbard. These events affect the total ice discharge and have the potential to considerably increase the sea level contribution from land ice within short time.

Permafrost, landslides and avalanches

Permafrost. Svalbard has the warmest permafrost this far north in the Arctic. Mean permafrost temperatures at 10-20 m depth vary from about -2.5°C at coastal western sites to about -5°C in central parts. Since 2009 the permafrost temperatures have increased at rates between 0.06°C and 0.15°C per year at 10 m depth. In central Spitsbergen, at Janssonhaugen, a significant temperature increase can be detected down to 80 m depth reflecting a multi-decadal permafrost warming. In western and central parts of Spitsbergen the present thickness of the active layer is in the range of 100 to 200 cm. Since 2000 the active layer thickness in Adventdalen (sediments) and Janssonhaugen (rock) has deepened by respectively 0.6 cm and 1.6 cm per year. At Kapp Linné (rock) the active layer increased by 6.2 cm per year between 2009 and 2017.

Modelled ground temperatures indicate that near-surface permafrost in coastal and low altitude areas is projected to thaw before the end of the century under emission scenario RCP8.5. At some sites permafrost thaws are projected to reach depths of at least 5 meters, while permafrost still persists at 10 m depth and below. For most of the lowland landscape in western Svalbard, all available modelling results suggest that the limit between "permafrost remains (at least partly)" and "the upper meters of the permafrost thaws completely" towards the end of the century will be somewhere between the emission scenarios RCP4.5 and RCP8.5. Increases in the active layer thickness and permafrost temperature will speed up slope processes controlled by permafrost, with a marked increase in slope instability. Present and future permafrost warming and degradation will affect coastal erosion processes, especially where the coastline consists only of sediments.

Solifluction. A warmer permafrost and increased rainfall will speed up solifluction; - i.e. slowly deforming active layers moving downslope due to gravity. Solifluction sheets and lobes are widespread on the lower slopes in the Svalbard landscape.

Landslides and avalanches. Because meteorological factors are important triggers for landslides and avalanches, future climate change will very likely increase the frequency of most types of avalanches and landslides in the coming decades.

If more extreme events with heavy snowfall or heavy rain on snow occur, an increase in the occurrence of snow avalanches including wet snow avalanches and slushflows, can be expected. Towards the end of the century, in areas with a shorter snow season and a reduction in the maximum annual snow amounts, the probability of dry snow avalanches will decrease. However, the probability of wet snow avalanches and slushflows is expected to increase.

Degradation of permafrost may play an important role in the detachment of larger rockslides. Rising temperatures will in some areas lead to more freeze-thaw events, and therefore rockfall events may increase in the future. Increased depth of the active layer and higher permafrost temperature lead to more active slope processes and significantly greater instability in the mountain slopes. Combined with more precipitation and increased frequency of episodes of heavy rainfall on sloping terrain, this will increase the likelihood of various types of soil slides, including quick clay-like landslides.

Ocean climate

Oceanography. During the early Holocene, the climate of Svalbard was considerably warmer than present climate. Between 8200 and 6000 years ago shallow water temperatures off Svalbard were about 4°C warmer than present. Subsequently, water temperature cooled to present-day values about 4500 years ago. The observed temperatures have increased since 1970, and have been particularly high since the late 1990s. Recent changes in the large-scale atmospheric circulation patterns have brought warm Atlantic Water from the West Spits-

bergen Current onto the West Spitsbergen Shelf and further into the fjords even during winter. Especially the northern Barents Sea has experienced a rapid climate shift and is described as the "Arctic warming hotspot" where the surface warming and loss of winter sea ice is the largest in the entire Arctic. Projections under emission scenario RCP4.5 show that in fifty years, the surface waters around Svalbard will be about 1°C warmer than present. This is generally true for most areas that today have low concentration of sea ice, but some areas further south have an even stronger projected warming. A few areas, like the outer parts of Storfjorden and Fram Strait are projected to cool about 1°C. The Nordic and Barents Seas will probably continue to warm after 2070 unless the thermohaline convection, and thus the northward oceanic heat transport, is reduced.

Acidification. East of Svalbard the surface pH values increase northwards and towards the bottom. Aragonite saturation state is a measure of the ability for carbonate (aragonite) to form or dissolve. Temperature strongly influences the aragonite saturation state and the highest surface values are found in the south, where pH is lower than in colder, fresher northern water. Fresh water from ice melting plays an important role in modifying the waters around Svalbard. This is especially prominent in the waters close to glaciers and in the fjords. Sea ice acts as a barrier for diffusion of gases between ocean and atmosphere, and the distribution of sea ice in time and space strongly influences carbon chemistry dynamics in the waters around Svalbard. For the Nordic and Barents Seas, the pH under RCP4.5 is projected to decline by around 0.12 from year 2005 to 2070.

Sea ice. The ocean warming has halted sea ice from forming and has opened up large areas of ice-free waters around Svalbard. Global warming has likely lead to more wind-generated upward mixing of warm and saline Atlantic Water from about 200 m depth, preventing formation of sea ice. The ice export through the Fram Strait is an important part of the ice budget in the Arctic basin and since 1979 it has increased by about 6% per decade. In the last decade, the fjords on the west coast have been

almost ice-free in the winter and the whole Barents Sea, including the area east of Svalbard, has been ice-free for several months in the summer and autumn. For Kongsfjorden most years after 2006 had a low ice extent and a shorter season of fast ice than earlier, and during 1997-2016 the thickness of sea ice as well as snow cover on ice has become thinner.

The simulated changes in future sea ice concentration indicate a major reduction in the northern Barents Sea, a reduction in the western fjords, and a certain increase in the outer and western parts of Storfjorden. Areas with decreased sea ice concentration reflect increased sea surface temperature and vice versa. None of the global CMIP5 climate models are capable of simulating sufficient inflow of relatively warm Atlantic Water through the Barents Sea Opening, explaining a systematic bias for the recent Barents Sea ice loss. Because the Barents Sea also dominates the Arctic Ocean sea ice variability during winter, this missing warm Atlantic inflow has importance far beyond the region, possibly through altering the large-scale atmospheric circulation.

Sea level. Tide gauge records from Spitsbergen show negative trends in relative sea level from the mid-20th century to present. The main reason for the reduced sea level is high land uplift rates largely caused by the Earth's response to present-day glacier changes. The high uplift rates show large spatial variability; in west Spitsbergen the uplift rates are between 7 and 10 mm per year. Projections indicate that Spitsbergen will experience a fall in relative sea level over the 21st century for all emission scenarios. This fall is driven by reduced gravitational pull and by land uplift owing to future local ice mass losses. Thus increasing global

temperatures lead to more negative changes in relative sea level on Spitsbergen. This is the opposite of what is projected along the majority of the world's coastlines. The future sea level may deviate significantly from the latest IPCC main report if a collapse of the marine portions of the Antarctic ice sheet is triggered.

Uncertainties and use of projections

Traditionally, the major uncertainties in climate projections are related to 1) future anthropogenic emissions, 2) natural climate variations and 3) non-perfect climate models. In regions close to the marginal ice zone, such as Svalbard, systematic biases in the initial sea ice extent comes in as a fourth source of uncertainty, because it can influence projections far longer than a few decades.

The first type of uncertainty is here taken into account by using 2-3 emission scenarios wherever available. The second and third types of uncertainties are to some degree taken into account by giving intervals based on ensembles of several model calculations. However, these span only a part of the total uncertainty. Thus it cannot be ruled out that future climate changes could fall outside the intervals. Further, as a majority of the global climate models have too much sea ice for present day climate in the Svalbard area, the upper part of the span in changes in temperature and precipitation may be unrealistic.

If you plan to use climate projections in research and management, we therefore recommend that you contact relevant scientific communities. This may help in the interpretations of the results and to gain information on new knowledge.
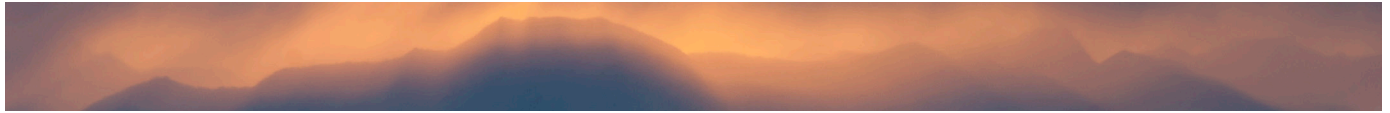
Sammendrag

Hovedfunn

For middels til høye scenarier for fremtidige klimagassutslipp beregnes følgende endringer for Svalbard fra 1971-2000 til 2071-2100:

- Årstemperaturen vil øke (ensemble-median ca. 10 ºC for høye og 7 ºC for middels utslipp)
- Årsnedbøren vil øke (ensemble-median ca. 65 % for høye og 45 % for middels utslipp)
- Hendelser med kraftig nedbør vil forekomme hyppigere og bli mer intense
- Vannføringen i elvene på Svalbard vil øke, men hvor mye vil være svært avhengig av hvor mye nedbør, temperatur og bidrag fra bresmelting øker
- I områder hvor det beregnes reduserte snømengder, forventes mindre snøsmelteflommer
- Økt nedbør, og en økende andel som regn, vil gi flere og større regnflommer og kombinerte snøsmelte-/bresmelte- og regnflommer
- Snøsesongen vil bli kortere
- Erosjon og sedimenttransport vil øke
- Permafrosten varmes opp over hele Svalbard og de øverste meterne av permafrosten vil tine i kyst- og lavereliggende områder (for høye utslipp)
- Mange typer snøskred og løsmasseskred vil forekomme hyppigere
- Både massebalanse for breer og breareal forventes å bli betydelig redusert innen 2100
- Økningen i massetap fra isbreer vil gi betydelig økning i bidrag til havnivåøkning
- På grunn av endringer i gravitasjon og stor landheving vil midlere havnivå ved Spitsbergen sannsynligvis bli lavere

En klimaprojeksjon for havområdene (for middels utslipp) gir fra 2010-2019 til 2060-69:

- En oppvarming av overflatevannet rundt Svalbard på i gjennomsnitt ca. 1 °C
- En betydelig reduksjon av sjøiskonsentrasjonen nord i Barentshavet

Mangelfull kunnskap om klimasystemets følsomhet og om fremtidige naturlige klimavariasjoner, samt utilstrekkelige klimamodeller, fører til stor usikkerhet i beregningene selv under et gitt utslippsscenario. Det er likevel klart at reduserte klimagassutslipp vil føre til reduserte forandringer i det fysiske klimaet.

Bakgrunn

Denne rapporten ble bestilt av Miljødirektoratet for å gi et kunnskapsgrunnlag for klimatilpasning på Svalbard. Rapporten inneholder beskrivelse av historisk klima, samt beregninger av fremtidig klimautvikling i atmosfæren, hydrosfæren, kryosfæren og havet, og inkluderer også effekter på fysisk natur, f.eks. knyttet til skredfare. Fremskrivningene for fremtidig klima er hovedsakelig basert på klimamodeller som ble benyttet i IPCCs femte hovedrapport (IPCC, 2013). Avhengig av tilgjengeligheten av modelldata benyttes tre scenarier for utslipp av klimagasser: "RCP8.5" ("business as usual", "høye utslipp"), "RCP4.5" (reduksjon etter 2040, "middels utslipp") og "RCP2.6" (drastiske kutt fra 2020; "lave utslipp"). Klimaendringene er beregnet frem til år 2100 i atmosfæren og frem til 2070 i havet.

Rapporten er i stor grad en oppsummering av eksisterende kunnskap fra vitenskapelig litteratur og modellresultater, f.eks. de regionale klimamodellene benyttet i Arctic CORDEX. I tillegg blir det også presentert nye resultat fra en finskala atmosfærisk regional klimamodell (COSMO-CLM). Disse resultatene er benyttet til å beregne endringer i bl.a. kraftig nedbør, frost-dager, snø, permafrost og isbreer. Det er også kjørt en hydrologisk modell for Svalbard for både nåtids og forventet fremtidig klima, basert på inngangsdata fra Arctic CORDEX. Også for havet er det blitt utført nye analyser basert på de beste tilgjengelige modelldataene. Nedenfor følger en oppsummering basert på en kombinasjon av foreliggende publisert kunnskap og nye resultater.

CLIMATE IN SVALBARD 2100

Atmosfæriske variable

Lufttemperatur og avledede variabler. Den gjennomsnittlige årstemperaturen (1971-2000) for de bemannede værstasjonene på Svalbard varierer fra -1,7 °C (Bjørnøya) til -5,9 °C (Svalbard lufthavn). Estimert årlig gjennomsnittstemperatur for Svalbards landområder er -8.7 °C. Forskjellen mellom denne verdien og stasjonsverdiene kan forklares ved at alle målestasjonene ligger i lavlandet i vestlige kystområder. Fra 1971 til 2017 var det en oppvarming på 3 - 5 °C (mindre i sør, mer i indre fjordstrøk), med størst økning om vinteren og minst om sommeren. For RCP8.5 viser medianprojeksjonene fra både regionale modeller og statistisk nedskalering en økning på nesten 10 °C i gjennomsnittlig årstemperatur fra 1971-2000 til 2071-2100. Den beregnede økningen er størst i nordøst og minst i sørvest. Usikkerheten er stor, og med finskala modellen beregnes det en økning på 7 °C for RCP8.5. For utslippsscenario RCP4.5 er beregnet medianverdi for økning i årstemperatur 6 - 7 °C, og for RCP2.6 ca. 4 °C.

Den beregnede temperaturøkningen medfører en betydelig økning i antall vekstdager for gress og en nedgang i antall frostdager. For antall dager per år med maksimumstemperatur over 0 °C og minimumstemperatur under 0 °C forventes det kun moderate endringer. Imidlertid forventes det en reduksjon i slike dager om sommeren og en økning om vinteren.

Nedbør. Gjennomsnittlig årsnedbør (1971-2000) målt på værstasjonene på Svalbard varierte fra 196 mm (Svalbard lufthavn) til 581 mm (Barentsburg). Estimert gjennomsnittlig årsnedbør for Svalbards landområder er ca. 720 mm. En del av forskjellen mellom målte og estimerte verdier skyldes at nedbøren øker med økende høyde over havet, samt at modellene ofte overestimerer nedbør i dette området. Det er imidlertid også kjent at nedbørmålerne, spesielt under snøfall og kraftig vind, ikke fanger opp all nedbør som faller. Historiske og beregnede fremtidige endringer er gitt i prosent av verdiene fra 1971-2000. På Bjørnøya og Hopen var det signifikant økning (20-30 %) i årsnedbør fra 1971 til 2017, hovedsakelig på grunn av økt nedbør vinter og vår. På Spitsbergen er det for året som

helhet lite tegn til endring i denne perioden, men det er en tendens til økning høst og vinter og minking vår og sommer. For utslippsscenario RCP8.5 viser de beregnede medianverdier fra regionale modeller en økning i årsnedbør for Svalbard på ca. 65 % fra 1971-2000 til 2071-2100. Usikkerheten er stor, og med finskala modellen beregnes det en økning på ca. 35 % for RCP8.5. For RCP4.5 er medianverdien for økning i årsnedbør ca. 45 %.

På Spitsbergen kan episoder med kraftig nedbør som regn forekomme når som helst på året, til og med midt på vinteren. For Svalbard lufthavn og Ny-Ålesund er de høyeste målte døgnsummene hhv. 43 og 98 mm; - dvs. omtrent 25 % av gjennomsnittlig årsnedbør kan falle i løpet av ett døgn. I de siste tiårene har hyppigheten av kraftige nedbørepisoder økt, og frem mot slutten av århundret er det forventet en økning både i hyppighet og intensitet av slike kraftige regnskyll. Simuleringer med finskala modellen for utslippscenario RCP8.5 gir en økning i kraftig 1-døgns nedbør på ca. 20 %, dvs. mindre enn økningen i total årsnedbør for den samme modellen.

Vind. Svalbard ligger i overgangssonen mellom kald arktisk luft i nord og mild maritim luft i sør. Dermed er lavtrykksaktiviteten høy, spesielt om vinteren. Området domineres av storstilt nordøstlig vind, men den lokale vindretningen blir påvirket av topografiske effekter. Med finskala modellen beregnes det økt gjennomsnittlig vindhastighet nordøst for Spitsbergen, litt redusert vindhastighet vest for Spitsbergen, og bare små endringer i fjordområdene.

Hydrologi

Vannføring/avrenning. Fordi det er få og korte vannføringsserier på Svalbard, er utviklingen i avrenningen de siste årene basert på modellberegninger med reanalyse-data (nedbør og temperatur: Sval-Imp data) som inngangsdata i den hydrologiske modellen. I perioden 1980-2015 har avrenningen økt med mer enn 35 %. Trolig skyldes økningen i hovedsak stor økning i bresmelting. Midlere årsavrenning for Svalbard i referanseperioden 1971-2000 er estimert til 600 mm. Fremskrivningene viser rask og stor økning fremover i

dette århundret. Avrenningen ved bruk av RCP4.5 og RCP8.5 er ganske lik frem mot midten av århundret (2031-2060) med over 100 % økning relativt til referanseperioden. Økningen skyldes delvis økt nedbør, men det store bidraget kommer fra nedsmeltning av breene forårsaket av økt temperatur. Mot slutten av århundret (2071-2100), øker avrenningen basert på RCP8.5 ytterligere. Dette er forårsaket av stor temperaturøkning (og følgelig økt mengde smeltevann fra breer) og stor økning i nedbør.

Modellerte endringer i avrenning for individuelle nedbørfelt kan avvike betydelig fra de beregnede endringene for hele Svalbard, avhengig av bidraget til avrenning fra bresmelting. Ett eksempel er Bayelva nær Ny-Ålesund hvor nedbørfeltet går fra 4 m o.h. til 742 m o.h., og med 50 % bre. Her viser fremskrivningene med RCP8.5 en mer moderat økning i vannføringen mot midten av århundret og en svak reduksjon etter dette fordi brearealet og volumet minker så mye at bresmeltingen avtar selv om temperaturen øker.

Flom. Flomestimatene for Svalbard er svært usikre, men endringen i antallet og størrelsen på flom er sterkt knyttet til endringer i nedbør, snøforhold og breer. I områder hvor en forventer reduserte snømengder, vil snøsmelteflommene bli mindre, mens økt nedbør og mer nedbør som regn vil gi flere og større regnflommer og kombinerte snø-/ bresmelte- og regnflommer. Med det høye utslippsscenariet vil brearealet og volumet i flere nedbørfelt reduseres så kraftig at bidraget fra bresmelting til flom blir neglisjerbart mot slutten av århundret. Med fortsatt kraftig temperaturøkning og nedsmelting av breene, kan forekomsten av jøkullaup øke, men slike flommer vil ikke nødvendigvis berøre bebodde områder.

Snø. Snøsesongens lengde for Svalbard sett under ett i perioden 1958-2017, er redusert med omtrent 20 dager. Fremtidige snøforhold for perioden 2071-2100 avhenger sterkt av utlippsscenario. Simuleringene med median RCP4.5 viser områder som fortsatt vil ha den samme eller litt økte snømengder, mens simuleringen med median RCP8.5 viser en reduksjon i maksimalt snømagasin på 50 % eller

mer for det meste av Svalbard. Finskala simuleringen gir økte snømengder (opp til 100 % økning) for store områder i nordøst, og reduserte snømengder i vest og sør. Snøsesongens lengde vil i følge simuleringene avta for hele Svalbard med både RCP4.5 og RCP8.5. Noen steder er reduksjonen liten, mens den andre steder er dramatisk. Med økt vintertemperatur vil snøgrensen ligge høyere over havet og tidspunktet for maksimalt snømagasin vil forskyves fra juni i perioden 1971-2000 til mai i perioden 2071-2100 i finskala RCP8.5 simularingen.

Sedimenttransport og erosjon. Et varmere klima vil gi økt vannføring og erosjonsintensitet både fra breer med morene og fra brefrie områder. Dette vil øke tilførselen av sedimenter til elvene. Økt sedimenttransport i vassdragene vil påvirke elveløpene. I de fleste vassdragene er det utviklet sandurer som er karakterisert ved mange løpsforgreninger og hyppig sideveis forflytning av elveløpene. Denne typen løpsendringer vil øke ytterligere når klimaet endres.

Isbreer

Etter nedsmeltingen av et større sammenhengende isdekke under tidlig Holocen, forsvant en stor del av de lokale isbreene på Svalbard for rundt 9 700 år siden. Isbreer ble dannet påny under den sene Holocen og nådde sitt historiske maksimum da den lille istid kulminerte i det 19. århundret. For tiden mister isbreene på Svalbard mer is gjennom smelting og kalving enn de øker på grunn av nedbør som snø. Alle de godt observerte isbreene minker, og modeller og satellittmålinger bekrefter at hele øygruppen mister ismasse. En gjennomsnittlig isbre-reduksjon på 7 % ble estimert fra perioden 1961-1990 til 2000-tallet. Brearealet ble redusert i alle regioner. Dette tapet av isbre-masse og -areal endrer landskapet og bidrar til havnivåstigning. I dag ender mer enn halvparten av Svalbards isbreer i havet, men fremtidig smelting vil føre til en nedgang i antall slike breer rundt Svalbard. Variabiliteten i ismassebalansen på Svalbard skyldes primært variasjoner i avsmelting om sommeren. Varmere somre og en forlengelse av smeltesesongen i de kommende tiårene vil trolig fortsette å drive økt smelting og tilbaketrekning av

isbreer. Med den temperaturøkningen som beregnes av finskala modellen for utslippsscenario RCP8.5, blir den modellerte nettobalansen for isbreer stadig mer negativ utover i dette århundret. Vinterbalansen har ingen klar trend; - den sterke negative utviklingen i nettobalansen er drevet utelukkende av stadig mer negativ sommerbalanse. Sammenligning av de to tidsperiodene 1971-2000 og 2071-2100 viser at like-vektshøyden (ELA) stiger med i gjennomsnitt 400 m, og at det er en fem ganger økning i masse-tap. Det er betydelig romlig variabilitet i disse endringene, med større ELA økninger i nordvest og sør på Svalbard enn i den nordøstlige regionen. Men på grunn av det store isbrearealet i sistnevnte region er endringen i det totale massetapet størst i nordøst. Det er mulig at økt smelting kan ha en utløsende effekt på rask fremrykking og kalving av isbreer, og det har blitt rapportert om en rekke slike hendelser på Svalbard. Disse hendelsene påvirker den totale nettobalansen av isbreer, og har potensial til å øke bidraget til havnivånivåendring fra landis i løpet av kort tid.

Permafrost og skred

Permafrost. Svalbard har den varmeste permafrost-en så langt nord i Arktis. Gjennomsnittlig perma-frost temperaturer på 10-20 m dybde varierer fra ca -2,5 °C langs kysten i vest til ca -5 °C i sentrale deler av Spitsbergen. Siden 2009 har temperaturen i permafrosten i gjennomsnitt økt med mellom 0,06 °C og 0,15 °C per år på 10 meters dyp. I sentrale deler av Spitsbergen (ved Janssonhaugen), kan en signifikant temperaturøkning observeres ned til 80 m dybde. Dette gjenspeiler en oppvarm-ing som har pågått over mange tiår. I vestlige og sentrale deler av Spitsbergen er den nåværende tykkelsen av det aktive laget (som tiner og fryser hver sommer over permafrosten) på mellom 100 og 200 cm. Siden 2000 har tykkelsen av det aktive laget i Adventdalen og ved Janssonhaugen økt med henholdsvis 0,6 cm (sedimenter) og 1,6 cm per år (fjell). På Kapp Linné økte det aktive laget med 6,2 cm per år mellom 2009 og 2017 i fjell.

Modellering av temperatur i bakken indikerer at de øverste metrene av permafrosten i kyst- og lavere-liggende områder tiner før slutten av århundret ved utslippsscenario RCP8.5. På enkelte steder tiner permafrosten ned til minst 5 meter under bakke-overflaten, mens det fortsatt vil være permafrost dypere enn 10 meter. For de fleste lavtliggende- og vestlige områder på Svalbard antyder alle tilgjengelige modelleringsresultater at grensen mellom at "permafrost forblir (i hvert fall delvis)" og "de øverste meterne av permafrosten tiner helt" mot slutten av hundreåret, ligger et sted mellom utslippsscenarioene RCP4.5 og RCP8.5. Økt dybde av det aktive laget og høyere permafrosttemperatur fører til mer aktive skråningsprosesser og betydelig større ustabilitet i fjellsidene, noe som øker skred-faren. Nåværende og fremtidig oppvarming og tining av permafrost vil påvirke erosjonsprosesser langs kysten, spesielt der kystlinjen bare består av sedimenter.

Solifluksjon. Varmere permafrost og økt nedbør vil øke hastigheten på solifluksjon; - dvs. langsom deformering av aktive lag som beveger seg nedover på grunn av tyngdekraften. Solifluksjon er utbredt på nedre skråninger i Svalbard-landskapet.

Skred. Fordi meteorologiske faktorer er viktige utløsningsårsaker til skred, vil klimaendringer føre til økt sannsynlighet for de fleste typer skred i de kommende tiårene.

Ved en økning av ekstreme hendelser med kraftig snøfall eller kraftig regn på snø, kan vi forvente en økning i antallet snøskred, inkludert våtsnøskred og sørpeskred. Mot slutten av århundret, i områder hvor snøsesongen blir kortere og snømengdene reduseres, vil sannsynlighetne for tørrsnøskred reduseres. Imidlertid øker sannsynligheten for våtsnøskred og sørpeskred.

Oppvarmingen av permafrost kan spille en rolle i fremtidig utløsning av større fjellskred. Økt tem-peratur vil mange steder gi flere fryse-tine-sykluser og kan dermed føre til flere steinsprang. Økt dybde av det aktive laget og høyere permafrosttemperatur fører til mer aktive skråningsprosesser og betydelig større ustabilitet i fjellsidene. Sammen med mer nedbør og økt hyppighet av episoder med kraftig nedbør i skrånende terreng, vil dette øke sannsyn-ligheten for ulike typer løsmasseskred, inkludert kvikkleire-lignende skred i utsatte områder.

CLIMATE IN SVALBARD 2100

Havklima

Oseanografi. Under tidlig Holocen var klimaet på Svalbard betydelig varmere enn i dagens klima. Fra ca. 8200 til 6000 år siden var overflatetemperaturen i havområdene utenfor Svalbard ca. 4 °C høyere enn i dagens klima. Deretter avtok havtemperaturen til omtrent dagens nivå for ca. 4500 år siden. Observert havtemperatur har økt siden 1970, og har vært spesielt høy siden slutten av 1990-tallet. Nylige endringer i de storstilte atmosfæriske sirkulasjons-mønstrene har ført til at varmt atlanterhavsvann fra Vestspitsbergenstrømmen også vinterstid strømmer inn på sokkelen vest for Spitsbergen og videre inn i fjordene. Spesielt har det nordlige Barentshavet opplevd et raskt klimaskifte; - dette blir beskrevet som "the Arctic warming hotspot" fordi oppvarmingen og tapet av sjøis om vinteren er større her enn i andre deler av Arktis.

Fremskrivninger under utslippsscenario RCP4.5 viser at om 50 år vil overflatevannet rundt Svalbard være ca 1 °C varmere enn for dagens klima. Dette gjelder generelt for de fleste områder som i dag har lav konsentrasjon av sjøis, men noen områder lenger sør får sterkere oppvarming. Noen få områder, som de ytre delene av Storfjorden og Framstredet, avkjøles med rundt 1 °C. Norskehavet og Barentshavet vil sannsynligvis fortsete å varmes opp etter 2070, med mindre transporten nordover av varmt atlanterhavsvann blir redusert.

Havforsuring. Øst for Svalbard øker pH-verdien nordover og nedover i dypet. Aragonittmetning gir et mål for muligheten for dannelse eller oppløsning av kalsiumkarbonat (aragonitt).Temperaturen på-virker aragonittmetningen, og de høyeste overflate-verdiene er funnet i sør. Her er pH-verdien lavere enn i nordlige farvann, som er kaldere og som inneholder mer ferskvann. Ferskvann fra issmelting spiller en viktig rolle i å modifisere vannmassene rundt Svalbard. Dette er spesielt fremtredende i vannmasser nær isbreer og i fjordene. Havis fungerer som en barriere for diffusjon av gasser mellom hav og atmosfære, og fordeling av sjøis i tid og rom påvirker i betydelig grad dynamikken i karbonkjemien i farvannet rundt Svalbard. For Nor-skehavet og Barentshavet er pH-verdien for

utslippsscenario RCP4.5 antatt å falle med rundt 0,12 fra 2005 til 2070.

Sjøis. Oppvarmingen i havet har hindret dannelsen av sjøis om vinteren og store areal rundt Svalbard er blitt isfrie hele året. Den globale oppvarmingen har sannsynligvis medført en mer vindgenerert vertikal blanding av varmt og salt atlanterhavsvann fra ca. 200 m dybde, noe som har hindret dannelsen av sjøis. Iseksporten gjennom Framstredet er en viktig del av isbudsjettet i det Arktiske bassenget, og siden 1979 har denne transporten økt med om lag 6 % per tiår. Det siste tiåret har fjordene på vestkysten vært nesten isfrie om vinteren, og hele Barentshavet, inkludert området øst for Svalbard, har vært isfritt i flere måneder om sommeren og høsten. Etter 2006 har Kongsfjorden de fleste år hatt lite sjøis og en kortere fastis sesong enn tidligere. Fra 1997 til 2016 har også tykkelsen av sjøis og snødekke på is blitt tynnere.

Den beregnede fremtidige sjøis-konsentrasjonen viser fortsatt stor reduksjon i det nordlige Barentshavet, noe reduksjon i de vestlige fjordene og en viss økning i de ytre og vestlige delene av Storfjorden. Områder med redusert sjøis-konsen-trasjon gjenspeiler økt sjøoverflatetemperatur og omvendt. De globale CMIP5-klimamodellene simulerer ikke tilstrekkelig tilførsel av relativt varmt atlanterhavsvann inn i Barentshavet, noe som forklarer en systematisk feil i det simulerte tapet av sjøis i Barentshavet om vinteren de senere årene. Da variasjonene i Barentshavet også dominerer variasjonene i sjøis i Arktis om vinteren, har denne manglende innstrømmingen av varmt atlantisk vann stor betydning også utenfor regionen, fordi den muligens kan påvirke beregningene av den storstilte atmosfæriske sirkulasjon.

Havnivå. Tidevannsmålinger fra Spitsbergen viser negative trender i relativt havnivå fra midten av det 20. århundret til i dag. Hovedårsaken til synkende havnivå er stor landheving som i stor grad skyldes jordoverflatens respons på minkende isbremasse. Den kraftige landhevningen har stor romlig variabilitet; - for vestlige deler av Spitsbergen er landhevingen mellom 7 og 10 mm / år. Prognoser indikerer at Spitsbergen vil oppleve et fall i rela-

tivt havnivå videre utover i det 21. århundret for alle utslippsscenarioer. Dette fallet skyldes i stor grad landheving og redusert gravitasjonskraft på grunn av fremtidige lokale ismassetap. Dermed fører økende globaltemperatur til økende negative endringer i relativt havnivå på Spitsbergen; - dvs. det motsatte av det som beregnes for det meste av jordens kystlinjer. Utviklingen av fremtidig havnivå kan avvike vesentlig fra resultatene fra den siste hovedrapporten fra IPCC dersom det skjer et sammenbrudd av de marine deler av iskappen rundt Antarktis.

Usikkerhet og bruk av fremskrivninger.

Tradisjonelt er de store usikkerhetene i klimaprojeksjonene knyttet til 1) fremtidige menneskeskapte utslipp, 2) naturlige klimavariasjoner og 3) utilstrekkelige klimamodeller. I regioner nær isgrensen, som Svalbard, kommer systematiske feil (bias) i starttilstanden av sjøisutbredelse inn som en fjerde kilde til usikkerhet. Denne biasen kan påvirke fremskrivninger betydelig lenger frem enn noen få tiår.

Den første typen usikkerhet er i denne rapporten tatt i betraktning ved å bruke 2-3 utslippsscenarioer når dette er tilgjengelig. Den andre og tredje type usikkerhet er til en viss grad tatt i betraktning ved å gi intervaller basert på grupper av flere modellberegninger (ensembler). Imidlertid spenner disse bare en del av den totale usikkerheten. Det kan således ikke utelukkes at fremtidige klimaendringer kan falle utenfor disse intervallene. Videre, ettersom et flertall av de globale klimamodellene har for mye sjøis i Svalbard-området, kan øvre del av spennet i endringer i temperatur og nedbør være urealistisk.

Hvis du vil bruke klimaberegninger i forskning og forvaltning, anbefaler vi derfor at du kontakter de relevante vitenskapelige miljøer. Disse kan bidra til tolking av resultatene og til å gi informasjon om ny kunnskap.

1. Introduction

1.1 Rationale and background

The air temperature in Svalbard has increased by 3 to 5 °C during the last 4 to 5 decades. In the later years, there have been episodes of heavy rainfall during winter. Fjords along the west coast have become ice free most of the year. The permafrost has warmed considerably, and there have been a number of avalanches in and near Longyearbyen. These changes affect ecosystems as well as societies in a number of ways. The global warming is projected to continue in the coming decades. How will this warming affect the climate, hydrology and physical nature in and around Svalbard?

The present report was commissioned by the Norwegian Environment Agency, to provide information relevant for climate change adaptation and climate change effect studies in Svalbard. Svalbard was not included in the similar reports for the Norwegian mainland, "Climate in Norway 2100" (Hanssen-Bauer et al. 2015, 2017), for several reasons. Observational data as well as model data are more limited in the Svalbard area than for the Norwegian mainland. Further, discrepancies between different climate models are especially large in the Arctic, indicating an even larger uncertainty than at lower latitudes. It was thus concluded that a special report for Svalbard would be needed to achieve a useful knowledge base for climate change adaptation in this area.

This report summarizes updated information on the past, present and projected future climate in the Svalbard area. The word "climate" is here used in a broad sense, including the atmosphere, hydrosphere, cryosphere and ocean. The report also includes effects on the physical nature e.g. permafrost and various types of landslides and avalanches. The projections for future climate are based on results from the CMIP5 global climate models (IPCC, 2013), and on available regional climate model results for the atmosphere and ocean. Dependent on availability of model data, three scenarios for emissions of greenhouse gases are used: "RCP8.5" ("business as usual"), "RCP4.5" (reductions after 2040) and "RCP2.6" (drastic cuts from 2020) and the time horizon for the projections varies from 50 to 100 years.

The report is to a large degree an assessment of existing literature and model results. However, it also includes results from novel atmospheric and hydrological models. Statistical methods were applied to downscale temperature from all CMIP5 models. Further, a fine scale atmospheric regional climate model was applied for estimating changes in e.g. heavy rainfall, frost days, snow, permafrost and glaciers. Emission scenario RCP8.5 was chosen for this model run, as the Norwegian white paper on climate change adaptation (Meld. St. 33 (2012–2013)) says that to be precautionary, the government wants risk assessments of climate change to be based on the high climate projections. The hydrological model was run using bias-adjusted and downscaled input from the regional climate models made available through the Arctic CORDEX initiative (http://www.climate-cryosphere.org/activities/targeted/polar-cordex/arctic) under emission scenarios RCP8.5 and RCP4.5.

1.2 Contents of the report

The report is organized as follows:

Chapter 2 provides general background information about the climate system in the Svalbard area.

Chapter 3 provides information on datasets, models and methods applied in the report.

Chapter 4 to Chapter 8 describe the past, present and projected/expected future conditions concerning atmospheric variables (Chapter 4), hydrological variables (Chapter 5), glaciers (Chapter 6), permafrost, avalanches and landslides (Chapter 7) and ocean variables, including sea ice and sea level (Chapter 8).

In Chapter 9, sources for uncertainty and application of results from the report are discussed.

Chapter 10 is a crosscutting chapter, where results from all chapters are combined and specifically presented for Longyearbyen, which is the largest settlement and the administrative centre of Svalbard.

2. The climate system in the Svalbard area, including adjacent sea areas

2.1 Atmospheric circulation

Large scale atmospheric circulation

The large scale circulation in the Arctic is in the winter strongly influenced by the semi-permanent low and high pressure systems in the mid latitudes governing the heat and moisture transport into the Arctic (Figure 2.1.1 a). Over the ocean there are two distinct low-pressure systems (the Icelandic low in the north Atlantic and the Aleutian low in the Pacific) while land areas are dominated by high pressure systems (Siberian high over Russia and the weaker Beaufort high over North America).
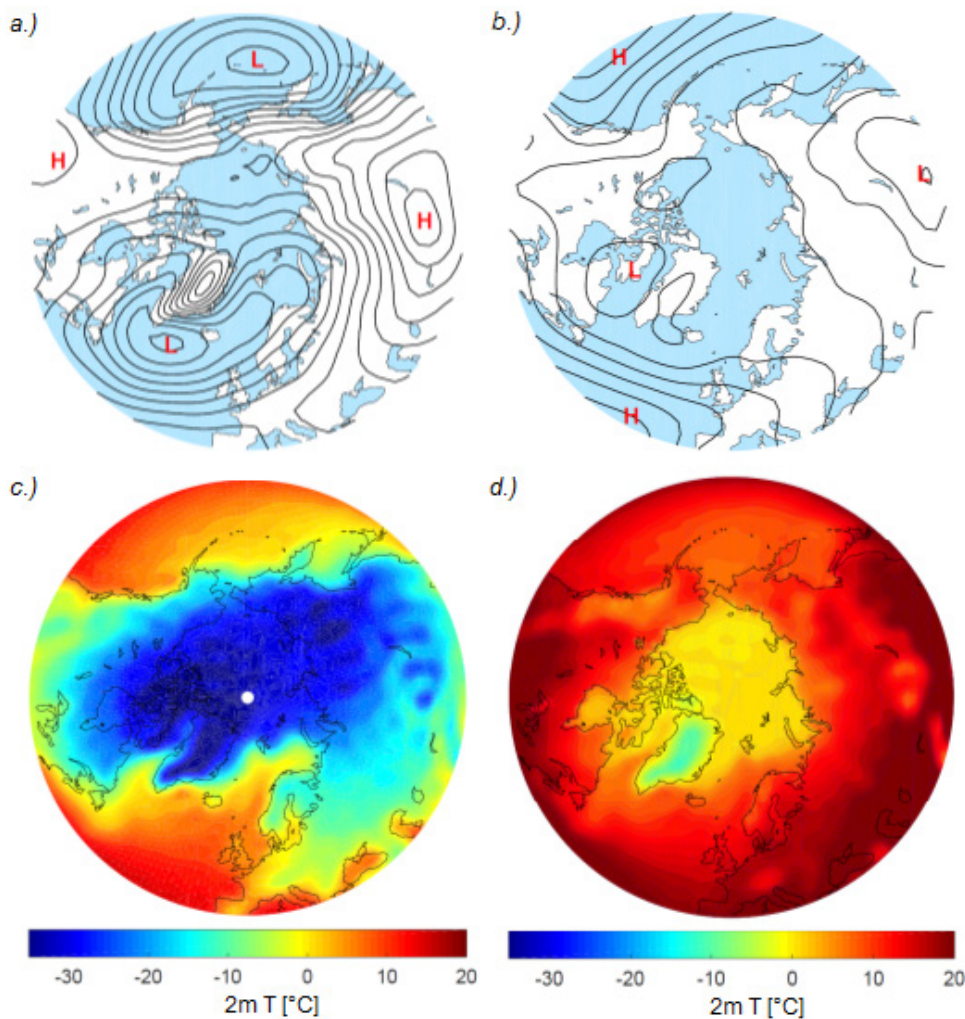
Figure 2.1.1: (a) 1961-1990 average wintertime (DJF) and (b) summertime (JJA) Mean Sea Level Pressure (L indicates low pressure centers and H high pressure centers). Estimated 2m temperatures (°C) in (c) winter (DJF) and (d) summer (JJA) based on reanalysis data. Source: NCEP reanalysis.

In summertime the pressure centers weakens considerably and the central Arctic is dominated by a weak low pressure (Figure 2.1.1 b). The imprint of the large scale circulation can be seen clearly on Arctic winter temperatures (Figure 2.1.1 c) with intrusion of warmer air west of the oceanic low pressure centers and tongues of cold air east of the Siberian and Beaufort High. In summertime (Figure 2.1.1 d) the temperature is to a large extent following the sea-ice cover and is near 0 °C across large parts of the central Arctic.

Climate in Svalbard and surrounding areas

Svalbard and the surrounding ocean are considerably milder, wetter and cloudier than the average for the latitude. This is mainly caused by atmospheric heat and moisture transport associated with the Icelandic low and the warm West Spitsbergen Current (WSC), which runs along the western coastline of Spitsbergen. The West Spitsbergen Current is particularly important in the shaping of the island's climatic conditions through its release of heat during wintertime and its influence on the concentration of sea ice (Walczowski and Piechura, 2011). As a consequence of the strong influence of atmospheric heat transport and the West Spitsbergen Current Spitsbergen, cold season temperature variability is very pronounced at Svalbard.

Averaged over the year cyclonic (counterclockwise) atmospheric circulation patterns are more frequent than anticyclonic (clockwise) with the share of cyclonic patterns increasing in winter and autumn. The most often frequented air mass is flow from the east sector (particularly in autumn and winter) as a consequence of the low pressure systems in the Norwegian Sea (Przybylak and Maszewski, 2012).

The meteorological stations are to a large extent situated on the western side of Spitsbergen and close to the coast. Thus, the climate of Spitsbergen interior and the surrounding islands is still rather unknown. Attempts have been made to downscale coarse resolution atmospheric reanalysis using detailed topographical information (Østby et al. 2017) in order to get a spatial picture of Svalbard's climatology. The downscaled reanalysis dataset, Sval-Imp (more information can be found in Chapter 3.1) has been evaluated against observed temperatures in Vikhamar-Schuler et al. (2019). The main conclusion was that this reanalysis gives a realistic picture of the temperature conditions in the Svalbard area with annual biases being less than ±1°C. The lowest temperatures are found in mountain- and glacial areas in the north (in Spitsbergen: north of Isfjorden; Figure 2.1.2 a). In winter (see Figure 4.1.2), the coastal areas in the north-east are particularly cold as a consequence of the cold air masses from the north east.
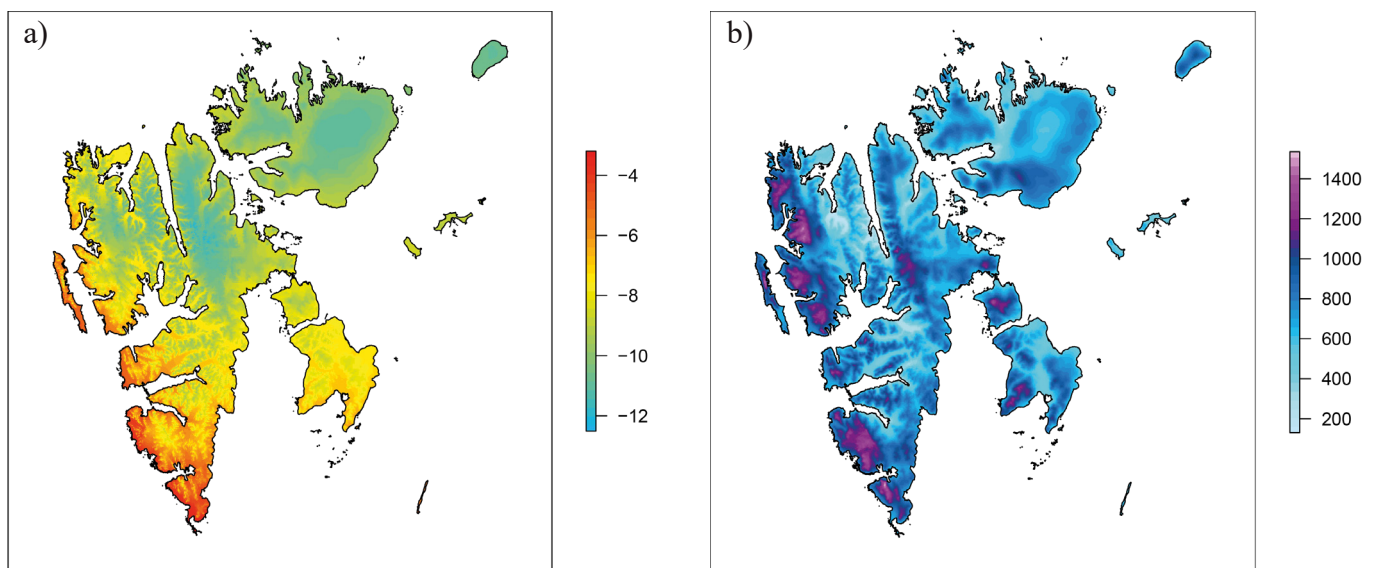
Figure 2.1.2. Downscaled annual temperature (°C; a) and precipitation (mm; b) from the Sval-Imp dataset (Østby et al., 2017) averaged over the period 1971-2000. Seasonal maps for summer and winter are found in Chapter 4.

The highest temperatures are found in the south-southwestern parts of the archipelago where the West Spitsbergen Current is playing an important climatic role.

In situ precipitation observations from Svalbard are sparse and undercatch in precipitation gauges during snowfall at high wind speeds reduces the quality of the measurements (Førland and Hanssen-Bauer, 2000). Additionally, the limited number of stations makes the observational data insufficient to provide a representative description of precipitation over the entire Svalbard archipelago (Chapter 3.1). A spatial picture covering Svalbard

was attempted by Østby et al. (2017) by down-scaling the reanalysis using a simple orographic precipitation model (Figure 2.1.2 b). There is a clear topographic influence on the precipitation, which is particularly pronounced in autumn and winter (Vikhamar-Schuler et al., 2019). The main features in this map are supported by a shorter dynamical downscaling simulation by Dobler (2019), but the seasonal cycle is stronger in the Dobler (2019) results with early summer being the driest and autumn the wettest. Highest annual precipitation is seen on the western side of the mountain ranges, with secondary maxima on the eastern part of Edgeøya and on the southwestern part of Nordaustlandet.

2.2 Ocean circulation and sea ice

The ocean climate around Svalbard is closely connected to the large-scale circulation between the North Atlantic and the Arctic Ocean as sketched in Figures 2.2.1, where the red arrows indicate relative warm waters and the blue relative cold. The Atlantic Water in the Gulf Stream propagates northeast-wards as the North Atlantic Current from the North American coast across the North Atlantic between the Subpolar Gyre and the Subtropical Gyre and further towards the Nordic Seas. The relative strength of these to gyres contributes to variability

of the hydrographic properties in the Atlantic Water (Hatun et al, 2005). Similarly, atmospheric pressure systems and the corresponding variability in these are essential to the exchange of waters between the North Atlantic and the Nordic Seas over the Greenland-Scotland Ridge (Sandø et al., 2012).

The branch of the North Atlantic Current that continues into the Nordic Seas, follows the continental slope along the Norwegian Coast as the Norwegian Atlantic Current and releases heat to the
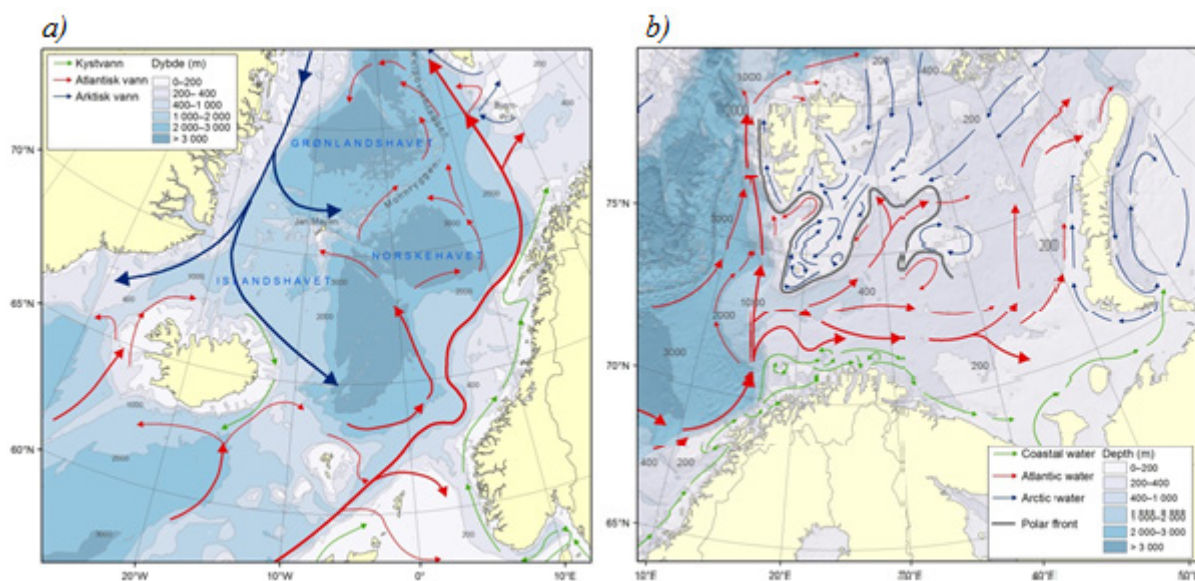
Figure 2.2.1 Circulation and bathymetry in the Nordic Seas (a) and circulation and bathygraphy around Svalbard and in the Barents Sea (b).

atmosphere in terms of air-sea fluxes (Mork et al., 2014), which is decisive for the relative mild climate in the regions surrounding the Nordic Seas. There is also a continuous mixing between the Atlantic Water in the Norwegian Atlantic Current and cold and fresh Arctic Water from the East Icelandic Current as well as fresh water from the Norwegian Coastal Current. Finally, when the Atlantic Water reaches the Arctic Ocean around Svalbard, it submerges below the sea ice and further into the Arctic Ocean. Due to a fresh halocline between the sea ice and the Atlantic Water deeper below, there is usually limited direct contact between the sea ice and this water mass, preventing large scale melting of sea ice along the path of the northward flowing Atlantic Water into the Arctic.

Cold and fresher waters enter the Nordic Seas from the Arctic through the Fram Strait west of Svalbard as the East Greenland Current. In addition, there is a quite substantial transport of sea ice along with the current. This current continues along the Greenland coast in the Labrador Sea and further southward along the Canadian coast as the Labrador Current. East of Newfoundland the Labrador Current meets the northeastward flowing Gulf Stream and parts of it is deflected eastwards. The mixing of these currents constitutes thereby the North Atlantic Current which propagates northeastwards along the southern limb of the Subpolar Gyre (see also Figure 8.1.1). The strength and width of this Subpolar Gyre is mainly governed by a complex interplay between the deep overflow from the Nordic Seas, convective processes in the Labrador Sea, and the atmospheric phenomenon called the North Atlantic Oscillation (Langehaug et al., 2012). The North Atlantic Oscillation is defined as fluctuations in the relative strength of the Icelandic low and the Azores high, and controls the strength and direction of the south-westerly winds as well as storm tracks in the North Atlantic, and thereby also the climate in the Nordic Seas region.

As mentioned above, the varying width and strength of the Subpolar Gyre generates hydrographic anomalies that propagates northeastwards in the North Atlantic, and to some extent also into the Nordic Seas and further northwards along the

Norwegian coast. At the continental shelf break close to the Barents Sea Opening, the Norwegian Atlantic Current splits into two branches where the western part continues towards Svalbard as the West Spitsbergen Current and the eastern part into the Barents Sea. The Atlantic waters enter the Barents Sea between the Bear Island (Bjørnøya) and Norway through the Barents Sea Opening and flows northeastwards until it enters the Arctic Ocean between Franz Josef Land and Novaya Zemlya. In the Barents Sea the warm and saline Atlantic Water meets the colder and fresher Arctic Water in the Polar Front, as indicated by the grey line in Figure 2.2.1 b. Close to Svalbard this front is strongly attached to the bathymetry and follows the southern continental slopes of Svalbard. Further east, the front is wider and more variable.

The heat anomalies associated with the propagating hydrographic anomalies from the North Atlantic have shown to be important for the regional climate both in the Barents Sea and in the waters close to Svalbard. In the Fram Strait, the West Spitsbergen Current also splits into two branches where one continues through the Fram Strait and then eastwards along the northern coast of Svalbard, whereas the other branch turns left in the Fram Strait and then southwards into the Greenland Sea. Due to the cold air and relative warm water masses, the air-sea fluxes in the Greenland Sea can be quite large where the ocean is in direct contact with the atmosphere. During winter, the surface waters may then be subject to strong cooling, become denser than the intermediate waters below and sink to great depths, a process referred to as convection and deep-water formation. The air temperatures during winter is strongly influenced by the North Atlantic Oscillation, and when this index is low, the surface cooling is particularly high, and large amounts of dense water can be formed and flow over the Green-land-Scotland Ridge into the North Atlantic as a deep-water current. These series of events constitute important components of the North Atlantic-Arctic Ocean climate variability which also affects Svalbard. The most important of these is probably the northward propagation of salt and heat anomalies which contribute to major anomalies in the sea ice extent north of Svalbard (Ivanov et al., 2016),

but also further downstream at intermediate depths in the Arctic Ocean and into the Barents Sea between Svalbard and Franz Josef Land.

Episodes of Atlantic Water intrusion on the West Spitsbergen Shelf represent an increased oceanic heat flux into the fjord systems and toward the Svalbard glaciers (Nilsen et al., 2008). Convergence, mixing, and exchange of Atlantic Water, Arctic water, and freshwater from land characterize the West Spitsbergen Shelf. Within an annual cycle, the waters on the shelf and in the adjacent fjords switch from a state of Arctic dominance (cold and less saline in winter) to one of Atlantic dominance (warm and saline in summer) and back. Hence, the local climate in Svalbard is dependent on important interaction processes between the fjord/shelf and the Atlantic Water from the West Spitsbergen Current (WSC). The WSC is topographically steered along the continental slope, and is the major source of warm and saline Atlantic Water to the Arctic Ocean. The WSC is subject to cooling and freshening as it flows northward, and interactions with West Spitsbergen fjords such as Isfjorden and Kongsfjorden

can make a significant contribution to this modification. Understanding the mechanisms governing the interaction between the WSC and West Spitsbergen fjords is therefore important, not only for explaining environmental conditions inside the fjords, but also for explaining variability in the Arctic Ocean.

The regional effects of climate change can be heavily modulated by internal variability such as the Atlantic Multidecadal Oscillation which works on timescales from seasons to decades. In addition, the effects may be modified by feedbacks in the climate system such as an increased warming in the Arctic regions due increased melting of sea ice, less reflection of solar radiation, and thereby more absorption of solar heat, the so-called ice-albedo effect (Screen and Simmonds, 2010). Such changes in sea ice extent and thickness in combination with propagating hydrographic anomalies in the Atlantic Water may lead to even stronger anomalies in the sea ice cover along the path of the Atlantic Water as shown (Ivanov et al., 2016, Polyakov et al., 2017) and illustrated in Figure 7.1.1.

2.3 Arctic amplification and feedbacks

The term *Arctic amplification* refers to a greater temperature change near the poles compared to the rest of the globe for a given global climate forcing (change in greenhouse gasses, solar insolation etc.). This can be seen clearly in the observational record where the warming trend in the Arctic is twice as

large as the global average in recent decades (Figure 2.3.1).

The cause of this is partly linked to climate feedbacks. A climate feedback is an internal climate process that amplifies or dampens the initial climate
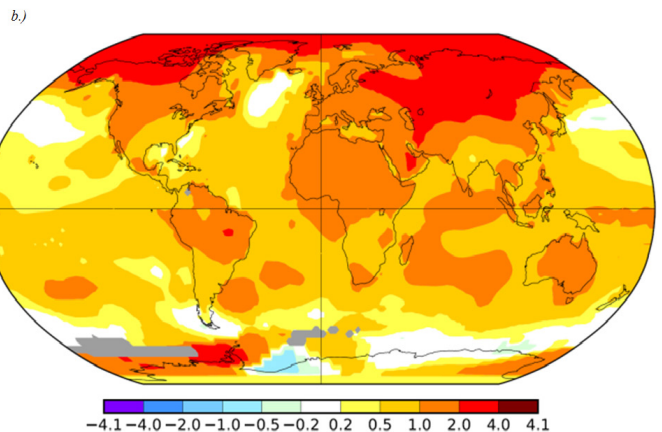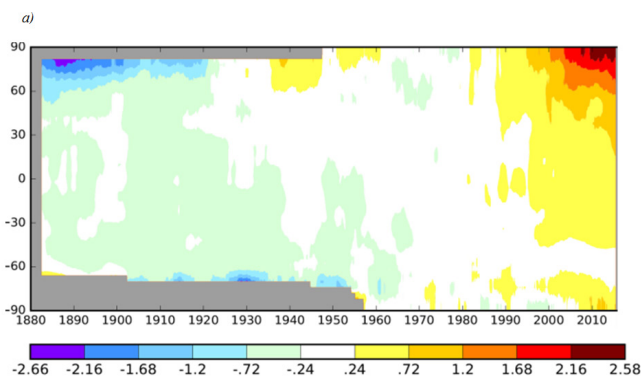
Figure 2.3.1: 5-years zonal mean temperature anomalies (°C) compared to the 1961-1990 normal (a) and temperature trends (°C) from 1950-2017 (b). Data from NASA Goddard Institute for Space Studies (NASA GISS).

response to a specific climate forcing. If a process amplifies the climate response it is denoted as a positive feedback, if it dampens the response it is a negative feedback.

The direct response of an object to increased radiation is that it heats up and efficiently radiates out (emits) energy to dampen the effect of the increased incoming radiation. This is done rather efficient as the amount of emitted radiation goes with the fourth power of the temperature. This is known as Stefan-Boltzmann's law. If no feedbacks were present in the climate system one would still expect a weak Arctic amplification as the temperature of the atmospheric layer that efficiently radiates to space is lower in the Arctic than the in lower latitudes, meaning that the Arctic is less efficient in getting rid of energy (Pithan and Mauritsen, 2014). In the literature this is often termed the Planck feedback, despite the fact that it refers to the direct response. Another direct effect is caused by dismissing sea ice (not including the feedbacks related to change in albedo) which expose the Arctic atmosphere to a larger area of relatively warm oceanic temperatures which will amplify the near surface temperature change.

Other potential candidates for the amplification are the water vapour feedback, the surface albedo feedback, cloud feedbacks and the lapse rate feedbacks (see Figure 2.3.2 for a description of the different feedbacks). Studies suggest that the largest feedback in the Arctic is the lapse rate feedback (Pithan and Mauritsen, 2014; Graversen et al, 2014). The lapse rate feedback is the coupling between surface air temperature changes and changes in the atmospheric layers that radiates efficiently out to space (around 5000 meters above the surface). For the greenhouse effect to work, the atmospheric temperature has to be colder in the region that efficiently radiate out to space than at the surface. If this temperature difference is altered it will change the efficiency of the greenhouse effect. This is what is called the lapse rate feedback. In the Arctic the temperature change space than at the surface. If this temperature difference is altered it will change the efficiency of the greenhouse effect. This is what is called the lapse rate feedback. In the Arctic the temperature change for a given climate forcing is largest near the surface. This means that temperature difference between the surface and the atmospheric layers that radiates efficiently out to space is getting larger and the efficiency of the greenhouse effect increases. The surface albedo feedback connected to the reduction of snow and ice is thought to be the second large contributor to the Arctic amplification. However, model simulations where the two feedbacks explained above are suppressed indicate that a large portion of the Arctic amplification is unexplained by these feedbacks. This indicates an important role of the direct effects and other feedbacks.
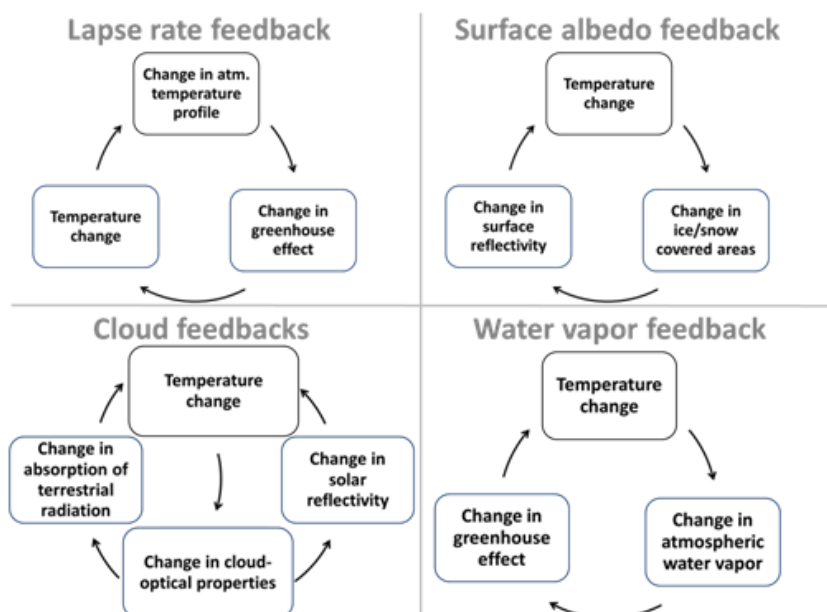
Figure 2.3.2: Four important radiative feedbacks.

It should be noted that feedback analysis do not give much insight into which physical processes that are the driving causes of the Arctic amplification as the feedbacks are the sum of the interplay between a wide range of physical processes that are closely coupled to each other. Among others, changes and variability in the northward atmospheric and oceanic energy transport (Feldl et al. 2017), clouds and atmospheric moisture content (Cao et al, 2017) and the stability of the atmospheric boundary layer (Esau and Zilitinkevich, 2010) has been shown to play important roles in the amplification.

3. Methods, data, models

This chapter comprises methods, data and models that have been used to assess the state of the current climate and future climate change. The chapter is divided into six subchapters covering methods and data with respect to atmosphere (3.1), hydrology (3.2), glaciers (3.3), permafrost (3.4), ocean (3.5) and sea level (3.6).

3.1 Methods and data, atmosphere

3.1.1 Observations and observation-based datasets

The first permanent weather station in the Svalbard region was established in Green Harbour (near Barentsburg) in 1911. During the past 100 years, Norway, Russia and Poland have operated regular weather stations for shorter or longer time periods at several sites in the region. The measurements include temperature, atmospheric pressure, humidity, wind speed, wind direction, and precipitation. Manual observations are usually taken 4-8 times daily, while at automatic weather stations (Figure 3.1.1) measurements are taken at least once an hour. A survey of regular manual and automatic weather stations in the Svalbard area is given in Vikhamar-Schuler et al. (2019).

Due to large climate gradients and harsh weather conditions in the Arctic, even small relocations or changes in environment at the measuring sites may cause substantial changes in measuring conditions. Also, instrumental changes and transition from manual to automatic observations may influence the homogeneity of the long-term climate series. Measuring precipitation in the Arctic is a challenge; - precipitation may be overestimated because of contributions from blowing and drifting snow. In addition, depending on wind exposure, precipitation gauges do not completely capture precipitation, resulting sometimes in a considerable "undercatch". This is especially significant for snowfall during strong winds. Førland and Hanssen-Bauer (2000) found the "true" precipitation to be almost twice the measured amount in Ny-Ålesund.

Figure 3.1.1 Campaign weather station at Klauva, with view towards Sassendalen. Photo: Ketil Isaksen, MET.

It is not trivial to study long-term changes in observed weather elements in the Svalbard region. Just a few stations have long observational series, and identification and adjustment of inhomogeneities in Arctic climate series is hampered by the sparse station network. By combining series from several measuring sites - including observations made by hunting and scientific expeditions - a homogenized, composite temperature time series for Longyearbyen/Svalbard Airport has been extended back to 1898 (Nordli et al., 2014), and a precipitation time series back to 1912 (Nordli et al., 1996). Also, for other Svalbard stations (e.g. Ny-Ålesund and Isfjord Radio) the observational precipitation and/or temperature series have been extended back in time and homogenized (Nordli et al., 1996; Førland et al., 1997b). At Hopen, a relocation of the gauge in 1997 led to a severe homogeneity break in the precipitation series; - and the values before 1997 are adjusted by a factor of 0,60 for annual precipitation and between 0,41 and 0,82 for seasonal values (Vikhamar-Schuler et al., 2019). Original as well as extended, homogenized series for all weather stations are available at www.eklima.met.no.

Most of the regular weather stations are situated in western parts of Spitsbergen (Figure 3.1.2), and none are elevated above 40 m above sea level. Thus, neither temperature nor precipitation from these stations is representative for the Svalbard land area. Temperatures are usually lower in the inland, and because of orographic enhancement, precipitation at higher elevations may be substantially higher than at the coastal stations. Near Ny-Ålesund an increase of 20 % per 100 m was found for summer precipitation, at least for elevations up to 300 m a.s.l. (Førland et al., 1997a). For snow precipitation, Sand et al., (2003); - based on three years of snow surveys as well as previous studies, found an average vertical gradient of snow precipitation of 16 % per 100 m elevation. Figure 2.1.2b illustrates the strong topographical influence on precipitation in the Svalbard region.

To illustrate historical climate conditions also in areas without measurements, high-resolution datasets based on reanalysis are applied. Combining the TOPOscale method (Fiddes and Gruber, 2014) with a linear model of orographic precipitation (Smith and Barstad, 2004; Schuler et al., 2008), Østby et al. (2017) used a statistical model to downscale ERA-40 and ERA-Interim reanalyses to spatial resolution of 1 km with a model output frequency of 6-hours covering the period 1958-2017. The dataset ("Sval-Imp" (Svalbard impact assessment forcing dataset, version 1; (Schuler, 2018)) comprises variables to resolve the surface energy balance (downwelling shortwave and longwave radiation, temperature, humidity and windspeed) as well as precipitation. Also MET Norway carried out a regional climate model simulation with the COSMO-CLM forced by ERA-Interim to produce simulations with hourly output with a spatial resolution of 2.5 km. This simulation covers the period 2004-2017 and is named "CCLM data set" (see details in ch. 3.1.4). In this report, the Sval-Imp data set is used for the reanalysis-based description of present climate conditions (see ch. 4).

The Sval-Imp and CCLM data sets were evaluated against observed temperature and precipitation at Hopen, Svalbard Airport and Ny-Ålesund (Vikhamar-Schuler et al., 2019). For Hopen, the Sval-Imp data set has a warm bias of 0.2 – 0.7 °C for all seasons in the reference period 1971-2000 (annual bias 0.5 °C). For the period 1988-2017 there was no bias. The other stations have cold annual biases (Ny-Ålesund: 0.4 °C; Svalbard Airport: 0.8°C) in the period 1971-2000. These were rather similar for the last 30 years. The cold biases are at maximum in summer, while minor warm biases are seen during winter.

In terms of precipitation amount, the Sval-Imp data set shows a positive bias (overestimation) at Hopen, Svalbard Airport and Ny-Ålesund (Vikhamar-Schuler et al., 2019). The Sval-Imp data set overestimates the annual precipitation by 50-150 % for the period 1988-2017. For most stations the difference between modelled and measured precipitation may be explained by undercatch in the precipitation gauges during events with snowfall and strong winds.
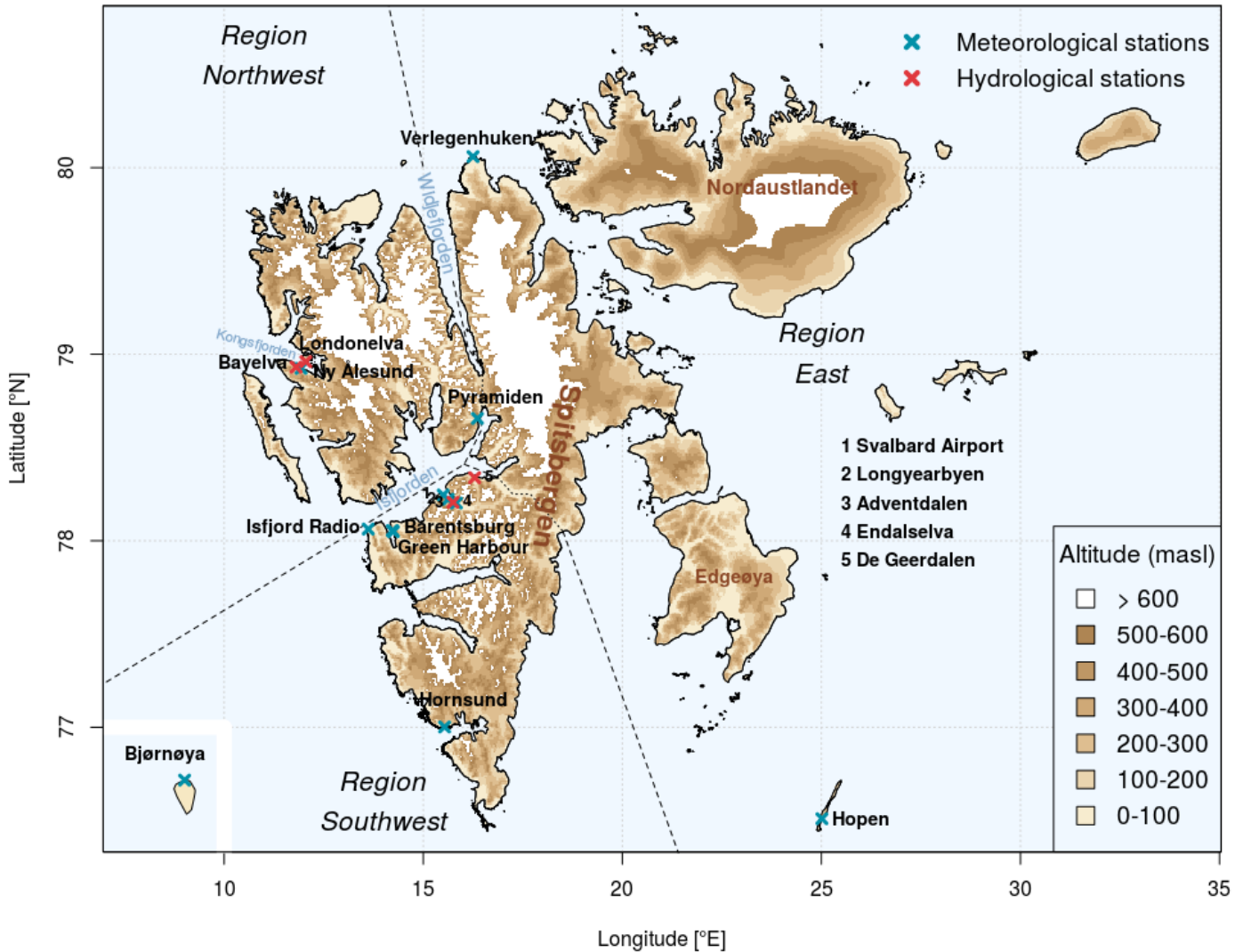
Figure 3.1.2 Regular meteorological and hydrological measurement stations at Svalbard.

Testing for historical trends in observed and modelled time series was performed with the non-parametric Mann-Kendall test, which may be used without knowing the distribution of the time series as it is a rank test. In order to study variations on selected time scales, graphs of the time series were smoothed by a Gaussian filter. Details on the use of Mann-Kendall trend test and Gaussian smoothing on Svalbard temperature series are presented by Gjelten et al. (2016).

3.1.2 Emission scenarios and climate models

Climate projections depend on different global emission scenarios. These are given in so-called "Representative Concentration Pathways (RCPs)" that are based on concentrations of greenhouse gases (GHG) in the atmosphere over time (IPCC,

2013). RCPs are given as an additional human-induced radiative forcing affecting the atmosphere since 2006 until 2100. The unit is Watt per square meter, e.g., the scenario RCP2.6 gives an additional warming effect of 2.6 W/m$^{-2.}$ In this report we mainly address the scenarios RCP8.5, RCP4.5 and RCP2.6 depending if climate model data is available. The scenario RCP2.6 implies drastic reduction of GHG emissions throughout the century, starting already before 2020 (see Figure 3.1.3 left). RCP4.5 implies a slow increase of emissions until 2050 followed by emission reductions. RCP8.5 implies that GHG emissions will continue to increase with a similar rate as before 2005 and reach a rate of approximately 100 Gt/year around 2070 (see Figure 3.1.3a)). For the high GHG emission scenario, RCP8.5, a mean global temperature
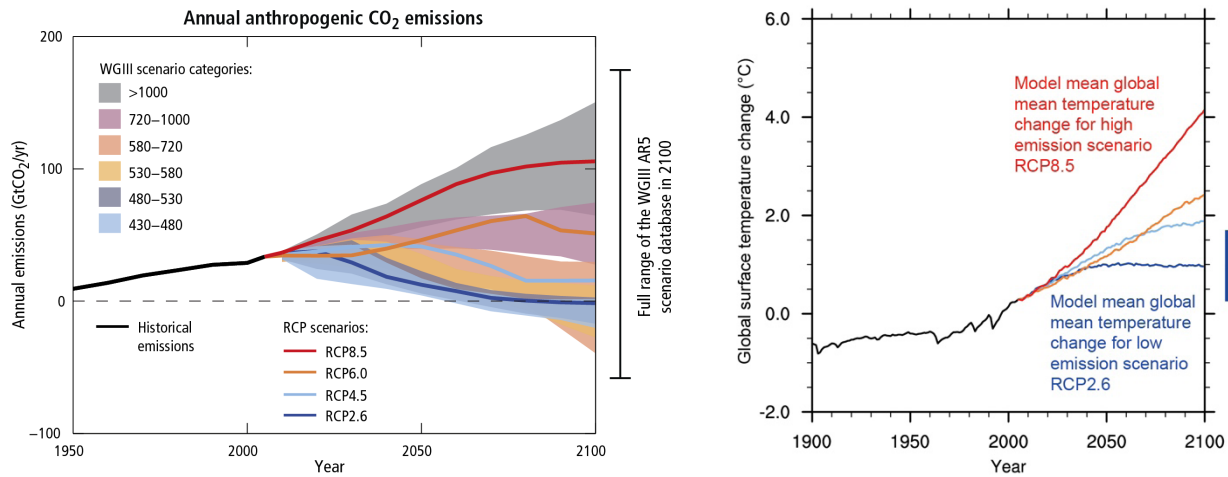
Figure 3.1.3 left) Historical and projected annual greenhouse gas emission pathways in gigaton carbon dioxide per year from 1950 until 2100 according to four scenarios (IPCC, 2013); right) annual global mean temperature anomalies w.r.t. the 1986-2005 global average (IPCC, 2013).

increase of 4°C is projected (see Figure 3.1.3 right)). For the low GHG emission scenario, RCP2.6, a warming by 1°C is projected by year 2040 and remains constant until the end of the century. Note that these temperature changes are given relative to the period 1986-2005. To find the warming compared to preindustrial time, about 0.6 °C should be added.

3.1.3 Climate models and downscaling

The only approach to calculate a possible future climate on Earth is to use data from global climate models or Earth system models (ESMs) that are forced with different future GHG emission scenarios (see Figure 3.1.3). These simulations are performed by several research institutions around the world coordinated by the World Climate Research Programme. Current experiments comprise the fifth phase of the Coupled Model Inter-comparison Project (CMIP5). Since ESMs are run over the whole globe over a long period of time, such simulations are computationally very expensive and have therefore constrains, e.g. in terms of horizontal and vertical resolution.

To project future climate for the archipelago of Svalbard is a challenge due to two main reasons. (i) global climate models have a coarse horizontal resolution of typically 100x100 km^2, thus they are not fit-for-purpose to resolve key atmospheric processes, such as atmospheric circulation and its

interaction with the ocean and sea ice or the topographical influence on the airflow (Koenigk et al., 2015). (ii) Sea-ice concentration and extent is often overestimated for the present climate in ESMs. This may lead to a large, probably unrealistically high, temperature increase when the sea-ice cover around Svalbard will have been disappeared in a future climate. Despite improvements of the sea-ice representation in ESMs, there is still a large spread between the models in calculating present and future climate conditions (Stroeve et al., 2012; Koenigk et al., 2014).

Climate models are used to simulate the state of the Earth's climate for both the past and the future. They are able to reproduce observed large-scale phenomena, such as major wind systems and temperature patterns, based on many grid boxes. However, global climate models have a minimum skilful scale due to the way they are constructed, which means that individual quite coarsely sized grid box calculations are subject to substantial inaccuracies. This means that global climate models provide only limited information about the character of local climate (e.g. for Spitsbergen, Bjørnøya, and Hopen). Consequently, it is necessary to downscale results from climate models to a higher horizontal and temporal resolution. There are two approaches to perform downscaling, (i) empirical-statistical and (ii) dynamical. Although both methods have advantages and disadvantages, they can act

complementary. Both methods are briefly described below.

The local climate is affected by geography, the large-scale phenomena, and processes over a wider region. The dependency between the different spatial and temporal scales can be used to enhance the information about the local climate. **Empirical-statistical downscaling** (ESD) is a technique that makes use of the dependency between both the large-scale conditions as well as systemic effects of the geography to estimate the local temperature or precipitation. It makes use of different sources of information (empirical from observations and statistical theory), requires little computational resources, and can make use of large-scale features that are skilfully simulated by the ESMs and bypass biases associated with local details.

One of the main strengths of empirical-statistical downscaling is that it is ideal for downscaling large multi-model ensembles of ESM simulations to capture the range of natural variability and accommodate for biases between ESMs. Hence, it provides a picture of both the likely outlook as well as information about uncertainties. Drawbacks with empirical-statistical downscaling differ to those of dynamical downscaling models and include weak connections between predictors and predictands and the requirement of high-quality and long series of observations. In this report ESD was applied for downscaling temperature from all available CMIP5 models (see Appendix 2, Table A.2.2).

The calibration of ESD models was done with detrended data, and the models were subsequently evaluated by replacing the detrended with the original data for comparing the predicted trends with those observed. The models were also tested through a standard cross-validation. The predictors used to describe the large-scale conditions were represented through common empirical orthogonal functions (EOFs) (Benestad, 2001) to ensure the same spatial patterns used for model calibration were also used in projections. Furthermore, these common EOFs facilitated an evaluation of the

representation of the large-scale conditions in the ESM simulations. The downscaling applied to Svalbard involved multi-model ensembles, and the evaluation of the downscaled ensemble also involved testing whether the downscaled temperatures were subject to similar statistics as those observed. Hence, an evaluation was carried out on an ensemble basis in addition to the traditional evaluation of individual simulations (Benestad et al., 2016).

In **dynamical downscaling**, data from global climate models are used as input to regional climate models. Just as ESMs, regional climate models are formulated on the basis of dynamic and thermo-dynamical laws. They are applied for the region of interest and can therefore be run with an increased horizontal grid resolution. The increased grid resolution enables regional climate models to resolve regional weather phenomena on a smaller scale and therefore in a more realistic way. In practice, at the end of such a computationally expensive modelling chain, more data points with more valuable information within a region is available. Due to the huge computational costs, dynamical downscaling is performed in international initiatives for chosen regions. **Arctic CORDEX** is an international initiative to dynamically downscale atmospheric data from CMIP5 simulations for the Arctic region by using an ensemble of regional climate models.

The Arctic CORDEX simulations (Appendix A1, Table A1.1) enable the analysis of future changes in temperature, precipitation and many more variables often used in impact models. One should be aware of, that a horizontal grid of 0.44° (~50 km) is still quite coarse with respect to Svalbard's size, complex topography and complex processes between open sea, sea-ice, land and atmosphere.

In this report, the reference period (current climate) is defined as the period 1971-2000. Projected mean annual and seasonal changes in temperature and precipitation have been calculated for the middle (2031-2060), and the end of the century, 2071-2100.

3.1.4 Fine-scale modelling

As discussed by Prein et al. (2015), climate model simulations at a convection-permitting scale (i.e., a grid resolution < 4 km) can provide a clear added-value compared to lower resolution simulations due to improved representation of physical processes. Additionally, a study by Mölg and Kaser (2001) has shown that statistical post-processing (bias-correction or downscaling) and its associated uncertainties can be avoided due to the high grid resolution. High-resolution regional climate models have thus the potential to provide local climate information as well as data suited to directly drive impact models.

MET Norway has therefore run the COSMO-CLM (Früh et al., 2016) at a convection-permitting scale focusing over the Svalbard area (Dobler, 2019). The meteorological fields from the global MPI-ESM-LR Earth system model (Giorgetta et al., 2013) have been downscaled to 0.22° over northern Europe, followed by a further dynamical downscaling step to 0.022° (around 2.5 km) over Svalbard. The simulations cover the time periods 1971-2000 and 2071-2100, using the high GHG emission scenario RCP8.5.

In the COSMO-CLM (CCLM) simulations, the sea surface temperature and concentration of sea-ice is specified by the driving ESM. Although the ESMs include an ocean model with a higher spatial resolution than the atmospheric part, the resolution is still coarser than in the regional climate model. This is partly considered by interpolating the global data to the regional climate model grid and land-sea mask, but biases originating from the global model will still remain.

Evaluation of sea-ice concentration in the MPI-ESM-LR driven 0.22° CCLM run against HadISST analyses (Rayner et al., 2003) shows that the model is capable to reproduce historical sea-ice concentrations (Dobler, 2019), although it simulates too high sea-ice concentrations north of Svalbard and west of Novaya Zemlya. For summer, the MPI-ESM-LR shows generally too low concentrations of sea-ice for the high Arctic. Altogether, the MPI-ESM-LR

shows a good representation of sea-ice, but the shortcomings mentioned above should be kept in mind, since climate in the Svalbard region is strongly influenced by the sea surface temperature and sea-ice conditions.

At a grid resolution of 2.5 km, regional climate model simulations are extremely computationally expensive. Thus, the simulations are limited to the downscaling of a single ESM projection for two time slices of 30 years at the end of the 20th and 21st century. Although this single simulation does not provide robust projections, robustness can be achieved by comparison to other regional climate model projections (e.g. those available by Arctic CORDEX) and ensembles of statistically downscaled ESMs. Furthermore, Giorgi et al. (2016) showed that the downscaling signal for precipitation and temperature in all RCMs they looked at over the European Alps, is roughly in line with the ensemble average downscaling signal, regardless of the sign and intensity of the large-scale change in the single RCMs.

Thus, assuming the same downscaling signal for the Arctic CORDEX ensemble average and the CCLM, the signal from the CCLM simulation can be added to the mean Arctic CORDEX signal. Basically, this is a spatial interpolation, adding the CCLM residuals to the Arctic CORDEX mean to improve the spatial resolution but maintaining the spatial mean. Note that this method is only applied to create the maps of mean climate changes over Svalbard in Chapter 4, while for tables and quantitative measures, unaltered Arctic CORDEX data is used.

Due to the long-term temperature memory inherent in permafrost and poly-thermal glacier systems, data from transient runs are required for glacier mass balance and permafrost modelling, rather than time slices representative for different states of a long-term evolution. To fill the simulation gap 2001-2070, the STatistical Analogue Resampling Scheme (STARS, Orlowsky et al. 2008) is applied. STARS is a statistical climate model that has already been used to generate climate projections for different regions of the world (e.g., Zhu et al. 2013, Feldhoff et al., 2015,

Lutz and Gerstengabe, 2015) and is computationally much cheaper than a dynamical regional climate model. More information on the STARS model is provided at https://www.pik-potsdam.de/research/climate-impacts-and-vulnerabilities/models/stars/star-statistical-regional-model.

Usually, STARS is applied on observation or re-analysis data to extend them to the (near) future following a prescribed temperature trend. Here, we have applied STARS to the two 30-year time slices modelled by the CCLM to extend the simulations into the uncovered time period 2001-2070. The historical simulation (1971-2000) is used to simulate the near future (2001-2035) while the far future projection (2071-2100) is used to simulate the intermediate period (2036-2070). Thus, it is possible to combine the advantage of the high-resolution dynamical model (well resolved spatial fields, coherence between different variables) with the advantage of a statistical model (low computational costs) to provide transient climate projections for impact modelling.

3.2 Methods and data, hydrology

Two important purposes of this report are to: (1) characterize the present state of hydrological conditions in the Svalbard Archipelago based on observed data of the hydrology and the cryosphere supported by hydrological model results; and (2) describe the impacts of climate change on land surface water balance and flow processes using hydrological model simulations. The model has algorithms for describing hydrological processes including mass balance of glaciers at a range of temporal and spatial scales, and for solving problems relevant for climate change impact studies.

3.2.1 The rivers in Svalbard

In Svalbard, large parts of the rivers are braided. That is, they are composed of a network of river channels separated by bars. The channel splitting is caused by deposition of coarse sediment carried

Figure 3.2.1 The valley sandur system and the delta in the lower part of Adventdalen. Left: Todalselva with its old river fan is eroded by the river of the main valley. Photo: The Norwegian Polar Institute

as bed load during high water discharge. Braided rivers are characterized by relatively large sediment loads, steep gradients and broad and deep channels formed in coarse grain sizes. For a given gradient and moderate grain size, there is a threshold level of sediment load that may transform a meandering river into a braided one. In Svalbard, a major part of the sediment budget is supplied from glaciers and in such cases; the braided river systems are named sandurs. Meandering channel systems are rare in Svalbard and occur only in smaller streams. At least two types of sandur systems may be recognized. The extension and development of the smaller systems like the one in Bayelva reflect the activity of the nearby glaciers, Brøggerbreene and the erosion of their moraines. The large sandurs that are developed in the large open valleys of for example Adventdalen (Figure 3.2.1), are composed of sediment delivered from a number of glacier fed tributaries.

Valley walls confine most of the sandurs in Svalbard. These type of systems are termed valley sandurs according to the classification introduced by Krigstrøm (1962). River fans accumulate where the tributaries enter the main valley and the sandurs grow in size downstream as more sediment is supplied to the system. The lower part of Adventdalen is an example of delta formation as the sandur system meets the sea (Figure 3.2.1).

Anastomosing rivers or streams are similar to braided rivers in that they consist of a network of channels. However the channels are low-gradient, narrow, deep channels with stable banks in contrast to braided rivers, which form on steeper gradients and display less bank stability. Anastomosing river reaches with floodplains covered by fine fractions seems to be rare in Svalbard, but have been observed in the lower part of Reindalen.

Because the rivers consist of a network of constantly changing channels, it is difficult to obtain a stable river profile and maintain continuous river level and river flow measurements over time. Two problems arise, the profile itself can undergo a gradual displacement and the "moving river channel" may move or destroy measurement equipment.

3.2.2 Observations

Hydrological processes in Svalbard have been monitored by several institutions, including the Norwegian Water Resource and Energy Directorate (NVE) that have been running a program for observing streamflow in several catchments since the beginning of the 1990's. Today, there are only a few stations with continuous measurements of hydrological processes in the Svalbard Archipelago. This report makes use of discharge measurements in the two catchments Bayelva and De Geerdalen (Figure 3.1.2).
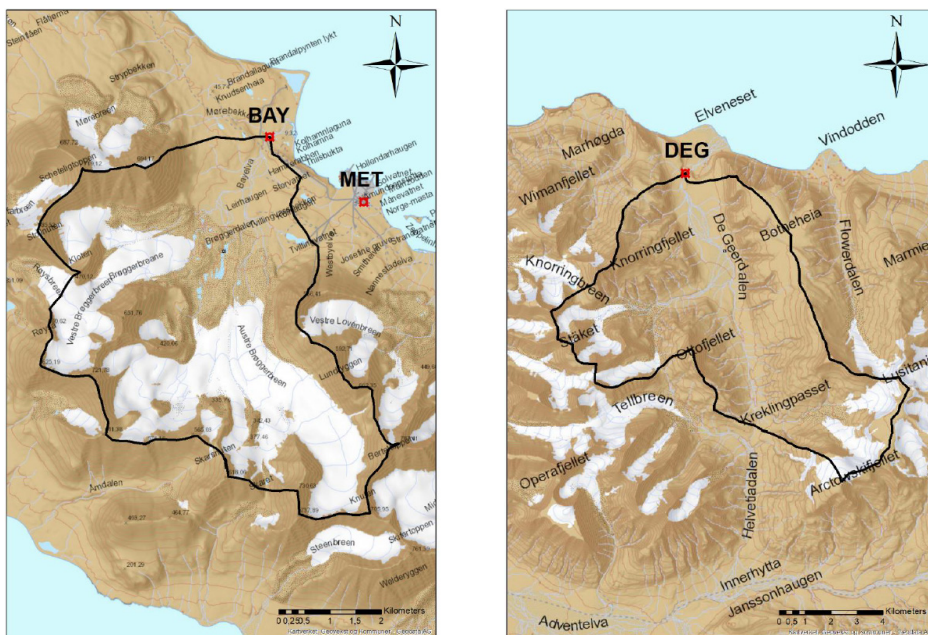
Figure 3.2.2 Location of the catchments Bayelva (left) and De Geerdalen (right), (Haagmans, 2018). (a) Details of Bayelva. Discharge gauging stations are located at BAY, meteorological station in Ny-Ålesund is marked as MET. (b) Details of De Geerdalen. Discharge gauging stations are located at DEG.

The Bayelva station is located close to Ny Ålesund, at 78°55'N, 11°56'E. It has a catchment area of 31 km^2 and a mean altitude of 265 m a.s.l. (Haagmans, 2018). With a mean annual temperature of -5.7 °C, conditions are favourable for glaciers. As much as 50 percent of the catchment is covered by glaciers (Figure 3.2.2a), with a maximum ice thickness of 100 m (Bruland and Hagen 2002; Sund 2008). The discharge station has been operated since 1989. The quality of the rating curve is considered poor due to an unstable profile situated on permafrost, and too few discharge measurements (Stenius, 2016).

The De Geerdalen station is located 20 km northeast of Longyearbyen, at 78°16'N, 11°19'E. At 78 km^2, its catchment is about twice the size of Bayelva (Figure 3.2.2b), and the mean altitude is 410 m a.s.l. (Haagmans, 2018). The mean annual temperature is -5.9 °C and the precipitation is approximately half of the precipitation received in Bayelva. Ten percent of the catchment is covered by glaciers. Discharge has been measured since 1991, but winter measurements are prone to errors due to ice jamming (Stenius, 2016).

As the gauging stations are encapsulated in ice during winter and river flow is freezing, river flow is set to zero in the winter period from approximately October to June (H. Songe, pers. comm.). The combined effects of a sparse stations network, short observation records and measurement errors due to difficulties with operating stations in the Arctic environment leads to a high degree of uncertainty in the discharge observations.

3.2.3 Hydrological modelling

Due to the sparse station network in the Arctic, hydrological models that describe the water balance of the land surface are necessary for determining the impacts of climate change on land surface hydrological processes. The Arctic landscape is characterized by mountains, glaciers, alpine and tundra vegetation species, a large number of lakes and bogs, and a shallow layer of surface deposits consisting of glacial tills. In this environment, water balance studies must focus on the spatial distribution of landscape elements that are significant for glacier mass balance, snow cover, subsurface moisture conditions, runoff and evapotranspiration fluxes. A framework for modelling of land surface hydrology in Arctic environments is therefore provided by models that integrate the contributions from several small scale elements.

A spatially distributed version of the HBV hydrological model (Bergström et al., 1995; Beldring et al., 2003) has been adopted to water balance simulations in Arctic environments with glaciers. The model performs water balance calculations for 1 by 1 km^2 grid cell landscape elements characterized by their elevation and land use. Each grid cell may be divided into a maximum of four land surface classes; two land use zones with different vegetation, a lake area and a glacier area. A regionally applicable set of model parameters was determined by calibrating the model with the restriction that the same parameter values are used for all computational elements of the model that fall into the same class for land surface properties. The model has been modified to take glacier melt into account. For the historic simulations, 1971–2005, the glacier area was kept static. For the simulations 2006–2100, the glacier thickness was reduced as a function of glacier melt. When/if no ice remained in the grid cell, the glacier covered area was reduced by 1 km^2 (the size of one grid cell). A dynamic treatment of glacier mass balance changes (Huss et al., 2010; Li et al., 2015) was also attempted, but was discarded because of too rapid melting and retreat of glaciers. The discharge from catchments in the Svalbard Archipelago is strongly influenced by snowmelt and glacier mass balance, as well as the input temperature and precipitation. The model parameter sets must take these processes into account in order to simulate discharge properly.

Data was available for calibration and validation of the model from the Bayelva catchment and the De Geerdalen catchment. Observed discharge data were derived from the Norwegian Water Resources and Energy Directorate, and mass balance and ice volume data were based on results from Hagen and Sætrang (1991) and Kohler et al. (2007). Two calibration strategies were applied; (1) calibration of the model for the two catchments with input precipitation and temperature data from the meteorological stations Ny-Ålesund and Svalbard Airport operated

by the Norwegian Meteorological Institute, and (2) calibration of the model with input precipitation and temperature data from 1 by 1 km² downscaled reanalysis (Sval-Imp; Chapter 3.1.1). The first calibration strategy allows the model to be run only for the two catchments Bayelva end De Geerdalen, while the second calibration strategy allows the model to be run for the entire Svalbard Archipelago, except the islands Hopen and Bjørnøya that were not included in the model domain. In both cases, the model parameters were based on a multi-objective calibration strategy where discharge data from the two catchments Bayelva and De Geerdalen were used to obtain a regional set of model parameters for 1 by 1 km² grid cells, with parameter values conditioned on land surface characteristics. Observed meteorological data are often more trustworthy than atmospheric model simulations and the performance of the hydrological model is better for the first calibration strategy. On the other hand, the second calibration strategy allows hydrological processes for the entire Svalbard Archipelago to be characterized.

The HBV model was driven by downscaled and bias-adjusted temperature and precipitation from Arctic CORDEX (Box 5.1). The systematic biases between the Arctic CORDEX climate model outputs and the observed temperature and precipitation (Sval-Imp reanalysis dataset) in the reference period, 1971-2000, in addition to the mismatch in scale, necessitate a post-processing of climate model outputs before they can be used as forcing data for hydrological modelling. The RCM outputs were first re-gridded to a 1 x 1 km² grid using a simple nearest neighbour method. The Sval-Imp data, which also have a 1 km resolution, were treated as 'observed' data. An empirical quantile mapping method (EQM) was adopted to bias-correct and bias-adjust the climate projections of temperature and precipitation (Gudmundsson et al., 2012; Sorteberg et al., 2014; Wang et al. 2016). The EQM method utilizes the empirical cumulative distribution functions (ECDFs) for both observed and modelled variables. A transfer function matching the modelled ECDF in the reference period with the observed ECDF was applied to adjust values from the climate projection quantile by quantile so that they yielded a better match with the observed.

Twelve calendar-month-specific transfer functions for each grid cell were derived. These derived transfer functions from the reference period were then assumed to be valid for use in the projection period. (Chapter 9).

3.2.4 Snow modelling

To estimate the amounts of snow and the length of the snow cover season at Svalbard, we have used the seNorge snow model (Saloranta, 2016). This model has been applied to produce snow maps for the Norwegian mainland since 2004 (www.senorge.no).

The seNorge snow model (v.1.1.1) requires the daily mean air temperature T [°C] and the daily sum of precipitation P [mm] as input forcing. The model consists of two main sub-models: 1) the *SWE* (Snow Water Equivalent) sub-model for snowpack water balance and 2) the snow compaction and density sub-model for converting *SWE* to snow depth. The *SWE* sub-model is independent of the snowpack compaction and density sub-model, implying that the *SWE* is not affected by snow density in the model. The *SWE* sub-model uses a threshold air temperature T_S to separate between precipitation as snow and rain, handles separately the ice and liquid water fractions of the total *SWE* and keeps track of the accumulation and melting of snow. The snowpack can retain liquid water from snowmelt and rain up to a percentage r_{max} (default 11 %) of its ice content, while the excess goes to runoff. The liquid water in the snow pack can also be refrozen to ice. An extended degree-day algorithm is used to calculate potential snowmelt rates $M*$

$$M* = b_0 T + c_0 + S* \quad , \text{ if } \quad T > 0 \text{ °C} \quad (1)$$

where b_0 and c_0 are empirical parameters and $S*$ the potential incoming daily solar irradiance [J/day]. The melt parameters b_0 and c_0 are estimated on the basis of over 3500 daily melt rate observations from the Norwegian mainland snow pillow network. Incoming solar irradiance is a function of the geographical latitude and the day of the year. Moreover, the average grid cell snowmelt rates are also affected by the simulated fraction of snow covered area (*SCA*) in the model grid cells. The snow compaction and density sub-model calculates changes in snow depth

due to snowmelt and new snowfall events, as well as due to viscous compaction, where the compaction rate is dependent on the mass, density, temperature and liquid water content of the snow pack.

For this report, the seNorge snow model was forced by daily temperature and precipitation values from all the bias-adjusted Arctic CORDEX simulations described in Chapter 3.1.3 (Appendix A1, Table A.1.1) and the COSMO-CLM fine-scale modelling (Chapter 3.1.4). This includes both the reference period, and RCP4.5 and RCP8.5 projections.

3.3 Methods and data, glaciers

Roughly 60% of the total land area of Svalbard is covered by glaciers (König, et al. 2014). Svalbard represents ~10% of the total Arctic glacier area, excluding the Greenland ice sheet (König et al., 2014). Svalbard's glaciers range from small valley glaciers to large ice caps and ice fields, whose type depends on the local precipitation and the underlying bedrock topography. There are roughly 1,100 glaciers whose area is greater than one square kilometre. While most glaciers on Svalbard end on land, about 15% are tidewater glaciers, that is, glaciers whose fronts terminate in seawater. While their number is small, more than 60% of the total glacier ice area flows end in a tidewater glacier.

Mass loss from the world's "small" glaciers, that is, all ice bodies apart from the Greenland and Antarctica ice sheets, is one of the main contributors to current sea-level rise (Gardner, et al. 2013). Furthermore, freshwater from glacier melt is an important component in the hydrological cycle, affecting ecosystems and ocean flow (Lydersen et al. 2014). Accordingly, glaciologists seek to estimate the mass gain or loss in all glaciated regions of the world, the so-called glacier mass balance.

Glacier mass balance is the amount of snow and ice lost or gained on a glacier over a certain period, and is influenced primarily by winter precipitation and summer temperature. Svalbard glaciers as a whole are losing mass (Wouters, et al. 2008; Moholdt, et al. 2010; Nuth et al. 2010); summer temperature

Projected changes in mean annual maximum snow water equivalent, as well as number of snow cover days, have been computed for two 30-year periods: mid-century (2031-2060), and the end of the century (2071-2100). Absolute and relative changes are computed by comparison with the reference period (1971-2000). Snow conditions for the current climate have been computed by running the seNorge model with daily temperature and precipitation from the Sval-Imp dataset (Chapter 3.1.1). Snow cover duration is computed by counting the number of days per year with snow water equivalent >= 20 mm.

has the strongest influence on Svalbard glacier mass loss (van Pelt et al. 2012), and decadal-scale Arctic summer warming has led to increasing rates of mass loss (Kohler et al. 2007). With the further warming predicted (Chapter 4.1.3), Svalbard glaciers can be expected to continue losing mass.

Glacier mass loss manifests itself most noticably as a retreat of the glacier front. The short-term exceptions on Svalbard are due to the many "surge" glaciers found there. Surging is a cyclical dynamic instability in which a relatively slow-moving glacier suddenly starts flowing at high speeds, with frontal advances of up to many kilometres occur over the course of a few years. Following this advance, the glacier stagnates and its front begins to retreat. The quiescent phase of a surge-type glacier can last from decades to over a century. Surging is not directly related to climate change, and during a surge mass is simply transferred from the upper glacier to the front. Following a surge, in a warming climate, mass loss and the long-term frontal retreat will continue regardless of these short-term advances. This can be seen on the few glaciers on Svalbard that have been observed to undergo a surge more than once since the records start, in the early 1900s. Nevertheless, it is important to determine the mass balance since changes in front positions can be affected by internal glacier dynamics as well as climate.

There are two basic approaches to directly measuring mass balance: the *glaciological* and the *geodetic* method.

3.3.1 Glaciological mass balance

The *glaciological mass balance* is obtained from regular field visits to a few selected glaciers, and comprise end-of-winter winter snow-depth sounding and repeated measurement of heights of an array of stakes. Typically, these are installed in the glacier ice along its centreline, since much of the variability of a glacier's balance is explained by elevation, obviating the need for a dense network of stakes distributed over the entire glacier.

The winter balance B_w is obtained by sounding snow-depth over as much of the glacier as is practical, estimating the superimposed ice formed during the winter at the base of the snowpack from shallow ice-cores, and measuring snow depths at the stakes. Snow density measurements are used to convert snow depth to water equivalent. In Svalbard, this work is carried out at the end of the accumulation period, in April or May. Obtaining the winter balance strictly from sounding to the previous year's summer surface in the spring defines the so-called stratigraphic method. For glaciers with a wide range of elevations, the method is time-transgressive; that is, the sounded surface is formed at different times along the glacier's extent. This violates the assumption that the balance can be calculated uniformly over the whole glacier for a single period. Therefore, autumn measurements are preferred for establishing the reference horizon for stake measurements at known dates.

The summer balance is obtained directly from changes in exposed stake heights over the course of the melt season. This is usually done at the end of summer, in September or October. The snow and ice facies at each stake must be known since their density varies from 0.5-0.9 g cm^{-3}.

Balance estimates are extrapolated over the entire glacier basin by determining the balance terms as functions of elevation, and averaging them after applying weights determined from the glacier's hypsometry, that is the relative distribution of glacier area as a function of elevation.

An additional important mass balance component is the dynamic loss at the front of tidewater glaciers, that is, glaciers that terminate in seawater and lose ice by calving. About 60% of Svalbard's total glacier area drains through tidewater fronts (Błaszczyk, et al. 2009), such that a significant part of the total ice mass loss occurs via calving. Warmer ocean water around Svalbard, in combination with the overall atmospheric warming, has led to retreat of Svalbard's tidewater glaciers (Luckman et al. 2015).

Ice flux through the calving front is typically obtained (e.g. Błaszczyk, et al. 2009; Luckman et al. 2015) as the product of the average glacier speed along a profile or gate located at or near the tidewater front and the average ice thickness of the gate, with an additional term for change for frontal advance or retreat.

At present, there are thirteen glaciers with annual mass balance measurements currently being made, and that have continuous records 5 years or longer (Table 3.3.1). For logistical reasons, these are mostly located along the western coast (Figure 3.3.1), and most are in the Kongsfjorden area. The longest-term field measurements of mass balance in Svalbard are on the two small glaciers Austre Brøggerbreen and Midtre Lovénbreen, with records that start in the mid-1960s (Table 3.3.1).

3.3.2 Geodetic mass balance

While the glaciological mass balance is accurate in describing short-term glacier changes on individual glaciers, it becomes less accurate when summed over time. Furthermore, measuring mass balance in the field is time-consuming and costly, and therefore spatially limited. The geodetic mass balance is computed by differencing glacier-wide elevation data from two or more different times. Elevation data can be from a variety of sources: surface surveys; contours from older maps; digital elevation models made photogrammetrically from aerial photographs or satellite imagery; or satellite altimeters.

1. **Austre Brøggerbreen (1967)**
2. **Midtre Lovénbreen (1968)**
3. **Kongsvegen (1987)**
4. **Waldemarbreen (1996)**
5. **Irenebreen (2002)**
6. **Kronebreen/Holtedahlfonna (2003)**
7. **Austre Lovénbreen (2006)**
8. **Pedersenbreen (2006)**
9. **Austre Lovénbreen (2008)**
10. **Vestre Brøggerbreen (2012)**

Etonbreen (2004)

Nordenskiöldbreen (2006)

Hansbreen (1996)

Svalbard

Norway	**Norwegian Polar Institute**
China	**Chinese Academy of Sciences, Polar Research Institute of China, Wuhan University**
Poland	**Nicolaus Copernicus University**
France	**Université de Franche-Comté, CNRS, French Polar Institute (AWIPEV)**
India	**National Centre for Antarctic and Ocean Research**

Figure 3.3.1 Location of mass balance studies in the Ny-Ålesund Kongsfjord area. Map to lower right shows the locations of the three programs outside of Kongsfjord.

The geodetic mass balance is more accurate over longer periods and data can be acquired over larger areas. However, only recently has it been possible to collect Svalbard-wide elevation data within a single year, mostly due to advances made in satellite remote sensing.

3.3.3 Glacier mass balance modelling

Data from the few glaciers where it is measured can be directly extrapolated to larger areas or regions, but major assumptions must be made (e.g. Hagen et al. 2003). Field measurements of mass balance are more profitably extrapolated to larger scales when combined with mass balance models.

Climatic mass balance models (CMBs), forced either by meteorological observations or output from regional climate models, evaluate the surface energy balance to determine surface temperature and melt production. The most complete models couple the surface module to subsurface routines to account for the impact of water storage and refreezing on the mass and energy budgets. Field data are used to calibrate model parameters and to validate model output.

There are at present only a few studies modelling historical Svalbard-wide mass balance using fully physical surface models, as opposed to those that calculate the surface energy balance using statistical (Day et al., 2012) or temperature-index (Möller et al., 2016) approaches. Aas et al. (2016) perform a mass balance simulation for all of Svalbard over the period 2003-2013, using output from the WRF RCM forced by ERA-Interim data. Østby et al. (2017) simulate mass balance over the longer period

Glacier	Agency	Region	Area (km²)	Elevation range (m a.s.l.)	Years
Austre Brøggerbreen	NPI	Kongsfjord	5.8	80-680	1967-present
Midtre Lovénbreen	NPI	Kongsfjord	5.1	50-690	1968-present
Kongsvegen	NPI	Kongsfjord	106.9	0-1000	1987-present
Hansbreen	PAS	Hornsund	63.4	0-695	1989-present
Waldemarbreen	UNC	Kaffiøyra	2.7	140-590	1996-present
Irenebreen,	UNC	Kaffiøyra	3.4	110-780	2002-present
Kronebreen-Holtedahlfonna	NPI	Kongsfjord	380.0	0-1400	2003-present
Etonbreen	NPI/UiO	Nordaustland	633.0	0-800	2004-present
Nordenskiöldbreen	UU/UU	Billefjorden	141.2	0-1230	2006-present
Austre Lovénbreen	PRIC/CAS	Kongsfjord	5.0	95-650	2006-present
Pedersenbreen	PRIC/CAS	Kongsfjord	6.1	50-790	2006-present
Austre Lovénbreen	CNRS	Kongsfjord	5.0	95-650	2008-present
Vestre Brøggerbreen	NCPOR	Kongsfjord	4.6	50-580	2012-present

Table 3.3.1: Long-term ongoing glacier mass balance measurements around Svalbard. NPI: Norwegian Polar Institute; PAS: Polish Academy of Science; UNC: University of Nicolaus Copernicus, Poland; UiO: University of Oslo; UUS: Uppsala University, Sweden; UUN; Utrecht University, Netherlands; PRIC: Polar Research Institute of China; CAS: Chinese Academy of Science; CNRS: French National Center for Scientific Research; NCPOR: National Center for Polar and Oceanographic Research, Goa India. Areas and elevation ranges are taken from most recent version of the Svalbard Glacier Database, covering the 2000s (Nuth, et al., 2013).

1957−2014, using a different CMB model forced by downscaled ERA-40 and ERA-Interim data. Both models are parameterized in part using the field-derived mass balance data described above, from a subset of the glaciers in Table 3.3.1.

For future prognoses we use a modified version of the CMB model of Mölg et al. (2008, 2009), which takes as input the fields of near-surface temperature, humidity, pressure, winds, incoming radiation, and precipitation from the regional climate model COSMO-CLM (Chapter 3.1.4). The model computes the column-specific mass balance from solid precipitation, surface and subsurface melt, refreezing, and liquid water storage in the snow-pack, and surface vapor fluxes. The model solves

the surface energy balance to determine the energy available for surface melt, and resolves the glacier subsurface down to a "user defined" depth (here, 20 m divided into 17 vertical layers). This is an offline-application of a model previously used by Aas et al. (2016). Further information about the interactive coupling between the CMB model and WRF is given by Collier et al. (2013, 2015). For the present simulation, we use the parameter settings of Aas et al. (2016).

Using this CMB model, two simulations have been conducted, one using the historically-driven down-scaled dataset from COSMO-CLM, 2004-2017 and the second one using the pseudo-transient scenario RCP8.5 (see Chapter 3.1.4).

The first dataset evaluates the quality of the product of this model chain, compared to direct field measurements of glacier mass balance, and compared to similar, Svalbard-wide CMB simulations by Østby et al. (2017) and Aas et al. (2016).

3.3.4 Glacier mass balance from remote sensing

Remote sensing visible imagery can be used to determine spatial patterns of winter precipitation, as well as to determine losses through frontal retreat and calving. However, the most useful remote sensing product for estimating mass change comes from the GRACE (Gravity Recovery and Climate Experiment) satellite, which mapped the time-varying gravity field of the Earth over the period 2002-2017 (Tapley et al. 2004). GRACE data have been used to estimate changes in ice mass for glaciated areas around the world (e.g. Gardner, et al., 2013). The GRACE footprint is large; in a region the size of Svalbard, elevation change is computed for a handful of pixels. Furthermore, corrections must be made for ongoing and long-term isostatic rebound. However, satellite gravimetry also sidesteps problems with the other methods, such as the need to account separately for temporally varying calving or frontal retreat terms, or to extrapolate point measurements to larger areas.

3.4 Methods and data, permafrost

Areas with permafrost consist of sediment or rock and included ice and organic material, which remain at or below 0°C for at least two consecutive years (French, 2018). The most direct indicators of changes related to permafrost, are the two essential climate variables (ECVs) for permafrost; permafrost temperature and active-layer thickness (ALT - the thickness of the layer that freezes and thaws annually over the permafrost). Permafrost temperature measured at a depth where there is practically no annual fluctuation in the ground temperature (the depth of zero annual amplitude (ZAA)) is the best indicator of long-term change. This depth varies from a few meters in warm, ice-rich permafrost to 20 m or more in cold permafrost and in bedrock (Romanovsky et al., 2010; Smith et al., 2010). The monitoring of the ECVs for permafrost is coordinated through the Global Terrestrial Network on Permafrost (GTN-P) by the International Permafrost Association and it consists of two specific monitoring programmes: The Thermal State of Permafrost and the Circumpolar Active Layer Monitoring (CALM) (Romanovsky et al., 2010; Shiklomanov et al., 2012). In addition, satellite-based ECV monitoring has recently been initiated in the "GlobPermafrost" (www.globpermafrost.info) and "Permafrost CCI" (http://cci.esa.int/Permafrost) projects by the European Space Agency (ESA). These techniques can complement terrestrial monitoring by providing spatially distributed estimates of ground temperatures and ground temperature changes over time (Westermann et al., 2016; Obu et al., 2019).

3.4.1 Observations

Systematic monitoring of active-layer thickness and permafrost temperature profiles are presently limited to sites in western and central parts of Spitsbergen (see Figure 7.1.1). Data from active permafrost monitoring sites have been examined as part of the international collaborative permafrost monitoring network in Svalbard Integrated Arctic Earth Observing System (SIOS) in Svalbard (Christiansen et al., 2019a). Very recently systematic permafrost observations were started in Barentsburg and Hornsund

As part of the State of Environmental Science in Svalbard (SESS) reporting a first overview of permafrost thermal conditions and active-layer thickness (ALT) at all the permafrost monitoring sites in Svalbard during the 2016/2017 hydrological year from 1 September 2016 to 31 August 2017 have been compiled (Christiansen et al., 2019b). Permafrost thermal monitoring at some sites in the Longyearbyen and Kapp Linne areas extend back to the International Polar Year (IPY) 2008-2009 (Christiansen et al., 2010) and for Janssonhaugen to 1998

(Isaksen et al., 2001), which allows for studies of changes in the permafrost temperatures since then.

3.4.2 Permafrost modelling

A new land surface scheme designed for permafrost applications, CryoGrid 3 (Westermann et al., 2016), is employed to simulate the present and future ground thermal regime for selected sites on Svalbard where active permafrost observations and/or meteorological stations exist. The CryoGrid 3 model framework simulate the permafrost temperatures based on input data sets of meteorological variables, such as incoming radiation, air temperature, wind speed and precipitation obtained from the COSMO-CLM (CCLM) datasets (Chapter 3.1.4). The properties of the applied future projection naturally is a main source of uncertainty for the obtained permafrost model results, which must be considered when comparing to existing studies.

3.5 Methods and data, ocean

3.5.1 Observations

Except from observations in the waters close to Svalbard, also areas upstream in the Nordic Seas are relevant for describing the climate and the corresponding variability at Svalbard. The Nordic and Barents seas are relatively well sampled when it comes to hydrographic observations, with some time series going back more than 100 years (Korablev et al., 2014).
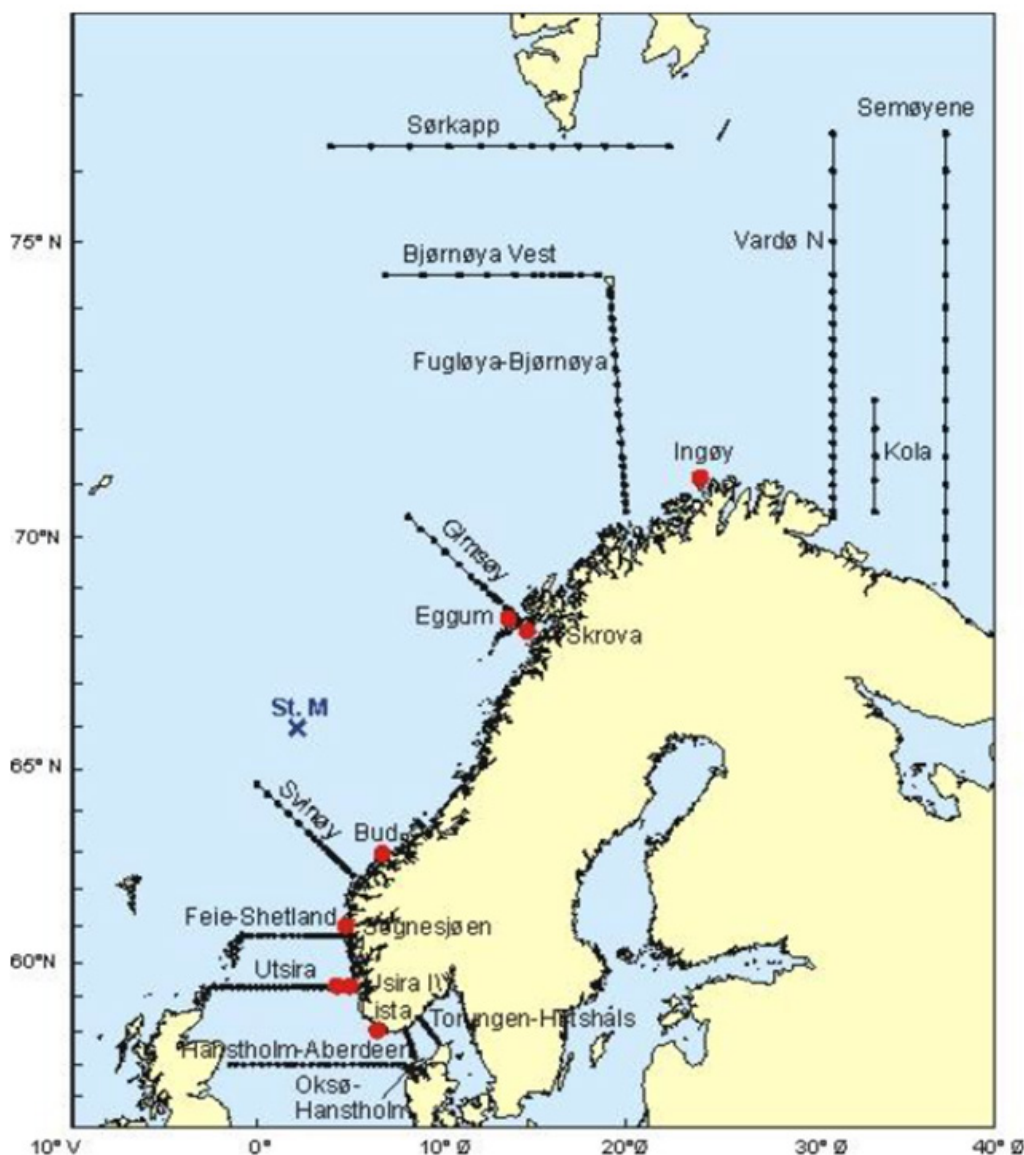
Figure 3.5.1 Map of fixed stations and sections with regular observations of hydrographic variables. Red dots show coastal stations with regular observations, and the blue cross shows the location of Ocean Weather Ship Station Mike (OWS M) at (66° N, 02° E), and the new buoy to observe currents, hydrography and biogeochemical properties.

Annual observations of hydrographic and biogeo-chemical properties have been carried out by the Institute of Marine Research (IMR) in many of the sections (see Figure 3.5.1) for more than 50 years using ship-borne conductivity temperature density (CTD) measurements. In the coastal waters around Svalbard, especially on the northern and eastern sides, such observations are less regular, but are also available some decades back. Today, it is addition-ally a continuous activity using Acoustic Doppler Current Profilers on anchored moorings, gliders and, temperature-salinity profiling floats, so-called ARGO buoys (Riser et al., 2016).

Figure 3.5.1 shows the fixed stations operated by IMR. Sections in the eastern Norwegian Sea illus-trate how the hydrographic properties develop along the path of the Atlantic water inflow at Svinøy-NW and Gimsøy-NW. Temperature and salinity have been sampled annually since 1950 in Svinøy and 1963 in Gimsøy, and 2-5 times every year since 1977 (Blindheim et al., 2000). Bjørnøya-W is also one of the fixed sections operated 2-5 times a year, while annual samples of hydrography from the Sørkapp section in the Fram Strait west of Svalbard have been taken since 1977.

Data from the Barents Sea Opening, Fugløya-Bjørnøya, and in the southern Barents Sea, Vardø-North (Figure 3.5.1), have been sampled annually since 1953, and 4-6 times each year since 1977. The variability of the Atlantic water inflow to the Barents Sea has been observed by moored current meters in the Barents Sea Opening since 1997
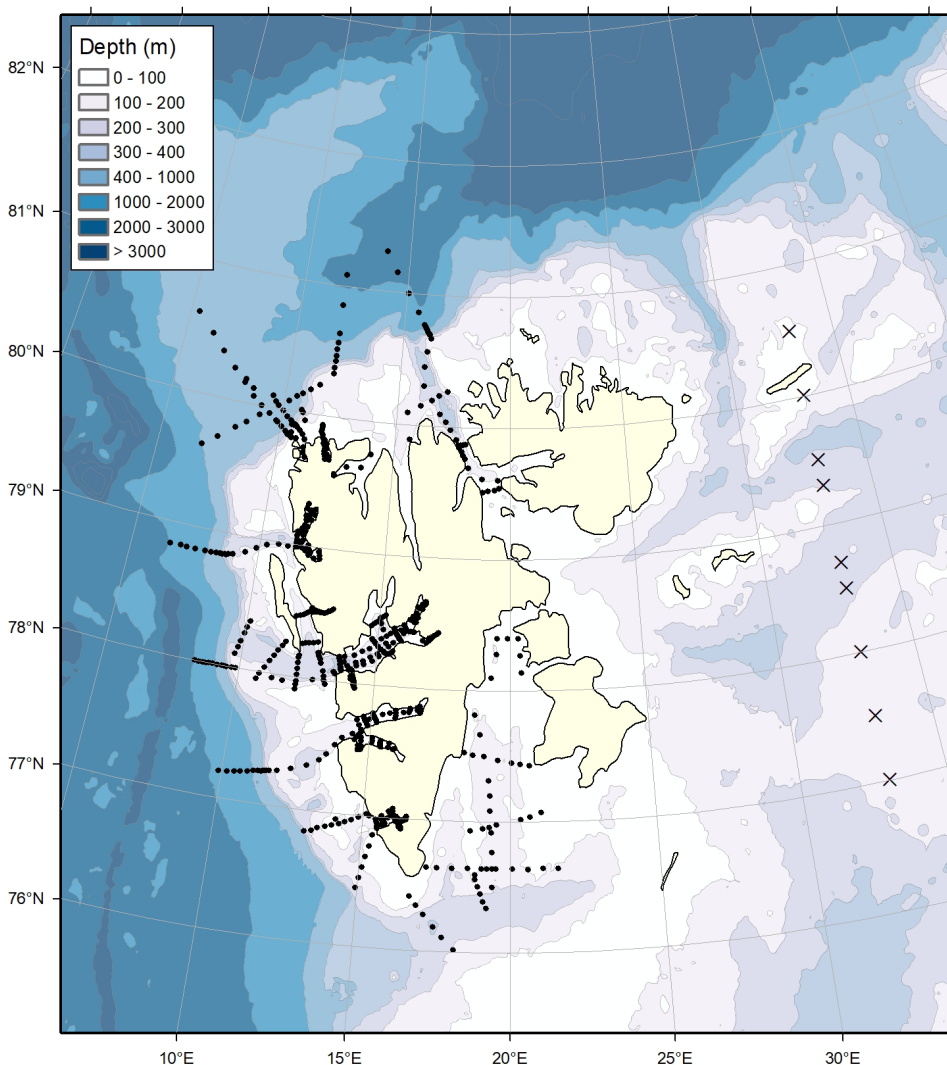
Figure 3.5.2 Fixed stations and sections where observations of hydrographic variables are collected regularly by UNIS. Dots show CTD stations and UNIS mooring positions observing current, hy-drography and oxygen over different periods. The longest mooring time series is situated on the southern side of Isfjorden mouth area (2006-present, UNIS) and in Kongsfjorden (2002-2014, UoB/UNIS). Crosses indicate stations east of Sval-bard sampled for ocean acidification variables throughout the water column.

(Ingvaldsen et al., 2004). Since 1995, also the Atlantic water inflow to the Nordic Seas in the Svinøy section has been monitored continuously by moored current meters (Orvik et al., 2001).

At the OWS M (Figure 3.5.1) daily meteorological and oceanographic measurements have been performed since 1948 by MET Norway and the University of Bergen (UoB). In 2009, the ship at OWS M was replaced by the operational Polar buoy, an ocean surveillance buoy transferring meteorological and oceanographic data directly to land via satellite. In general, the observational data shows an increase in temperature and salinity since the mid-1990s. However, this does not include the most recent years.

Since 1994 the University Centre in Svalbard (UNIS) has collected hydrodynamic data on the west Coast of Spitsbergen, north of Svalbard and in the fjords indenting the west coast (Figure 3.5.2). The longest hydrographic time series are the sections from the inner part of Isfjorden and Kongsfjorden across the West Spitsbergen shelf and the West Spitsbergen Current confined to the slope in eastern Fram Strait. Most of the CTD profiles have been collected in summer and autumn, but the Isfjorden and Kongsfjorden sections have also been collected during some winter/spring seasons since 1994. The UNIS data is organised and calibrated in a UNIS hydrographic database (UNIS HD) with additional data from the Norwegian Marine Database (IMR), PANGEA (Alfred Wegener Institute), ICES data and from the NISE database (Norwegian Polar Institute). A subset of the data in the UNIS HD is synthesised for the Kongsfjorden section (Tverberg et al., 2018) and Isfjorden section (Skogseth et al., pers. comm.). In addition, the Institute of Oceanology Polish Academy of Sciences (IOPAS) in Sopot, Poland, started their monitoring program in 1936 with yearly summer cruises to the west coast of Spitsbergen, Kongsfjorden and Hornsund, undertaking both physical and biological sampling (not shown).

On the east coast of Svalbard, no regular hydrographic observations are currently in operation. A non-regular time series exist from Storfjorden (Figure 3.5.2) between 1997 and 2007 (Skogseth et al., 2008, 2013) documenting effective ice growth and brine release in the Storfjorden polynya.

In order to evaluate future climate model projections, historical climate variability reconstructed from proxy data prior to 1850 is important. Such marine reference data sets are based on temperature reconstructions using alkenones and planktonic foraminifers from sediment cores acquired along the Atlantic water inflow pathway and are available in the Faroe-Shetland Channel area, at the Vøring Plateau, and south of Svalbard (Eldevik et al., 2014).

The "Flagship programme for Ocean Acidification and effects in northern waters" within the Fram Centre, has surveyed waters around Svalbard since 2012. NPI and IMR have annually sampled Svalbard fjords and the Fram Strait at the hydrographic "UNIS stations" (Figure 3.5.2).

The water column section at 33°E shows that the water masses surrounding Svalbard have a large span of ocean carbon chemistry characteristics like alkalinity, total inorganic carbon, pH and aragonite saturation state. There are clear differences between the water in the Arctic Ocean, and the Atlantic water. East of Svalbard there is, in addition, a component of recirculated Atlantic water from the Fram Strait at 100 m depth between 77°N and 80°N. Generally, fresh water from ice melting plays an important role in modifying the waters around Svalbard. This is especially prominent in the waters close to glaciers and in the fjords (Fransson et al., 2015).

3.5.2 Ocean modelling

Regional numerical models are an important tool to describe the large-scale ocean circulation upstream of Svalbard and thus provide valuable information for the area around Svalbard. These models provide results for the present and future ocean climate and are mainly based on dynamical downscaling of ESMs from the CMIP5 archive (Taylor et al., 2012).

The simulations utilised here are performed with the regional ocean model ROMS (Shchepetkin and McWilliams, 2005) for the periods 1958-2007 and 2006-2070. The future climate simulation

uses initial conditions, boundary conditions, and atmospheric forcing from the Norwegian Climate Model (NorESM, Bentsen et al., 2013) following the RCP4.5 scenario. The horizontal resolution of the model setup used here is around 10 km in the

Norwegian and Barents Seas. The choice of global CMIP5 model for downscaling is based on evaluation of different models with respect to poleward ocean heat transport and sea ice extent (Sandø et al., 2014).

3.6 Methods, data and models, sea level

3.6.1 Instrument record

There are two tide gauges on Svalbard, Barentsburg and Ny-Ålesund, which provide observations of Relative Sea Level (RSL) change. Data from these tide gauges are available for download from the Permanent Service for Mean Sea Level (PSMSL, Holgate et al. 2013). For Barentsburg, we focus on BAR1 (PSML-id 541), as this tide gauge provides the longest record, i.e. it starts in 1948 and is still in operation. (A second Barentsburg tide gauge record is available but stops in the early 1990s).
The Barentsburg tide gauge is operated by the Russian Federal Service for Hydrometeorology and Environmental Monitoring. The Ny-Ålesund

tide gauge is operated by the Norwegian Mapping Authority. It was established in 1976 and is still in operation. Unfortunately, there is a gap in the record from 1988 to 1992.

The Svalbard tide gauge records were analysed using the same method as Breili et al. (2017). We use records with a monthly sampling interval and the revised local reference datasets, as recommended by the PSMSL. A linear regression model with a first order autoregressive (AR(1)) covariance structure was fitted to the observations (McKinney et al., 2011). We included terms accounting for the sea-level trend and the initial height of the sea-level in the regression model, as well as periodic terms accounting for annual and semi-annual variation
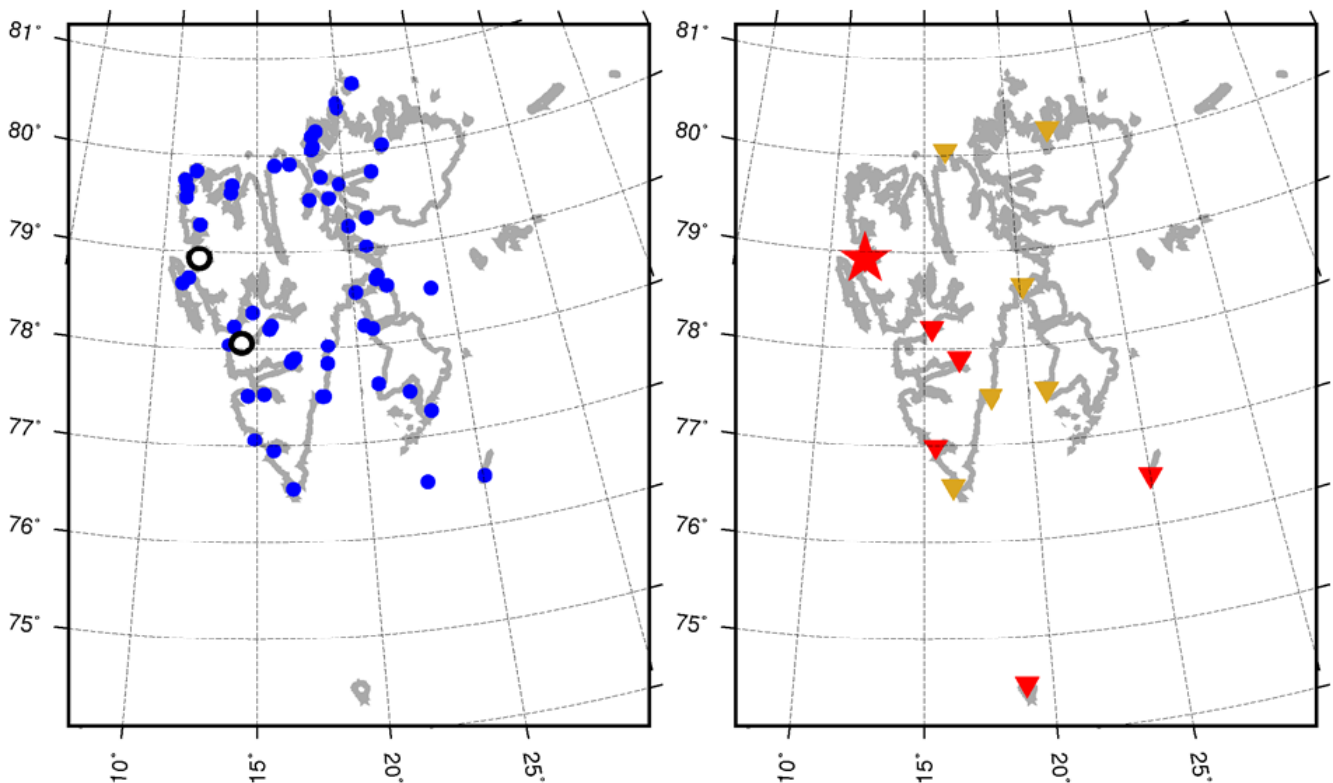
Figure 3.6.1 Left panel shows the locations of the permanent tide gauges (circles) and measurements from temporary tide gauges (blue dots). Right panel shows the locations of the existing GNSS stations (red triangles) and planned GNSS stations through the EPOS-N project (orange triangles). The red star marks the Earth observatory at Ny-Ålesund which is a core geodetic site.

in sea level. Two study periods were analysed, i.e., the entire length of each record and from 1992 to 2017. The latter interval was chosen as it enables a comparison to estimates from satellite altimetry and because for both tide gauges it is a period with no major data gaps.

While tide gauges observe RSL and are influenced by vertical land motion, altimetry satellites measure sea level heights in a global geodetic reference frame. In addition, altimetry is primarily a technique for observing sea level in the open ocean and does not provide direct a measurement at the coast. There is therefore a significant conceptual difference between these two techniques, and measurements from altimetry and tide gauges may differ significantly, especially in areas characterised by vertical land motion. It is important to be aware that the waters around Svalbard are not sampled by several altimetry missions, i.e., Topex/Poseidon and the Jason-satellites observe the oceans between ±66 degrees latitude only. In addition, altimetry measurements at high latitudes are occasionally disrupted by the presence of sea ice, no calibration/validation facilities exist at high latitudes, and several range corrections are less accurate in the Arctic Ocean. As a consequence, the altimetry record of the waters around Svalbard is less reliable than at lower latitudes.

3.6.2 Observed contributions to regional sea-level change

Changes in the distribution of mass on the Earth's surface produce a non-uniform sea level pattern due to gravitational changes (Farrell and Clark, 1976). This sea level response is often referred to as a "fingerprint". Estimates of regional sea-level change owing to land ice and terrestrial water storage changes can be calculated by solving the elastic sea level equation. In a recent study, Frederikse et al. (2017) use the sea level equation to model regional sea-level changes for different mass contributions. We discuss their results for Svalbard in Chapter 8.4. Steric trends in sea level can be calculated from in-situ observations of ocean temperature and salinity. Here we make use of the EN4 data (Good et al., 2013) to calculate local steric trends for the period 1993-2013.

3.6.3 Land motion and gravity measurements

Glacial isostatic adjustment plays an important role in determining RSL changes for Svalbard. The primary method for measuring present-day uplift is from Global Navigation Satellite System (GNSS) stations. The Norwegian Mapping Authority operates a network of five continuous GNSS stations on Svalbard (Ny-Ålesund, Longyearbyen, Svea, and on the islands of Hopen and Bjørnøya). The Polish Department of Polar and Marine Research operates a station in Hornsund. There is also a smaller campaign network in the Kongsfjorden area which has been measured regularly since 1998.

Figure 3.6.2 The Earth observatory at Ny-Ålesund which is a core geodetic site, i.e. a number of different geodetic instruments are collocated. The site is part of a global network that is of fundamental importance for determining accurate measurements of sea level from satellite altimetry. The twin VLBI telescope is pictured. Photo: Bjørn-Owe Holmberg

There are currently no observations in the northern and eastern parts of Svalbard. However, provided the necessary permissions from the local authorities are granted, the EPOS-N project is planning to install six new GNSS stations collocated with seismological stations in these areas. Better geographical coverage with GNSS is crucial for constraining ice mass changes, projections of sea level, and improving our understanding of GIA and other geophysical processes.

The observatory in Ny-Ålesund is a core geodetic site and, in addition to GNSS, hosts several other instruments; an existing Very Long Baseline Interferometry (VLBI) telescope, a new twin VLBI telescope, a satellite laser ranging instrument, absolute gravity points, and two superconducting gravimeters. Among other things the instruments provide information about land motion and gravity changes.

The GNSS stations give daily coordinates at an accuracy level of around five millimetres. Time series of the daily coordinates give information on crustal deformation processes and land uplift rates with an accuracy of a few tens of a millimetre per year. The method applied here to derive daily solutions for the Svalbard stations is the same as in Kierulf et al. (2014) and employs the GAMIT/GLOBK software (Herring et al., 2011). We use data up until 2018 and the velocities presented here are realised in the ITRF2008 reference frame (Altamimi et al., 2011). Visual inspection of the time series from Svea and Hopen (both grounded in permafrost) indicates that these sites are unfortunately not sufficiently stable for glacial isostatic adjustment and sea level studies. These stations are therefore omitted from our results.

3.6.4 Observed sea level extremes

Storm surges occur when a low-pressure weather system and increased surface wind stress simultaneously contribute to increase sea level and push water up against the coast. Depending on the astronomical tide, extreme water levels can occur. The surge observed on Svalbard is generally smaller than on most of mainland Norway. As mentioned, the Norwegian Mapping Authority operates the tide gauge in Ny-Ålesund; here there is data available to allow a statistical analysis of the extremes. For the Barentsburg tide gauge only the monthly and annual averages are available from PSMSL and, therefore, no analysis of the extremes is possible.

The average conditional exceedance rate method is used for estimating the return periods of the extreme sea levels at the Ny-Ålesund tide gauge. For a detailed description of the method see Næss and Gaidai (2009) and Skjong et al. (2013). This is the same approach used for calculating the official return periods for Norway; the results are given in Ravndal and Sande (2016). Data up until 2015 is used to estimate the extremes at the Ny-Ålesund tide gauge.

There are also a number of shorter time series of water level data from Svalbard, Bjørnøya and Hopen dating from the beginning of the 20th century to present day and thus of varying quality. These series are too short to be analysed with respect to sea level extremes but can be used to analyse variations of the astronomical tide in the area. Based on the shorter tide gauge records from across the region it is known that the amplitude and time of the tide varies significantly. Using this information, the return heights from Ny-Ålesund can be extrapolated to other parts of the coast e.g. Longyearbyen. This approach assumes that the meteorological conditions affecting sea level are large-scale phenomena that have a similar effect on sea level over a large area and vary smoothly.

3.6.5 Sea level modelling

Our regional sea level projections are based on findings from IPCC (2013) and CMIP5-output (Chapter 3.1.3). An important component of sea-level change in Svalbard is glacial isostatic adjustment. This contribution to future sea-level change in this region is dependent on both the long-term response of the solid Earth to past ice mass changes and the present and future response to glacier changes on Svalbard. We therefore pay special attention to how glacial isostatic adjustment is treated in our sea level projections. The projections presented here show changes to mean sea level, i.e., the average over some period of time. We do not consider future changes to sea level extremes (e.g. storm surges) and/or waves. There is generally low confidence in our ability to project regional changes of these effects, so we generally assume no future changes in their amplitude or frequency.
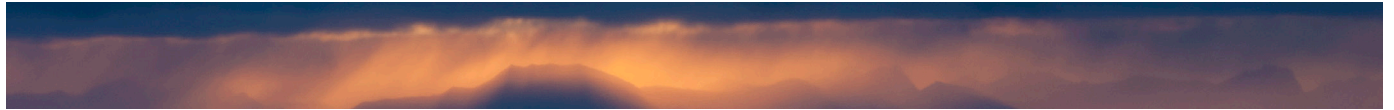
4. Atmospheric climate

This chapter deals with observed and modelled atmospheric climate in Svalbard during the period 1900 – 2100. A short summary of paleo climatic evidence for climate variability during Holocene (the last 10 000 years) based upon data from glaciers is given in Chapter 6.

4.1 Air temperature

4.1.1. Temperature climatology

The temperature climatology of Svalbard has earlier been described in a number of scientific publications (e.g. Førland et al., 2011; Nordli et al., 2014; Gjelten et al., 2016). The following description is mainly based on observations from Svalbard weather stations with measurements or composite series covering at least the period from 1971 to present (see Figure 3.1.2 for station locations). These stations are all situated at low altitudes, and close to the coast. To get a more consistent picture of the climate, covering all parts of Svalbard, we have also applied a 1x1 km² dataset derived from downscaled ERA40/ERA-Interim reanalysis for the period 1958 to 2017 (Østby et al., 2017). More information on this "Sval-Imp dataset" is given in Chapter 3.1.1.

Figure 4.1.1 shows the temperature climatology for selected weather stations at Svalbard for the period 1971-2000, which is used as reference period in this report.
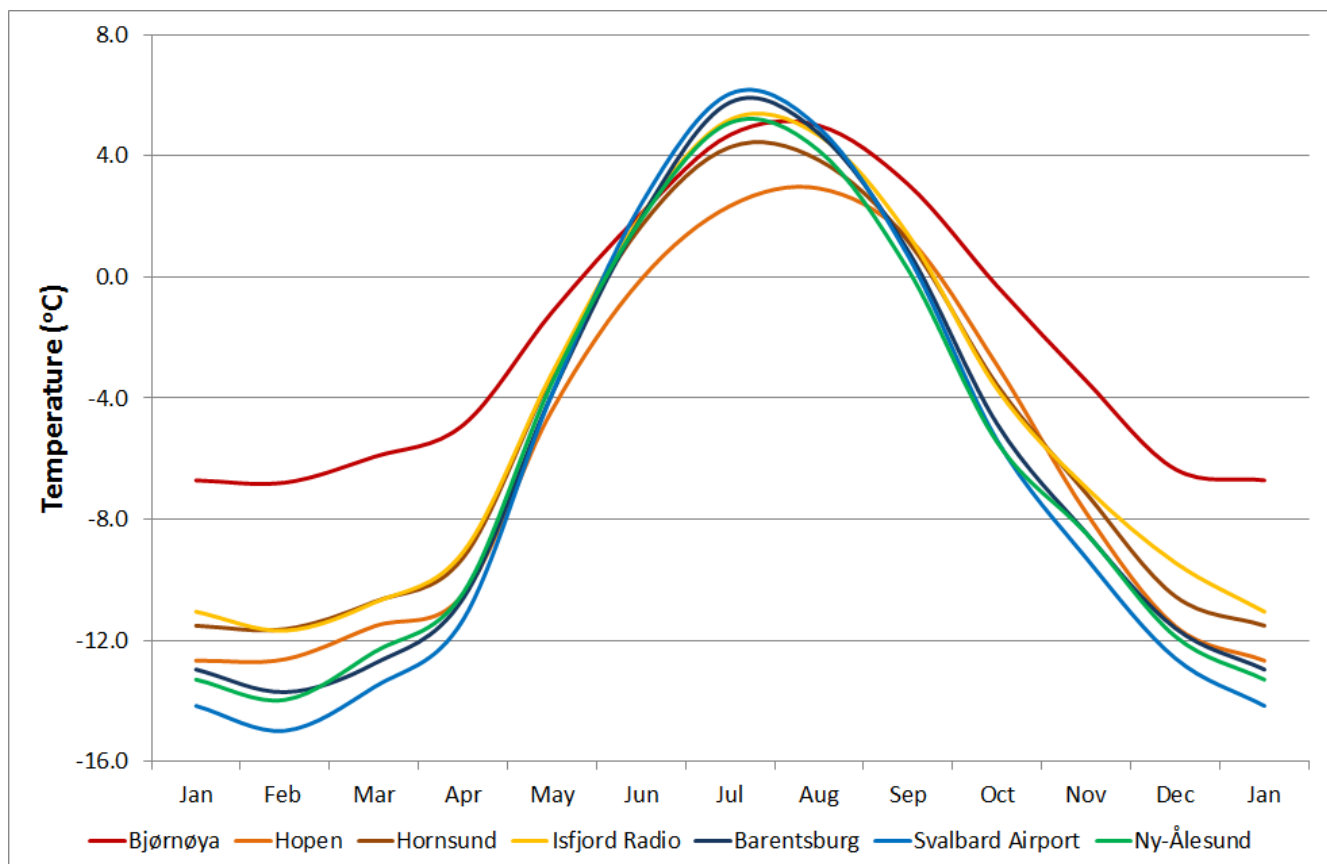
Figure 4.1.1. Seasonal cycle (averages for 1971-2000) for temperature [°C] for selected meteorological stations at Svalbard. Positions of the stations are given in Figure 3.1.2.

February is on average the coldest month at the Svalbard meteorological stations, while the highest monthly mean temperatures usually are measured in July or – for the most maritime stations Bjørnøya and Hopen – in August. Bjørnøya is considerably milder than the Spitsbergen stations and Hopen during winter, while the summer temperatures at Bjørnøya are similar to the most maritime of the Spitsbergen stations (Isfjord Radio and Ny-Ålesund). The highest summer temperatures and the lowest winter temperatures are measured at the stations situated furthest into the fjords of Spitsbergen.

As all the above stations are situated close to the coast and fjords, the reanalysis Sval-Imp dataset is applied to give a more spatially consistent picture of the local climatology. Average summer (Jun-Jul-Aug) and winter (Dec-Jan-Feb) temperatures for the reference period 1971-2000 are presented in Figure 4.1.2. (Figure 2.1.2 shows corresponding annual temperatures). The downscaled reanalysis dataset has been evaluated against observed temperatures (see Chapter 3.1.1 and Vikhamar-Schuler et al., 2019). The main conclusion is that the downscaled ERA40/ERA-Interim reanalysis gives a realistic picture of the temperature conditions in the Svalbard area, though at the coastal stations in Spitsbergen, the Sval-Imp dataset has a cold bias of approximately -0.5 °C.

Figure 4.1.2 shows that though the winter temperatures are 10 to 20 °C lower than the summer temperatures, the spatial temperature variation is rather similar in winter and in summer. The highest temperatures are found in the south-southwestern parts of the archipelago, while the lowest temperatures occur in mountainous and glacial areas in the north and east. In winter, also coastal areas in the northeast are among the coldest sites in the region.

To simplify the description of historic and future climate, Svalbard, with the exception of Bjørnøya, is divided into three regions, roughly based upon the temperature map: (1) A south-western region including Spitsbergen south of Isfjorden, (2) a northwestern region including Spitsbergen north of Isfjorden and west of Widjefjorden, and (3) an eastern region including the rest of Spitsbergen and the islands further east. These regions are used in addition to the climate stations to describe the present climate at Svalbard. They are also used for describing the recent climate development and projections for future climate.

Average annual and seasonal temperatures for Svalbard weather stations and regions are listed in Table 4.1.1. The eastern region is coldest in all seasons. This is the region with the highest sea ice concentration (cf. Chapter 8.3.1), which affects the local air temperatures considerably (Isaksen
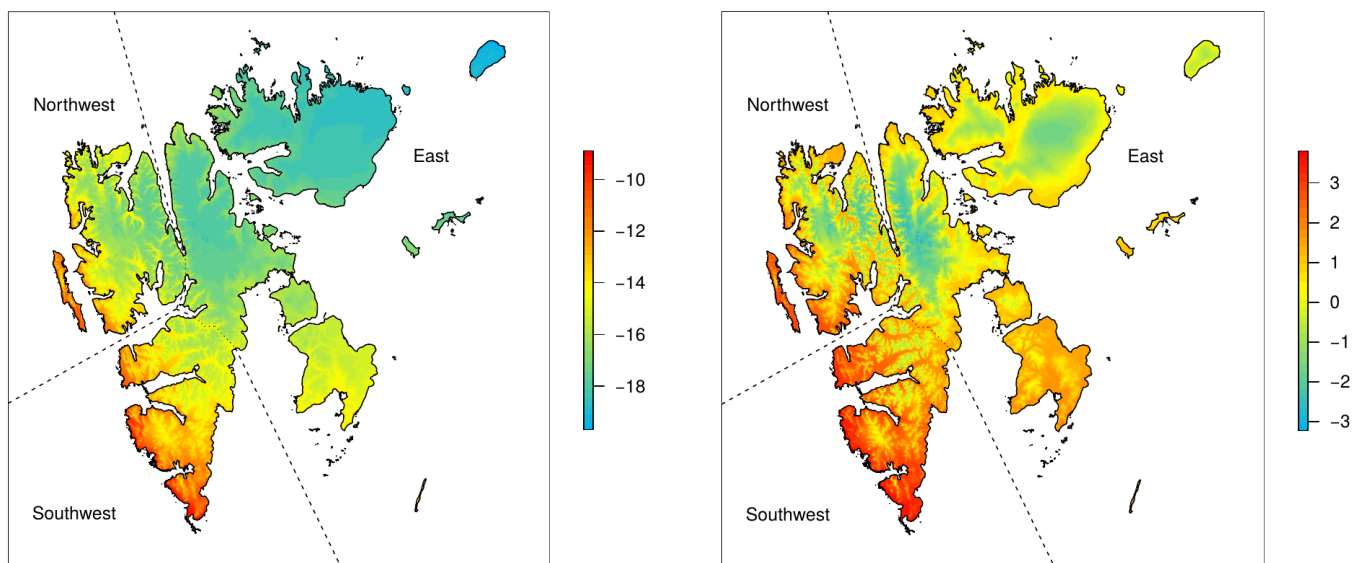
Figure 4.1.2. Winter (Dec-Jan-Feb; left) and summer (Jun-Jul-Aug; right) temperature [°C] averaged over 1971-2000 based upon the Sval-Imp dataset. Note that the colour scales are different!

Station name	1961 – 1990 average					1971 – 2000 average				
	Annual	Winter	Spring	Summer	Autumn	Annual	Winter	Spring	Summer	Autumn
Bjørnøya	-2.3	-7.5	-4.8	3.6	-0.5	-1.7	-6.6	-4.0	3.9	-0.2
Hopen	-6.4	-13.3	-9.9	1.3	-3.7	-5.6	-12.3	-8.8	1.7	-3.1
Hornsund	-5.4	-12.2	-8.8	3.0	-3.6	-4.7	-11.2	-7.7	3.3	-3.2
Isfjord Radio	-5.0	-11.4	-8.6	3.6	-3.6	-4.4	-10.7	-7.7	4.0	-3.1
Barentsburg	-6.1	-13.7	-10.0	3.9	-4.6	-5.5	-12.8	-9.1	4.1	-4.2
Svalbard Airport	-6.7	-15.0	-10.8	4.1	-5.2	-5.9	-13.9	-9.6	4.5	-4.7
Ny-Ålesund	-6.3	-13.7	-9.7	3.5	-5.3	-5.7	-12.9	-8.8	3.7	-4.7
Svalbard total	-9.3	-17.2	-12.4	0.3	-8.1	-8.7	-16.0	-11.8	0.5	-7.4
Svalbard E	-10.1	-18.6	-13.2	-0.1	-8.8	-9.5	-17.2	-12.7	0.1	-8.1
Svalbard NW	-9.1	-16.6	-12.0	0.2	-8.1	-8.4	-15.4	-11.3	0.5	-7.6
Svalbard SW	-7.2	-14.3	-10.3	1.4	-7.4	-6.7	-13.4	-9.8	1.8	-5.4

Table 4.1.1 Average annual and seasonal temperature [°C] for weather stations (observations) and Svalbard regions (Sval-Imp dataset).

et al., 2016). The difference between summer and winter temperatures is highest in this region. The southern region is warmest in all seasons, and the temperature difference between winter and summer is smaller than in the other regions. The station temperatures are in general higher than the average temperatures for the corresponding regions. This is due to the stations' locations at low altitudes and in coastal areas. For stations as well as for regions, both the north-south and the east-west temperature gradient can be seen (cf. Gjelten et al., 2016).

4.1.2 Temperature development at Svalbard in the instrumental period

The 1990s were significantly warmer than the 1960s, thus the average annual temperatures over 1971-2000 are between 0.5 and 1 °C higher than the 1961-1990 values, for regions as well as stations. Temperatures during winter increased considerably more than during summer, thus, the difference between winter and summer temperatures has decreased slightly.

Station name	1961-1990	1981-2010	1988-2017
Bjørnøya	-0.6	0.5	1.1
Hopen	-0.8	0.8	1.7
Hornsund	-0.7	0.6	1.4
Isfjord Radio	-0.6	0.5	1.2
Barentsburg	-0.6	0.6	1.4
Svalbard Airport	-0.6	0.8	1.7
Ny-Ålesund	-0.6	0.5	1.2
Svalbard total	-0.6	0.7	1.5
Svalbard E	-0.7	0.8	1.6
Svalbard NW	-0.7	0.6	1.3
Svalbard SW	-0.6	0.5	1.2

Table 4.1.2 Difference in average annual temperature [°C] between different 30-year periods and the reference period 1971-2000 for weather stations (observations) and Svalbard regions (Sval-Imp).

The temperatures have continued to increase after year 2000. Temperature differences between the reference period 1971-2000 and other 30-year periods for regions and weather stations are summarised in Table 4.1.2. Note that the temperature average for Svalbard for the latest 30 years is already 1.5 °C higher than it was during the reference period 1971-2000.

The annual mean temperatures for all weather stations in Svalbard show a similar long-term pattern (Figure 4.1.3). The smoothed time series indicate multi-decadal variability, leading to a general warming before the 1930s, a relatively warm period during the subsequent two decades, a temperature decrease from the 1950s to the 1960s, and thereafter a general temperature increase. These features are discussed by Hanssen-Bauer (2002), and can also be seen for other parts of the Arctic (e.g. Polyakov et al. 2003). The warming of the Arctic that started in the 1910s and lasted for two decades is often referred to as the "early 20th century warming", and is one of the most spectacular climate events of the twentieth century (Bengtsson et al., 2004). The data coverage was extremely limited in the Arctic in the first half of the 20th century,

but it is still clear that the spatial pattern of the earlier warm period in the 1930's and 40's was different from that of the current warm anomaly. In particular, the current warm period is partly linked to the Northern Annular Mode and affects a broader region (Polyakov et al. 2003).

Regional time series based on reanalysis are available from 1958. They show similar trends as the individual stations. The eastern region, which includes Hopen, shows a stronger warming during the latest decades than the other regions.

Linear trends are used to quantify the temperature development in Svalbard (Table 4.1.3), even though there is certain scepticism against using linear trends as a measure for climate change, because such changes not necessarily occur linearly (e.g. Benestad, 2003). Earlier studies (e.g. ACIA, 2005; Førland et al., 2011) have shown that the longest Arctic series can be divided into three periods where the first and the last show statistically significant warming ("early 20th century warming" and the present period of warming), while the middle period shows statistically significant cooling.
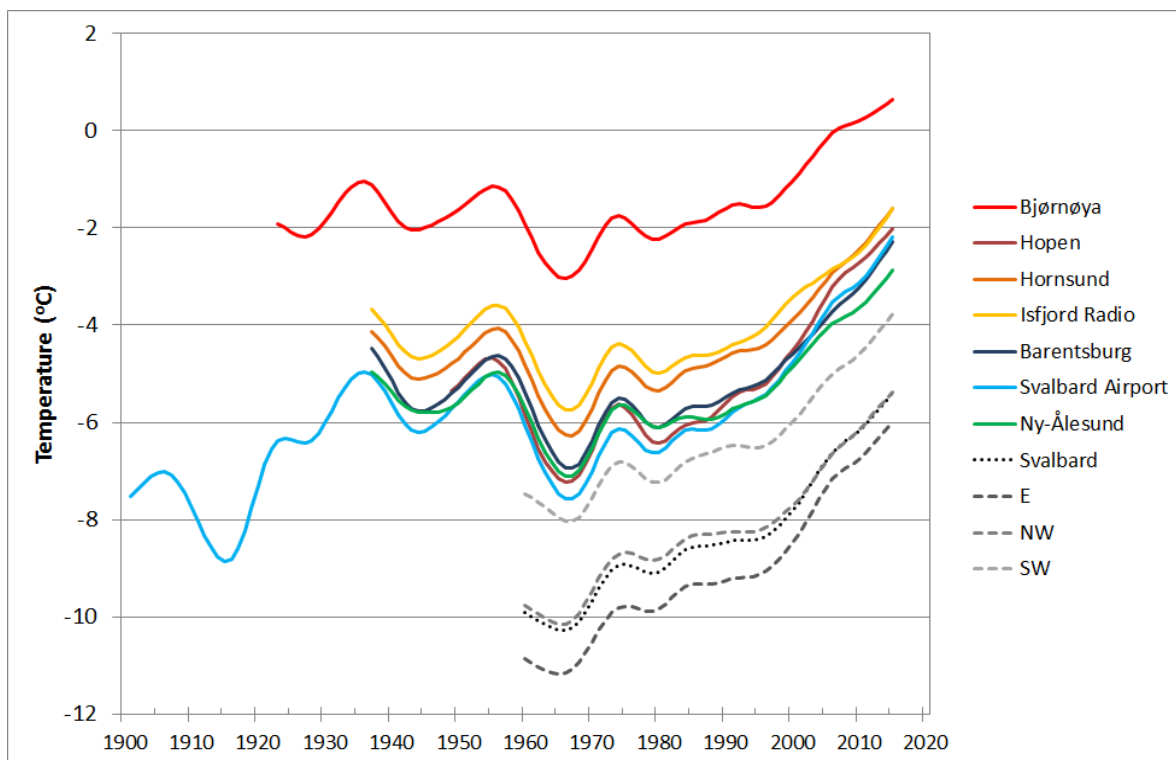
Figure 4.1.3. Annual mean temperature [°C] for weather stations (observations) and regions (Sval-Imp dataset). The series are smoothed by a Gaussian filter to show decadal scale variability.

In this report, we present the trends only for the full length of the series, and for the period 1971 to present. The last period is chosen because 1971 is the first year of the reference period in this study.

Trends for the full series (Table 4.1.3, left), show that the annual mean temperature has increased significantly for all stations and regions. For the series starting in the warm period in the 1930s, this is new compared to earlier studies. The temperature has increased in all seasons – with the strongest increase in winter and/or spring. For Svalbard Airport/Longyearbyen the linear trend indicates an increase in mean annual temperature of 3.7 °C during the latest 118 years, which is about three times the estimated global warming during the same period. The trend is statistically significant (5% level) for all seasons. For the period 1971-2017, trends are calculated for all weather stations as well as for the regions. The linear trends (Table 4.1.3, right part) indicate that the annual temperature at all stations

and regions has increased by between 3 and 5 °C during this 47-year period. The temperature increase was largest in winter, where it adds up to 5 to 8 °C for all stations and regions. All seasonal and annual temperature trends are statistically significant at the 5% level during this period.

While the reasons for the Svalbard warming in the 1930s are still unclear, Hanssen-Bauer and Førland (1998) argue that the warming from the 1960s to the mid-1990s can be mainly linked to changes in the large-scale atmospheric circulation. From a study of radiosonde measurements from Ny-Ålesund, Maturilli and Kaiser (2017) also conclude that changes in atmospheric circulation lead to an enhanced advection of warm and moist air from lower latitudes during the period 1993 to 2014, causing warming and moistening of the atmosphere particularly during winter. However, Dahlke and Maturilli, (2017) estimate that only about 25% of the winter warming from 1996 to 2015 could be

Station name	Full time series (start – 2017)					1971 – 2017				
	Annual	Winter	Spring	Summer	Autumn	Annual	Winter	Spring	Summer	Autumn
Bjørnøya (start 1920)	0,17	0,15	0,32	0,1	0,13	0,64	1,04	0,52	0,29	0,74
Hopen (start 1946)	0,47	0,76	0,53	0,25	0,38	0,99	1,76	0,86	0,36	1,02
Hornsund (start 1935)	0,29	0,39	0,45	0,15	0,18	0,81	1,45	0,69	0,29	0,86
Isfjord Radio (start 1935)	0,23	0,24	0,38	0,16	0,17	0,71	1,21	0,68	0,27	0,72
Barentsburg (start 1934)	0,26	0,32	0,41	0,16	0,16	0,81	1,4	0,78	0,33	0,76
Svalbard Airp. (start 1899)	0,31	0,41	0,43	0,13	0,31	1,01	1,67	0,95	0,47	1,01
Ny-Ålesund (start 1935)	0,24	0,26	0,36	0,14	0,21	0,71	1,35	0,57	0,24	0,74
Regions (start 1958)	Full time series (1958 – 2017)					1971 – 2017				
	Annual	Winter	Spring	Summer	Autumn	Annual	Winter	Spring	Summer	Autumn
Svalbard total	0,81	1,61	0,54	0,35	0,78	0,87	1,58	0,57	0,35	1,01
Svalbard E	0,88	1,79	0,55	0,3	0,9	0,95	1,78	0,61	0,31	1,11
Svalbard NW	0,78	1,47	0,56	0,43	0,67	0,8	1,38	0,51	0,42	0,91
Svalbard SW	0,67	1,25	0,47	0,42	0,57	0,75	1,27	0,51	0,39	0,84

Table 4.1.3 Linear trends in temperature [°C/decade] for weather stations (observations) and regions (Sval-Imp dataset). Bold types: Significant trends (5% level)

attributed to changes in circulation. Isaksen et al. (2016) conclude that the warming at Svalbard was mainly related to changes in air mass properties during the period 2001 to 2015. The air is now milder for all seasons, regardless of large-scale wind direction. The warming of air masses appears to be primarily caused by heat exchange from increasingly ice-free sea areas north of Svalbard and the Barents Sea. This is in agreement with conclusions drawn by Kohnemann et al. (2017). In addition, reduced sea ice cover in the fjords contributes to increased temperature locally, especially during the winter months. This effect has been particularly clear after 2006 (Muckenhuber et al., 2016). In summary, the increase in temperature after 2000 is not primarily driven by more "southerly winds", but rather from the retreat of sea ice, along with higher sea temperatures and a general background warming (Isaksen et al., 2016). It is not possible, yet, to say how much of the warming in Svalbard is due to natural climate variation, and how much is due to increased man-made greenhouse gas emissions. However, for the entire Arctic the image is clearer: Increasing concentrations of greenhouse gases in the atmosphere are the primary underlying cause of the warming observed over the last 50 years (AMAP, 2017).

4.1.3 Projected temperature development towards 2100

4.1.3.1 Projections from global models

Sea ice reduction has influenced the warming in the Svalbard region in the later decades, and it will also be an important factor in the future. Applying projections directly from global climate models (without involving downscaling) results, for the Svalbard area, on average in an increase in annual mean temperature of about 3 °C, 6 °C, and 10 °C for emission scenarios RCP2.6, RCP4.5 and RCP8.5, respectively, from 1971-2000 to 2071-2100 (Figure 4.1.4). This corresponds roughly to two to three times the estimated global warming under the same scenarios (IPCC 2013).

Large contrasts are, however, expected within the Svalbard area, due to regional patterns in the sea ice retreat. The withdrawal of sea ice in the northern and eastern Svalbard areas will continue, while southern and western areas are already ice-free most of the year in present climate. A generally large heating of the surface and near surface atmosphere in areas becoming ice-free may also affect weather systems, as low pressures may move further into the Arctic (e.g. Moore et al. 2018). Thus, downscaled climate projections are necessary to investigate how large scale changes might affect the climate locally.

Svalbard (8E-34E/76N-82N)
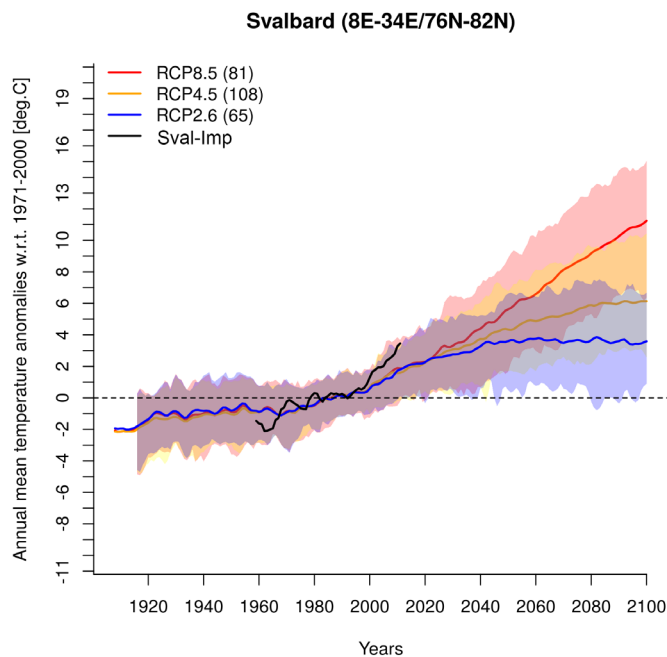
Figure 4.1.4. Annual mean temperature anomalies [°C] as simulated by the CMIP5 global climate model runs (without downscaling) following RCP2.6 (blue), RCP4.5 (orange) and RCP8.5 (red) emission scenarios. The envelopes are based on the 5th and 95th percentiles of the multi-model simulations, hence, display the 90 % spread over the number of runs (indicated in the legend between parentheses) used for each ensemble simulations. The black line shows the Sval-Imp dataset, which is applied as reference dataset. All the simulations have been subject to a spline smoother to extract the inter-annual climate change signal.

4.1.3.2 Downscaled projections

The following downscaled projections of future temperature development for Svalbard are based upon (a) empirical statistical downscaled (ESD) projections from all available global CMIP5 models and for the emission scenarios RCP2.6, RCP4.5 and RCP8.5, (b) results from the Arctic CORDEX ensemble of regional climate models (RCMs) for RCP4.5 and RCP8.5, and (c) the fine scale climate model COSMO-CLM (CCLM) for RCP8.5. See Chapter 3.1 for information on the methods, and Appendix 1 for information on global models that are applied in the different approaches. For all models except CCLM, annual and seasonal temperature changes from 1971-2000 towards 2031-2060 and 2071-2100 are calculated. For CCLM, only temperature changes from 1971-2000 towards 2071-2100 are available. Calculations are performed for the Svalbard land area, as well as for the regions "E", "NW" and "SW" defined in Chapter 4.1.1. Some projections are also given for Svalbard Airport. All results are tabled in Appendix 2. The main results are summarised in the following paragraphs.

a) ESD results; large ensembles

Table 4.1.4 shows projected temperature changes towards the end of the century for the Svalbard land area, based on ESD of the available CMIP5 ensemble under the emission scenarios RCP2.6, RCP4.5 and RCP8.5, respectively. The ensembles are shown as median values and the 5th and the 95th percentiles. The span between the 5th and 95th percentile

may be interpreted as a measure for the uncertainty (cf. Chapter 9). The annual values correspond well with the values deduced directly from the global models (Figure 4.1.4).

A majority of the global models have too much sea ice in the "present climate" (cf. Chapter 8.1.2). This may lead to unrealistic local temperature trends, as these trends are sensitive to if, and when, the local sea ice disappears. Thus, a sub-ensemble was selected, where the GCMs with most sea ice in the "present climate" were excluded. The differences between the temperature projections in the sub-ensemble and the full ensemble are moderate. Thus, the results from the ensemble of "selected models" are shown only in Appendix 2 (Table A2.2 and A.2.3), and the full ensemble will be applied to represent the results from ESD. This does not necessarily imply that using the full ensemble is advisable. A closer investigation would, however, be necessary to remove all models with unrealistic control climate.

b) Arctic CORDEX results, and comparison with ESD results

Table 4.1.5 shows projected temperature changes towards the end of the century for the Svalbard land area, based on Arctic CORDEX projections under emission scenarios RCP4.5 and RCP8.5. The ensembles are shown as median values and the full span of projections due to the small number of ensemble members.

Region	Season	Scenario: RCP2.6 (65 runs)			RCP4.5 (108 runs)			RCP8.5 (81 runs)		
		Med	Low	High	Med	Low	High	Med	Low	High
	Annual	3.8	0.6	6.5	6.2	3.6	10.0	9.5	6.4	13.3
Svalbard	DJF	5.8	-0.4	10.6	9.9	4.4	16.6	15.1	9.0	23.9
total	MAM	3.2	0.5	5.4	5.7	2.8	9.6	8.3	5.1	12.6
(land area)	JJA	1.4	-0.3	3.2	2.4	0.2	4.8	4.2	1.5	7.2
	SON	4.8	0.6	8.0	7.1	4.1	11.2	10	7.0	15.6

Table 4.1.4. ESD results for changes in temperature [°C] from 1971-2000 to 2071-2100 over the Svalbard land area following the scenarios RCP2.6, RCP4.5 and RCP8.5. "Low" corresponds to the 5th percentile, "High" to the 95th percentile and "Med" to the median projection based on all available CMIP5 runs ("large ESD ensemble"). Tables for regions can be found in Appendix 2.3.

In spite of a considerable difference in number of models included in the full ESD and the RCM ensembles, the median estimated temperature changes for the Svalbard land area towards the end of the 21st century are quite similar, both for RCP4.5 and for RCP 8.5 (Tables 4.1.4 vs. 4.1.5 and Figure 4.1.5). The "high" and "low" projections from the ESD and RCM ensembles differ more than the median values. The full ESD ensemble is more likely to give a realistic measure of the uncertainty, as the RCM ensemble is too small to represent the total natural climate variability in the area (Deser et al., 2012). Further, outliers may have a large impact on small ensembles.

In order to distinguish between discrepancies caused by different methods and by different ensemble sizes, Table 4.1.6 shows annual and sea-sonal results at the end of the century for ESD-ensembles where only the CMIP5 models applied in Arctic CORDEX are included. The model results are further weighted to be directly comparable to Table 4.1.5. The results confirm that the small ensembles do not completely represent the spread of the results from the full ensemble, especially for RCP4.5 where only 5 runs are considered. For RCP8.5, the 90% spread in the full ESD ensemble is nevertheless nearly covered when considering the complete spread in the Arctic CORDEX projections.

Tables 4.1.4 to 4.1.6 also indicate that ESD projected temperature changes are slightly smaller than comparable Arctic CORDEX projected changes. For both methods, seasonal projections indicate that the temperature increase in winter will be around three times as large as in summer in these areas.

Scenario:		RCP4.5 (5 runs)			RCP8.5 (8 runs)			RCP8.5
Region	Season	Med	Low	High	Med	Low	High	CCLM
Svalbard total (land area)	Annual	6.9	4.9	9.4	9.8	6.7	15.6	7.2
	DJF	10.3	6.8	13.2	14.4	10.6	21.9	9.1
	MAM	6.5	4.1	8.4	9.2	7.7	16.1	7.2
	JJA	3.3	2.3	4.7	5.8	2.0	8.4	4.9
	SON	8.2	6.0	11.4	10.3	6.5	16.2	7.4

Table 4.1.5. RCM results for changes in temperature [°C] from 1971-2000 to 2071-2100 over the Svalbard land area following scenarios RCP4.5 and RCP8.5. "Low" corresponds to the lowest, "High" the highest and "Med" the median projection from Arctic CORDEX. "CCLM" corresponds to the 2.5 km CCLM projection. Tables for regions can be found in the Appendix 2.1.

Scenario:		RCP4.5 (5 runs)			RCP8.5 (5 runs. weighted)			RCP8.5
Region	Season	Med	Low	High	Med	Low	High	MPI-ESM-LR
Svalbard total (land area)	Annual	6.2	4.7	8.2	8.8	8.4	11.6	8.4
	DJF	8.5	6.5	12.7	14	12.6	18.5	12.8
	MAM	5.7	4.6	6.5	8.5	7.3	9.3	8.3
	JJA	2.8	2.0	3.8	4.1	3.8	6.6	3.9
	SON	7.2	5.7	10.7	9.5	7.8	13.2	8.8

Table 4.1.6. As Table 4.1.5, but for an ESD-ensemble based on the global models applied in Arctic CORDEX ("common models"). "MPI-ESM-LR": ESD results from the model used for the CCLM-run.

c) CCLM projection, and comparison with the ensembles

The fine-scale CCLM temperature projection is close to the "low" ensemble projections (Figure 4.1.5 and Table 4.1.5, last column). It is also clearly lower than the ESD projections based on the same global model (Table 4.1.6, last column). It has earlier been documented that the improved spatial resolution in CCLM leads to reduced warming rates in Svalbard land grid boxes (Isaksen et al. 2017). Though we are not ready to conclude on the reason
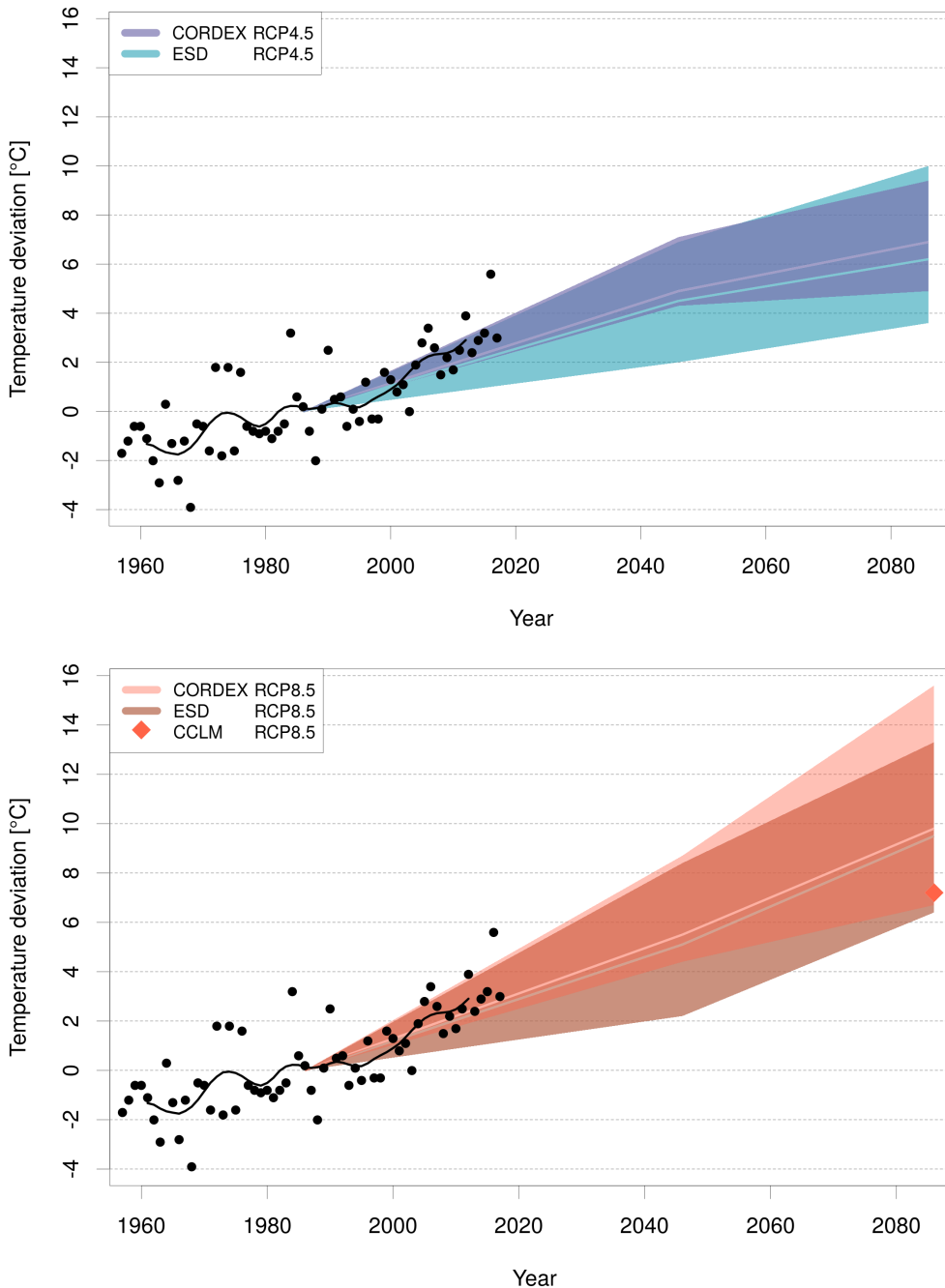
Figure 4.1.5. Annual mean temperature for the Svalbard land area given as deviation [°C] from the reference period 1971-2000. The points and black curve show historical values based on reanalysis from 1958 to 2017 (Chapter 4.1.2). Future projections are given for RCP4.5 (a) and RCP 8.5 (b). ESD projections are based upon 108 CMIP5 models for RCP4.5, and 81 models for RCP8.5. RCM projections are based upon the 5 and 8 Arctic CORDEX simulations respectively. Changes are projected to the periods 2031-2060 and 2071-2100. Median, "high" and "low" projections are shown. The result for the CCLM RCP8.5 projection towards the end of the century is indicated by a diamond.

for this, we assume that the improved spatial resolution leads to more realistic results. Further, the CCLM is downscaled from a global model with reasonable sea ice climatology in the control period. However, it is important to keep in mind that results from only one model run must be used with caution and always placed in conjunction with other projections.

4.1.3.3 Application of the downscaled projections

Our preliminary advice is to apply the medians of the temperature ensembles as a main guideline for assessing consequences of climate change. This is supported by the similarity of the medians from the ESD and RCM projections, which indicate a robust result. The spread of the model results is often used as a measure for the uncertainty of the results. In the Svalbard area one should, however, consider the re-alism, particularly of the "high" projections, before applying them for assessing consequences of climate change. Under emission scenario RCP8.5 for example, the regional models with the highest warming rates give average winter temperatures for Svalbard well above 0 °C towards the end of

the century when adding them to the 1971-2000 temperatures (Figure 4.1.6). This is not realistic, and is probably caused by a control climate that is too cold (see Box 4.1). The "high" ESD projection is also unreasonably warm, even though application of the 95 percentile as the "high" projection excludes the highest model runs (Figure 4.1.6).

The increased spatial resolution of the CCLM projection can definitely add value to local climate change assessments. The fact that the CCLM control period temperatures are rather realistic in the Svalbard area (Box 4.1) also enables us to derive climate indices without adding to the uncertainty by application of bias adjustment (cf. Box 5.1). Hence, results from CCLM will in this and the following chapters be applied both for improving the spatial resolution of temperature and precipitation projections, and for estimating changes in temperature indices (Chapter 4.2), snow conditions (Chapter 5.2), glaciers (Chapter 6) and permafrost (Chapter 7.1). When assessing the results from these analyses, one should take into account that the CCLM projection is close to the low temperature projections in the RCP8.5 ensembles except during
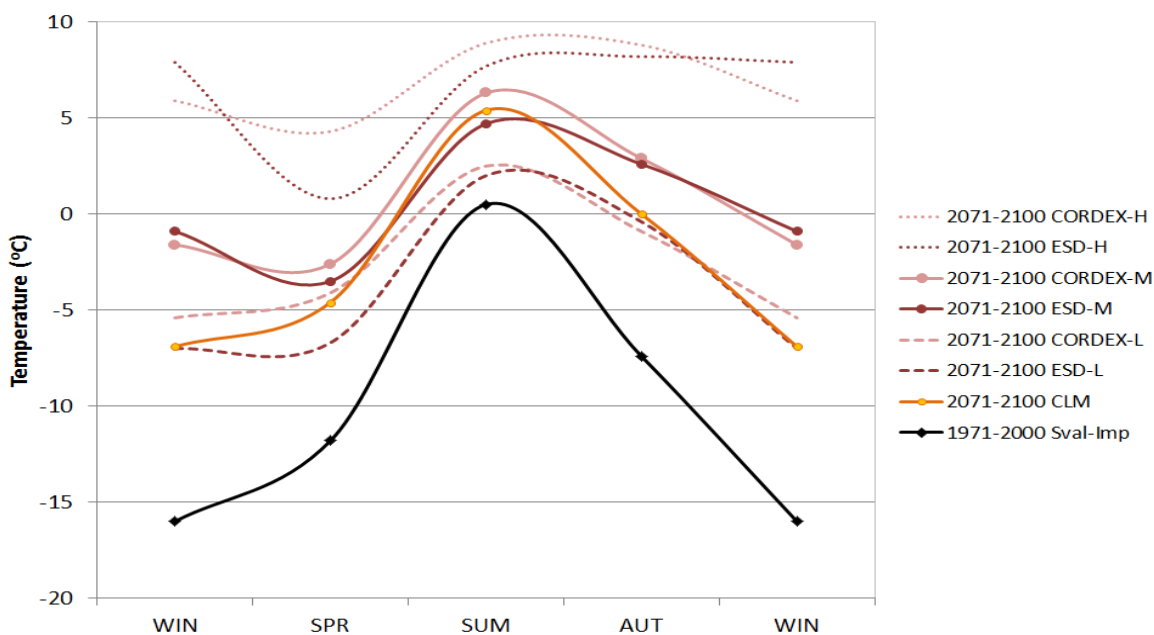
Figure 4.1.6. Winter (Dec-Jan-Feb), spring (Mar-Apr-May), summer (Jun-Jul-Aug) and autumn (Sep-Oct-Nov) temperature [°C] for the period 1971-2000 based on the Sval-Imp dataset (black curve), and projections for the period 2071-2100 under the emission scenario RCP8.5 (coloured curves) for the Svalbard land grid points. Winter is plotted in both ends to show the whole seasonal cycle. Future projections are given for the fine scale CCLM (yellow), and for the Arctic CORDEX (pink) and ESD (red) ensembles. Ensembles are represented by the "low", "median" and "high" ensemble members.

BOX 4.1 Temperature projections from regional climate models (RCMs)

The Arctic CORDEX ensemble of RCM projections includes five projections for emission scenario RCP4.5, and eight for RCP8.5. These are applied to project changes in temperature from the control period 1971-2000 towards 2031-2060 and 2071-2100 for Svalbard (Figure 4.1.5).

The projected changes will depend not only on the general climate sensitivity of the models, but also on temperature conditions in the "present climate". A majority of the Arctic CORDEX ensemble members are colder in the control period compared to the observed climate (Figure B4.1). In such models, melting of the surplus ice may through feed-back mechanisms lead to locally enhanced warming. The modelled temperature change may then be larger than it would have been for the same model under a more realistic control climate. When adding this temperature change to the observed temperature during the period 1971-2000, the results may be unrealistic. E.g. the EC-EARTH-based projections (Figure B4.1, green curves) have 1971-2000 annual temperatures for Svalbard land areas about 5 °C below those estimated from the Sval-Imp dataset. This "bias" is even larger in winter (Figure B5.1), and the mean winter temperatures would end up well above 0 °C (Figure 4.1.6). This is not likely during the "Polar night". One should thus be aware that the upper end of the uncertainty span indicated by adding the ensemble to the observed temperature is unrealistically warm, and should therefore be applied with great caution. Throughout this report, all available Arctic-CORDEX models are still applied. Only a small model ensemble is available: eight members for RCP8.5 and five memebers for RCP4.5, whereas an ensemble consisting of at least 30 models would be preferable to obtain robust statistics. Excluding models from the ensemble is therefore not a viable solution.
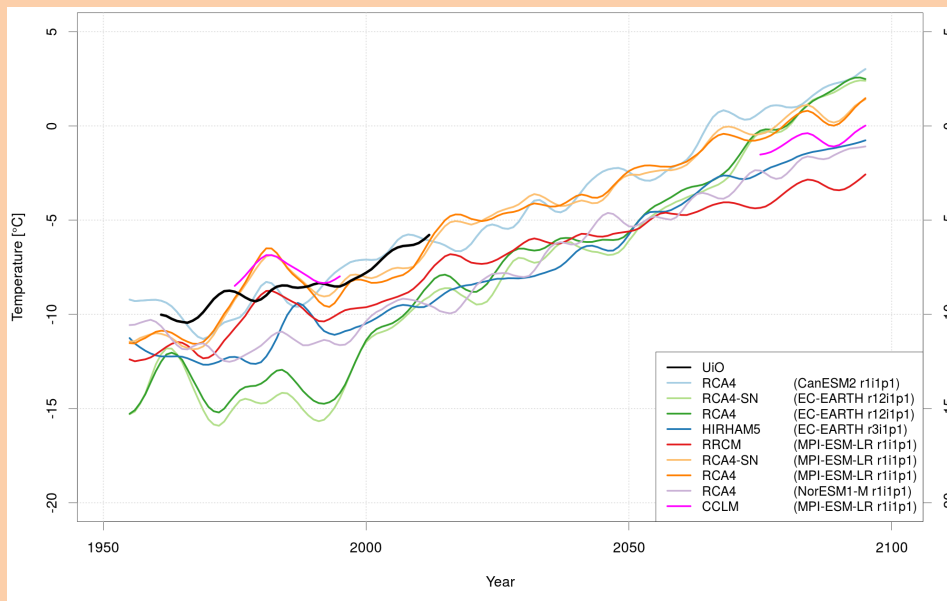
Figure B4.1 Arctic CORDEX and CCLM projections of annual mean temperatures for Svalbard under emission scenario RCP8.5. The black curve shows results for the Sval-Imp dataset. The curves are smoothened to show decadal scale variability.

The fine scale CCLM projection (purple curves in Figure B4.1) is based upon the same global model (MPI-ESM-LR) as two Arctic CORDEX projections (yellow and orange curves) with rather realistic temperatures compared to the Sval-Imp dataset. However, the control period 1971-2000 happens to be in the warmer part of a multi-decadal variation in this model, and thus the control period has a warm bias. Though the CCLM model projects an average annual temperature of around -1°C for the last 30 years of the century, which is in the middle of the span of the Arctic CORDEX models (Figure B4.1), the temperature change projected by this model is in the low end of the RCP8.5 ensemble and close to the median of the RCP4.5 ensemble (Figure 4.1.5). The results from the CCLM model may thus be regarded as an example of a possible future climate under either scenario. It will be applied for projecting changes in indices where an improved spatial resolution is of importance.

summer (Figure 4.1.6), and actually closer to the median of the RCP4.5 scenario (Box 4.1). Anyway, these results serve the purpose of pointing out the direction and spatial patterns of the projected climate changes.

4.1.3.4 Projections of temperature development through the 21st century

Figure 4.1.5 summarises the temperature projections under RCP4.5 (a) and RCP8.5 (b) towards the end of the century. For the period 1971 to present, the observed trend is slightly above the median projections. This may be because the loss of sea ice in the area has been larger in reality compared to the model medians.

The projections for RCP4.5 (a) and RCP8.5 (b) are rather similar until the mid-century (medians: + 4.0 to +5.5 °C) , while they differ considerably towards the end of the century (medians: +6 to +10 °C). As pointed out earlier, the CCLM result towards the end of the century is low in the RCP8.5 ensembles, and may be regarded as more representative for the RCP4.5 ensembles. The median increase of the ESD projections under RCP2.6 is 3.6 °C for the mid-century (Appendix 2, Table A.2.3), and 3.8 °C for the end of the century (Table 4.1.4). The difference between the RCP2.6 and RCP8.5 medians is thus less than 2 °C for the mid-century, and more than 6 °C towards the end of the century.

Inter annual-temperature variations are in general large at high latitudes. Even averaged over the total Svalbard land area, the annual mean temperature can vary with several degrees from one year to the next (Figure 4.1.5). Also decadal variability is considerable, and inter-annual as well as decadal scale variability is in the future expected to be superposed on the linear trends depicted in Figure 4.1.5. Thus shorter periods with decreasing temperatures are expected to occur also in the future.

4.1.3.5 Projections of the geographical variation of warming towards the end of the 21st century

The geographical variation within the Svalbard land area for the median of the Arctic CORDEX projections under RCP8.5 towards the end of the century, is illustrated in Figure 4.1.6. In order to improve the spatial resolution, the results have been scaled using the CCLM projection (see Chapter 3.1.4 for details on the scaling method). Figure 4.1.7 shows large gradients in projected temperature change, with the largest warming in the northeastern part. This is true for all seasons except summer (Figure 4.1.7, lower left panel). The pattern is especially pronounced in winter (Figure 4.1.7, lower right panel): While the western part of Svalbard shows an increase of about 12-14 °C, the northeastern part shows changes of up to almost 20 °C for the time period 2071-2100 following the RCP8.5 scenario. For the RCP4.5 scenario (not shown), the changes are about 4 °C smaller, and the gradient is less pronounced.

Average temperature changes on annual and seasonal basis for the regions defined in Chapter 4.1.1 are calculated based upon RCMs (Table 4.1.7) and ESD (Table 4.1.8). The results for the southwestern and northwestern regions are rather similar, while the warming of the eastern region according to the models is expected to be larger than in the other regions, except for the summer.

4.2 Variables derived from air temperature

In this section the RCP8.5 temperature projections from Arctic CORDEX-models and from CCLM are used to calculate present and future number of days per year with average temperature above 5°C (growing days), number of days with average temperature below 0 °C (frost days), and number of days when the temperature crosses 0 °C (zero-crossings). These indicators, and their changes, depend not only on temperature changes, but also on the absolute temperature in the control period. The median for the Arctic CORDEX models is slightly too cold over the major part of Svalbard in this period (Box 4.1), while CCLM is slightly too warm. This explains why the numbers of growing

Region	RCP4.5 (5 runs)					RCP8.5 (8 runs)					RCP8.5 (CCLM)				
	Ann	DJF	MAM	JJA	SON	Ann	DJF	MAM	JJA	SON	Ann	DJF	MAM	JJA	SON
Total	6.9	10.3	6.5	3.3	8.2	9.8	14.4	9.2	5.8	10.3	7.2	9.1	7.2	4.9	7.4
E	7.4	11.1	6.8	3.0	9.0	10.5	16.1	9.8	5.8	11.2	7.6	10.2	7.5	4.9	8.0
NW	6.2	8.4	6.2	3.2	7.1	8.9	12.1	8.7	6.0	9.6	6.7	8.0	6.8	5.0	6.8
SW	6.1	9.1	6.3	4.3	6.5	9.3	13.0	8.7	5.5	9.8	6.4	7.5	6.6	5.0	6.4

Table 4.1.7 RCM results for changes in annual and seasonal temperatures [°C] from 1971-2000 to 2071-2100 over the Svalbard land area and the regions defined in Chapter 4.1.1. The displayed values correspond to median values from the ensemble of Arctic CORDEX results for the RCP4.5 and RCP8.5 emission scenarios and the CCLM results for the RCP8.5 emission scenario.

Region	RCP4.5 (108 runs)					RCP8.5 (81 runs)					RCP8.5 (MPI-ESM-LR)				
	Ann	DJF	MAM	JJA	SON	Ann	DJF	MAM	JJA	SON	Ann	DJF	MAM	JJA	SON
Total	6.2	9.9	5.7	2.4	7.1	9.5	15.1	8.3	4.2	10.0	8.4	12.8	8.3	3.9	8.8
E	6.3	9.8	5.8	2.3	7.3	10.0	16.3	8.6	4.2	10.4	9.0	13.9	8.9	4.1	9.2
NW	5.9	8.5	5.3	2.3	7.3	9.0	13.6	7.4	4.0	10.1	7.7	11.2	7.1	4.0	8.4
SW	6.3	10.1	5.7	2.7	6.7	9.4	15.0	8.1	4.4	9.3	7.8	11.7	8.0	3.4	8.0

Table 4.1.8 ESD results for changes in temperature [°C] from 1971-2000 to 2071-2100 over the whole Svalbard land area and the regions defined in Chapter 4.1.1 following the scenarios RCP4.5 and RCP8.5. The displayed values correspond to the median (50th) from the ensemble of ESD results for the RCP4.5 and RCP8.5 emission scenarios and the MPI-ESM-LR results for the RCP8.5 emission scenario. Similar tables for the RCP2.6 can be found in the Appendix 2.3.
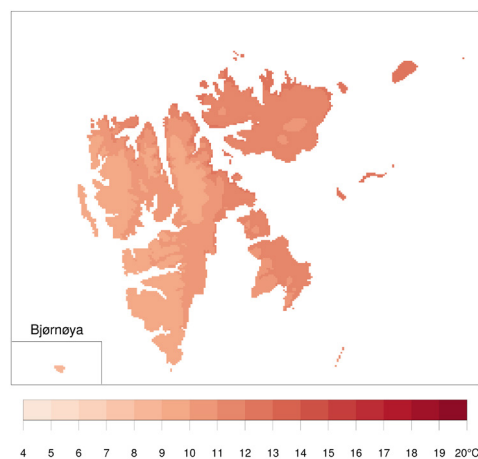
Figure 4.1.7: Ensemble mean temperature changes [°C] from 1971-2000 to 2071-2100 in the Arctic CORDEX simulations assuming the RCP8.5 emission scenario. The spatial resolution is improved by scaling with the signal from the CCLM run. Upper panel: Annual temperatures. Lower panels: Summer (left) and winter (right).
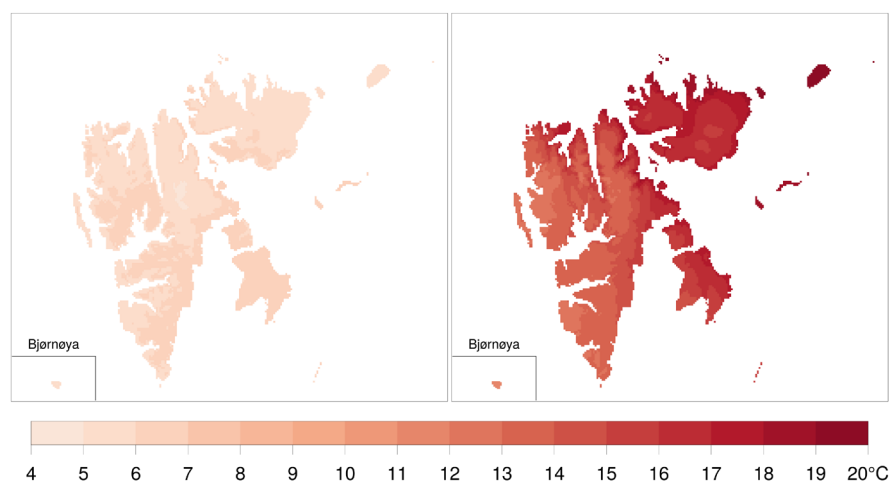
days per year during 1971-2000 are higher and the numbers of frost days lower in the CCLM than in the Arctic CORDEX median (Table 4.2.1). On the other hand, the Sval-Imp dataset is slightly too cold in the coastal zone of Spitsbergen, including the Spitsbergen stations (Cf. Chapter 3.1). Bjørnøya is not covered by the Sval-Imp dataset. The climate models tend to have too high temperatures at Bjørnøya in the control period.

4.2.1. Number of days pr. year with T > 5 °C (Growing season)

The average number of growing days (Førland et al., 2004) for the Svalbard land area is very low in the control period (Table 4.2.1), as considerable parts of the archipelago are covered with glaciers and have no such days (Figure 4.2.1 left). The highest values (about one month) occur on Bjørnøya and along the western coast of Spitsbergen – including the fjords. The spatial pattern is similar in all datasets, though the CCLM dataset shows the highest values. For the weather stations at the west coast of Spitsbergen the observed number of growing days are somewhere between the CCLM estimates and the Sval-Imp dataset.

The projected changes in number of growing days towards the end of this century under RCP8.5 (Figure 4.2.1 b) indicate a considerable increase in southern coastal areas, while northeastern inland areas still will have very few growing days even under this high emission scenario. The CCLM and the Arctic CORDEX median agree rather well on the projected number of growing days towards the end of the century (Table 4.2.1, blue columns). For the coastal Spitsbergen stations, the projections show approximately 120 to 145 growing days. This corresponds to a growing season of three to four months, or three to four times more than observed during 1971-2000.

4.2.2. Number of days with T < 0 °C (Frost days)

All datasets agree that the average number of frost days in Svalbard was about 300 in the period 1971-2000 (Table 4.2.1). The highest values occurred in the northern and northeastern glacial areas (Figure 4.2.2 left). The lowest values occurred in Bjørnøya and along the west coast of Spitsbergen. The spatial pattern is similar in all datasets, though the CCLM simulation shows slightly lower values than the others. For the west coast weather stations, the observed values are about 240 days, which is between the CCLM and the median Arctic CORDEX estimates (Table 4.2.1).

Station name	Svalbard average		Bjørnøya		Hopen		Hornsund		Isfjord Radio		Svalbard Airport		Ny-Ålesund	
Growing days per year														
Observed	–	–	37	–	6	–	–	–	30	–	40	–	31	–
Sval-Imp	3	–	–	–	7	–	19	–	14	–	6	–	4	–
CORDEX	1	86	60	230	7	162	5	144	2	123	2	123	1	118
CCLM	14	64	106	227	25	155	45	142	66	147	55	128	51	122
Frost days per year														
Observed	–	–	194	–	245	–	–	–	238	–	241	–	242	–
Sval-Imp	294	–	–	–	240	–	248	–	248	–	273	–	272	–
CORDEX	306	153	148	18	254	33	246	84	253	120	253	120	264	117
CCLM	288	195	139	21	216	56	220	109	218	110	230	134	239	142
Zero-crossing days per year														
Observed	–	–	86	–	78	–	69	–	59	–	60	–	63	–
Sval-Imp	–	–	–	–	45	–	36	–	35	–	34	–	34	–
CORDEX	52	67	68	30	66	35	61	59	63	65	63	65	63	66
CCLM	50	60	73	32	66	51	63	63	52	58	50	59	53	61

Table 4.2.1: Observed and simulated number of growing days, frost days and zero-crossing days in the reference period 1971-2000 (white columns) and in 2071-2100 (blue columns) for Svalbard land areas and for different stations and surrounding model grid-boxes.

Number of growing days (T > 5°C)

0 10 20 30 40 50 60 70 80 90 100 110

Changes in growing days (T > 5°C)

0 20 40 60 80 100 120 140 160 180
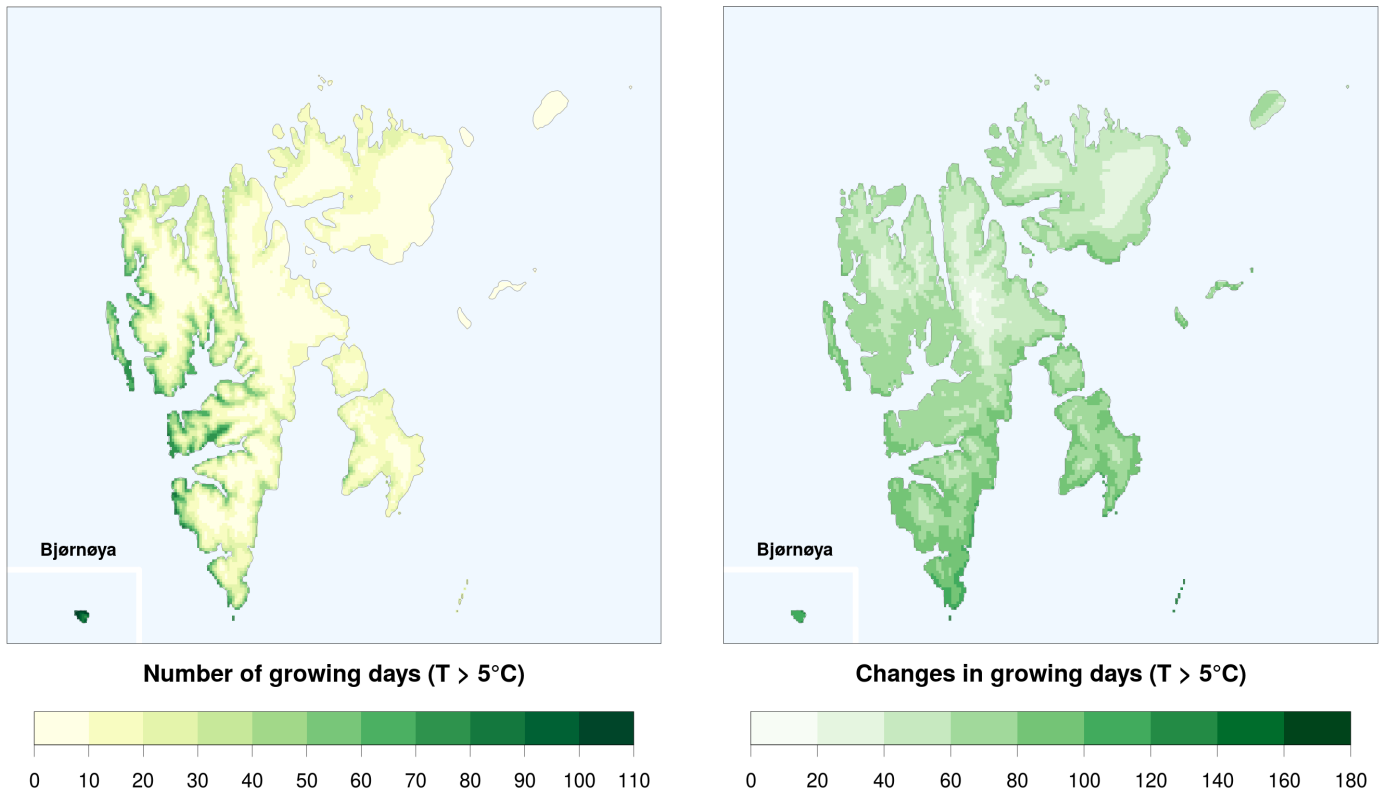
Figure 4.2.1: Average number of growing days per year in the control period 1971-2000 (left), and projected change from 1971-2000 to 2071-2100 (right) according to CCLM under the RCP8.5 emission scenario.

The projected changes in number of frost days under RCP8.5 indicate a considerable decrease in southern coastal areas, while the reduction is limited in northern and northeastern inland areas (Figure 4.2.2 right). For the Spitsbergen stations, the projected number of frost days towards the end of the century varies from 84 to 142, implying roughly a 50% reduction compared to the control period.

4.2.3. Number of days with Tmax > 0 °C and Tmin < 0 °C

Annual number of days with zero crossings (also called frost-change days; Geiger, 2012) for the control period is rather similar in the CCLM and the median CORDEX dataset (Table 4.2.1, white columns). The values also correspond well with observations at the Spitsbergen stations. In Bjørnøya and Hopen, the modelled values are too low, because the small islands are not well resolved in the models and they have a warm bias there.

The largest number of days with zero crossings in the control period is located in southern and coastal areas, while the lowest occurrence of such days can be found in the cold glacial inland areas in the north and northeast (Figure 4.2.3 left). The projected change of the annual values shows mainly an increase, except for Bjørnøya and Hopen (Table 4.2.1, blue columns; Figure 4.2.3 right). The largest increase is projected in the colder areas, while only minor changes in annual number of days with zero crossings are projected along the west coast of Spitsbergen.

The seasonal changes (not shown) are larger than the annual changes, as the warming leads to more frequent zero crossings in winter (DJF) and spring (MAM), especially along the coast, and less frequent crossings in summer (JJA).

Number of frost days (T < 0°C)

120 140 160 180 200 220 240 260 280 300 320 340 360

Changes in frost days (T < 0°C)

-250 -230 -210 -190 -170 -150 -130 -110 -90 -70 -50

Figure 4.2.2: Average number of frost days per year in the control period 1971-2000 (left), and projected change from 1971-2000 to 2071-2100 (right) according to CCLM under the RCP8.5 emission scenario.

4.3 Precipitation

4.3.1 Precipitation climatology

In situ precipitation observations from the Arctic are sparse and are subject to many site and gauge issues (e.g. gauge undercatch, station/instrumental shifts, changes in measurement protocols, automation), while atmospheric reanalyses often contain wet biases linked to inadequate representation of sea ice as well as inhomogeneities from changes in data streams over time (AMAP 2017). Despite several relocations, composite homogenised precipitation series are established (cf. Chapter 3.1.1) for Bjørnøya (1920-present), Hopen (1946-present), Svalbard Airport/Longyearbyen (1912-present) and Ny-Ålesund (1968-present) (Vikhamar-Schuler et al., 2019). The observation-based precipitation results in this report are not corrected for undercatch.

Average annual and seasonal precipitation for Svalbard for the standard normal period 1961-1990 and the reference period 1971-2000 is presented in

Table 4.3.1. The table includes values from measuring stations as well as for modelled regional values from downscaled reanalysis data (Chapter 3.1.1). The model data indicates an average annual precipitation for Svalbard around 700 mm, with highest values for the southwestern region. The modelled precipitation is higher than the measured, but considering effects of gauge undercatch, the downscaled reanalysis in general seems to give a realistic picture of precipitation totals (Vikhamar-Schuler et al., 2019). Further, water balance assessments indicate that areal precipitation for two catchments is twice the measured precipitation at the closest meteorological stations (Chapter 3.2.1).

The measured annual precipitation at Svalbard Airport is less than half of what is measured at Ny-Ålesund and Barentsburg (Table 4.3.1), and also the model datasets indicate values more than twice the measured amount at Svalbard Airport

Number of zero-crossing days (Tmin < 0°C & Tmax > 0°C)

0   10   20   30   40   50   60   70   80   90

Changes in zero-crossing days (Tmin < 0°C & Tmax > 0°C)

-50   -40   -30   -20   -10   0   10   20   30   40   50
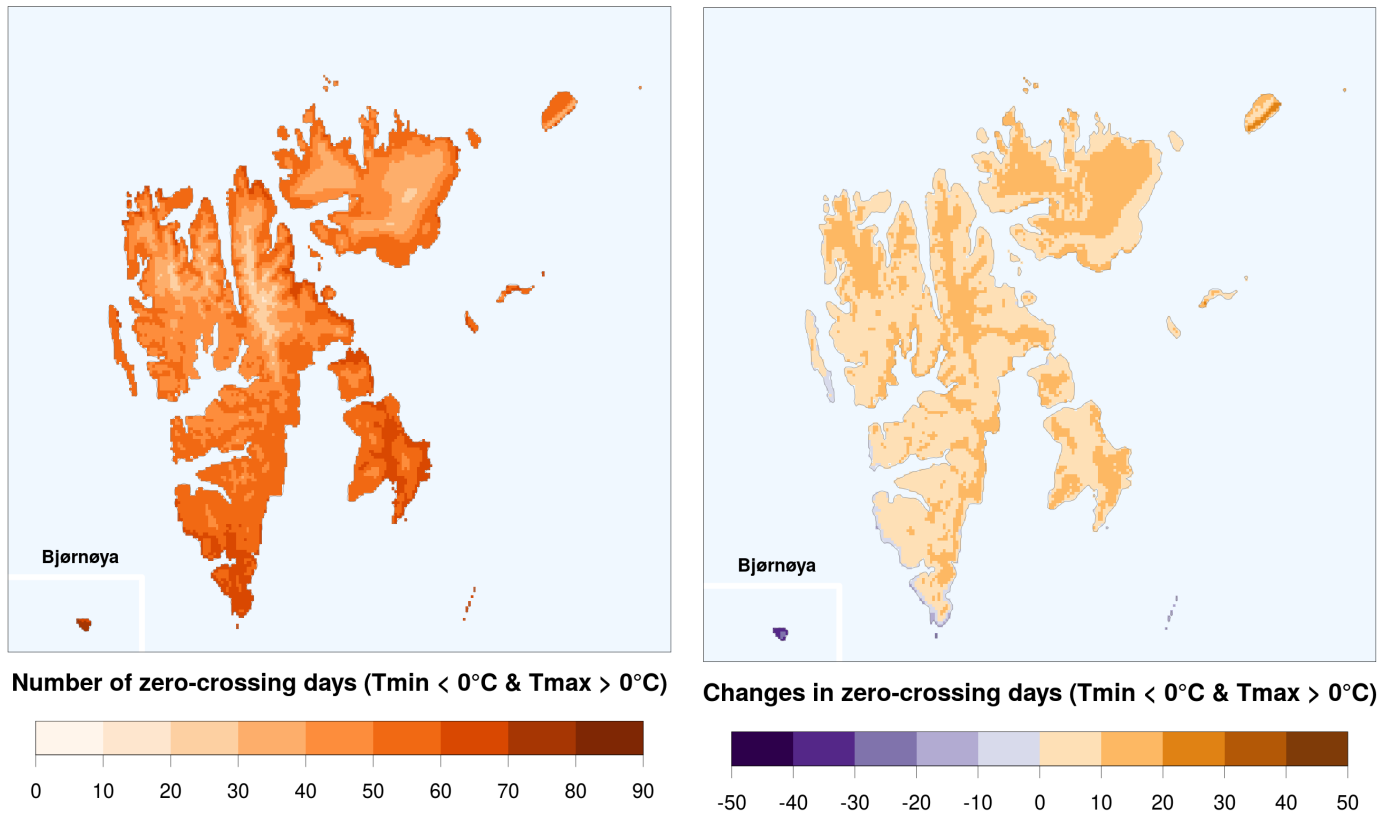
Figure 4.2.3: Average number of zero crossing days per year in the control period 1971-2000 (left), and projected change from 1971-2000 to 2071-2100 (right) according to CCLM under the RCP8.5 emission scenario.
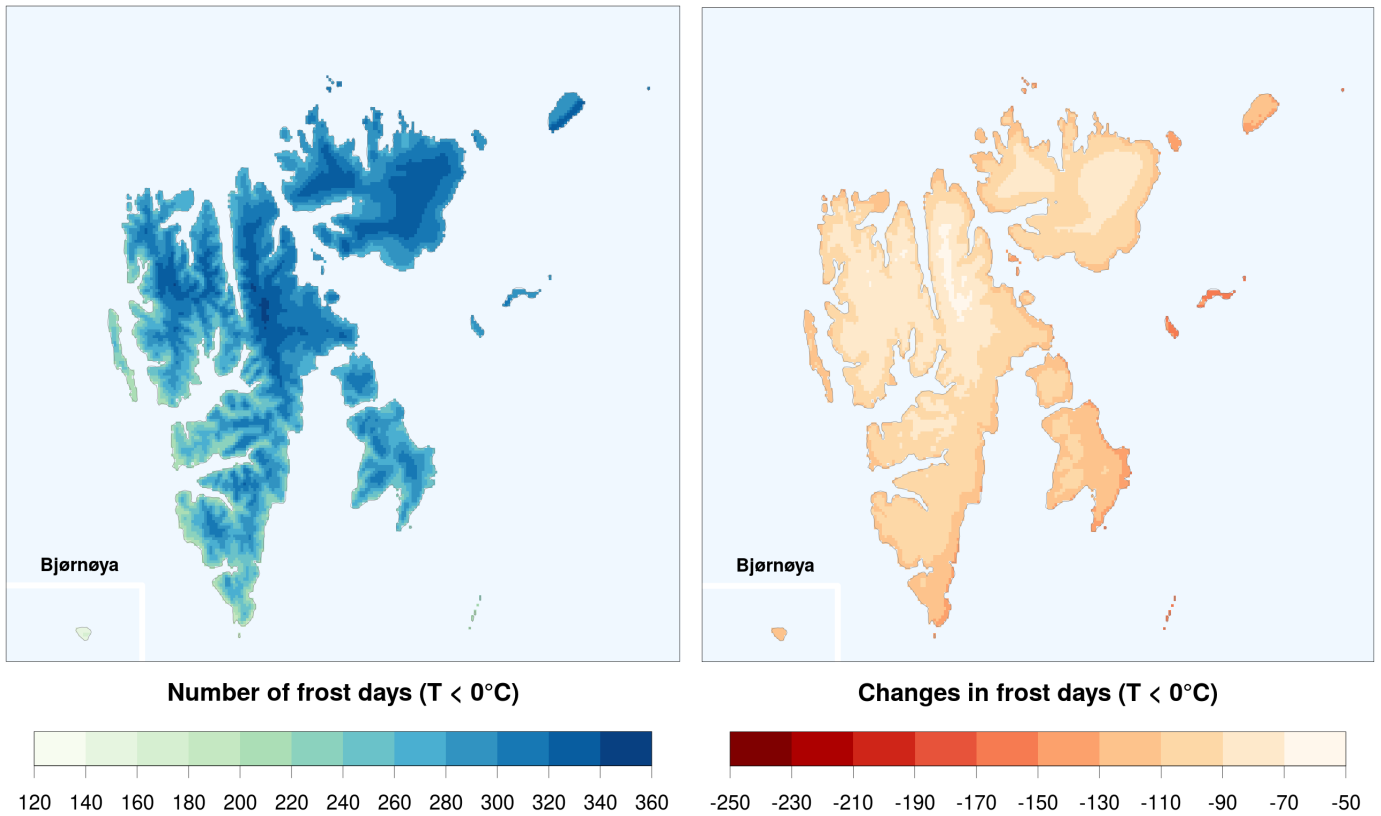
(Vikhamar-Schuler, 2019). The reason is probably that Longyearbyen is lying in a "rain shadow area" that is not resolved by the spatial resolution in the models (Vikhamar-Schuler et al., 2019). At most stations the seasonal differences are rather small, but in general May-June are the driest months, and September-October the wettest (Figure 4.3.1). Except for Bjørnøya, all stations have a secondary maximum in March.

Annual precipitation from the downscaled reanalysis is shown in Figure 2.1.2. The maps of summer and winter precipitation (Figure 4.3.2) demonstrate highest amounts in western mountain areas and lowest values in sheltered valleys and low-elevation areas in the centre and the northeast of Svalbard. More details on the model data, as well as maps for all seasons are presented in Vikhamar-Schuler et al. (2019).

4.3.2 Precipitation development in the instrumental period

4.3.2.1 Linear trends

Obtaining reliable estimates of solid precipitation trends over the Arctic is a challenge (Yang et al., 2005; Groisman et al., 2014; AMAP, 2017). According to ACIA (2005) the Arctic precipitation increased by about 2% per decade during the Arctic warming in the first half of the 20th century (1900-1945), with significant trends in the Nordic region. During the two decades of Arctic cooling (1946-1965), the high latitude precipitation increase was roughly 1% per decade. Since 1966, annual precipitation in the Arctic has again increased by about 2% per decade.

Linear precipitation trends for the Svalbard stations are outlined in Table 4.3.2. The left part presents trends from the start of the series, while the right part shows trends onwards from 1971; - the starting year for the reference period used in this report.

	1961-1990 average					1971-2000 average				
Station name	Annual	Winter	Spring	Summer	Autumn	Annual	Winter	Spring	Summer	Autumn
Bjørnøya	371	93	67	89	121	396	114	82	78	122
Hopen*	250	47	41	84	77	276	58	55	83	79
Hornsund**	405	88	70	122	125	428	90	72	124	142
Isfjord Radio	480	120	99	121	140	NA	NA	NA	NA	NA
Barentsburg	565	173	127	93	173	581	172	134	100	175
Svalbard Airport	189	50	40	51	48	196	51	41	52	52
Ny-Ålesund	385	99	86	84	116	409	110	95	82	122
Svalbard total	694	164	143	162	224	723	181	153	164	225
Svalbard E	659	148	131	158	220	690	170	142	156	222
Svalbard NW	714	171	155	173	214	745	181	165	181	219
Svalbard SW	770	197	162	163	245	791	213	172	167	240

* Adjusted for a severe homogeneity break in 1997, see Chapter 3.1.1

** Start August 1978. Values for 1961-1990 from Førland (1993). Values for 1971-2000 based on 1978-2000

Table 4.3.1. Annual and seasonal precipitation [mm] for weather stations (observations) and Svalbard regions (Sval-Imp dataset)

For Svalbard Airport and Bjørnøya, the (statistical significant) centennial trends for annual precipitation show a linear increase of 3 - 4% per decade. For Svalbard Airport the seasonal trends are highest for autumn, while for Bjørnøya the increase is largest for winter and spring. For the latest fifty years (1971-present) just Bjørnøya, Hopen and Ny-Ålesund have significant (positive) trends for annual precipitation. The stations on the Svalbard mainland have experienced the largest seasonal increase in autumn. For spring and summer, there is a (non-significant) tendency of negative trends for all the Spitsbergen stations.
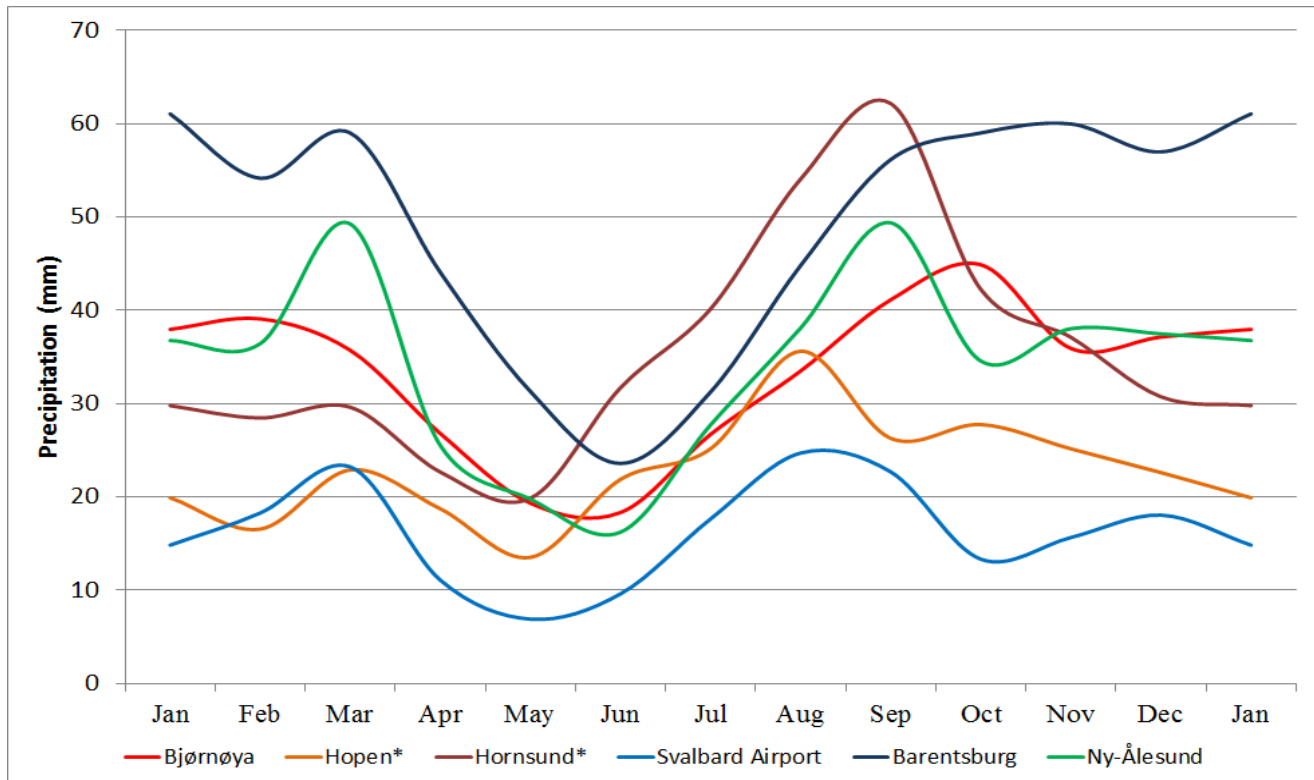
Figure 4.3.1: Seasonal cycle (averages from 1971-2000) in precipitation [mm/month] for selected meteorological stations in the Svalbard region. (* see legend for Table 4.3.1)
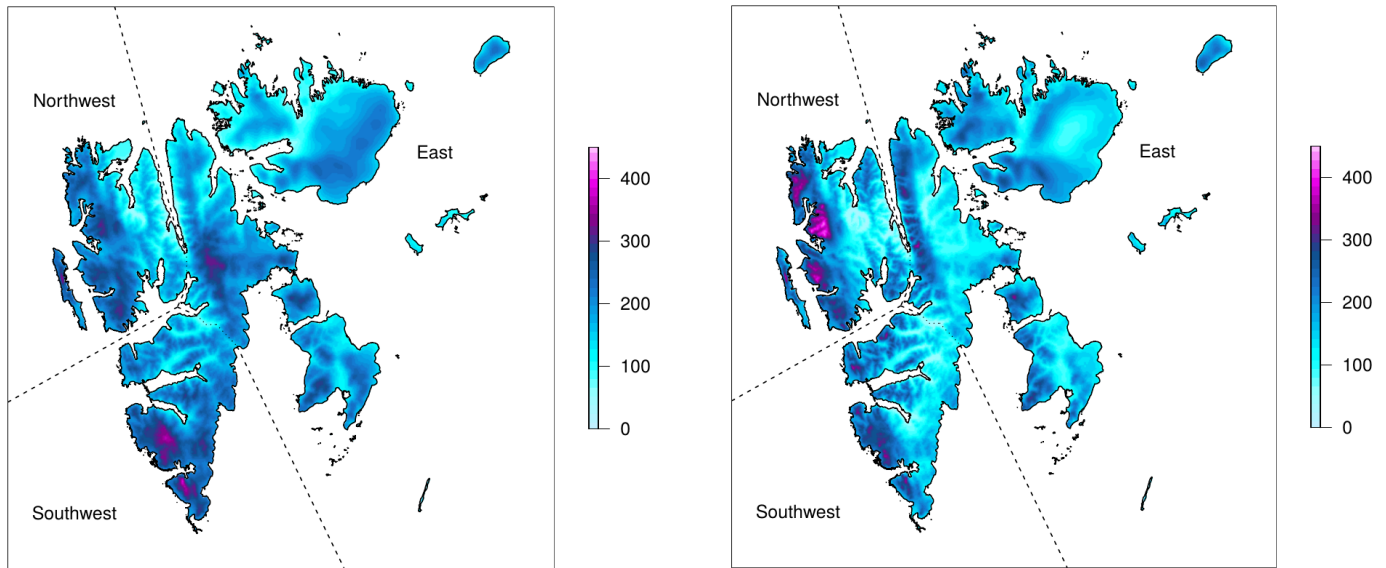
Figure 4.3.2. Downscaled precipitation [mm] for the reference period 1971-2000.Left: Winter (Dec-Jan-Feb), right: Summer (Jun-Jul-Aug)

For the period 1971-2017 with mostly complete records for observational as well as reanalysis-based datasets, the annual regional trends from Sval-Imp dataset are negative in the western region, while the observation-based trends are positive. These differences may be fictitious as the trends are small and not statistically significant, except for Ny-Ålesund. However, as more precipitation is falling as rain (Figure 4.3.4), the undercatch in the precipitation gauges is reduced (Førland and Hanssen-Bauer, 2000). Thus the gauges catch a larger fraction of the "true" (and modelled) precipitation. It is therefore possible that while the measurements show increased precipitation during 1971-2017, the "true precipitation" has decreased slightly, though not statistically significant (Vikhamar-Schuler, 2019).

The statistically insignificant precipitation trends during the period 1971-2017 may still seem surprising, taking into account the strong temperature trend in this period, and thus the increased potential of precipitable water in the airmasses (Box 4.2). Hanssen-Bauer and Førland (1998), however, concluded that for Svalbard the local precipitation trends to a larger degree than temperature trends are governed by atmospheric circulation patterns. Several studies have shown that the temperature trend during the later decades can be explained only partly by changes in atmospheric circulation patterns (e.g. Isaksen et al., 2016; Dahlke and Maturilli, 2017).

4.3.2.2 Decadal variability

Annual and decadal variations are superimposed on the linear trends depicted in Table 4.3.2. Figure 4.3.3 shows long-term variability on a decadal time scale. In contrast to temperature (Figure 4.1.3), the precipitation series show quite different individual long-term patterns. The main reason is that precipitation varies locally on a smaller spatial scale than air temperature. However, most series have some common features: Secondary maxima in the warm periods in the 1930s and late 1950s (cf. Figure 4.1.3); and secondary minima in the cold period in the late 1940s and 1960s. Unlike most of the observational series, the model data indicates a maximum in the 1970s. Most series indicate increasing precipitation in the warming period after year 2000. Hanssen-Bauer and Førland (1998) showed that the precipitation trend at Svalbard Airport from 1912 to the 1990s to a large degree could be explained by variations in the atmospheric circulation.

Station	Start	Start - 2017					1971-2017				
		Annual	Winter	Spring	Summer	Autumn	Annual	Winter	Spring	Summer	Autumn
Bjørnøya	1920	**3,2**	**4,9**	**5,2**	0,1	**2,3**	**6,4**	**12,1**	**11,7**	-4,7	4,3
Hopen*	1946	**6,8**	**12,2**	**13,2**	-0,1	**5,7**	**5**	**12,5**	**11,8**	-7,2	7,4
Hornsund**	1979	6,7	9,4	-5,7	-7,3	**23,6**	6,7	9,4	-5,7	-7,3	**23,6**
Barentsburg	1948	**3,9**	**3,7**	**4,3**	1,2	**5,6**	0,8	-2,3	-4,7	-6,6	6,6
Svalbard Airp.	1912	**3,7**	2,4	2,7	**4,2**	**5,2**	4,1	8,4	-8,5	-1,2	**14,8**
Ny-Ålesund	1969	**7,8**	**13,3**	-0,4	-1,1	**15,2**	7,1	**14,4**	-3,3	-2,3	15,5
Svalbard total	1958	1,9	6	1,6	-1,3	1,7	-1	4,2	-2,5	-6,2	0,6
Svalbard SW	1958	0,5	3,2	1	-1,2	0	-2,3	1,8	-3,7	-7,1	0
Svalbard NW	1958	1,6	4,9	-0,2	0,1	2,7	-2,1	2,7	-6,2	-6,4	2,4
Svalbard E	1958	2,5	7,7	2,7	-2,1	1,9	0	5,8	-0,3	-5,8	0,1

* Adjusted for a homogeneity break in 1997, see Chapter 3.1.1   ** Data from Hornsund from 1979

Table 4.3.2. Linear trends [% per decade] in precipitation for weather stations (observations) and regions (Sval-Imp dataset). Bold types: Significant trends (5% level)

Table 4.3.3 indicates that, except for Barentsburg, the measured precipitation is higher for the most recent 30-year period than for the reference period. These features are in line with the graphs in Figure 4.3.3. The modelled data show small differences between the various periods, but a tendency to highest values during the reference period because of the high values in the 1970s (Figure 4.3.3). One of the reasons why the downscaled reanalyses show reduced values while observations show increased values for the latest period, may be reduced undercatch in the precipitation gauges during the recent mild winters. Higher winter temperatures increase the likelihood that precipitation will fall as rain instead of snow, resulting in increased catch efficiency of the precipitation gauges (Førland and Hanssen-Bauer, 2000). Figure 4.3.4 demonstrates that the annual fraction of solid precipitation during 1975-2017 indeed has decreased at Bjørnøya, Svalbard Airport and Ny-Ålesund. Hansen et al. (2014) and Vikhamar-Schuler et al. (2016) found a clear tendency for increase in wintertime rainfall events: During November-April 1995-96, 2009-10, 2011-12 and 2016-17; more than 50 % of the total precipitation was falling as rain. A large proportion of the rainfall occurred in just a few events (cf. Chapter 4.4).

4.3.2.3 Rain-on-snow and freezing rain

By studying 37 state-of-the-art climate models, Bintanja and Andry (2017) stated that rain is projected to become the dominant form of precipitation in the Arctic region at the end of this century. Rain on snow causes a crust on existing snow, with implications for wildlife, infrastructure, transportation and other outdoor activities. It may also cause more unstable snow layers with implications for avalanches throughout the winter (Chapter 7.3.3). Figure 4.3.5 shows that the frequency of rain on snow had a minimum in the late 1960s, but has increased during the last fifty years. Isaksen et al. (2017) found that in the winter months, there may be a threefold in the number of mild weather episodes with precipitation as rain up to the end of the 21st century compared to the current situation. Hansen et al. (2014) concluded that the frequency of rain on frozen ground is likely to increase in the future.

Vikhamar-Schuler et al. (2016) found an increase in number of "mild weather days" (i.e. rainfall and average temperature >0°C) as well as for the precipitation sum on rainy "mild weather days" in the winter months (October-April) in the Longyearbyen area during the period 1961-2100.
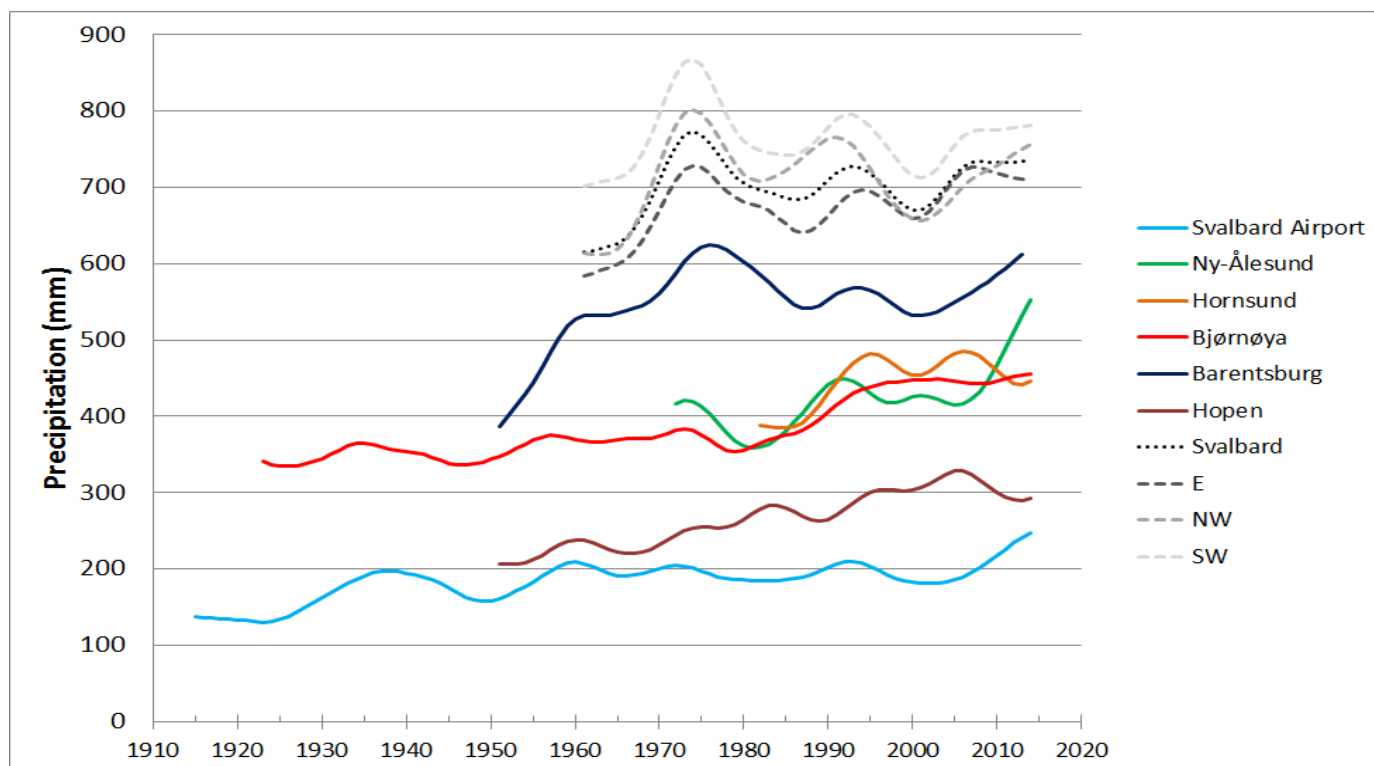
Figure 4.3.3. Annual precipitation [mm] for weather stations (observations) and regions (Sval-Imp dataset). The series are smoothed by a Gaussian filter to show decadal scale variability.

Periode	1961-1990	1981-2010	1988-2017
Bjørnøya	0.93	1.06	1.12
Hopen*	0.91	1.08	1.08
Hornsund*	0.95	1.04	1.09
Barentsburg	0.97	0.95	0.97
Svalbard Airport	0.97	0.96	1.02
Ny-Ålesund	0.94	1.01	1.12
Region-Southwest	0.97	0.95	0.96
Region-Northwest	0.96	0.95	0.97
Region-East	0.96	0.99	1.00
Svalbard-Total	0.96	0.97	0.99

* Hopen and Hornsund: See legend for Table 4.3.1

Table 4.3.3 Ratios between annual precipitation for different 30-year periods and the reference period 1971-2000 for weather stations (observations) and regions (Sval-Imp dataset).

Groisman et al. (2016) found that freezing rain occurrences had increased substantially in the Norwegian Arctic during 1975-2014. Freezing rain and freezing drizzle events may even at low intensities result in natural hazards that cause damage to housing, communication lines, and other man-made infrastructure.
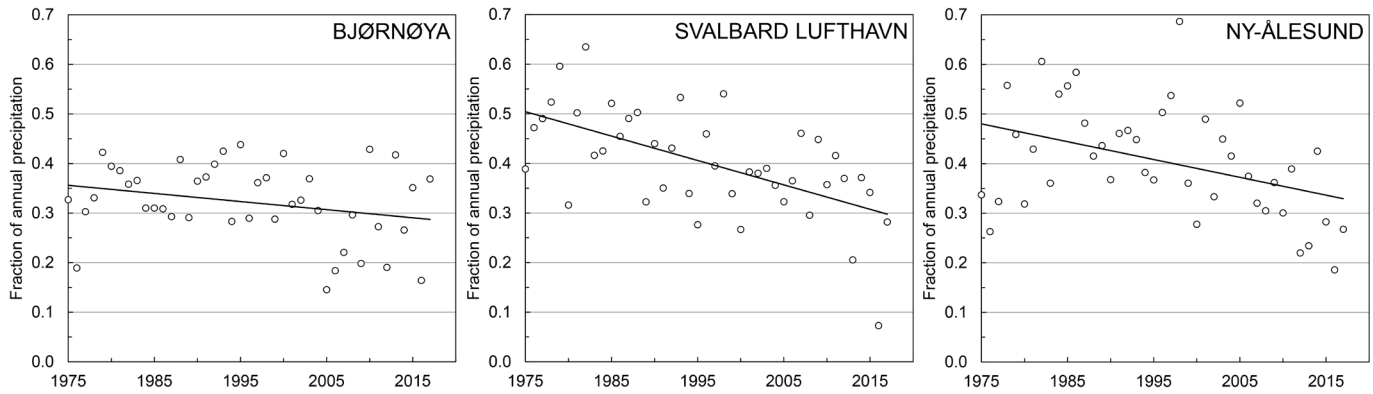
Figure 4.3.4 Fraction of annual precipitation amount falling as snow at Bjørnøya, Svalbard Airport and Ny-Ålesund.

4.3.3 Projected precipitation development towards 2100

The Arctic water cycle will intensify in the future. Higher temperatures and thus increased moisture content are expected to lead to more precipitation in the area around Svalbard. Climate models project increases in cold-season precipitation of 20-50 % over the Arctic Ocean towards the end of this century, with an increasing portion of that precipitation falling as rain instead of snow (AMAP, 2017). Previous simulations with a regional climate model used in the NorACIA project (Førland et al., 2011) showed an increase of about 10% in annual rainfall at Svalbard Airport from 1961-90 to 2071-2100. For autumn and winter the increase was more than 20%.
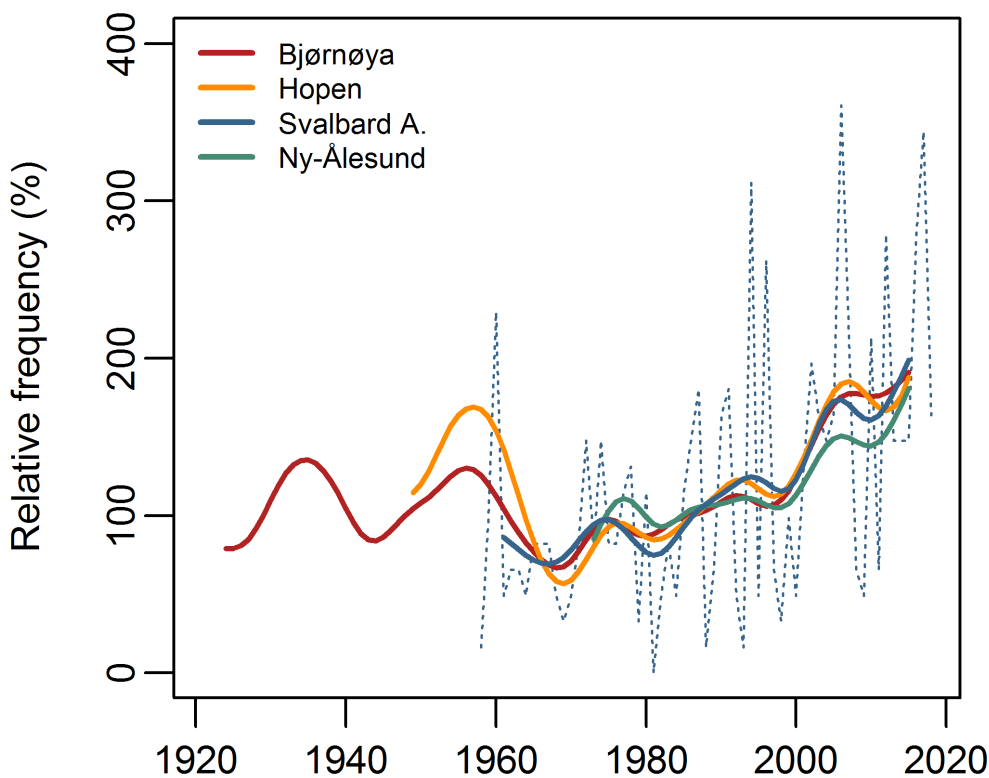
Figure 4.3.5 Number of days per year, relative to the 1971-2000 average, with observed precipitation and a daily mean temperature above 0°C during the winter season (NDJFMA). The dotted blue line shows annual values for Svalbard Airport, while the full drawn curves show decadal scale variability for several stations.

4.3.3.1 Limitations using empirical-statistical downscaling (ESD) for precipitation

Benestad et al. (2016) found that for Svalbard the skill of empirical-statistical downscaling (ESD) models was moderate for the wet-day frequency, but the projections indicated both increases and decreases within the range of -5 to +10 % by 2099. The ESD-results for wet-day mean precipitation were poor, and consequently the precipitation projections in this report are concentrated on results from regional climate models (cf. Chapter 3.1).

4.3.3.2 Arctic CORDEX results

Up to the end of the century, the regional Arctic CORDEX simulations show an increase in annual precipitation for the Svalbard land area of approximately 40 % for emission scenario RCP4.5 and 60 % for RCP8.5 (Table 4.3.4). For RCP8.5 the spread between low and high projections is large (Figure 4.3.6), with the results from the COSMO-CLM (CCLM)-simulations in the lower end. The Arctic

CORDEX runs indicate largest increases for the winter season; smallest for the summer season.

The change in annual precipitation is highest in the northeastern parts (Figure 4.3.7) and smallest in the southwestern parts. This is also reflected in the regions (Table 4.3.5), where the annual increase for the Arctic CORDEX runs under RCP8.5 is 70 % for the eastern region and 40 % for the southwestern region. Seasonal projections for all regions and both scenarios are listed in Appendix 3 (Table A.3.1).

4.3.3.3 CCLM projection and comparison with the Arctic CORDEX ensembles

Table 4.3.4 and 4.3.5 reveal a substantial lower precipitation increase for the CCLM simulation than for the Arctic CORDEX simulations. For the summer season, the CCLM simulation gives an increase of approximately 15 %, while the lowest Arctic CORDEX simulation gives ca. 30 % increase.
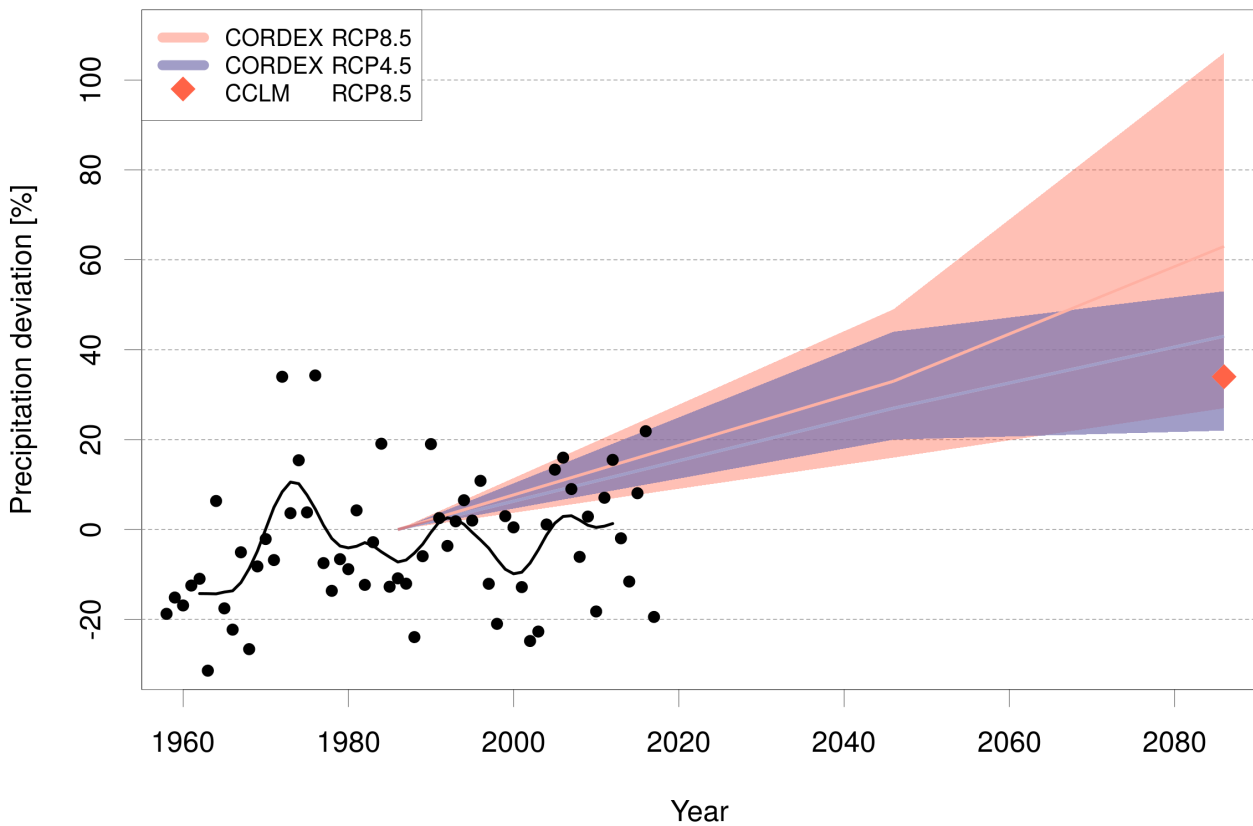
Figure 4.3.6 Annual mean precipitation for the Svalbard land area as deviation [%] from the reference period 1971-2000. The points and black curve show single year and smoothed historical values based on downscaled reanalysis data from 1958 to 2017 (Ch. 3.1.1). Future projections are given for Arctic CORDEX RCM simulations. Changes are projected to the periods 2031-2060 and 2071-2100, and for the scenarios RCP4.5 and RCP8.5. For RCP8.5, the result for the COSMO-CLM (CCLM) projection is indicated.

	Scenario:	RCP4.5 (5 runs)			RCP8.5 (8 runs)			RCP8.5
Region	Season	Med	Low	High	Med	Low	High	CCLM
Svalbard (land area)	Annual	43	22	53	63	27	106	34
	DJF	49	22	73	78	22	147	39
	MAM	44	14	47	55	22	110	40
	JJA	26	22	32	48	29	67	16
	SON	46	27	66	59	30	110	40

Table 4.3.4 RCM results for changes in precipitation [%] from 1971-2000 to 2071-2100 over the whole Svalbard land area following the scenarios RCP4.5 and RCP8.5. "Low" corresponds to the lowest, "High" to the highest and "Med" to the median projection from Arctic CORDEX. CCLM corresponds to the COSMO-CLM projection. Similar tables for regions are given in the Appendix 3.

Also the regional CCLM projections (Table 4.3.5) indicate lower precipitation increase than the median projections from the Arctic CORDEX simulations, e.g. ca. 5 % vs. 50 % for summer for the NW region. Possible reasons for these discrepancies are outlined in Box 4.2.

4.3.3.4 Application of the downscaled precipitation projections

As for temperature (cf. Chapter 4.1.3), we assume that the improved spatial resolution in CCLM leads to a more realistic description of precipitation conditions than the coarser resolution used in the Arctic CORDEX simulations. However, results from only one model run must be used with caution and always placed in conjunction with an ensemble of other projections. Our preliminary advice is thus, as for temperature, to apply the Arctic CORDEX ensemble medians as a main guideline for assessing consequences of climate change. However, it is important to keep in mind that the CCLM projections indicate that the Arctic CORDEX simulations may give a high estimate for the increase in future precipitation. As for temperature, large inter-annual and decadal variability will also in the future be superposed on the linear precipitation trends depicted in Figure 4.3.6.

	RCP4.5 (5 runs)					RCP8.5 (8 runs)					RCP8.5 (CCLM)				
Region	Ann	DJF	MAM	JJA	SON	Ann	DJF	MAM	JJA	SON	Ann	DJF	MAM	JJA	SON
Total	43	49	44	26	46	63	78	55	48	59	34	39	40	16	40
SW	32	41	38	25	32	39	43	40	41	33	17	13	27	10	20
NW	41	44	40	26	50	61	78	51	50	59	24	32	25	6	33
E	49	54	46	27	55	70	90	62	48	66	44	52	51	23	50

Table 4.3.5. RCM results for changes in annual and seasonal precipitation [%] from 1971-2000 to 2071-2100 over the Svalbard land area and the regions defined in Chapter 4.1.1. Arctic CORDEX (median) results are given for the scenarios RCP4.5 and RCP8.5, and CCLM results for RCP8.5.

Box 4.2 Precipitation projections from regional climate models

The potential amount of precipitable water in the atmosphere depends on the temperature (Clausius-Clapeyron equation). The temperature considerations outlined in Box 4.1 accordingly influence also the precipitation simulations; models with the largest (and probably unrealistic) future warming also will tend to have the largest precipitation increase. As the temperature increase projected by the fine-scale CCLM model is in the lower end of the ensembles (Box 4.1), this may contribute to the lower precipitation increase for CCLM compared to the Arctic CORDEX runs.

The CCLM run gives a realistic level of present annual precipitation compared to the Sval-Imp dataset, but is in the upper end of the model ensemble for present day precipitation (Figure B4.2). Thus, the same absolute increase (in millimetre) would give a smaller relative increase (in percent) than for the other Arctic CORDEX simulations. Further, the three Arctic CORDEX runs using the same global forcing as the CCLM (i.e., the MPI-ESM-LR RCP8.5 run) are showing the smallest precipitation changes of all Arctic CORDEX RCP8.5 projections (Figure B4.2). This indicates a major influence of the driving global model on the projected changes, for instance due to changes in humidity transportation towards Svalbard.

It is notable that the present-day annual precipitation for CCLM is higher than the two Arctic CORDEX runs (yellow and orange curves) with realistic temperatures (see Box 4.1), although the present-day annual temperatures are quite similar (Figure B4.1). Thus, also enhanced orographic effects of the finer terrain model used in the CCLM simulations, as well as differences in parametrisation of precipitation processes, may contribute to the differences between the CCLM and Arctic CORDEX results in Tables 4.3.4 and 4.3.5.

However, a deeper analysis of this is out of the scope of this report, and would need further investigations and benefit from a larger RCM ensemble. The CCLM results for precipitation are still regarded as a realistic example of a possible future under RCP8.5, and will be used for projecting changes in precipitation indices (e.g. heavy rainfall (Chapter 4.4) and snow (Chapter 5.3.2)) where an improved spatial resolution is of importance.
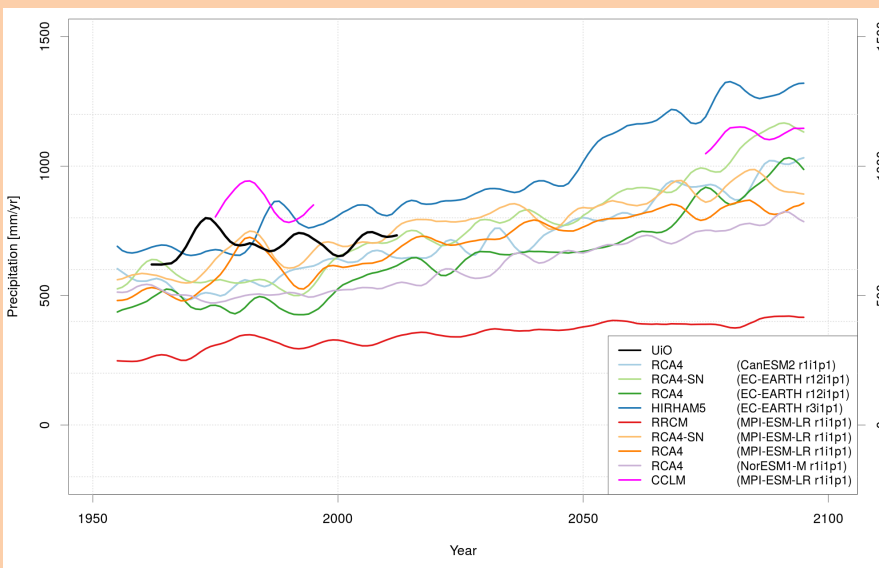
Figure B4.2 Arctic CORDEX and CCLM projections of annual precipitation for Svalbard under emission scenario RCP8.5. The black curve shows results for the Sval-Imp dataset. The curves are smoothened to show decadal scale variability
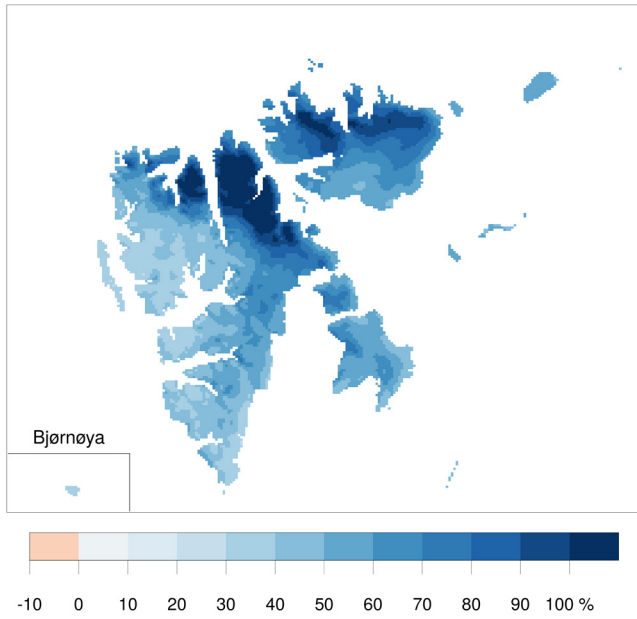
Figure 4.3.7. 'Ensemble mean precipitation changes [%] from 1971-2000 to 2071-2100 in the Artic CORDEX simulations assuming the RCP8.5 emission scenario. The spatial resolution is improves by scaling with the signal from the CCLM simulation (cf. Chapter 3.1.4). Upper panel: Annual values. Lower panel: Summer (left) and winter (right).
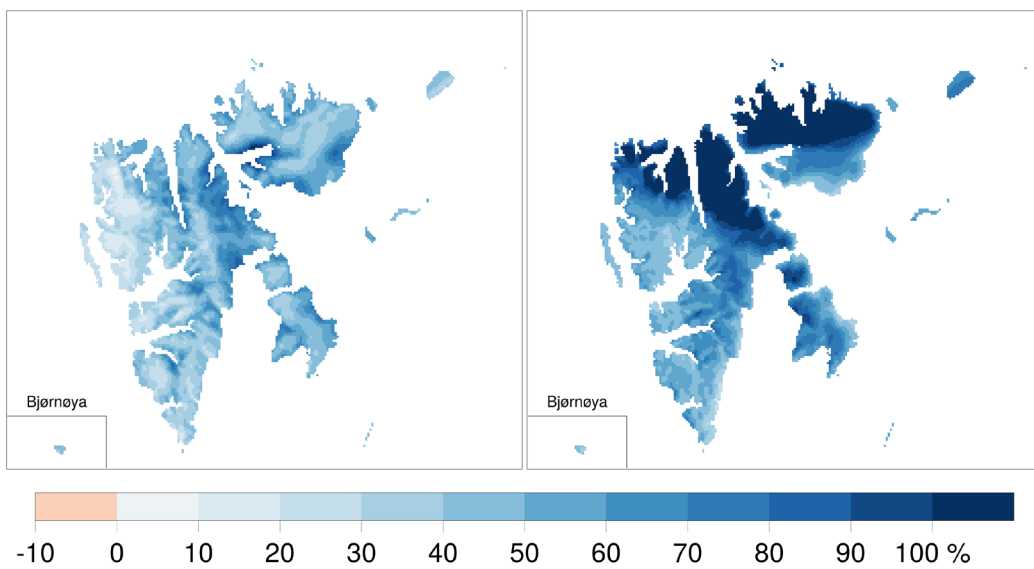
4.4 Heavy rainfall

4.4.1 Present conditions

Similar to annual precipitation, large local differences are found for observed large daily rainfalls (Table 4.4.1). The highest measured daily rainfall in Ny-Ålesund (98 mm) is thus more than twice the highest value recorded at Svalbard Airport. (In November 2016 a mini-logger in Longyearbyen recorded a rainstorm of 75 mm during 26 hours, see Chapter 10.3.2). It is notable that the highest observed daily values at Ny-Ålesund and Svalbard Airport make up around 25 % of the stations' total

average annual precipitation. High daily rainfalls may occur even mid-winter: 40 % of the five highest rainfall events at the five stations in Table 4.4.1 occurred in December-February and 28 % in September-November (Dobler et al., 2019). Figure 4.4.1 indicates that in the latest decades, the number of days with heavy precipitation has increased at Svalbard Airport and Ny-Ålesund.

Heavy rainfall events may cause flooding (Chapter 5.1.5), landslides (mainly debris flows) and slush avalanches on Spitsbergen (Chapter 7.3.2). Table

4.4.1 demonstrates the large local differences in heavy rainfalls: The return period estimates for daily rainfalls for Ny-Ålesund and Hornsund are more than twice the values for Svalbard Airport. For Svalbard Airport as well as Ny-Ålesund the observed daily maximum rainfalls exceed the estimated 100-year return period value. Table 4.4.1 shows that the 100-year estimates for Bjørnøya, Hopen and Svalbard Airport are quite similar for both periods, while for Ny-Ålesund they are substantially higher in the most recent period.

The general weather situation favouring heavy rainfalls is a strong south-southwesterly flow with advection of water vapour from warmer areas. For 16 out of 21 events where 12-hour precipitation at Svalbard Airport exceeded 10 mm, Dobler et al. (2019) found that the large-scale wind direction was from southwest. In several of the heavy rainfall events there is a link with "atmospheric river"-like features in the precipitable water anomaly field (Serreze et al., 2015). A heavy rainfall event with "atmospheric river"-like features for precipitable water anomalies is demonstrated in Figure 4.4.2. For this kind of events, Spitsbergen is atypical of most of the Arctic: Lying towards the northern end of the North Atlantic cyclonic track, it can readily draw from more southerly Atlantic moisture sources.

Serreze et al. (2015) stated that each heavy rainfall event at Spitsbergen has its own characteristics, and that strong influences of local topography imply that extreme events recorded in Ny-Ålesund are typically not well represented at other Spitsbergen stations (and vice versa). Strong influences of topography in the Ny-Ålesund area were also documented by Førland et al. (1997a).

4.4.2 Projected changes in heavy rainfall

According to AMAP (2017), future daily precipitation extremes will increase over mid- and high latitudes, with implications for the management of water resources, flow of freshwater into the Arctic Ocean, changes in sea ice temperature, and amplification of regional warming (through reduced surface reflectivity caused by shift from snow to more rain). Towards the end of the century, a marked increase is projected for frequency and intensity of heavy rainfalls in the Svalbard region (Isaksen et al., 2017).

An evaluation of the high-resolution simulations with COSMO-CLM (CCLM), indicates that observation-based extreme rainfall statistics (Table 4.4.1) are reasonably represented by the model for present day climate (Table 4.4.2, left columns). The CCLM model is therefore used for projections of heavy rainfall in the Svalbard region (Dobler et al., 2019).

Future changes in 1-day rainfall deduced from the CCLM runs with emission scenario RCP8.5 are outlined in Table 4.4.2. For the 99.5 percentile, i.e. the daily value exceeded approximately twice per year, an increase of approximately 20 % is projected for most stations. This is well in line with the projected increase in the 99.5 percentile for the

	1976-2005					**1988-2017**				
	Bjørn	Hopen*	Horn*	Sv. Ap	Ny-Ål	Bjørn	Hopen	Horn*	Sv. Ap	Ny-Ål
q99.5	14	17	25	10	21	15	15	24	11	23
M10	30	38	NA	23	46	33	33	54	25	59
M50	41	52	NA	32	60	45	45	79	34	73
M100	46	58	NA	36	66	50	50	89	37	82
Max	42	49	NA	43	57	42	47	74	42	98

Table 4.4.1. Extreme daily rainfall [mm] at the weather stations Bjørnøya, Hopen, Hornsund, Svalbard Airport and Ny-Ålesund. For each station values are presented for the 99.5 percentile (q99.5) and maximum observed (Max) as well as estimates for return periods (M) 10, 50 and 100 years

*Hornsund data from 1995; Hopen: Not adjusted for homogeneity break in 1997
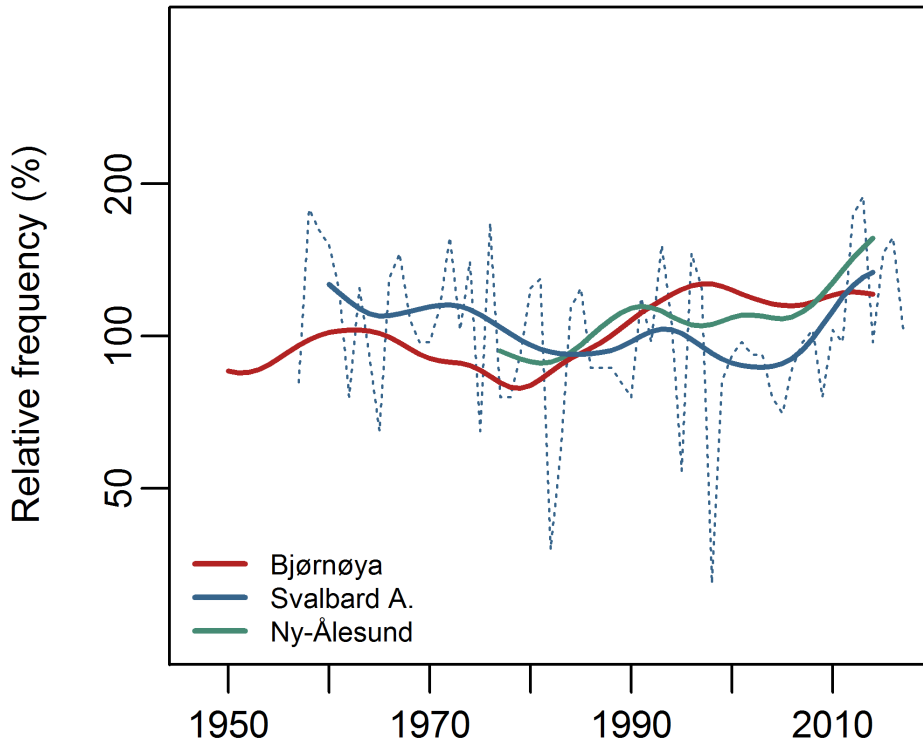
Fig 4.4.1. Number of days per year, relative to the 1971-2000 mean, with observed precipitation above the 95th percentile. The dotted blue line shows annual values for Svalbard Airport, while the full drawn curves show decadal scale variability for several stations.
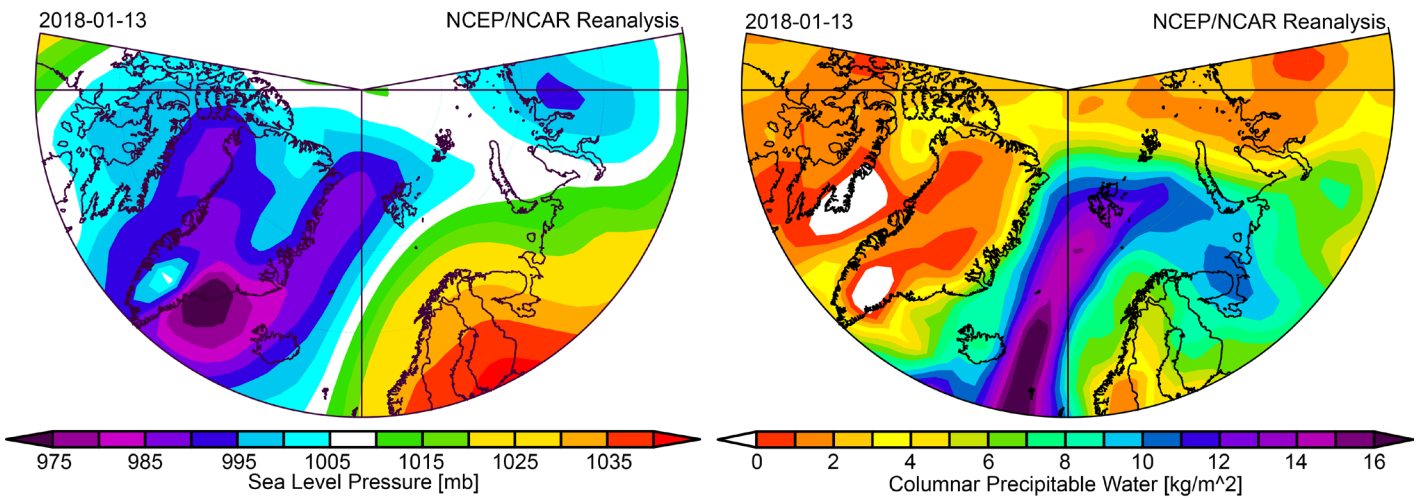
Figure 4.4.2 Left: Sea level pressure (left) and precipitable water (right) during the heavy rainfall event on 13.January 2018. (From NOAA)

Norwegian mainland (Hanssen-Bauer et al., 2017). For return periods 10, 50 and 100 years the picture is more complex; the 100-year estimates vary from a decrease at Hornsund to an increase of more than 30 percent for Svalbard Airport and Hopen.

Return period estimates based on short, single series are vulnerable for outliers, but even analyses of changes for all Arctic CORDEX models for all grid points in the Svalbard region did not show any

common pattern, except that the results mostly indicated an increase in future heavy rainfalls (Dobler et al., 2019). The most robust projections for future heavy daily rainfalls are those deduced for q99.5. For emission scenario RCP8.5 this means a 20 % increase in heavy daily rainfall totals from 1971-2000 to 2071-2100 at Bjørnøya, Hopen and Svalbard Airport. More results on present and future heavy rainfall statistics in the Svalbard region are outlined by Dobler et al. (2019).

4.5 Wind, cyclonic activity and waves
4.5.1 Present conditions

As the Norwegian Arctic lies in the transit zone between cold Arctic air in the north, and mild maritime air in the south, the cyclonic activity is high. Unstable and stormy weather is therefore common, especially in winter. The area of atmospheric low pressure from Iceland towards the Barents Sea (Chapter 2.1) reflects the major tracks of low pressure systems. The air pressure is lowest in winter and autumn, and the strongest pressure gradients and the highest wind speeds usually occur during winter (Førland et al., 2009).

Extreme cyclone events often occur during Arctic winters, and are of concern as they are associated with anomalous warming events. Rinke et al. (2017) found that typically 20-40 extreme cyclone events (sometimes called "weather bombs") occur in the Arctic North Atlantic per winter season, with an increasing trend of 6 events per decade over 1979-2015, according to 6-hourly observations from Ny-

Ålesund. Rinke et al. (2017) related this regional pattern of trends in extreme cyclones to anomalously low sea-ice extent in recent years, together with associated large-scale circulation patterns. This also affects the wave climate, as receding sea ice cover opens up new regions to both locally generated wind waves and intrusion of remote swell.

The southern coast of Svalbard is exposed to swell propagating large distances across the Norwegian Sea, as well as local waves associated with cyclones in the vicinity of Svalbard. Aarnes et al. (2012) and Breivik et al. (2013) estimated the 100-year return levels for significant wave height from NORA10 (Reistad et al., 2011) to be 12-14 m south of Svalbard. The northern coast of Svalbard is far less exposed, but is sensitive to the ice extent since significant wave height scales with the fetch (the length of open ocean over which the wind blows (Hasselmann et al., 1973)). Thomson and Rogers (2014) showed that the Arctic Ocean and the Beaufort Sea has experienced an increase in fetch in recent years

	Simulated (mm) for 1971-2000					Projected changes (%) (RCP8.5, CCLM)				
	Bjørn	Hopen	Horn	Sv.Ap	Ny-Ål	Bjørn	Hopen	Horn	Sv.Ap	Ny-Ål
q99.5	18	16	23	16	24	22	20	8	21	14
M10	36	28	40	30	50	15	33	4	26	14
M50	47	36	52	39	69	12	48	-5	32	11
M100	52	40	58	44	78	11	55	-9	35	9
Max	38	35	49	39	72	27	142	-2	75	-11

Table 4.4.2 Extreme heavy daily rainfall: Modelled (CCLM) present day values [mm] and changes (%) from 1971-2000 to 2071-2100 under RCP8.5. For legend details, see Table 4.4.1

as a consequence of the receding ice cover. Since waves help break up the ice, this could also accelerate the receding ice cover.

Svalbard Airport, Ny-Ålesund and Hopen have 50-60 days per year where the maximum (10 minutes) wind speed is strong breeze or stronger (Table 4.5.1). At Bjørnøya and Isfjord Radio, the frequency of strong winds is twice as high. The easterly winds at Isfjord Radio are strengthened locally by Isfjorden, which is narrower at the mouth than further in. The mean wind speeds (Figure 4.5.1) and frequencies of high wind speeds (Table 4.5.1) are lowest during the summer season.

4.5.2 Projected changes

The NORACIA-RCM simulations of average daily maximum wind speed for the period 1980-2050 indicated small changes during summer, but an increase north and east of Svalbard during the other seasons (Førland et al., 2009). Also up to the end of the 21st century rather small changes were projected, but for sea areas north and east of Svalbard an increase larger than 10 % was found for average maximum daily

wind speed during winter. For the Barents Sea, Benestad et al. (2016), by use of ESD (see Chapter 3.1.3), found an increase in number of deep cyclones and synoptic storms associated with a warming Arctic.

The simulations by the high-resolution COSMO-CLM (CCLM) model indicate that the main wind directions remain fairly unchanged towards the end of the century throughout Svalbard, while the wind force is estimated to increase over the sea in the northeastern part, and decrease somewhat along the northeastern coastal and fjord areas (Figure 4.5.2). The changes in wind conditions are largest during winter.

For maximum daily wind speed the projections generally indicate an increase in northeastern areas and a decrease in the southwest (Figure 4.5.3), i.e. the same pattern as found by Førland et al. (2009). For December-February the daily maximum wind speed is projected to increase by more than 2 m/s in the northernmost areas. The larger increase in this area is probably linked to diminishing sea ice.
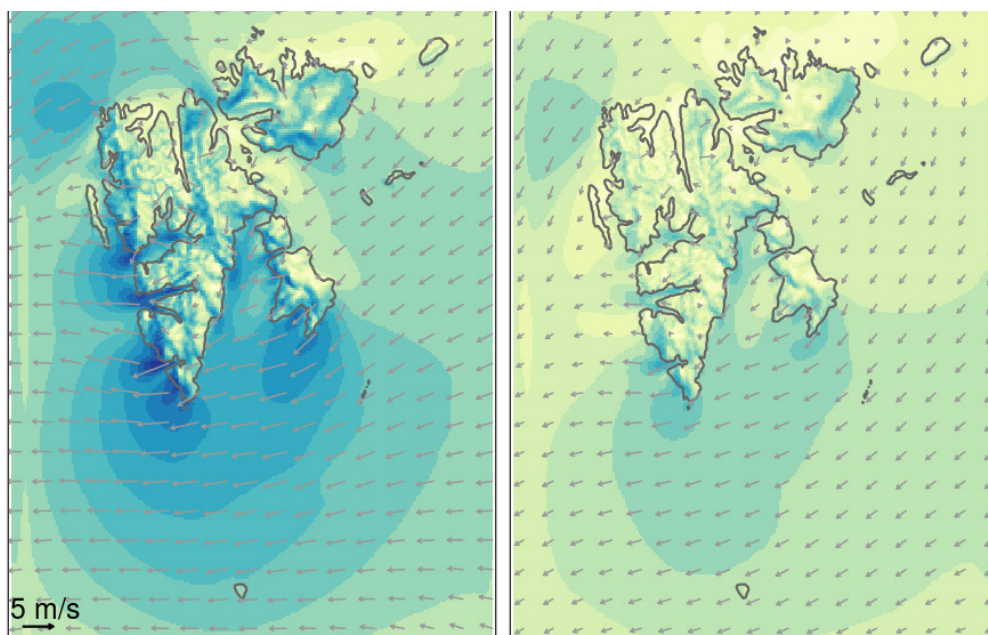
Figure 4.5.1 Simulated average wind speed and direction in winter (November-April) and summer (May-October) for the reference period 1971-2000, based on the CCLM 2.5 km model.

Wind speed [m/s] and direction
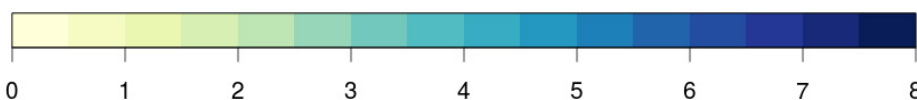
Aarnes et al. (2017) calculated the future wave climate (2071-2100) with a regional wave model forced with winds from six CMIP5 models under the RCP4.5 and RCP8.5 scenarios. The largest increase was found in the area south and southeast of Svalbard. As the wind field showed a reduction in a majority of the six CMIP5 models, the primary cause was the receding ice cover. The average impact was a 10 % increase in annual mean significant wave height, but individual CMIP5 models exhibited considerable variability in both wind speed and ice cover.

	1971-2000	1988-2017				
	Annual	Annual	Winter	Spring	Summer	Autumn
Bjørnøya	119	120	45	30	12	33
Hopen	47	54	22	11	5	16
Hornsund*	66	87	32	22	10	23
Isfjord Radio*	133	NA	NA	NA	NA	NA
Svalbard Airport*	51	61	26	15	5	15
Ny-Ålesund*	35	51	21	13	3	14

Table 4.5.1 Number of days with wind force "strong breeze" or stronger (>10.8 m/s).

*Data: Hornsund from 1995; Isfjord Radio 1947-1975; Svalbard Airport from 1975; Ny-Ålesund from 1974
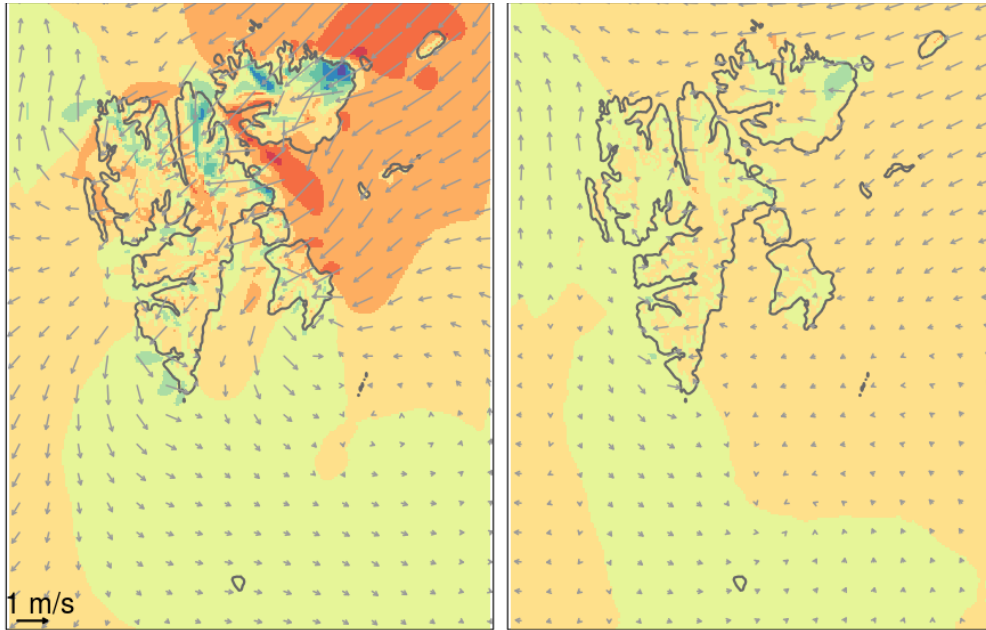
Figure 4.5.2 Projected changes in average wind speed and direction from 1971-2000 to 2071-2100 for winter (November-April) and summer (May-October). The simulations are based on the CCLM 2.5 km model run for emission scenario RCP8.5

Changes in wind speed [m/s] and direction

Changes in daily maximum 10m wind speeds [m/s]
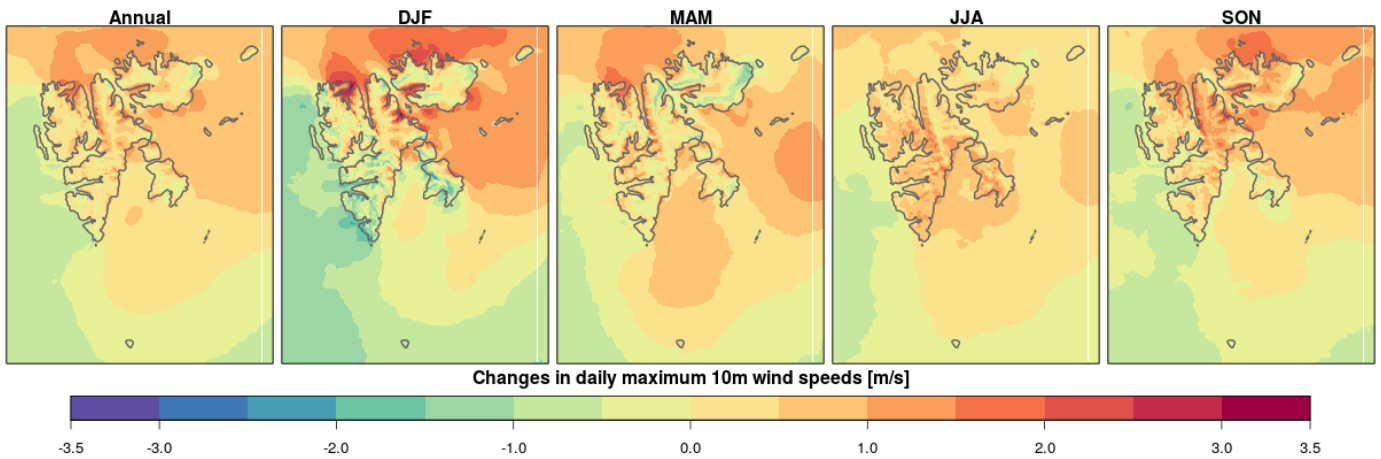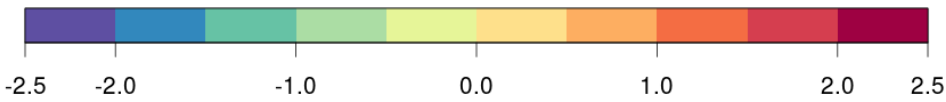
Figure 4.5.3. Annual and seasonal changes of daily maximum wind speed from 1971-2000 to 2071-2100. The estimates are based on the CCLM 2.5 km run for emission scenario RCP8.5.
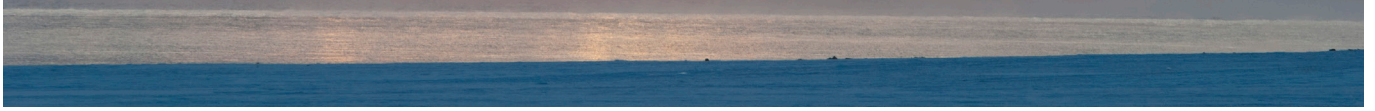
5. Hydrology

Hydrological processes in the Arctic have a large impact on the water and energy balances. Runoff, snow cover, glacier mass balance, erosion and sediment transport in Svalbard influence the natural environment through their impacts on for instance biological activity and water chemistry. Glaciers cover a majority of the land area in Svalbard (Chapter 6). Changes in precipitation and temperature will substantially alter glacier mass balance and snow conditions – both influencing river flow. Furthermore, water is a primary weathering agent

for rocks and soils, breaking them down, dissolving them, and transporting the resulting sediments and dissolved solids to the sea. Figure 5.1 shows parts of the Adventdalen catchment near the settlement Longyearbyen. Mountainous areas with plateaus and steep slopes intersected by wide valleys occupied by river plains are characteristic landforms of the Svalbard Archipelago. Glaciers are frequent, while lakes are rare compared to mainland Norway.

Figure 5.1 Adventdalen. Photo: Stein Beldring

5.1 Runoff

5.1.1 Water balance estimates

Killingtveit et al. (2003) reported the water balance for the three catchments (Figure 3.1.2) Bayelva at Ny-Ålesund, De Geerdalen and Endalen/Isdammen near Longyearbyen (Table 5.1.1). They report an annual runoff of 545 mm in Endalen/Isdammen, 539 mm/year in De Geerdalen and 1050 mm in Bayelva for the period 1990–2001, which is much higher

than the observed precipitation at the closest observation stations, Svalbard Airport and Ny-Ålesund. Observed annual runoff refers to the period within a year with reliable observations, normally the ice-free period from June to October. Glacier melt contributes about 450 mm/year. Average annual evaporation was estimated to approximately 80 mm per year from glacier-free areas. Comparing with the

		Bayelva	**De Geerdalen**	**Longyearelva**
Evapotranspiration[1]	mm/year	-40	-70	-
Net glacier contribution[1]	mm/year	450	450	-
Simulated areal precipitation[1]	mm/year	890	550	-
Measured point precipitation[2]	mm/year	385	189	189
Mean annual runoff[3]	mm/year	1100	530	–
Mean annual flood. QM[2]	mm/day	33	20	39
Mean annual flood. QM[2]	m³/s	12	17.6	9.9

Table 5.1.1 Water balance estimates at Bayelva, De Geerdalen and Longyearelva. Information taken from Killingtveit, 2003 (1, reference period: 1990–2001), Stenius, 2016 (2, reference period: 1961–1990) and this report (3, reference period: 1989–2017 for Bayelva and 1991–2015 for De Geerdalen). The mean annual flood is the mean of the maximum daily runoff each year.

results reported by Jania and Pulina (1994) from the Hornsund area in southern Spitsbergen, Killingtveit et al. (2003) found that both the measured runoff and the precipitation estimates in their own study in central and north-western parts of the island was considerably lower. Sand et al. (2003) did a study of regional snow distribution on Spitsbergen, which indicates that the Hornsund area receives approximately twice as much precipitation during the snow accumulation period (October–May) as the central region. This corresponds well with the results presented in Chapter 5.2 (Figure 5.2.2). Several studies in Svalbard have documented that discharge from groundwater springs, e.g. the water supply reservoirs for Ny-Ålesund, may provide a contribution to runoff and surface water (e.g. Haldorsen and Heim, 1999). The permafrost forms an impermeable barrier for subsurface water flow, but artesian groundwater may develop in lower areas and form pingos (Humlum et al., 2003) which traditionally have been used as a source of water supply in Polar regions.

Killingtveit et al. (2003) concluded that areal precipitation for these catchments is twice the measured precipitation at the closest meteorological stations (Table 5.1.1). This difference is partly due to undercatch in the precipitation gauges (Chapter 4.3.1), and partly that the precipitation stations are not representative for the whole catchment area, which extends up to higher elevations. Precipitation increases with elevation (Figure 2.1.2b, Killingtveit et al., 2003), and thus areal precipitation including high altitudes will tend to be higher than at measuring sites near sea level.

5.1.2 Annual and seasonal runoff in the present climate

The following analyses are based on observations from two active discharge stations in Svalbard: Bayelva and De Geerdalen. Both stations have short observation records (1989–2017 for Bayelva and 1991–2015 for De Geerdalen). Key characteristics of these stations are summarised in Table 5.1.2 and further elaborated in Chapter 3.2. Bayelva receives about twice as much precipitation as De Geerdalen. Note, however, that the observed annual precipitation is less than the observed annual runoff as pointed out in Chapter 3.1.1 and by Stenius (2016).

The average seasonal runoff in Bayelva and De Geerdalen for the observation periods is presented in Figure 5.1.1. River runoff mostly occurs during

	Bayelva	De Geerdalen	Longyearelva	All of Svalbard
Observation record	1989–2017	1991–2017w	–	–
Catchment area [km²]	31.1	77.7	22	60909
Fraction of glaciers [%]	50	10	30	57
Mean altitude [m a.s.l.]	265*	409*	495	375
Altitude range [m a.s.l.]	4–742*	41–987*	40–1000	25–1676

Table 5.1.2 Characteristics of the discharge stations Bayelva and De Geerdalen. Longyearelva and all of Svalbard are included for reference. Information for all of Svalbard are taken from the 1x1 km² grid (the lowest cell is located at 25 m a.s.l.). Information taken from Stenius (2016), except data marked with a *, taken from Haagmans (2018).

the months from June to September. In the autumn, all rivers freeze completely, except short reaches of rivers fed by springs or in front of some glaciers (Petterson, 1994). A major part of the runoff is caused by snowmelt in early summer. After this, runoff is fed by rainfall and melting of glacier ice (Sund, 2008).

From October to June, discharge values are set to zero because the rivers freeze and the loggers may freeze. Runoff caused by heavy rainfall events in this part of the year are therefore not captured, and the number of rain-on-frozen-ground events has increased (Chapter 4.3.2).

Hydrological model simulations show that the largest annual runoff rates are located in the west-

ern lowland regions, particularly in the southwest (Figure 5.1.2). This pattern resembles the precipitation pattern shown in Figure 2.1.2b, with the highest runoff rates in the western part of the archipelago. However, the largest runoff rates are found at lower elevations than the maximum precipitation, because melting is more efficient at lower elevations. The lowest runoff rates are located in the eastern high-altitude regions where temperatures are too low for melting and in sheltered valleys receiving the smallest precipitation amounts (Figure 4.3.2).

A majority of the annual runoff is generated in the summer, whereas a smaller fraction of the annual runoff occurs in the autumn (especially in the south), and almost no runoff is generated in the winter and spring, except at the coast (not shown).
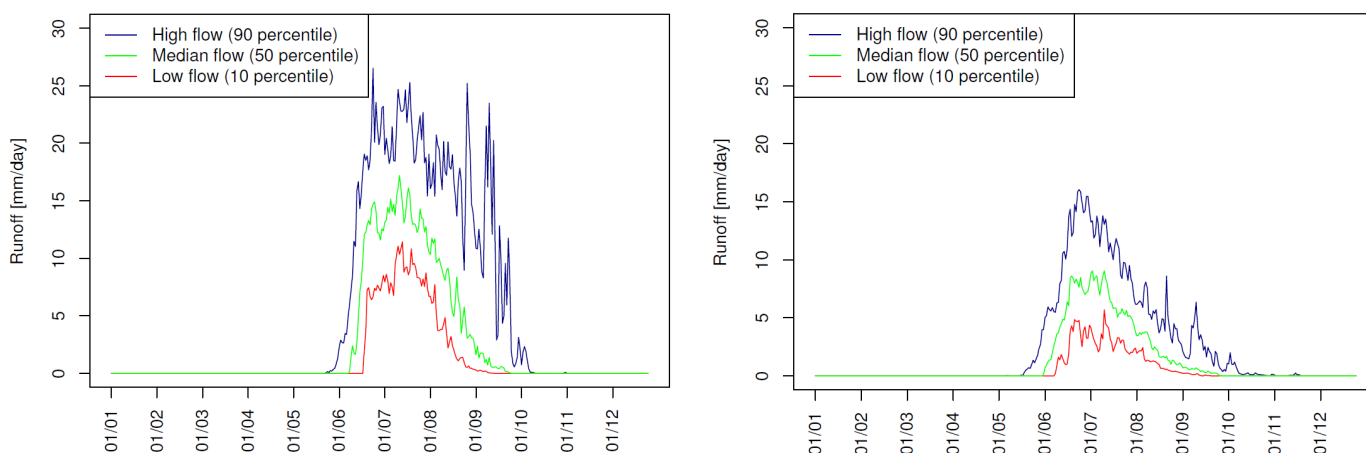
Figure 5.1.1 Seasonal cycle at Bayelva (1989–2017) and De Geerdalen (1991–2015).

Box 5.1 Downscaled and bias-adjusted temperature - effects on runoff estimation.

The primary meteorological variables from the Arctic CORDEX regional climate models were downscaled and bias-adjusted prior to the hydrological modelling. Original climate model outputs often contain biases (Koenigk et al., 2015). If the biased data are used directly in the hydrological modelling, the model responses will inevitably be different from what has been observed in the past and present climates. Altered precipitation and temperature patterns induced by model biases can for example affect snow accumulation and snowmelt patterns and consequently runoff generation processes. The simulated hydrological regime and seasonal flow patterns may differ significantly from observed patterns, and this mismatch will also have an effect on the simulated hydrological response to climate change.

As explained in Box 4.1, a majority of the Arctic CORDEX temperature projections are colder than observed temperatures in the control period. This characteristic is usually most pronounced in the winter. Some of the projections therefore most likely overestimate the temperature change signal towards the end of the century and this overestimation is more or less preserved after the bias-adjustment. Figure B5.1 shows how the coldest models before bias-adjustment end up being the warmest models after the procedure with winter temperatures well above zero. Figure 4.1.5b) illustrates that the high Arctic CORDEX ensemble with substantially fewer members are warmer than the more robust and larger empirical-statistical downscaling ensemble.

This overestimation of the temperature increase leads to for example too few snow days and too much glacier melt in the hydrological model. In particular, glacier melt is overestimated in the simulations driven by two of the EC-EARTH-based projections, which in turn results in too much runoff. The way glaciers are represented in the model also tends to give more melting. With a spatial resolution of 1 km, glaciers in the model melt at the same rate for the whole grid cell. In reality, however, most of the glacier melt would occur in a limited region at lower elevations.
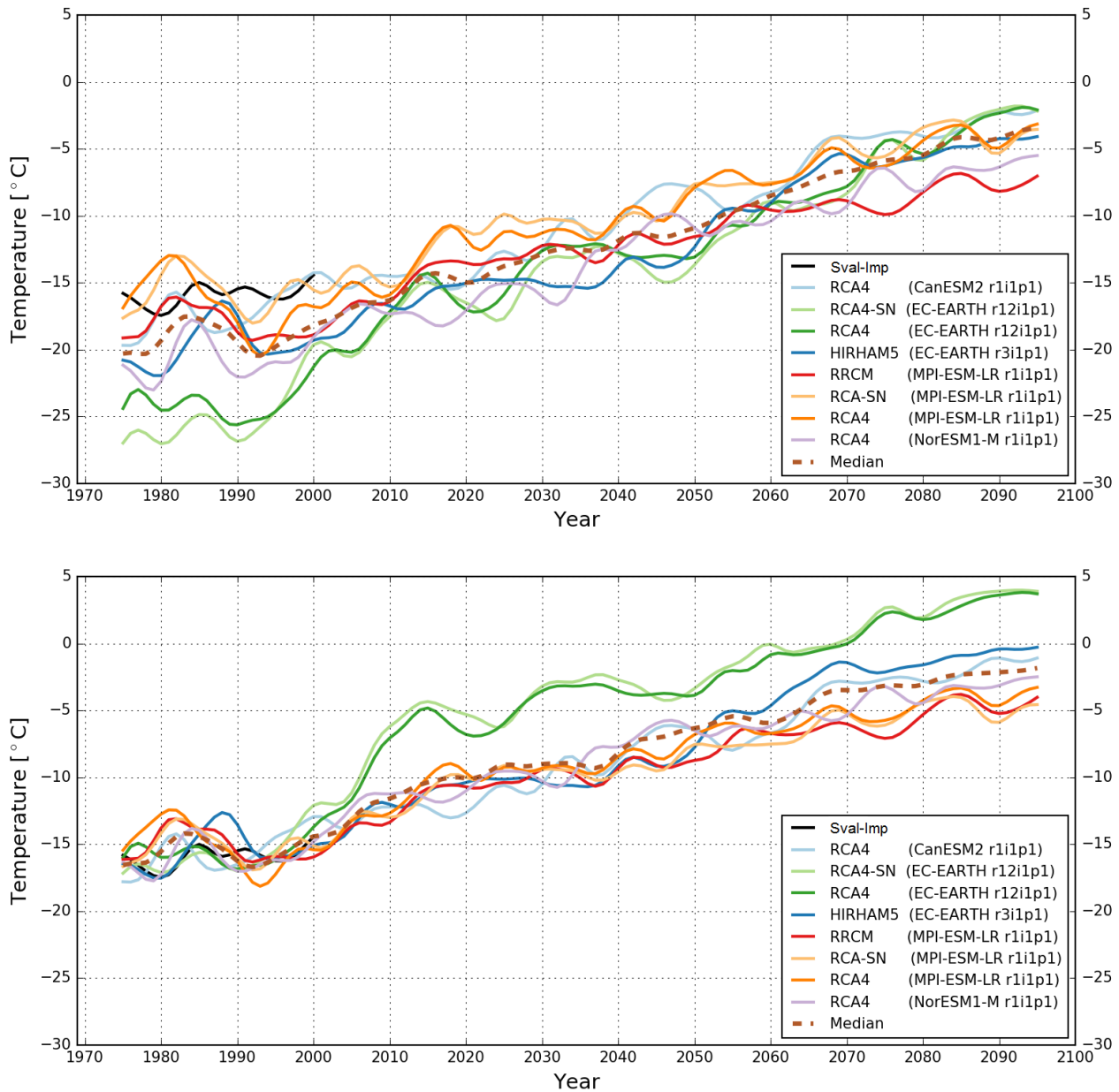
Figure B5.1 The Arctic CORDEX and CCLM projections of winter (DJF) temperatures for Svalbard under emission scenario RCP8.5. The solid black line shows results for the Sval-Imp. The dashed brown line indicates the median of the Arctic CORDEX ensemble. Upper panel: original Arctic CORDEX results. Lower panel: bias-adjusted Arctic CORDEX results.

5.1.3 Runoff development in Svalbard in the instrumental period

The mean annual runoff simulated for the whole of Svalbard is 700 mm/year for the period 1980–2015 (Figure 5.1.3). Annual runoff has increased in the historical period, as shown in Figure 5.1.3, both according to the observations at Bayelva and the HBV simulations for the Svalbard archipelago driven by the Sval-Imp data (Chapter 3.1). Measurements at De Geerdalen do not show any increase. Over the longer period 1971–2017, precipitation increased significantly in Ny-Ålesund near Bayelva, while there was no significant change at Svalbard Airport near De Geerdalen (Table 4.3.2). Due to sparse measurements, the runoff development in Svalbard is inferred from the HBV simulations for the period 1980–2015 (Table 5.1.3). Linear trends for all of Svalbard show a statistically significant increase in the annual runoff, and for all seasons except spring. Precipitation measurements tend to show negative trends in spring and summer and positive in autumn and winter though few trends are significant (Table 4.3.2). Further, the fraction of precipitation as rain has increased (Figure 4.3.4). The increased runoff in winter and autumn are thus partly attributed to increased precipitation as rain over the period. In the summer and annually, the increased runoff is likely mainly caused by enhanced glacier melt.

5.1.4 Projected runoff towards 2100

The hydrological projections show that the runoff in Svalbard will increase during the 21st century (Figure 5.1.4). For all of Svalbard, the future annual runoff is projected to gradually increase, relative to the present climate (1971–2000). Runoff in the two scenarios follow each other closely towards the middle of the century, after which the projected runoff in RCP8.5 increases more steeply than in RCP4.5. These results are expected, because RCP8.5 represents a stronger warming (Figure 4.1.4, 4.1.5) and a stronger increase in precipitation (Figure 4.3.6) than RCP4.5.

The maximum projected changes in annual runoff are likely overestimated because the glacier melt is overestimated in the hydrological model (Box 5.1). Runoff simulations are highly sensitive to the temperature input and the representation of glaciers in the hydrological model, because they control
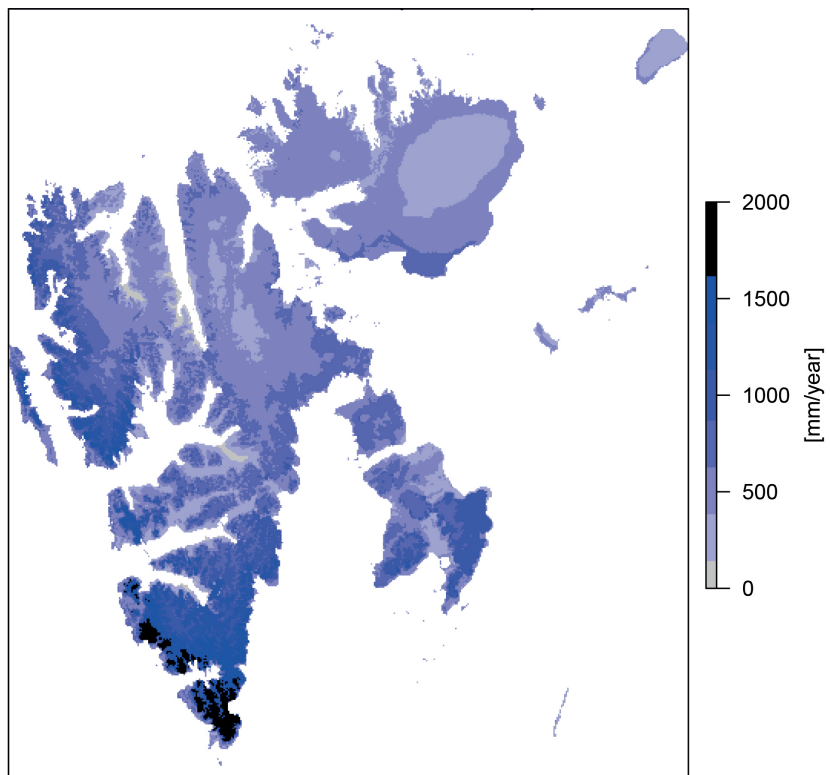
Figure 5.1.2 Annual runoff (absolute values in mm/year) averaged over 1971–2000 based on the ensemble median of eight HBV simulations driven with downscaled Arctic CORDEX RCPs for the control period.
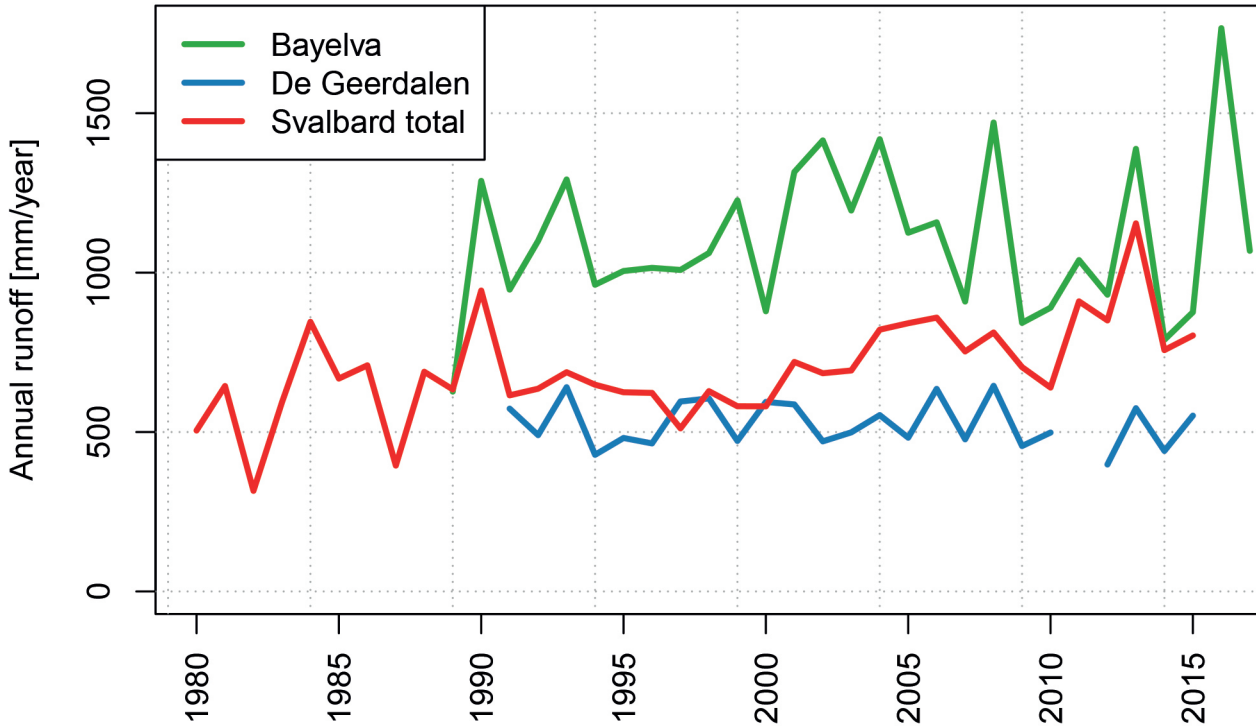
Figure 5.1.3 Observed annual runoff at the discharge stations and for the whole of Svalbard, based on the gridded HBV simulations forced with the Sval-Imp data.

	1980–2015				
	Annual	Winter	Spring	Summer	Autumn
Svalbard [mm/decade]	**83**	**4**	0,8	**57**	**21**

Table 5.1.3 Linear trends [mm per decade] in annual and seasonal runoff, as a median of the HBV simulations driven by the Sval-Imp data. Bold types: Significant trends (5% level).

meltwater contribution during the period of melt-down of glaciers. The glacier mass balance in Svalbard is expected to decrease towards the end of this century (Möller et al., 2016; Chapter 6). Some of the bias-adjusted Arctic CORDEX ensemble members (input to the HBV hydrological model) are assumed to have too high temperatures (Box 5.1), which likely leads to highly overestimated glacier melt. The result is therefore a too high contribution of glacier melt to the projected annual runoff estimates for these ensemble members (Figure 5.1.4).

A clear change in seasonality compared to the present climate is visible for all of Svalbard in Figure 5.1.5. The winter runoff increases for RCP8.5 in

the period 2071–2100 (red curve; due to higher winter temperatures and more rainfall events in the winter) and the frost-free season extends by several weeks (runoff starts earlier and lasts longer). The combined effect of higher summer runoff and higher winter runoff explains the strong increase in annual runoff towards the end of the century.

For Bayelva (Figure 5.1.6) and De Geerdalen (not shown), the projected runoff peaks around the middle of the century, and decreases thereafter because of a reduced contribution from glacier meltwater. These two catchments lie at lower elevations than Svalbard as a whole, so glaciers disappear in the model and the modelled contribution from glacier

melt reduces considerably towards the end of the century. Because of too high temperature input in particular for the high-end ensemble members, the modelled runoff is likely too high and likely peaks too fast.

For Bayelva, the seasonal runoff cycle reveals that the runoff increase towards the middle of the century is caused by increased runoff in the winter, spring and autumn (Figure 5.1.7, brown dotted curve). Towards the end of the century (red curve), the runoff peak is much reduced, the peak flow occurs earlier in the spring, and the winter runoff is sustained at

a higher level. The small peak in the beginning of the summer is likely caused by snowmelt from a smaller snow reservoir that melts completely at the beginning of the summer. Under RCP8.5, the snow storage decreases and the length of the season with snow covered ground will shorten (Chapter 5.2.2. and Figure 5.2.4). By the end of the century, summer runoff is to a lesser degree caused by glacier melt, as seen as a runoff reduction throughout summer, when temperatures are at their highest and the potential for glacier melt is highest. A similar pattern is visible for De Geerdalen (not shown).
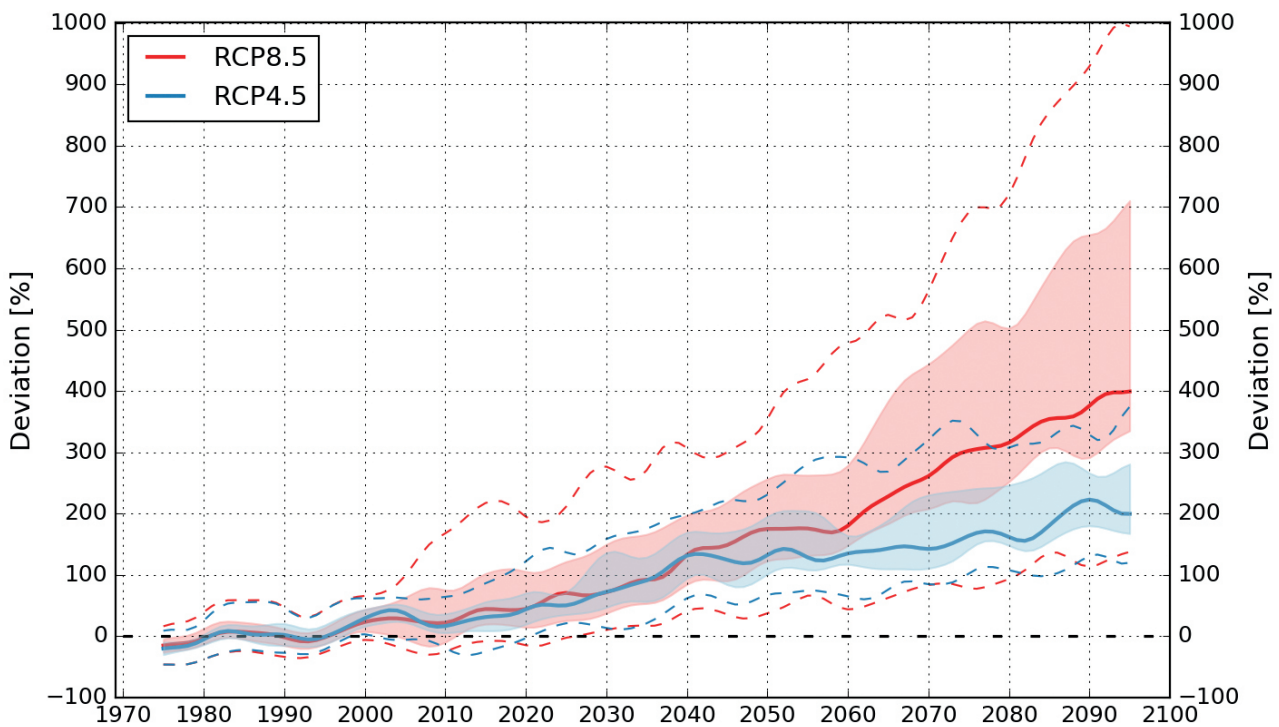
Figure 5.1.4 Mean annual modelled runoff for the total land area in Svalbard, simulated using the HBV model forced with downscaled and bias-adjusted Arctic CORDEX data (top). The solid red line shows the ensemble median of eight models; the band outlines the 25th and 75th percentile, whereas the dotted lines indicate the minimum and maximum. The pink colour refers to RCP8.5 and the blue colour refers to RCP4.5. The runoff values are given as the deviation (%) from the reference period 1971–2000. The low-pass filtered series are smoothed by Gaussian weighting coefficients, and show variability on a decadal time scale. For the period 1971–2000, the simulated mean annual runoff for Svalbard is 595 mm/year.

Seasonal runoff distribution, all of Svalbard
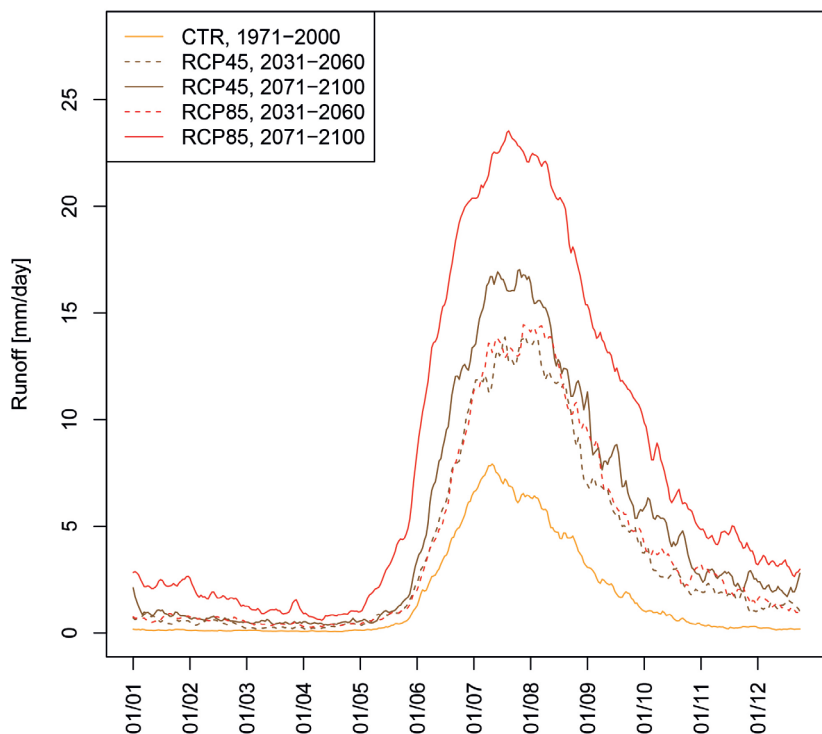
Figure 5.1.5 The seasonal runoff distribution for all of Svalbard for the period 1971–2000 versus 2031–2060 and 2071–2100. The future projections are given for the intermediate and high emission scenarios RCP4.5 and RCP8.5.
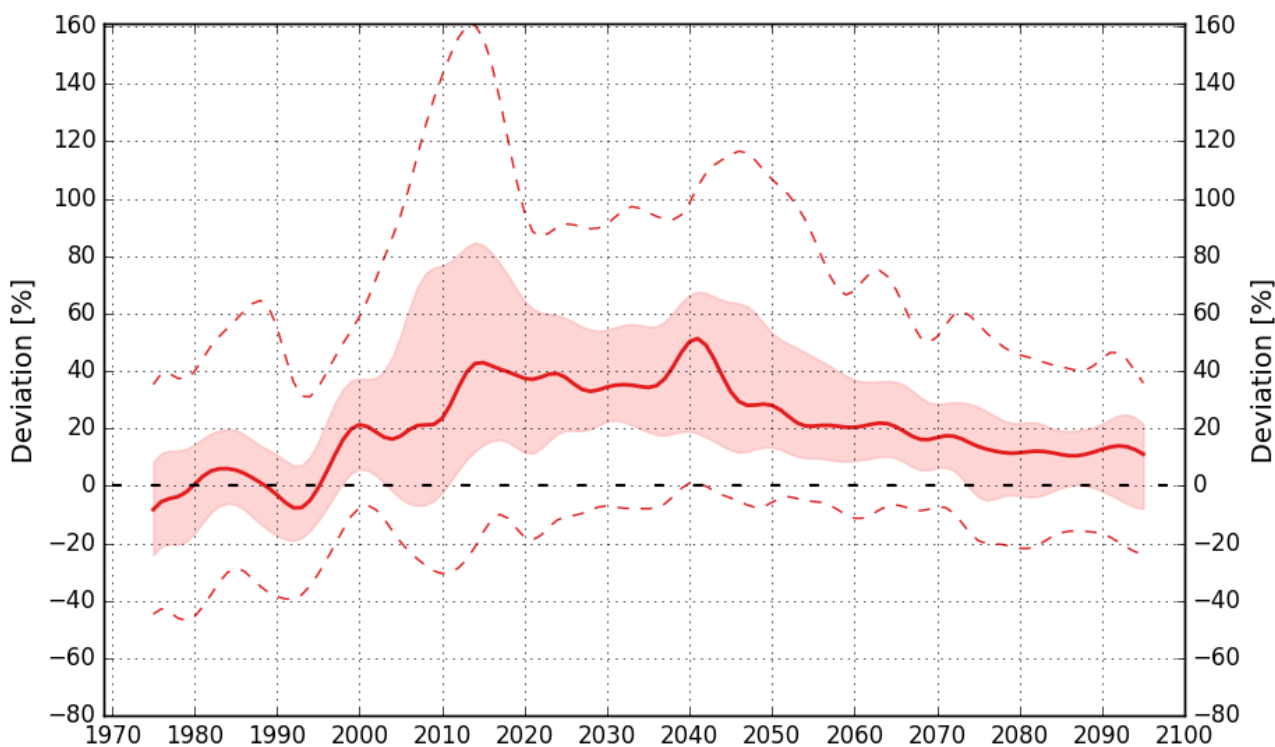
Figure 5.1.6 The mean annual modelled runoff for Bayelva given as the deviation (%) from the reference period 1971–2000. The 25th and 75th percentile of the RCP8.5 projections are given as the shaded area. The maximum and minimum projections are shown as dotted lines. The observed (1989-2017) mean annual runoff for Bayelva is 1100 mm/year.

Seasonal runoff distribution, Bayelva

Legend:
- CTR, 1971–2000
- RCP45, 2031–2060
- RCP45, 2071–2100
- RCP85, 2031–2060
- RCP85, 2071–2100
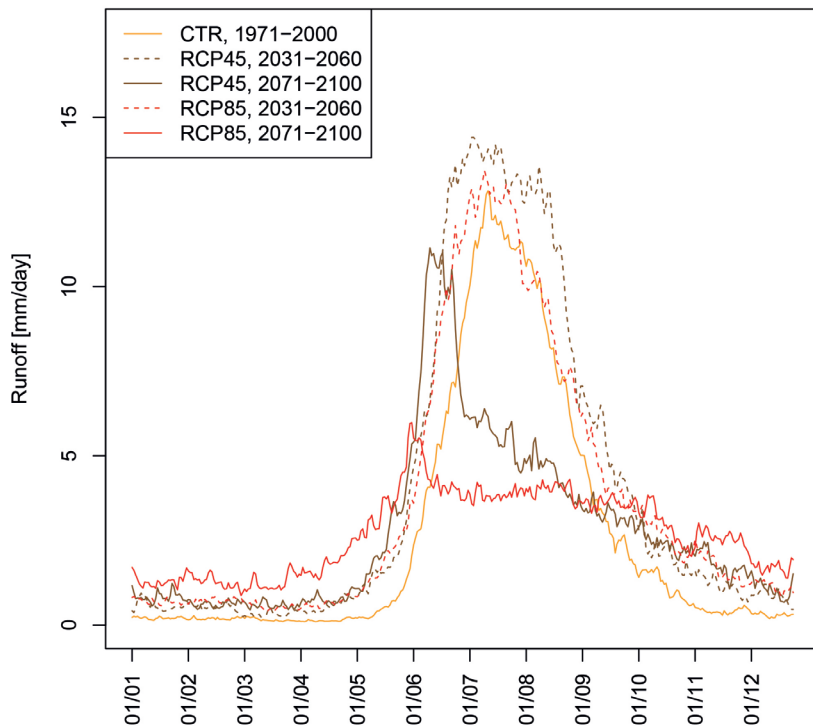
Figure 5.1.7 The seasonal distribution of Bayelva for the period 1971–2000 versus 2031–2060 and 2071–2100 for the median RCP8.5 projection.

Across Svalbard, the hydrological model simulations show an increase in the annual runoff, particularly at high elevations (Figure 5.1.8). This increase is attributed to increased precipitation (Table 4.3.4) and enhanced glacier melt. The future projections indicate that the glaciers will gradually decrease in most areas (negative mass balance; Figures 6.6.2 and 6.6.3). The maximum annual snow storage (snow water equivalent) will decrease, but not in the high elevation areas in the northeast (Figure 5.2.5).

Although the annual runoff will increase across Svalbard, the seasonal runoff changes vary (Figure 5.1.9). The smallest increases occur in the winter and spring and the largest increases in the summer. A decrease is seen in the lowlands because the snowmelt peak is shifted from June to May (Figure 5.3.3) and evapotranspiration increases. Glacierised regions will experience a strong increase in the summer runoff, whereas glacier-free areas will experience a decease in the runoff. The autumn runoff will increase due to increased precipitation and glacier melt, except in the lowlands.

Too much glacier melt may give too high values of runoff in Figures 5.1.8 and 5.1.9, but the spatial pattern is reasonable. Runoff changes are very sensitive to glacier changes, and the limited knowledge about how temperature and glaciers will develop throughout this century fosters a large uncertainty.

5.1.5 Floods

The flood estimates for Svalbard are highly uncertain, due to the factors described in Chapter 9.2. Time series of the mean annual flood (mean of the maximum daily runoff each year) in Bayelva and De Geerdalen are shown in Figure 5.1.10. The largest observed flood in Bayelva was recorded 11 September 1990, with a daily mean of 32 m^3/s (91 mm/day). The largest observed flood in De Geerdalen was recorded 20 July 2000, with a daily mean of 30 m^3/s (33 mm/day). Estimated flood values for these catchments are given in Table 5.1.1 (Stenius, 2016). The relatively short periods of discharge observations (23 and 29 years, respectively), render the analysis uncertain.
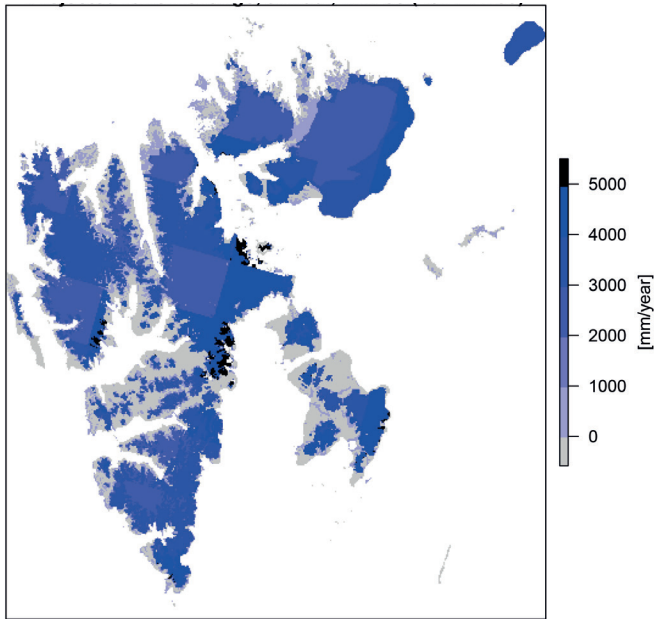
Figure 5.1.8 Projected mean annual runoff changes [mm] in the HBV simulations (RCP8.5) for the time period 2071–2100 compared to 1971–2000. The reason why large-scale squares are visible in the figure is explained in Box 5.2.

Box 5.2 Why are large-scale squares visible in the model figures?

Although the hydrological model results are produced using fine model grids, some of the hydrological results are poorly resolved due to poorly resolved input data. For example, in Figures 5.1.8 and 5.1.9, large-scale squares showing less runoff are visible in central Svalbard. As explained in Chapter 3.2, temperature and precipitation were regridded from Arctic CORDEX with a spatial resolution of about 50x50 km^2 to a spatial resolution of 1x1 km^2. Figure B5.2 shows how Svalbard is represented at this coarse-scale in three different RCMs. The RCM data are re-gridded to 1x1 km^2 resolution simply allocating the 50x50 km^2 grid cell value to the 1x1 km^2 grid cell. The bias-adjustment is then performed cell-by-cell on the 1 km scale using the Sval-Imp data as reference. Some grid cells take information from a RCM land cell, others take information from a model cell that represents ocean in the RCM. For example, the grid cell in central Svalbard (covering Pyramiden in its lower left corner), is generally colder than the surrounding land cells in most RCMs, resulting in less runoff for that coarse-scale grid cell. The resulting adjusted data set therefore outlines the land mask of the coarse-scale RCMs.

This adds to an already large uncertainty caused by a range of factors (Chapter 9).
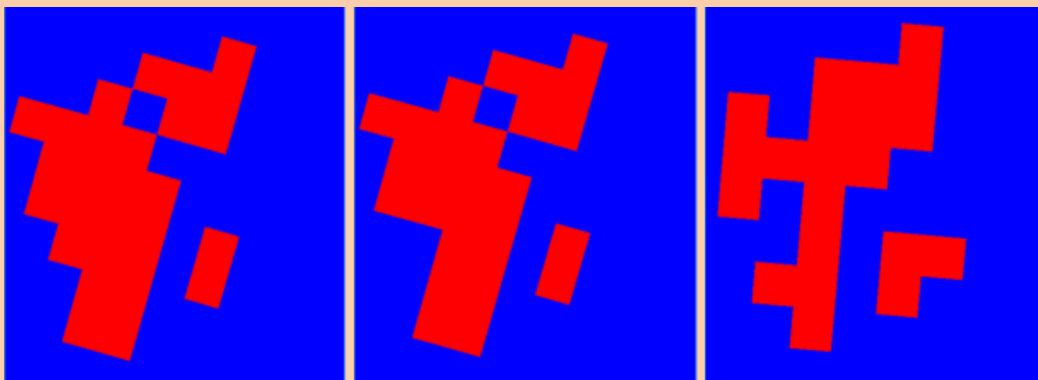
Figure B5.2 Land masks for Svalbard in SMHI-RCA4 (left), DMI-HIRHAM5 (middle) and MGO-RRCM (right). Red marks land gridcells in the RCM and blue marks ocean gridcells in the RCM.

Projected seasonal changes in runoff, rcp85 (2071−2100 − 1971−2000)
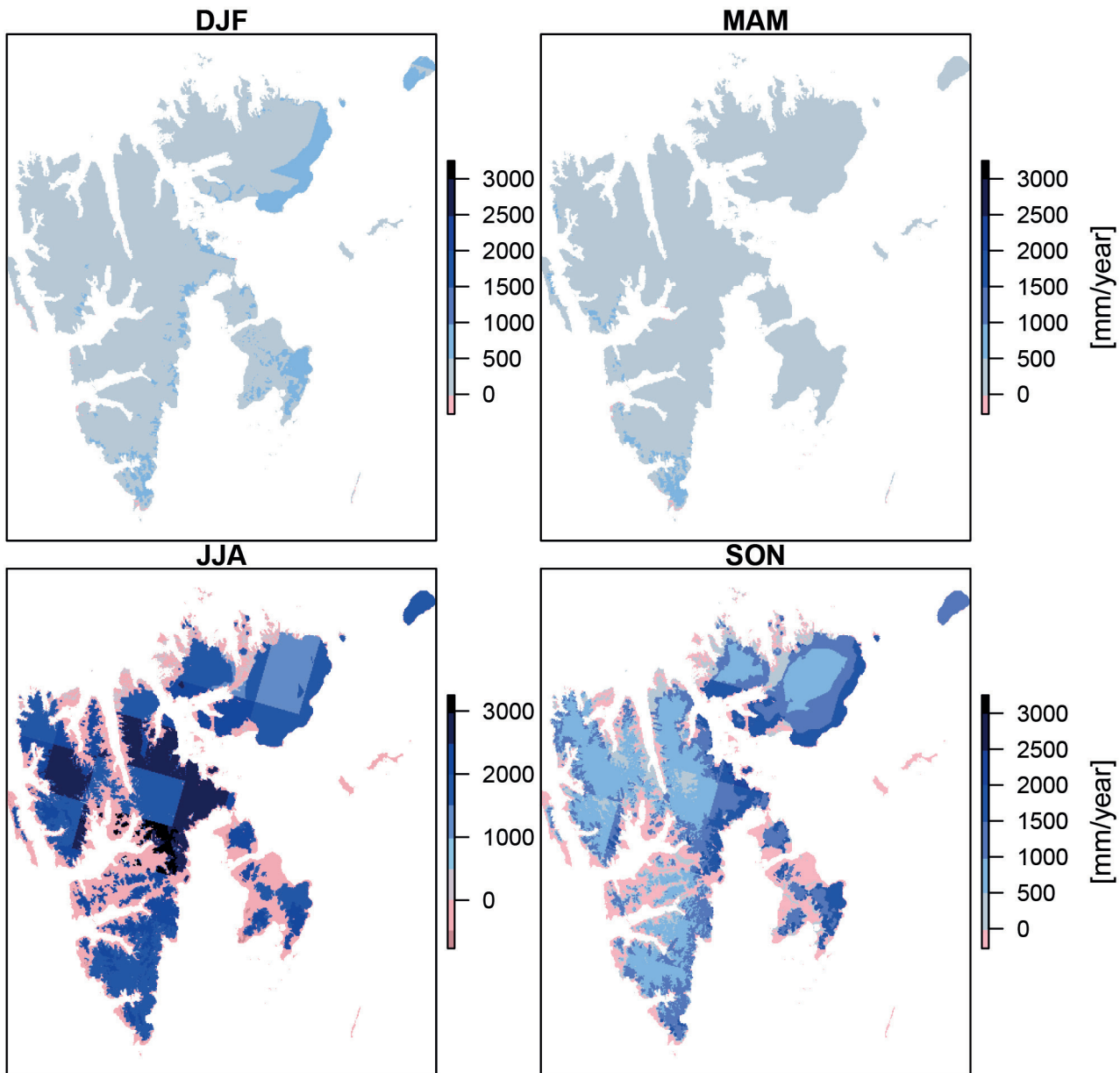
Figure 5.1.9 Projected mean seasonal runoff changes [mm] in the HBV simulations (RCP8.5) for the time period 2071–2100 compared to 1971–2000. Absolute values in mm/year. Note the different scales. The reason why large-scale squares are visible in the figure is explained in Box 5.2.

Changes in the frequency and magnitude of floods in Svalbard are strongly linked to changes in precipitation, snow storage and glacier regimes. In general, a reduced snow cover leads to smaller snowmelt floods, while increased precipitation and an increased fraction as rain, will increase rain floods and possibly also combined snowmelt and rain floods. The snow storage is projected to decrease, especially at low altitudes, under RCP8.5 and by

the end of the century. This will cause snowmelt floods to become less frequent and rainfall floods to become more frequent. In addition, the maximum snow storage is shifted several weeks earlier in the spring, leading to an earlier snowmelt runoff maxima (Figure 5.2.3). High runoff and floods may occur when heavy rainfall coincides with strong glacier melt in the summer, particularly in periods of negative mass balance. Eventually the retreat of
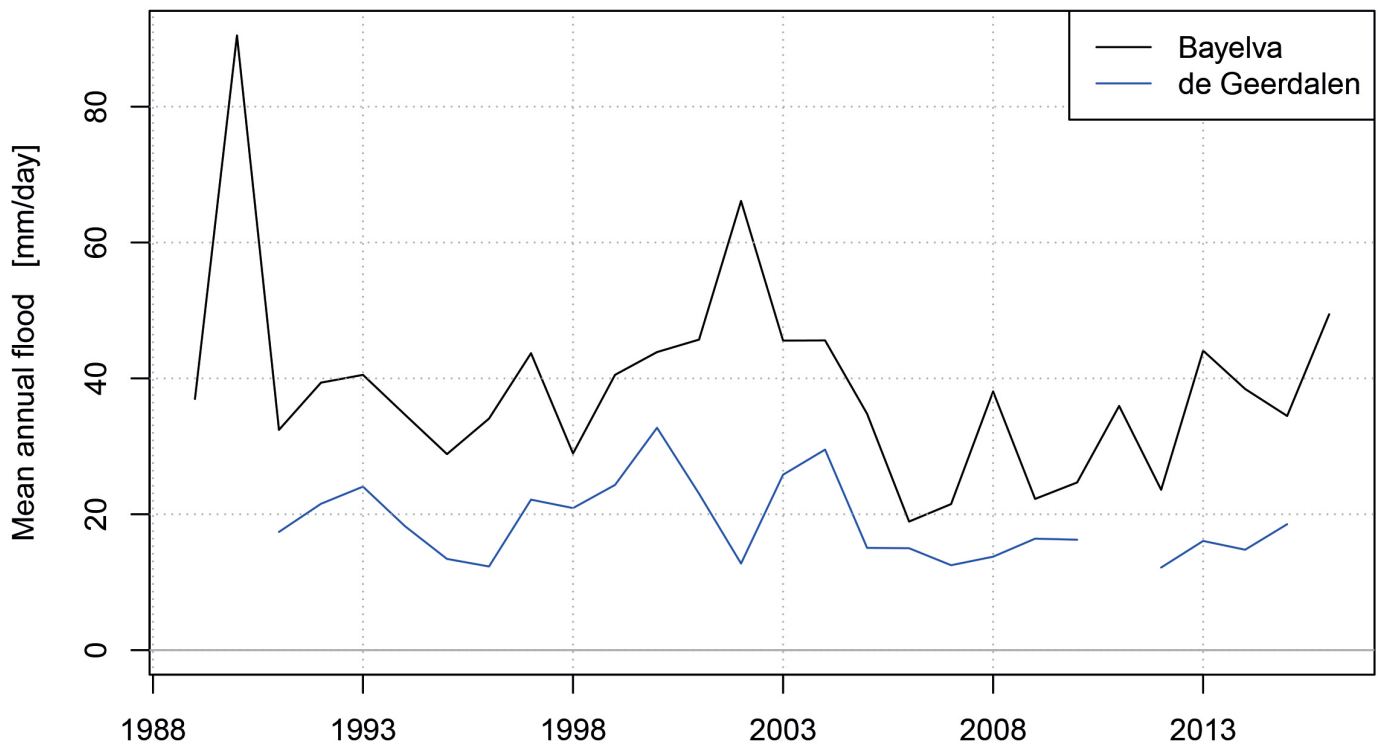
Figure 5.1.10 Historical annual maximum streamflow at the two runoff stations in Svalbard.

glaciers and reduced glacier ice volumes will reduce the contribution from glacier ice melt to runoff and floods. In Bayelva, De Geerdalen and Longyearelva, the simulated runoff peaks in the middle of the century whereafter the contribution from glacier melt is reduced. For Svalbard as a whole, the glacier mass is so large that simulated annual maximum runoff continues to increase towards the end of the century.

This section is based on observed runoff in the frost-free period because icing makes winter measurements unfeasible. In recent winters, periods of melting and intense rainfall have been reported, for example 26 January–9 February 2012 (Hansen et al., 2014), 13–14 January 2018 and 27–28 February 2018 (Isaksen, K. pers. comm.). If the rainfall intensity is small relative to the snow storage, the snow will absorb the rain, however, if the rainfall intensity is large relative to the snow storage, this rain water will drain and will subsequently freeze (Peeters et al., 2018). With continued winter warming, run-

off is expected to increase, but it is not possible to quantify this increase without reliable observations. In addition to inundation, intense rainfall in winter causes other consequences, such as slush flows and ground icing (Hansen et al., 2014).

These results are highly sensitive to the temperature input and glacier melt. Due to an increase in glacier melt, rainfall (including the fraction of precipitation as rain) and more intense snowmelt, an increase in the mean annual flood is expected in many rivers, until the contribution from glacier melt becomes negligible. However, it is difficult to quantify the expected increase because of sparse data and uncertain model results.

In a glacial landscape, meltwater may temporarily be dammed by glacier ice or glacier debris (ice or soil and rock). When the dam fails, the glacial lake drains in a so-called glacial lake outburst flood (GLOF). Glacier-dammed lakes are common in Svalbard (Liestøl, 1975), many of them drain

periodically (T. Schuler, pers. comm.). Today, none of these glacial lakes are known to be located upstream of settlements or infrastructure (T. Schuler, pers. comm.). With continued warming, there is reason to believe that glacial lake outburst floods will become more frequent, but GLOFs will not necessarily affect settlements.

5.2 Snow

5.2.1 Historical snow conditions

Snow cover is an important indicator of climate change in Arctic areas, since it is controlled by both temperature and precipitation. Changes in the snow cover are important for both the climate system and hydrological processes. At Svalbard, the snow is a dominant land cover for more than 7–8 months in the non-glacierized areas in the present climate (Figure 10.2.4, observed snow cover duration in Longyearbyen). Changes in the snow cover is a consequence of multiple environmental drivers and feedbacks (Brown et al. 2017 and references therein). These drivers include changing atmospheric circulation, warming, increased moisture availability, increased frequency of rain-on-snow events and winter thaws. Interaction between these drivers and feedbacks result in changing spatial, temporal and seasonal snow cover (extent, snow amounts and snow properties). Both the observed and projected changes in the snow cover, described in this report, support the findings described for the entire Arctic regions (Brown et al. 2017).

The modelled snow season duration (Chapter 3.2.3) for the entire Svalbard has decreased over the period from 1958–2017 with approximately 20 days, from 340 to 320 days (Figure 5.2.1, right). Low altitude and coastal areas have the shortest snow cover duration with less than 300 days per year (Figure 5.2.2, right). Northwestern and eastern parts are snow covered more than 300 days per year, particularly higher altitudes and glaciated areas. In Van Pelt et. al (2016) snow onset and disappearance dates were computed for the entire Svalbard archipelago between 1961 and 2012. They found that the snow onset date shifted to a later start due to autumn warming. The snow onset was delayed by up to 5 days per decade. However, they did not find significant trends for changes in snow disappearance dates. Particularly, in the low-lying valleys in central Svalbard, the snow melted on average in the beginning of June. These areas are typically low-precipitation and high-temperature areas. Van Pelt et al. (2016) also found a general trend of earlier snow disappearance in central Svalbard (minimum −1 day per decade) and later disappearance in the east and north of Svalbard (maximum 4 days per decade). Because of the similarities to the precipitation maps, Van Pelt et al. (2016) argue that trends in snow disappearance are to a larger extent controlled by trends in winter snowfall rather than trends in spring and summer melt. Still, the combined effect of changes in onset and disappearance dates resulted in a slightly shorter snow season duration in the period from 1961 to 2012. In the simulations with the seNorge model (Chapter 3.2.3), the definition of a snow day is a day with more than 20 mm snow water equivalent. This is a conservative definition, and is a better representation of good skiing conditions than the meteorological definition of snow available on the ground. There are often strong winds at Svalbard. Therefore, the modeled snow water equivalent is larger than the observed local snow amounts at weather stations. The wind blows the snow away, partly to the sea, and partly as redistribution on land. However, this effect is not taken into account with the seNorge snow model. We assume the snow to be redistributed within the 1x1 km^2 gridcells. The model probably overestimates the precipitation, which also contributes to too high snow storage estimates.

The maximum annual snow storage for Svalbard has slightly increased over the period from 1958 to 2017 (Figure 5.2.1, left). However, there are very large annual variabilities. Figure 5.2.2 (left) shows the mean annual maximum snow storage for the reference period 1971–2000 for the entire Svalbard, and the three subregions. The snow storage is largest in western, high-altitude regions with up

to 1000-1200 mm mean annual maximum snow water equivalent. The snow storage is continuously accumulating in autumn, throughout the winter and spring with maximum snow amounts in June (Figure 5.2.3, left). This pattern is very similar for all regions. The mean annual maximum snow storage map shows a strong similarity to the mean annual precipitation map (Figure 2.1.2b), because it represents the cumulative snow accumulation for each snow season. The presented results are in line with the results published by Van Pelt et al. (2016), who also found that the number of days with snow cover was decreasing, while the maximum annual snow storage was increasing in the period from 1961 to 2012.

5.2.2 Future snow conditions

Maximum annual snow storage and mean annual snow cover duration, have been computed for the two periods 2031-2060 and 2071-2100. The simulations are carried out using the seNorge snow model forced with the Arctic CORDEX simulations, RCP4.5 (5 simulations) and RCP8.5 (8 simulations) (described in Chapter 3.2.4). Additionally, the snow simulations are computed using the CCLM data, RCP8.5 for the period 2071–2100. For the Arctic CORDEX snow simulations, the ensemble median for the two 30 year periods are presented.
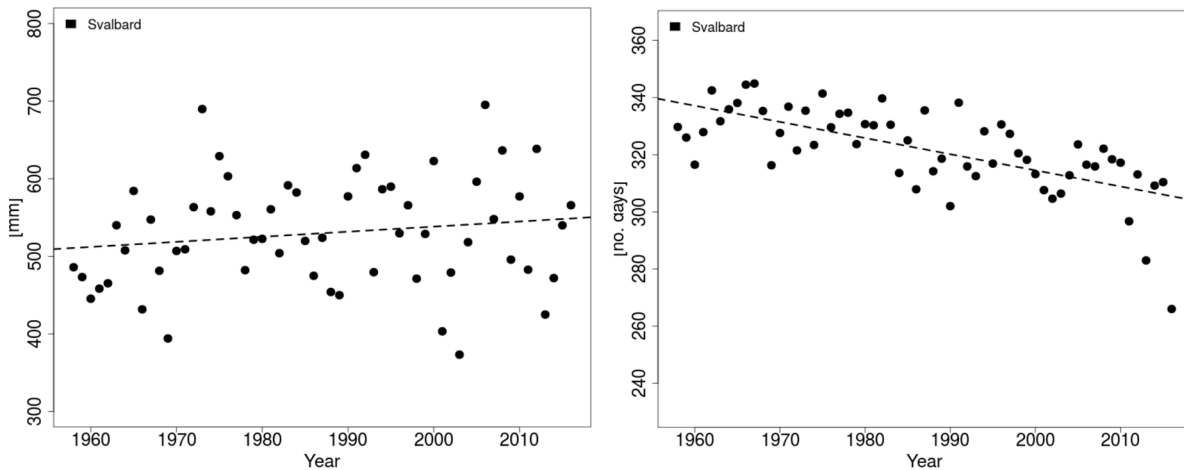
Figure 5.2.1 Trends in maximum annual snow storage (mm snow water equivalent) (left), and trends in snow cover duration (number of days with swe>20 mm) (right), for the period from 1958 to 2017.
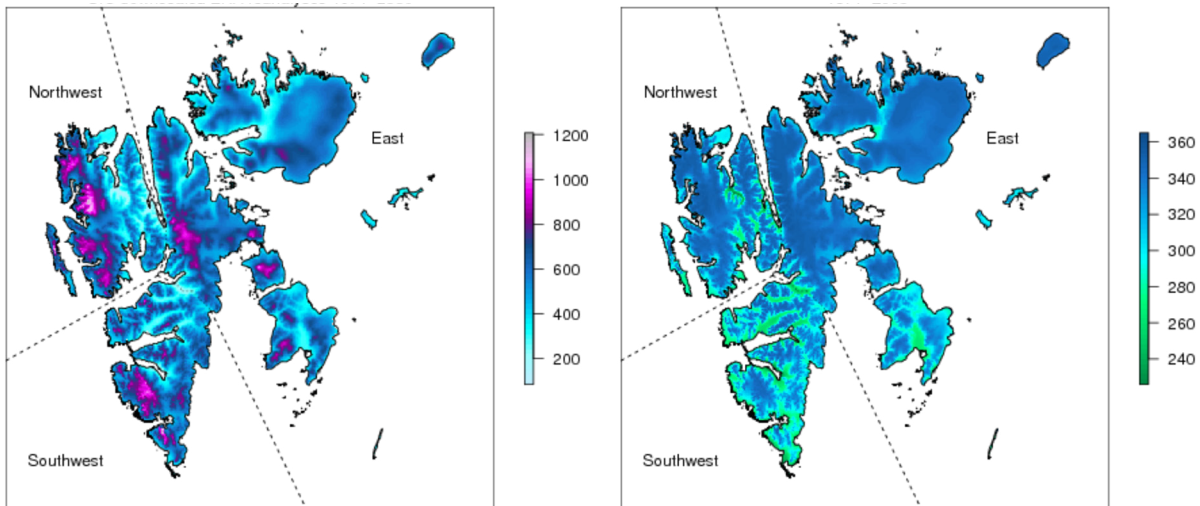
Figure 5.2.2 Mean annual maximum snow storage (mm snow water equivalent) (left) and mean annual snow cover duration (number of days with snow per year) (right) during the reference period 1971-2000 based upon the Sval-Imp dataset.
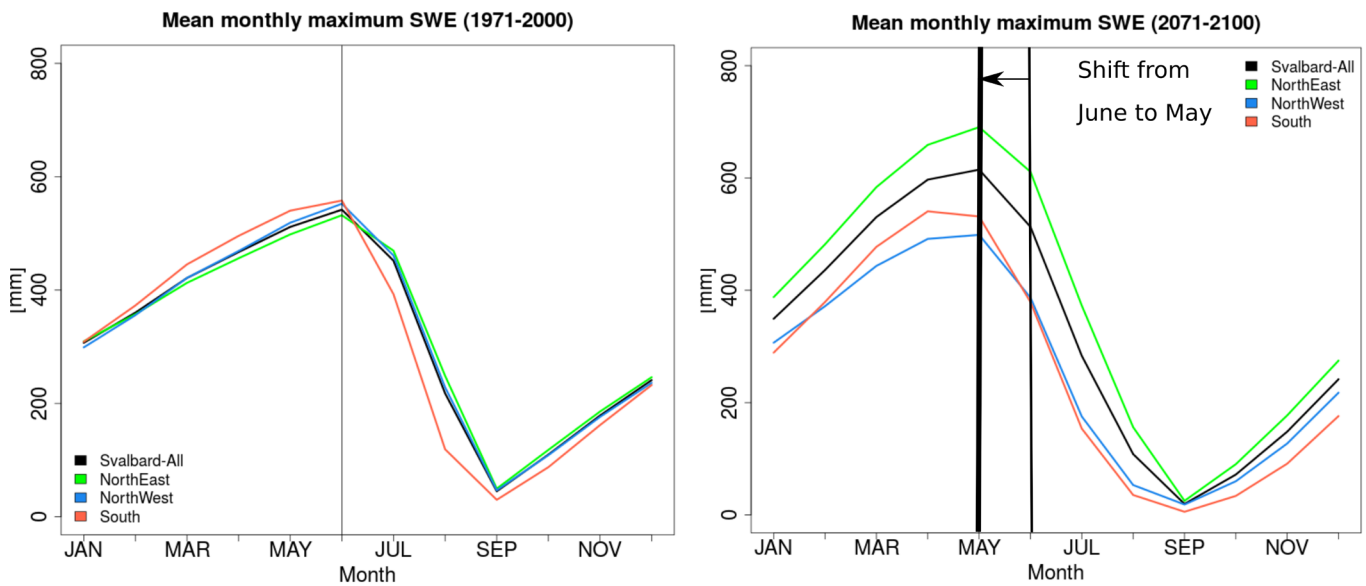
Figure 5.2.3 Mean monthly maximum snow storage (mm snow water equivalent) aggregated for Svalbard and the subregions during the reference period 1971-2000 (left) and the future period 2071-2100 (right). The reference period is simulated using the Sval-Imp as input, while the future period is simulated with forcing data from the 2.5 km CCLM model, following emission scenario RCP8.5.

2031–2060

Results for the period 2031–2060 show that maximum snow storage for RCP4.5 resembles RCP8.5, but RCP4.5 shows slightly more areas with increasing snow amounts than RCP8.5. This is expected as RCP8.5 is a warmer emission scenario. For both emission scenarios, higher altitudes in the northwestern and eastern areas will probably get more snow amounts compared to present climate, while most other lower located and coastal areas will get less snow amounts.

For the snow cover duration, the RCP4.5 also resembles RCP8.5. Both emission scenarios show a decrease in the annual number of snow days. The smallest reductions are expected in the northeastern and northwestern regions, and particularly at the high elevation sites. The largest decrease in snow cover duration is predicted for the low-elevated sites, and along the western coast.

The predicted changes in snow storage and snow cover duration is an effect of changes in predicted temperature and precipitation (Chapter 4 and Box 5.1). From the present climate to the future period 2031–2060, the precipitation is expected to increase with 28% for RCP4.5 and 34% for RCP85. In the same period the temperature is expected to increase with 4–5 °C (Arctic CORDEX median, RCP4.5 and 8.5). A temperature increase in the winter season leads to a shorter snow season (later start and earlier end) in areas that have the highest winter temperatures in the present climate. However, the increased amounts of precipitation that are predicted are probably the reason for an increased snow storage at the higher elevated sites.

2071–2000

The results for the simulations of snow storage and snow cover duration for the period 2071–2100 are shown in the Figures 5.2.4–5.2.7. The maximum snow storage is strongly different comparing the RCP4.5 and 8.5 (median for the Arctic CORDEX simulations), as a contrast to the period 2031–2060. The simulations with RCP4.5 still show areas with slightly the same or more snow storage, while the simulations with RCP8.5 show less snow amounts over most of Svalbard, with 50–100% less snow in many places. An estimation with CCLM RCP8.5

is shown in Figure 5.2.5. The CCLM simulation is more similar to the Arctic CORDEX RCP4.5 than the Arctic CORDEX RCP8.5. The CCLM simulation shows increased amounts of snow storage (up to 100% for certain areas) for large areas in the northeast, and reduced amounts in western and southern areas. The reason for this is probably that the CCLM simulation is predicting a temperature change by the end of the century of approximately 7 °C, which is similar to the Arctic CORDEX RCP4.5 median (Table 4.1.5). The Arctic CORDEX RCP8.5 median predicts an annual temperature increase of almost 10 °C, with up to more than 14 °C (median) temperature increase in the winter (Table 4.1.5).

For the snow cover duration, the simulations show that the number of days with snow will change from slightly reduced to drastically reduced all over Svalbard, for all the simulations, including both the

Arctic CORDEX runs (RC4.5, 8.5, median) and CCLM. The main difference is that the Arctic CORDEX RCP8.5 simulations show a much stronger decrease in the snow season duration than RCP4.5. With increasing winter temperatures, the snow line will increase, and precipitation as rain will be more frequent below the snow line.

Another change is the timing of the maximum snow storage (Figure 5.2.3, right). The present climate maximum snow storage is in June, while the CCLM simulation shows that the maximum period is shifted to May (one month earlier), for Svalbard and its subregions, except the southern subregion which will have maximum storage in April (two months earlier).
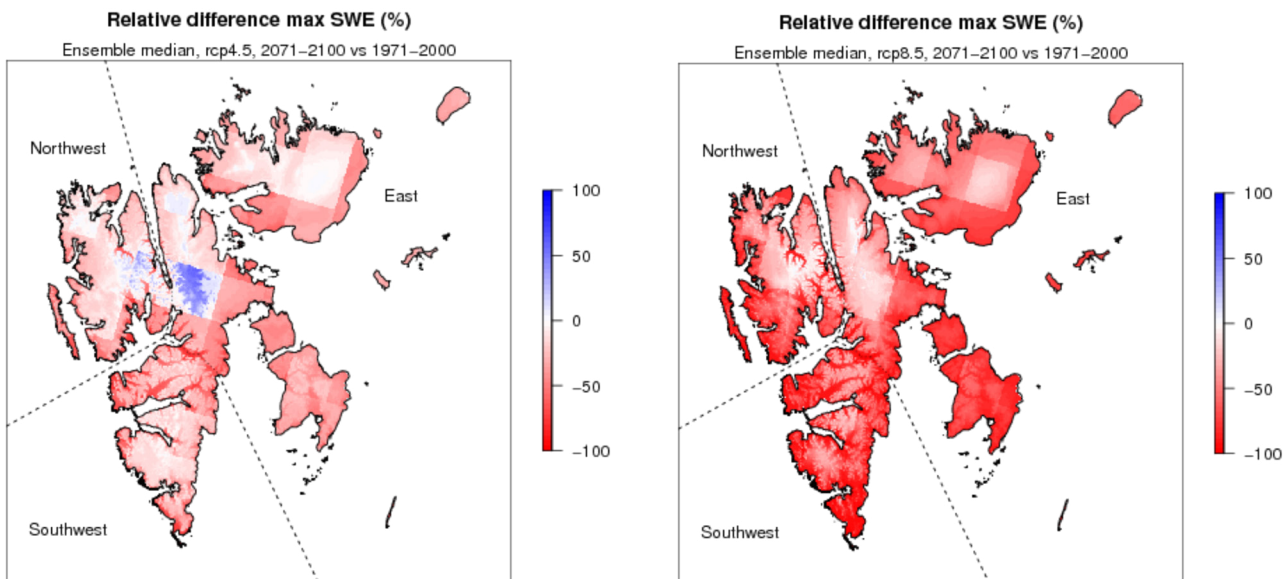
Figure 5.2.4 Relative changes in maximum annual snow storage from 1971–2000 to 2071–2100 (%), for RCP4.5 (left) and RCP8.5 (right). The simulations show the ensemble median for the bias-adjusted Arctic CORDEX runs (1 km spatial resolution).

Relative difference max SWE (%)
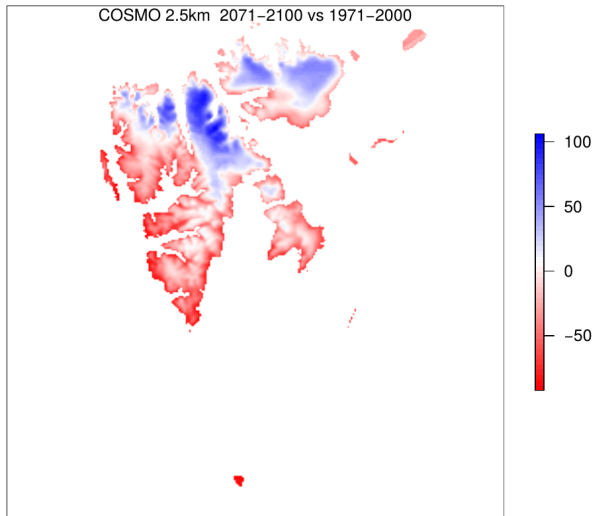
Figure 5.2.5 Changes in maximum annual snow storage from 1971–2000 to 2071–2000 (%). The simulations use the 2.5 km CCLM model as forcing data, following the emission scenario RCP8.5.

Snow days: Absolute difference

Ensemble median, rcp4.5, 2071–2100 vs 1971–2000

Snow days: Absolute difference

Ensemble median, rcp8.5, 2071–2100 vs 1971–2000
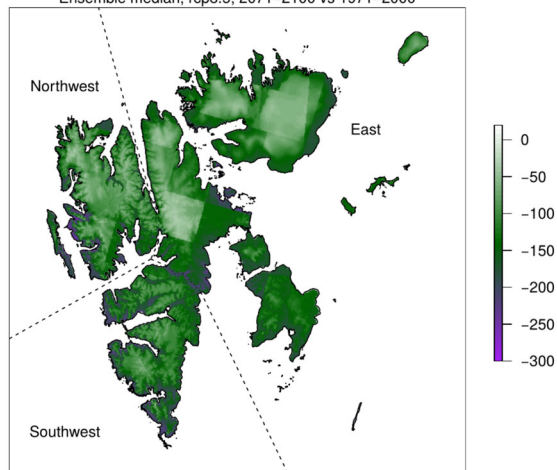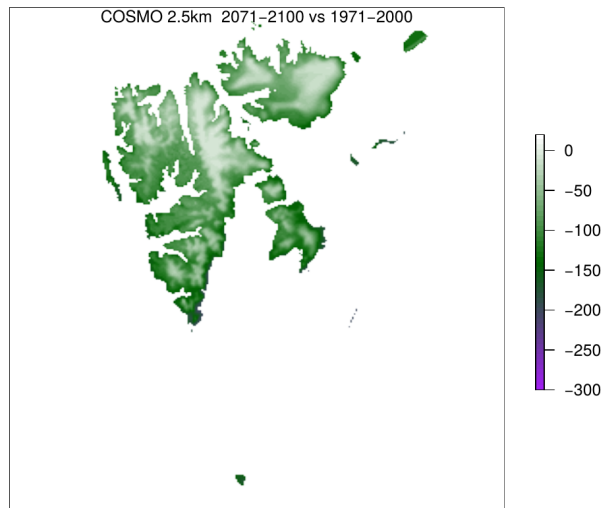
Figure 5.2.6. Changes in snow season duration (annual number of snow days) from 1971–2000 to 2071–2100, for RCP4.5 (left) and RCP8.5 (right). Simulations show the ensemble median for the bias-adjusted Arctic CORDEX runs (1 km spatial resolution).

Snow days: Absolute difference

Figure 5.2.7 Changes in annual snow season duration (mean annual number of snow days) from 1971–2000 to 2071–2000. The simulations use the 2.5 km CCLM model as forcing data, following the emission scenario RCP8.5.

5.3 Erosion and sediment transport

About 40 % of Svalbards area is outside the glaciated area and is drained by rivers. The stability of the different river reaches are dependent on hydraulic variables like water discharge, sediment discharge, grain size and slope and the supply from upstream erosion in the catchment. To analyse the impact of climate change on the sediment flux in rivers in Svalbard, a sediment budget equation may be used. This equation expresses the sediment transport on a particular reach as a sum of the delivery from various sources plus or minus the possible storage in upstream channel reaches (e.g. Jordan and Slaymaker, 1991). The sediment budget may be evaluated over a long term or short-term period. The latter one is probably the most important in the management plan of rivers affecting settlements.

In Svalbard, sediments derived from glaciers and their moraine deposits are the most important source contributing to the sediment load carried by the rivers. The results from long-term measurements of sediment transport of various rivers based on water discharge and sediment samples have been reported by Bogen and Bønsnes (2003), Table 5.3.1.

The sediment yield was measured to 586 t km^{-2} year^{-1} for the glaciers and their moraines in the catchment of river Bayelva and a relatively smaller volume of 82.5 t km^{-2} year^{-1} from weathering and frost shattering of bedrock in the unglaciated river Londonelva. Measurements from other rivers in Svalbard are within the same order of range for both types of erosion. More short-term measurements in other parts of Svalbard have provided estimates of specific sediment yields ranging from 28 to 38 t km^{-2} year^{-1} in non-glacierized catchments. In glacierized catchments, much higher specific sediment yields, in the range of 303 t km^{-2} year^{-1} to 2900 t km^{-2} year^{-1}, have been reported; Kostrzewski et al., (1989); Krawczyk & Opolka-Gadek (1994); Barsch et al., (1994); Hodson & Ferguson, (1999), Hodgkins et al. (2003) Lepkowska and Stachnik (2018). From seismic stratigraphy and sediment cores, Elverhøy et al. (1995) did estimate the Late Quaternary sediment yield of the glaciated area in the catchment of Isfjorden in Svalbard to 800 t km^{-2} year^{-1}.The sediment yield from the non-glacial part of the catchment was estimated to 35 t km^{-2} year^{-1} for the Holocene. The measurements thus indicate that the major part of the sediment in the rivers of Svalbard is derived from the glaciers and their moraine areas. However, erosion rates may increase considerably during large flood events caused by extreme rainfall. Such events may trigger debris slides and debris flows that may erode and supply to the rivers sediment that have accumulated from weathering processes over a long time period. Other processes like bank erosion are more rare in Svalbard, but known to be relatively intensive in areas of frost (Gatto 1995, Sidorchuk and Matveev, 1994). Kanevskiy (2016) did measure extremely high rates of riverbank erosion, up to 19 m/year in ice rich permafrost in northern Alaska. In Svalbard, at the lower part of the river fan where Todalen

Monitoring station	Area (km^2)	Glac. %	Specific annual sediment yield			Grain size/concentration		
			Mean annual transport (t/year)	Spec. Yield (t/km^{2}year)	Spec yield glacier (t/km^{2}year)	Mean grain size	Max (mg/l)	Mean (mg/l)
Bayelva	30.9	55	11104	359	586	0.014	11446	305
Londonelva	0.7	0	58	83	0	0.04	5343	162
Endalselva	28.8	20	8102	281	1077	0.021	9043	554

Table 5.3.1 Suspended sediment yield in selected rivers in Svalbard

meets Adventdalen, Matsuoka et al. (2018) carried out long-term studies of ice wedge formation. Heavy bank erosion of the terrace occur in this area due to reduced shear strength caused by high water content from melting ice wedges.

Water and sediment discharge from the catchments is affecting the equlibrium form of alluvial channels, and the channel forming bankful discharge event has an average of 1.5 years in a wide range of rivers. Longer return periods for bankful events, up to 20 years, have been found in arctic rivers. As the water discharge is expected to increase in the future, increased channel erosion will occur as the channels adapt to a new climate. This effect has been observed downstream from culverts associated with road constructions in Svalbard and elsewhere (Husebye et al., 1993). The lack of data from high arctic alluvial streams, however, limits a complete understanding of how arctic geomorphic systems might change in a shrinking cryosphere (Mc Namara and Kane, 2009).

A warmer climate will affect the erosion intensity and increase the water discharge and sediment supply to the rivers. Measurements indicate that the largest volumes of sediments are delivered from the glaciers and their moraine areas. The presence of permafrost limits the erosion. However, as the temperature of the active layer rise, more sediments are available for transport (Etzelmuller and Frauenfelder 2009). The expected increase in the frequency of debris flows and debris slides will also contribute to the volumes of the sediment loads. The increased sediment supply may increase channel splitting and lateral activity of channels and expose adjacent slopes to erosion. This accelerated erosion may affect the tributaries first, and after some time, the large sandurs in the main valleys.

6. Glaciers

6.1 Holocene glacier change

We can use the ubiquitous traces left by glaciers in the landscape to study glacier-climate interactions on Svalbard prior to the observational period -which didn`t begin until the second half of the 19th century. We are largely restricted to the Holocene epoch (11,700 years BP until present), as Late Weichselian ice sheets removed most evidence from previous glacial periods (Landvik et al., 2013). Researchers have primarily relied on three lines of evidence to unravel the terrestrial Holocene glacier history of Svalbard: moraines, vegetation kill dates and lake sediments. Moraine ridges, thrusted up by advanc-

ing ice, provide snapshots of past glacier dimensions when dated. The same holds true for fossil vegetation, killed and entombed in situ by over-riding non-erosive (cold-based) ice. Radiocarbon dates on such plant remains constrain the timing of glacier margin advances. Sediments in glacier-fed lakes may yield continuous records of Holocene glacier change. The rationale behind this approach builds on the link between size and erosion rates in alpine (erosive) glaciers: variations in evacuated glaciogenic lacustrine sedimentation capture relative variations in glacier size (e.g. Karlén, 1981).
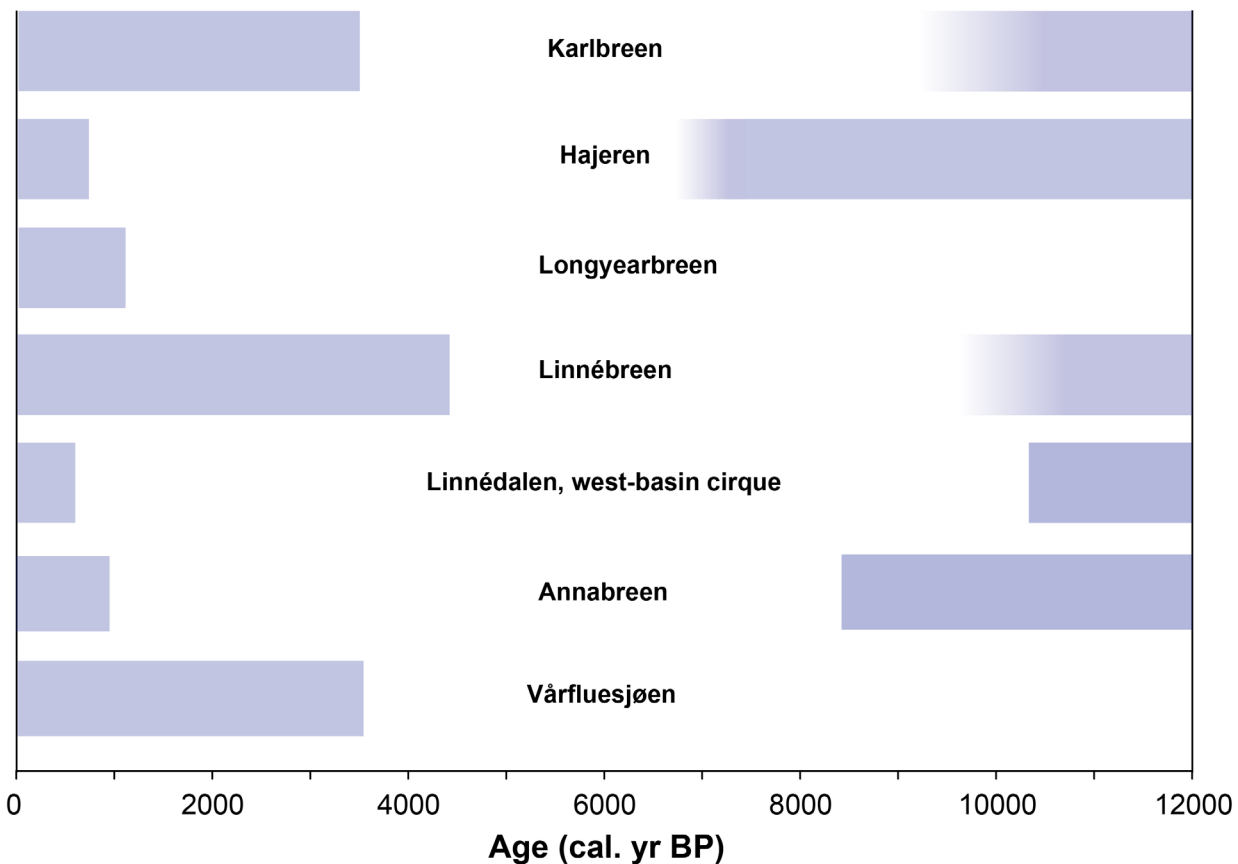
Figure 6.1.1. A compilation of Holocene glacier reconstructions from Svalbard, modified after De Wet et al. (2017). Blue fields indicate prolonged periods of glacier activity. Included records derive from (north) west Spitsbergen: Karlbreen and Hajeren from the Mitra peninsula (79°N, 11°E) (Røthe et al., 2015; van der Bilt et al., 2015), Long-yearbreen (78°N, 15°E) (Humlum et al., 2005), Linnébreen and the west-basin cirque in Linnédalen (78°N, 14°E), Annabreen on Amsterdamøya (79°N, 11°E)(De Wet et al., 2017), and Vårfluesjøen (79°N, 15°E)(Røthe et al., 2018).

Svalbard's Holocene glacier history was first established by analysing lake deposits in the glaciated catchment Linnédalen, in western Spitsbergen. Using radiocarbon-dated sediments from glacier-fed Lake Linnévatnet, Svendsen and Mangerud (1997) identified a three-phase Holocene glacier history. Following deglaciation after 12,000 years BP, local glaciers disappeared during the Early Holocene around 9,700 years BP (Fig. 6.1.1). Conditions subsequently remained unfavourable for glacier growth during the Middle Holocene period (~8-4 ka BP). Finally, glaciers reformed during the Late Holocene (Neoglaciation) and reached their historical maxima when the Little Ice Age (LIA) culminated in the 19th century. Werner (1993) used lichonometric dating of up-valley moraines to provide independent evidence for a LIA glacier maximum in Linnédalen. The outlined pattern of change is consistent with reconstructions of glacier change from other parts of Europe, and attributed to progressive cooling stemming from a gradual decrease in summer insolation during the Holocene (Wanner et al., 2008).

Reduced sample size requirements for radiocarbon dating, the advent of cosmogenic nuclide dating, and high-resolution scanning techniques such as X-Ray Fluorescence greatly improved the level of (chronological) detail of dated (lake) sediments and moraines over the last decades. This has enabled us to refine the Holocene glacial history of Svalbard (Fig. 6.1.1), resolving change over human-relevant (decadal to centennial) timescales. For example,

recent studies (Farnsworth et al., 2017; Henriksen et al., 2014; van der Bilt et al., 2015) have identified a phase of widespread glacier growth in the Early Holocene (~10,000-7,000 years BP), a period marked by high radiative forcing. In addition, Reusche et al. (2014), Røthe et al. (2015), van der Bilt et al. (2015) and Miller et al. (2017) show that the onset of Neoglaciation was characterized by episodic phases of glacier growth, instead of a gradual response to declining summer insolation.

These refinements have not only greatly expanded our knowledge of Holocene glacier variations on Svalbard, but also sparked interest in resolving their underlying climatic causes. For example, Van der Bilt et al. (2016), reconcile the coincidence of glacier growth and maximum summer insolation during the Early Holocene by inferring a phase of terrestrial cooling linked to freshwater forcing from melting ice sheets (Zhang et al., 2016). Moreover, the findings of e.g. Müller et al. (2012) and Werner et al. (2015) indicate that sea-ice and surface ocean feedbacks intermittently amplified radiation-driven Late Holocene cooling, explaining the stepwise pattern of Neoglacial glacier change. In conclusion, investigations of past (Holocene) glacier change on Svalbard yield critical insights about the sensitivity and drivers of the Arctic climate system, contextualizing the present and preparing us for a rapidly changing future.

6.2 Recent glacier front retreat

As stated in Chapter 3, front positions are not necessarily direct proxies for changes in glacier mass on annual to decadal time-scales. This can be seen in Kongsfjord, one of the best-mapped areas of Svalbard (Figure 6.2.1). The glaciers here were the first mapped in the late 1800s, and thereafter at irregular intervals, until after the mid-1970s, when satellite images became increasingly available. The frontal record shows the clearly episodic tidewater glacier retreat, with long periods of small fluctuations or minor retreat from stable positions, punctuated by rapid retreat to new stable positions. Occasionally there are front advances: following the

surge of Kongsvegen in 1948, the combined front of Kronebreen and Kongsvegen re-advanced several kilometres into the fjord (Figure 6.2.1). Blomstrandbreen has surged three times since the late 1800s (ca. 1910-1930; 1956-1966; 2006-2013; Burton et al. 2016), but as can be seen (Figure 6.2.1), once a surge is over, glacier retreat continues.

Nevertheless, changes in front position, or equivalently, glacier area, can give an indication of the long-term changes around the archipelago. Figure 6.2.2 (Nuth et al., 2013) shows the relative change in glacier area comparing the inventory of Hagen

et al (1993), whose dates vary regionally from the 1960s to 1990, with the 2000s inventory (Nuth et al., 2013), where change is averaged for all glaciers in the main drainage basins defined by Hagen et al (1993). The mean area change is -7% for the average 32-year time interval between the inventories, or ca. -0.2 % per year. While this change is spatially variable, it is notable that there are no regions with an increase in glacier area.

While tidewater glacier fronts are not reliable as climate indicators, they are nevertheless important to fjord circulation and ecosystems. Since more than half of Svalbard's ice area terminates in tidewater glacier fronts, a significant part of the glacier melt and rainfall on Svalbard enters the ocean at these fronts; this has a significant influence on the ocean circulation, particularly in constricted bays or fjords (Lydersen et al., 2014). In summer, glacier meltwater flows on and within the glacier towards the front, typically entering the ocean below the seawater

surface, usually at the base of the tidewater front. The relatively low density of the freshwater forces it to rise rapidly, entraining large volumes of ambient fjord water. These freshwater "plumes" breach the surface, then flow outward towards the mouth of the fjord, further entraining subsurface water. The steeper the calving face, the more vigorous is the potential circulation.

Plumes have two distinct effects on their local environment. First, organisms that are entrained in the rising plume will be brought towards the surface, where they will be more easily accessible for surface-feeding animals. Second, as the plume rises it will entrain large volumes of ambient water, from 10-100 times the original discharge volume. This water will be drawn from all depths that the plume passes through, leading to more thorough mixing. Entrainment ensures a continuous resupply of intermediate depth waters, including zooplankton and nutrients, to the glacier front area.
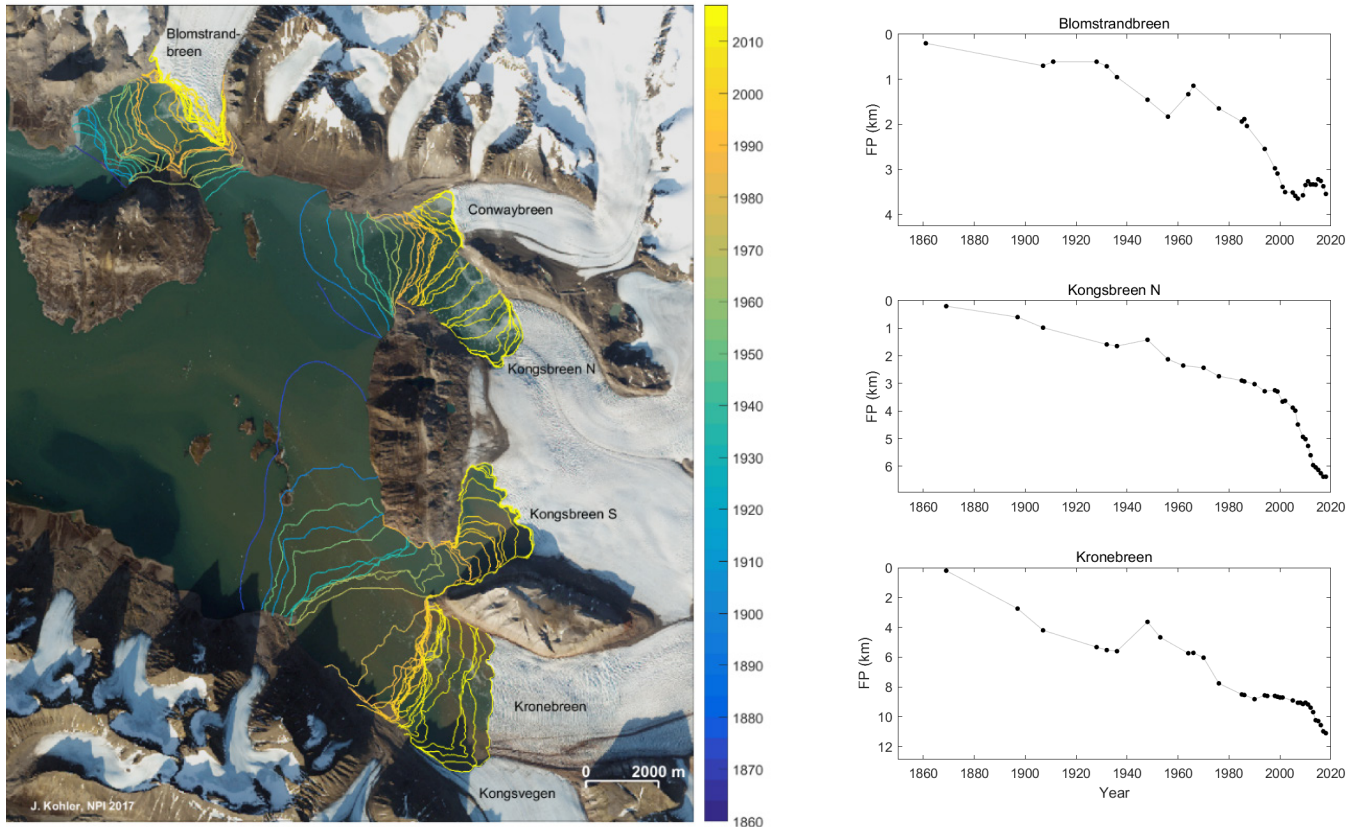
Figure 6.2.1 (a) Front positions of tidewater glaciers in Kongsfjord. (b) Front position along glacier centerlines of three of the glaciers, relative to their earliest measurements.
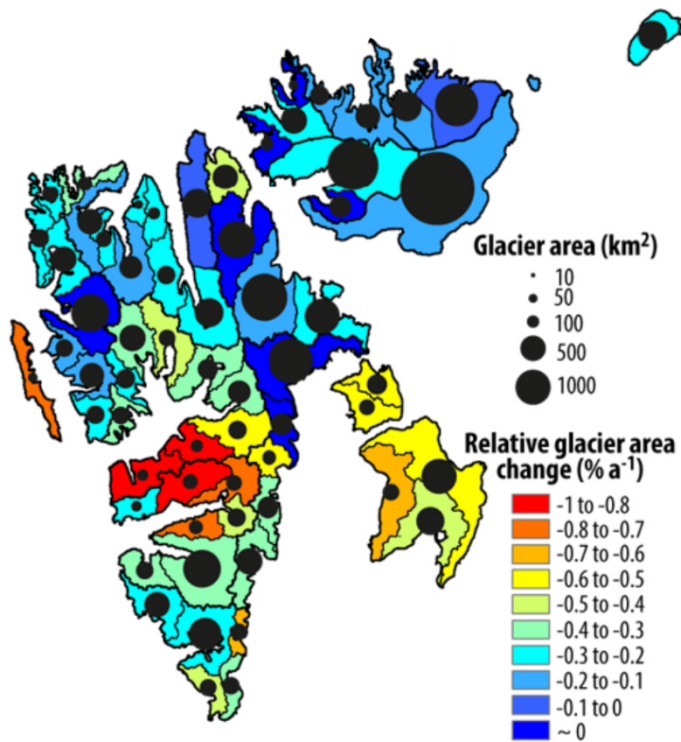
Figure 6.2.2: Relative changes in glacier area, comparing areas from Hagen et al (1993), whose dates vary regionally from the 1960s to 1990, and glaciers areas for the 2000s Drainage basins are defined in Hagen et al (1993). Total glacier area shown as size (area) proportional symbols.

Glacier fronts thereby are important feeding areas for seabirds and marine mammals (Lydersen et al. 2014). In Svalbard, several bird species can be found in large numbers, up to thousands of individuals, at tidewater glacier fronts. The birds are often found in the centre of the meltwater plume, which is ice-free due to currents and muddy due to upwelling suspended sediments. Plumes are also foraging hotspots for Svalbard's ringed seals and white whales. Additionally, prime breeding habitat for ringed seals in Svalbard occurs deep in the fjords where ice pieces calved from the glacier fronts become frozen into land-fast sea-ice, promoting accumulation of sufficient snow for female seals to dig out birth lairs above breathing holes. These seal pupping areas then become important hunting areas for polar bears and arctic foxes.

With further warming in the Arctic, we can expect continued retreat of Svalbard's glaciers, and a decline in the number of tidewater glaciers around Svalbard. This will impact fjord circulation once tidewater glaciers retreat to the point that they terminate on dry land, with implications for fjord ecosystems. Outflow into the fjord would then occur only via surface drainage, just as with any unglaciated fjord, with a cap of fresh river water flowing over the denser ocean water. There will be less nutrients and plankton brought to surface, which will impact bird, seal, and other animal populations. There will also be more limited entrainment of fjord water, resulting in less mixing and retention of less saline surface waters, which will in turn expedite sea ice formation. Furthermore, as glaciers retreat into narrower and more constricted geometries, with increasing numbers of subaqueous topographic barriers between the glacier front and the outer fjord, chances improve for preserving fjord ice throughout the winter season, even as outer fjord waters become warmer. An increase in inner fjord sea ice could counteract the negative effects of decreased food supply, at least for seal populations that depend on annually formed sea-ice for breeding.

It is not yet possible to forecast accurately tidewater front retreat in response to changes in the climatic forcing. However, using historic observations of front positions (Figure 6.2.1), and glacier bed mapping data which define the extent of the glacier bed below sea level (Lindbäck et al. 2018), we can estimate that full retreat onto land could occur over time-scales of up to decades or a century or two. For example, both Kongsbreen North and Kronebreen (Figure 6.2.1) have retreated through about half of

their submarine bed length since 1860; if the retreat rate were to continue at the same rate, both glaciers would terminate on land sometime after 2100. On the other hand, Blomstrandbreen and Conwaybreen are both near their submarine limits; they likely will terminate on land much sooner, perhaps within a few years to a decade.

Besides the well-investigated Ny-Ålesund/ Kongsfjord area, long-term (>10 years) glaciological

research on Svalbard takes place near the Polish Polar Station at Hornsund and at the Austfonna ice cap on Nordaustlandet. Other than the local significance for hydrology and ecology, the primary, global interest in glacier research is to assess the response of glaciers to climate change and the associated release of water. Change in the land-based ice volume is a major contributor to ongoing global sea-level rise.

6.3 Glaciological mass balance

Here we present and discuss data from the three glaciers with the longest continuous time-series records, all in Kongsfjord. Data from the other Svalbard glaciers with mass balance measurements (Chapter 3) show similar patterns and trends, although they have shorter records.

Austre Brøggerbreen (BRG) and Midtre Lovénbreen (MLB) are both small glaciers, less than 10 km^2 in area, and neither is higher than about 650

m a.s.l. Both have had consistently negative net balances since measurements started in the 1960s (Figure 6.3.1), due to their relatively low-lying and small accumulation areas. MLB is less negative than neighbouring BRG, in part due to its slightly higher elevation and steeper valley sides, both of which contribute to more accumulation on MLB. The time series for Kongsvegen (KNG) is shorter, starting in 198 (Figure 6.3.1). KNG is a larger glacier, with an area of 100 km^2, and whose elevations extend up to
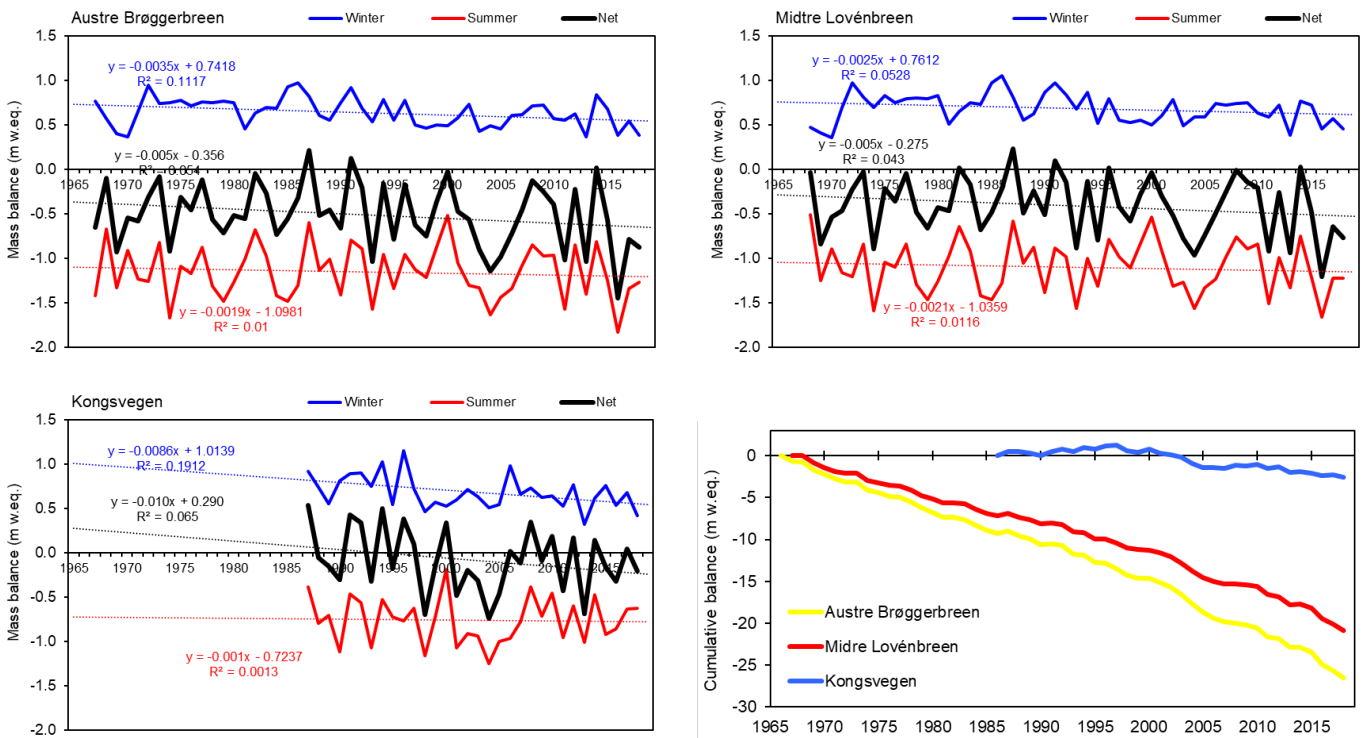
Figure 6.3.1: Winter, summer and net balance for a) Brøggerbreen, b) Midtre Lovénbreen, and c) Kongsvegen. Blue lines show the total accumulation on the glacier during the winter, converted to an area average thickness of water (metres of water equivalent, m w.eq.); red lines similarly show the net melt over the summer, while black lines are the sum of the two, or the total mass gained or lost through the glacier surface processes over the year. Trends are shown for the three balance terms. The summed net balance (d) is roughly equivalent to the volume change calculated in the geodetic mass balance.

850 m a.s.l. Because of the higher elevation, it has a significantly larger accumulation area, and therefore its net balance record is more positive than the lower-lying small glaciers BRG and MLB.

On Svalbard glaciers, winter accumulation is less variable than summer ablation, the latter of which provides more of the variability in the net balance, as can be seen in the longest time-series. (Figure 6.3.1). Finally, while trends for both winter and

summer balances are not statistically significant, the overall tendency over the measurement periods is for decreased winter accumulation and increased summer melting. The cumulative sum of the annual net mass balance, which is roughly equivalent to the volume change, shows that over the long term, these glaciers are losing mass (Figure 6.3.1), particularly the two smaller glaciers.

6.4 Geodetic mass balance

Nuth et al. (2010) compared satellite altimetry data from the Ice, Cloud, and Land Elevation Satellite (ICESat) mission for the period 2003–2007 to older topographic maps and digital elevation models for different epochs (1965–1990). Because the ICESat tracks are relatively sparsely distributed, they extrapolate along-track changes to the larger regions using the glacier hypsometry. Nuth et al. (2010) find significant thinning at the lower elevations of most glaciers, and either slight thinning or thickening in the accumulation areas, except for glaciers that surged during the observation period; these glaciers show thickening in the ablation area and thinning in the accumulation areas. However, the overall balance is very negative at -0.36 m w.eq./year, corresponding to -9.7 Gt/year (Table 6.4.1). This estimate excludes Austfonna and Kvitøya, and is averaged over different periods for different geographic regions. The most negative geodetic balances are found in the south and the least negative balances in the northeast.

Moholdt et al. (2010) determined elevation changes along the ICESat tracks for the period 2003-2008, extrapolating these changes to the remaining glacier area using the same hypsometric approach as Nuth et al (2010) to yield a Svalbard-wide estimate of -0.12 m w.eq./year, or -4.3 Gt/year. Similarly to

Nuth et al (2010), they find that most regions experienced low-elevation thinning and high-elevation balance or thickening, and that the largest ice losses occurred in the west and south, while northeastern Spitsbergen and the Austfonna ice cap gained mass.

Analysis of older maps and modern DEMs time (Kohler et al., 2007) of a few selected glaciers in western Svalbard shows that the rate at which these glaciers lost mass appears to have accelerated. For example, the average thinning rate for MLB, the glacier with the best cartographic data, increased steadily since 1936. Thinning rates for 2003−2005, the most recent period analysed, were more than four times the average for the first measurement period 1936−1962. On Slakbreen, south of Longyearbyen, thinning rates for the period 1990−2003 were more than four times that of the period 1961−1977 (Kohler et al., 2007). James et al. (2012) found a similar increase in thinning rates for other glaciers around Svalbard. This increasingly negative mass balance trend is consistent with both worldwide glacier trends as well as developments in the Arctic (Kaser, et al. 2006).

6.5 Mass balance modelling

Aas et al. (2016) simulate mass balance for all of Svalbard over the period 2003-2013 (Figure 6.5.1), and find a strongly negative average mass balance of −0.26 m w.eq./year, or -8.7 Gt/year. When the only available estimate of ice discharge from Svalbard glacier calving (Blaszczyk et al., 2009) is included, the overall Svalbard mass balance becomes even more negative (Table 6.4.1, Figure 6.6.1).

Østby et al. (2017) simulate mass balance over the longer period 1957−2014 using a different model and forcing (Figure 6.5.1) to find that while the total net balance was slightly positive over the whole model period, whereas the trend was significantly negative, with a shift from positive balance to negative occurring around 1980. The average for the most recent model period 2004−2013 is strongly negative at −0.2 m w.eq./year; when the Blaszczyk et al. (2009) calving estimate is included, overall Svalbard mass balance is even more negative, −0.39 m w.eq./year (Table 6.4.1, Figure 6.6.1). Further, Østby et al. (2017) find a strong correlation between mass balance and summer temperature, as observed

in the long in situ time-series (e.g. BRG and MLB, see above). This relation is explained by the strong correlation between mass balance and surface albedo, the latter of which largely controls the amount of available energy for melt.

Finally, Möller and Kohler (2018) use a parameterized mass balance model forced by statistically downscaled ERA-20C data to model climatic mass balance for the glacier areas on Svalbard for the period 1900–2010; the spatially averaged mean annual climatic mass balance for all Svalbard over this relatively long period is approximately zero at −0.002 m w.eq. However, this estimate does not include the calving flux, which we cannot estimate on the century scale, given the significant changes in glacier geometry that have occurred since 1900. Möller and Kohler (2018) also find comparable balances to those reported by Aas et al (2016) and Østby et al (2017) for the shorter periods 2003-2010 and 1957-2010, respectively.
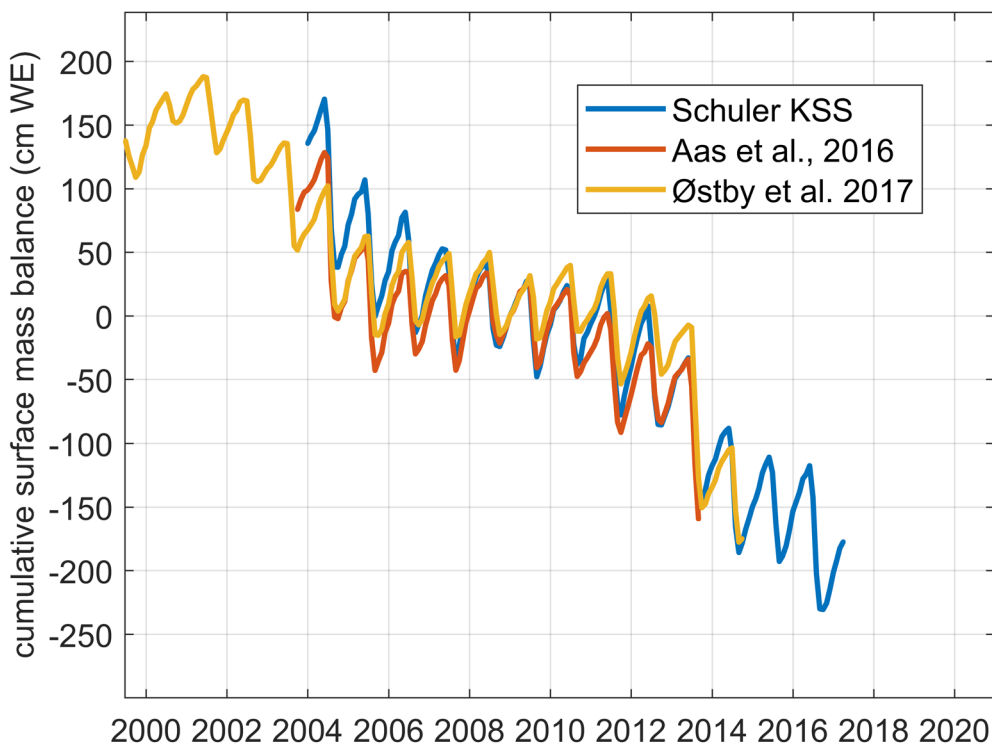
Figure 6.5.1: Cumulative monthly mass balances of Svalbard glaciated area, comparing results from three models: Aas et al (2016), Østby et al (2017), and Schuler (COSMO-CLM model, this report).

Reference	Period	Specific B_n (m w.eq./year)	B_n (Gt/year)	Method
Nuth et al. 2010	(1965-1990) to (2003 -2007) (period varies geograph-ically. and excludes Austfonna. Kvitøya)	-0.36 ± 0.02	-9.7 ± 0.55	Geodetic
Moholdt et al. 2010	2003-2008	-0.12 ± 0.04	-4.1 ± 1.4	Geodetic
Aas et al.. 2016	2003-2013	-0.26	-8.7	Model
		-0.46	-15.4	Model + calving
Østby et al.. 2017	2004−2013	-0.21	-7.1	Model
		-0.41	-13.8	Model + calving
Østby et al.. 2017	1957−2014	0.08	2.7	Model
		-0.12	-4	Model + calving
Möller and Kohler. 2018	1900-2010	-0.002		Model
	1957-2010	0.03		Model
Wouters et al.. 2008	2003-2008	-0.26 ± 0.09	-8.8 ± 3	GRACE
Jacob et al.. 2012	2003-2010	-0.09 ± 0.06	-3 ± 2	GRACE
Mémin et al. 2011	2003-2009	-0.27 ± 0.03	-9.1 ± 1.0	GRACE method 1
	2003-2009	-0.46 ± 0.07	-15.5 ± 2.4	GRACE method 2
Matsuo and Heki. 2013	2004-2012	-0.11 ± 0.09	-3.7 ± 3.0	GRACE
	2004-2008	-0.20 ± 0.11	-6.8 ± 3.7	
Gardner et al. 2013	2003-2009	-0.20 ± 0.06	-6.8 ± 2.0	GRACE Method A
	2003-2009	-0.13 ± 0.12	-4.4 ± 4.1	GRACE. IceSat

Table 6.4.1. Svalbard-wide long-term net balance using different methods.

6.6 Projections for future climate

To simulate future changes in mass balance, we dynamically downscale projected climate evolution (MPI-ESM-LR, RCP 8.5) for two time slices (1970-2000 and 2070-2100) using the regional climate model COSMO-CLM, with the gap bridged using the STARS method (see Chapter 4). A control simulation, forced by ERA interim re-analysis 2004-2017, is conducted to evaluate the quality of the COSMO-CLM model product; we find that mass balance evolution in good agreement to the carefully field-validated results of Aas et al. (2016) and Østby et al. (2017) (Figure 6.5.1). To assess the impact on glacier mass balance, we determine the change in mean mass balance of each time slice, separated by 100 years.

Given the projected temperature increase in the 21st century, it is not surprising that modelled glacier net mass balance becomes progressively more negative. The winter balance does not have a clear trend; the strong negative trend in net balance is driven entirely by increasingly negative summer balance. That winter balance is largely unchanged in the future simulation indicates that any increase in precipitation in a warming climate is compensated for by a decreasing snowfall fraction.

Comparing the two time periods 1971-2000 (Figure 6.6.2a) and 2071-2100 (Figure 6.6.2b)

shows that the equilibrium line altitude (ELA) rises by on average 400 m, and that there is a 5-fold increase in mass loss (Figure 6.6.3). There is considerable spatial variability in these changes, with more pronounced ELA increases in the northwest and south of Svalbard than in the northeastern region (Table 6.6.1, Figure 6.6.4), but due to the larger glacier area in the latter region, the change in overall mass loss is strongest there. These dramatic findings are derived from a so-called reference mass balance, which assumes no changes in the glacierized area or surface elevation. The net effect of this assumption is difficult to assess since changes in glacier area and surface elevation have opposite effect on the mass balance. The effect of a smaller area is that mass loss would be smaller than in the reference scenario, whereas a lower surface elevation would enhance mass loss, due to the mass balance-elevation feedback. To overcome this limitation, the evolution of glacier geometry changes in response to mass balance changes should be assessed with a glacier dynamics model. While such models exist for temperate mountain glaciers, a realistic application to Svalbard glaciers would require considerable model development to account for the complex behaviour of marine-terminating glaciers as well as for the polythermal structure, both of which are common and abundant features of Svalbard glaciers.
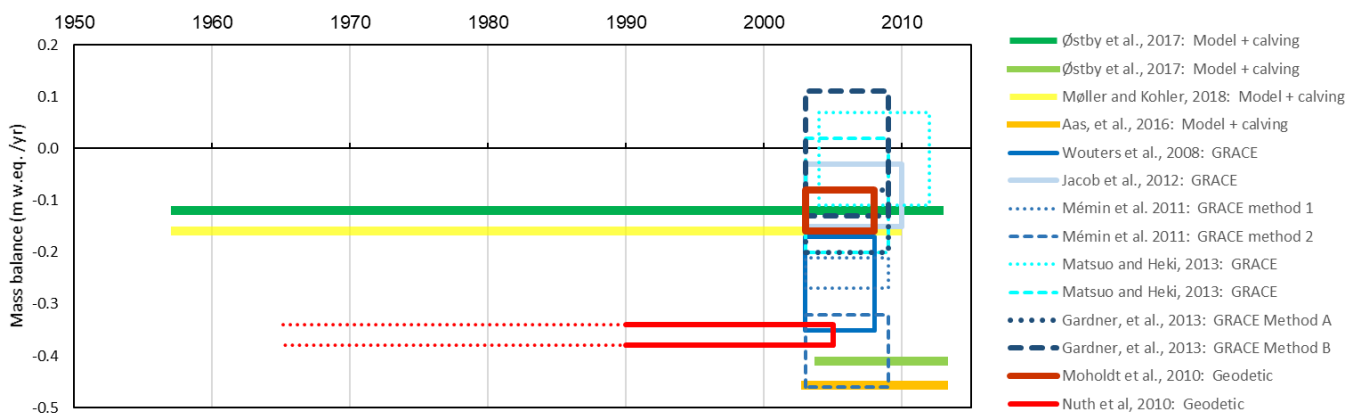
Figure 6.6.1. Svalbard-wide long-term net balance 1950-2010s, using different methods (see Table 6.4.1).
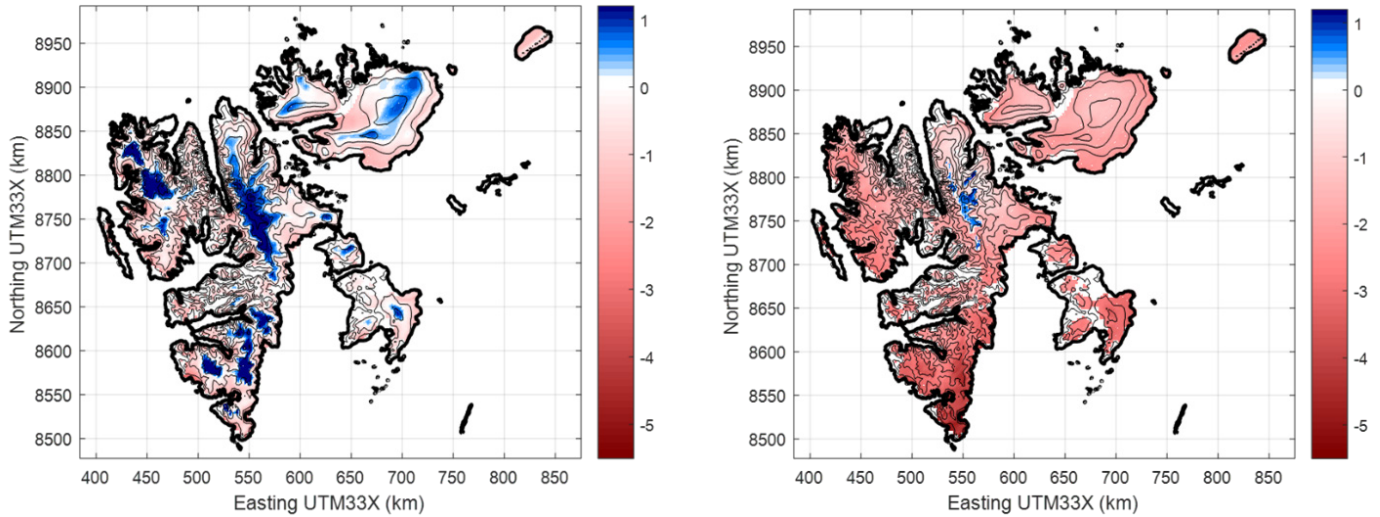
Figure 6.6.2: Mean mass balance (m w.eq. yr^{-1}) simulated for the time periods a) 1971-2000 and b) 2071-2100.
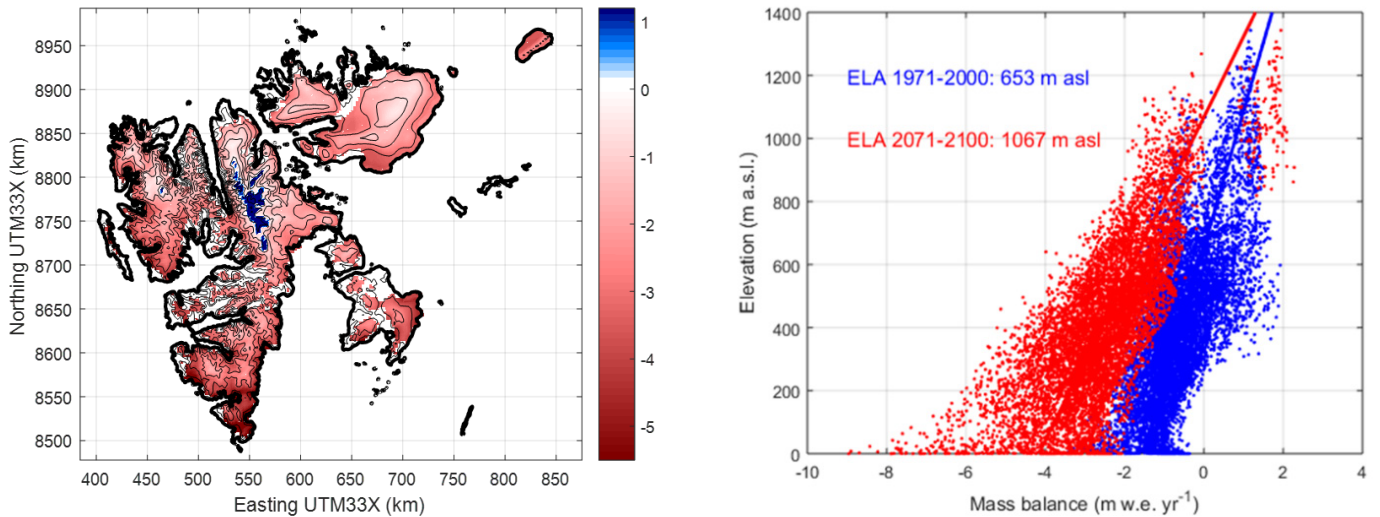
Figure 6.6.3: Change in mass balance (m w.eq. yr^{-1}) between the two time periods 1971-2000 and 2071-2100. a) Spatial change. b) Change as a function of elevation. ELA denotes the mean equilibrium line altitude determined from linear regression.

Furthermore, this simulated mass balance represents only the climatic mass balance and neglects the ice discharge component. The only available estimate of current ice discharge from Svalbard glaciers (Blaszczyk et al., 2009) is a composite of snapshots in the period 2000-2006 and amounts to 5.0-8.4 Gt yr^{-1} (mean 6.75 Gt yr^{-1}), hence, ice discharge is roughly equivalent to the mass loss by climatic mass balance in the same period. This work urgently needs to be updated, especially in light of several large glacier surges (see Chapter 3) which discharged large volumes of ice into the ocean over short periods. One single event, the surge of Ba-

sin-3 from Austfonna, NE Svalbard, has contributed to sea-level change equivalent to about 7 Gt yr^{-1} since 2012 (Dunse et al. 2015), hence doubling the ice discharge from Svalbard. There are some suggestions that increased melt hastens the triggering effect on surges and a number of other large-scale surges events have been reported in Svalbard (Sund et al, 2014) as well as other Arctic regions (e.g. Willis et al. 2018). These events affect the total ice discharge and have the potential to considerably increase the sea-level contribution from land ice within short time.

	Svalbard	NE	NW	S
CMB 1971-2000				
(Gt year^{-1})	-14.23	-7.45	-3.43	-3.35
(m w.eq. year^{-1})	-0.39	-0.32	-0.5	-0.5
CMB 2071-2100				
(Gt year^{-1})	-87.33	-46.77	-16.89	-23.67
(m w.eq. year^{-1})	-2.38	-2.02	-2.47	-3.52
CMB change				
(Gt year^{-1})	-73.01	-39.32	-13.46	-20.3
(m w.eq. year^{-1})	-1.99	-1.7	-1.97	-3.02
(%)	513	528	392	607
ELA 1971-2000 (m a.s.l.)	653	598	854	731
ELA 2071-2100 (m a.s.l.)	1067	976	Above terrain	1337
ELA change (m a.s.l.)	414	378	>414	606

Table 6.6.1: Changes in glacier mass balance between the two time periods 1971-2000 and 2071-2100, for all of Svalbard, and for the three regions NE, NW and S (Figure 6.6.4).
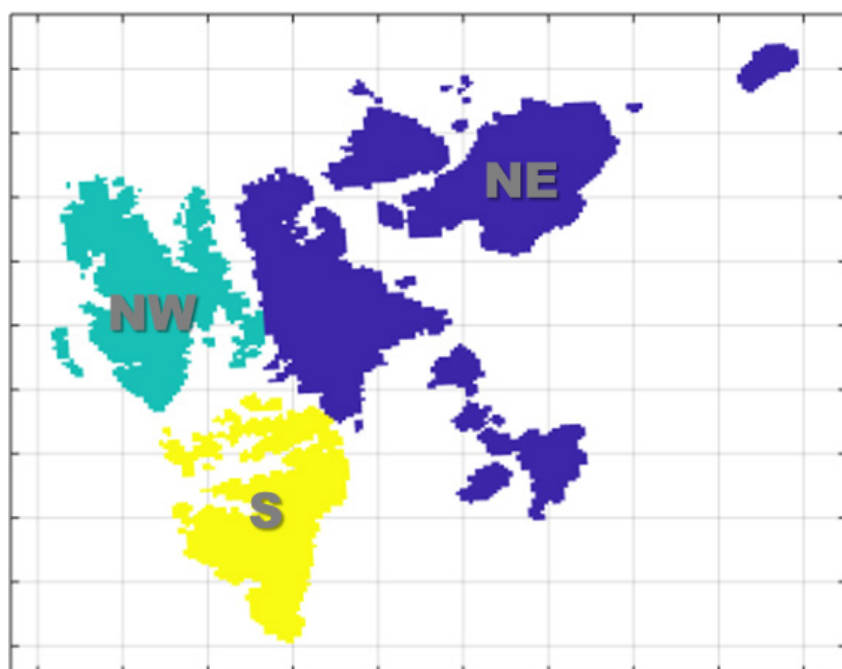
Figure 6.6.4: Svalbard regions used in Table 6.6.1.

The dramatically more negative mass balance is a function of the climate projection; the change in climatic forcing between the two simulation periods is discussed in comparison to the other analysed projections (e.g. Arctic CORDEX, see Chapter 4). Consistent with the observation that the climate simulation for 1970-2000 is on the warm end compared to other members of the ensemble, we find that the simulated 1970-2000 mass balance for Svalbard is more negative compared to other estimates using a variety of methods (Table 6.4.1). For the period 2070-2100, the projected temperature is on the colder end of the ensemble, such that the projected change between the two slices is on the conservative side within the ensemble of considered models (see Box 4.1). Therefore, the mass balance changes projected here most likely are underesti-

mated rather than exaggerated. Internal feedback mechanisms in the glacier system, such as water retention by refreezing or the influence of increased melt on glacier sliding, have considerable impact on the response of glaciers to climate change. In the simulated projection, the baseline period 1970-2000 is too warm, the mass balance too negative, and, as a result, the internal retention capacity is smaller than more realistic representations (e.g. Østby et al., 2017). The projected change of the retention capacity is therefore smaller than that expected, since a good part of the available retention capacity has been reduced; this would lead to even more negative mass balance.

6.7 Gravity

While satellite gravimetry provides an absolute measure of the total mass change in a region, the values obtained still need to be disentangled from crustal changes due to ongoing and long-term isostatic rebound. Regional gravitation change is also prone to "leakage" from regions outside of the area of interest. Furthermore, there are certain technical challenges to the data analysis. A number of groups (Wouters et al., 2008; Jacob et al., 2012; Mémin et al. 2011; Matsuo and Heki, 2013; Gardner et al., 2013) working with the same dataset covering only slightly different periods, but using different data filtering methods, obtain a range of values for the

total mass loss (Table 6.4.1, Figure 6.6.1). However, the main conclusion one can reach from the body of GRACE analysis is that all find a negative mass balance from Svalbard archipelago, with values ranging from -0.46 to -0.09 m w.eq./year, or -15.6 to -3.1 Gt/year (Table 6.4.1), even if the error range for some of the estimates extends into the positive territory (Figure 6.6.1). Nevertheless, the results are consistent with geodetic and modelling estimates (Table 6.4.1, Figure 6.6.1).

7. Permafrost, avalanches and landslides

7.1 Permafrost temperatures and active layer thickness

7.1.1. Background

Areas with permafrost consist of sediment or rock and included ice and organic material, which remains at or below 0°C for at least two consecutive years (French, 2018).

In recent years record-high annual mean ground temperatures (MGT) have been observed at many Arctic permafrost observatories with the largest increases in permafrost temperature since 2000 in the cold permafrost of the Alaskan Arctic, the Canadian high Arctic, and in Svalbard (Romanovsky et al., 2017). Svalbard has the warmest permafrost this far north in the Arctic (Romanovsky et al., 2010). It is typically about 100 m thick in the valleys and 400–500 m thick in the mountains (Liestøl, 1977).

7.1.2 Observed permafrost temperatures and changes since the International Polar Year [IPY]

In general, permafrost temperatures are highest at coastal sites (Kapp Linné and Bayelva), or where a thicker snow cover during the winter occur (Endalen). During the hydrological year 2016-2017 mean temperatures at the ground surface (MGST) ranged between -1.3°C and -4.1°C, while permafrost temperatures, at or close to the depth of zero-annual amplitude (MGT), varied from -2.6°C to -5.2°C, in the monitoring boreholes in the six permafrost observation sites in Svalbard (Table 7.1.1). Differences are attributed to variations in snow cover, landforms, the degree of continentality and ground ice contents. The results clearly show that rather warm permafrost occur in extensive parts of particularly the lowland Svalbard landscape, which
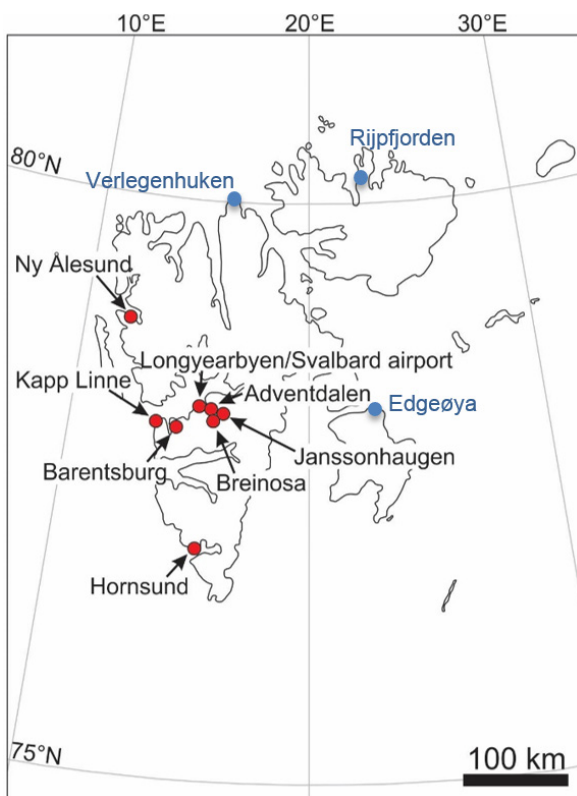
Figure 7.1.1. Location of the active permafrost observations in Svalbard (red dots, Table 7.1.1) and location of additional sites where meteorological stations exist and where permafrost modelling have been performed (blue dots). Figure from Christiansen et al., (2019a).

is especially sensitive to warming, and which is where the population is living. Along the west coast there is a clear gradient from the warmest permafrost in the south at Hornsund -1.1°C (measured at only 2 m depth in the summer), to the coldest in the north at Ny-Ålesund with -2.8°C (Christiansen et al., 2019a).

The permafrost temperature records (Figure 7.1.2) generally show a continuous increase of permafrost temperature in the upper 10-20 m of the ground. Since IPY ground temperatures have increased with rates between 0.06°C (Bayelva and Old Aurora Station 2) and 0.15°C (Breinosa) per year at 10m depth (Figure 7.1.2a) and between 0.07°C (Janssonhaugen P10 and Kapp Linne 1) and 0.08°C (Endalen) per year at 20 m depth (Figure 7.1.2b). On Janssonhaugen a significant temperature increase can be

detected down to 80 m depth reflecting a multi-decadal permafrost warming, with 2017 clearly as the warmest year in the observational record (Romanovsky et al. 2017).

7.1.3 Active layer thickness [ALT] and changes

The thickness of the active layer (ALT), as measured in the autumn 2017 in the two standard CALM grids (see Chapter 3.4) in Adventdalen and at Barentsburg, and in the permafrost boreholes, varied from 49 to 300 cm, but generally fell within the range of 100 cm to 200 cm (Figure 7.1.3; Christiansen et al., 2019a). Thinnest ALT are reported from blockfields at higher elevations and in sediments. Thicker ALT is encountered in bedrock settings.

Location	Borehole name/ ID	2016-17				2008-2009	
		MAT (°C)	MGST (°C)	MGT (°C)	ALT (cm)	MGT (°C)	ALT (cm)
Adventdalen	Old Aurora Station 2	-1.9	-1.3	-5.2 (9.9 m)	94	-5.6 (9.9 m)	90
	Endalen	-1.9		-2.7 (19 m)	190	-3.2 (15 m)	120
	Breinosa	-3.8	-4.1	-5.1 (10 m)	49	n/a	n/a
	Janssonhaugen/ P10	-3.8	n/a	-5.0 (20 m)	n/a	-5.5 (20m)[μ]	170
	Janssonhaugen/ P11	-3.8	-3.7 (0.2 m)	n/a	185	n/a	170
Ny-Ålesund	Bayelva	-2.3	-3.6	-2.8 (9 m)	200	-2.9 (9 m)[π]	180
Kapp Linné	Kapp Linné 1	-1.2	-1.6	-2.6 (20 m)	300	-3.1 (15 m)	250
	Kapp Linné 2	-1.2	-1.6	-2.8 (20 m)	190	-3.2 (15 m)	180

Table 7.1.1. Permafrost monitoring sites with mean ground temperature near or at the depth of zero annual amplitude during the hydrological year 2016-2017 (Christiansen et al., 2019a), and during the International Polar Year (IPY) 2008–2009 (Christiansen et al., 2010) in Spitsbergen.

MAT = mean air temperature of the closest meteorological station); MGST = mean ground surface temperature; MGT = mean ground temperature at the depth of zero annual amplitude (ZAA) if different from total borehole depth or at lower most sensor; ALT = active layer thickness as estimated from interpolating the depth of the 0 °C isotherm. ***Only recorded** during July and August 2017; μ From Romanovsky et al. 2017; π Recorded in 2010 (Boike, et al. 2018)
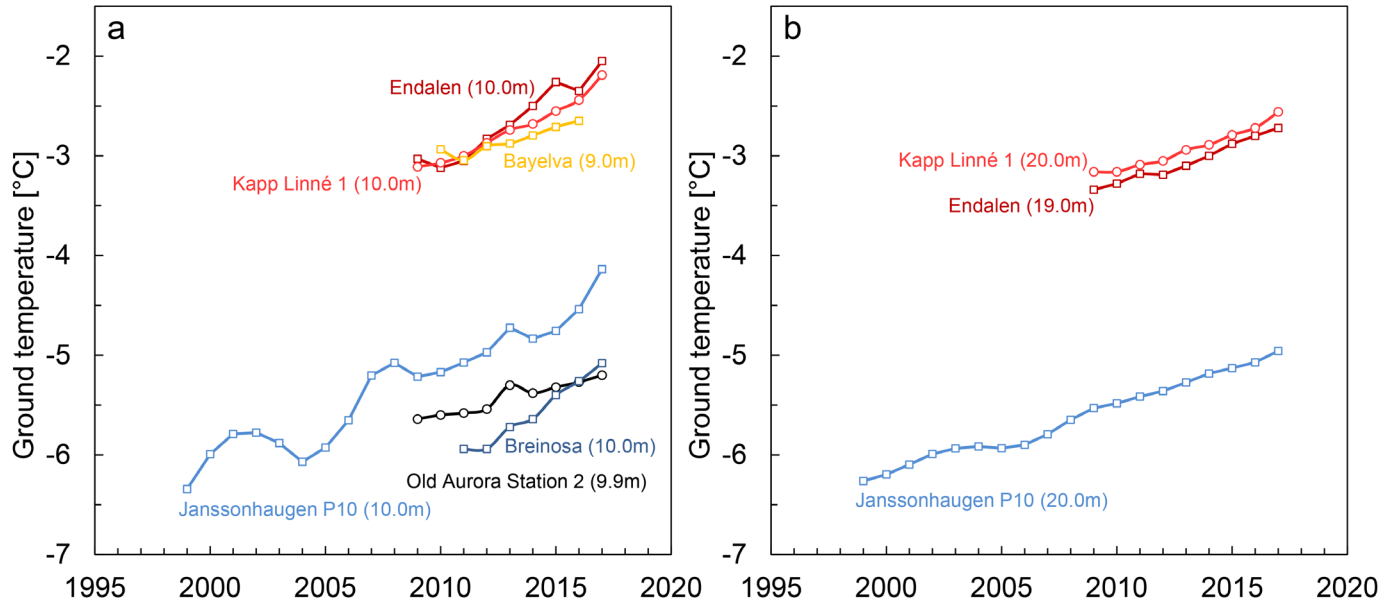
Figure 7.1.2 Annual mean ground temperatures (MGT) during hydrological years at selected permafrost monitoring sites on Svalbard. a) 10 m below the surface and b) at 20 m depth, near or at the depth of zero annual amplitude (ZAA), only available from Janssonhaugen, Kapp Linné and Endalen. Data series are updated from Isaksen et al. 2007a, Christiansen et al. 2010 and Boike et al. 2018.

ALT records from Janssonhaugen indicate a general increase in thickness of 1.6 cm/year between 1999 and 2018. In the sediments of the UNISCALM grid in lower Adventdalen, the average of the 121 point observations, show an increase of on average 0.6 cm/year in ALT from year 2000 to 2017. At Kapp Linne in the bedrock borehole ALT increased by 6.2 cm/year since IPY (2008-2009) to 2017.
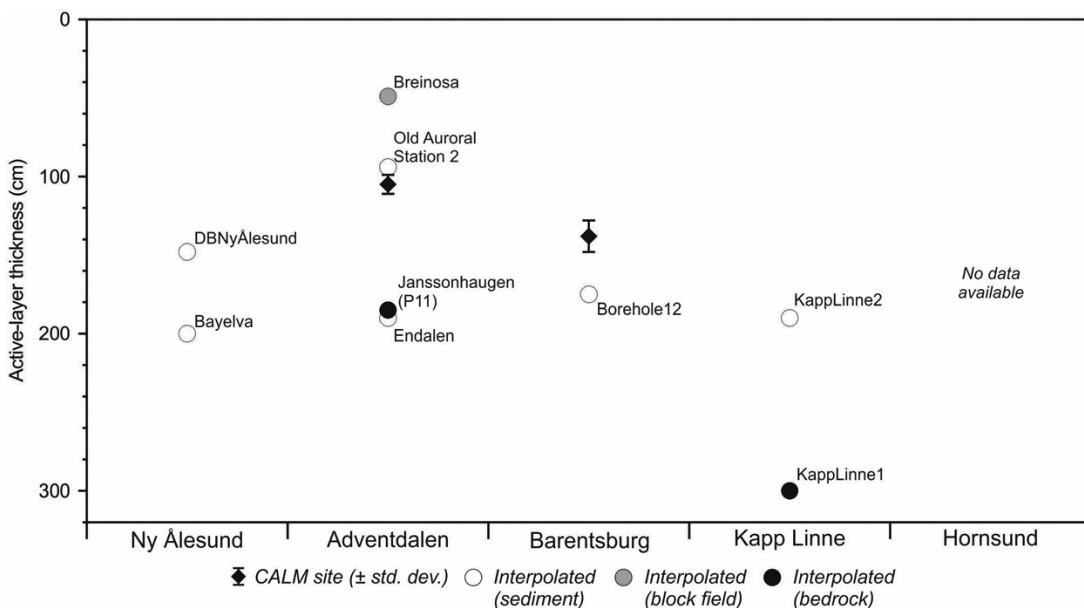
Figure 7.1.3: Active-layer thicknesses recorded at the end of August, 2017 from CALM grids and interpolated from the reported boreholes. The active-layer at the Bayelva site in Ny Ålesund was estimated using the Stephan equation. Note shading denotes substrate type (from Christiansen et al. 2019a).

7.1.4 Projected changes in permafrost temperature

For the period 1971-2000, the COSMO-CLM (CCLM, see Chapter 3.1.4) modelled mean annual 2 m air temperature is about 1.5 °C higher than the observed temperature, and 2.5 °C higher than the Arctic CORDEX model median. Following the emission scenario RCP8.5, the CCLM projects an increase in air temperature of 6.5 °C for the period 2071-2100, while the Arctic CORDEX runs show a median increase of 8.7 °C. Thus, while CCLM shows a smaller increase, both end up at around 2 °C in 2100. This is roughly two degrees higher than the Arctic CORDEX RCP4.5 runs and the forcing data used in previous modelling efforts by

Etzelmüller et al. (2011; see below), which is from a multi- General Circulation Model (GCM) ensemble based on Coupled Model Intercomparison Project CMIP3 (Meehl et al., 2007), using the A1b Special Report on Emissions Scenarios (SRES). We emphasize that the modelling procedure is in line with previous modelling efforts, (e.g. Etzelmüller et al., 2011), but does not take a range of crucial processes into account, such as wind redistribution of snow, or spatial patterns of soil moisture caused by lateral flow of water or excess ground ice layers. Furthermore, the model runs employ a standard soil stratigraphy typical for moraine materials (Westermann et al., 2013), which cannot do justice to site-specific variations in organic and ground ice contents.
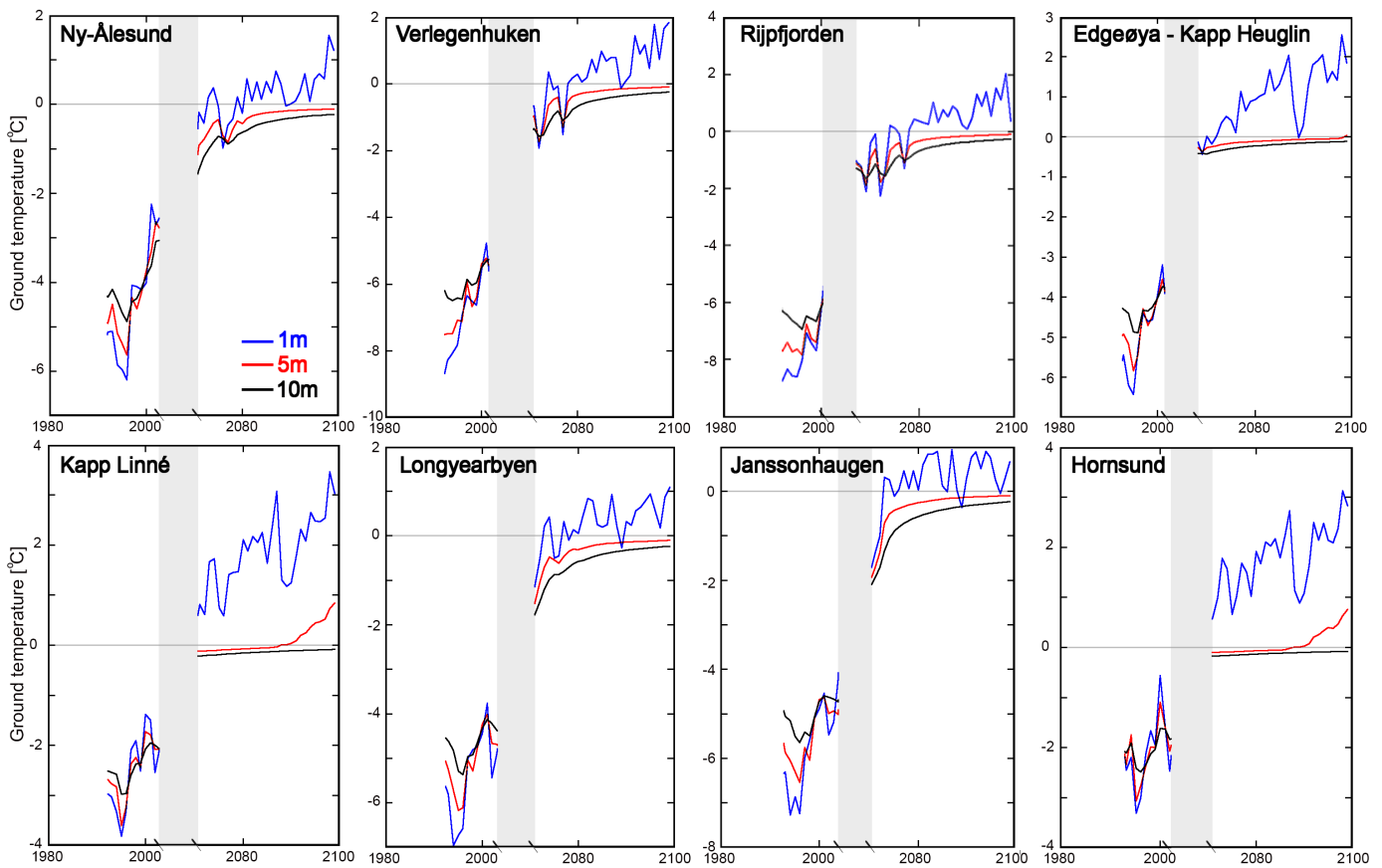
Figure 7.1.4. Permafrost temperature modelling results for 1 m (light blue), 5 m (red) and 10 m (dark blue) depth for selected sites on Svalbard where active permafrost observations exists and/or meteorological stations exist (see Figure 7.1.1). Note that while the CCLM data are only available for two time slices, 1971-2000 and 2071-2100, the CryoGrid 3 simulations are run by a continuous forcing from 1971-2100, with data synthesized from the two time slices used to fill the gap in between. Since this does not correspond to a physically-based projection driven by an Earth System Model, we only show results until IPY-period (2008-2009) and between 2071-2100. Furthermore, the model results in the first 20 years are strongly influenced by the selected initial condition, so that only results after 1990 (approximately the period for which measurements for validation are available) are shown.

Modelled ground temperatures (Figure 7.1.4) are generally in the range of in-situ observations for the IPY-period (Table 7.1.1), although the coarse model set-up does not allow representing the site-specific ground thermal regime. At all modelled sites, near-surface permafrost is projected to thaw before the end of the present century, with some sites in western Svalbard developing a talik to a depth of several meters, while permafrost still persists at 10 m depth and below. The modelling suggests that this development will be initiated first at sites, which today already feature high ground temperatures, such as Kapp Linné and Hornsund. While northern sites like Verlegenhuken and Rijpfjorden are projected to have permafrost until the 2080s, a general degradation trend and talik development is underway in 2100 as well.

Previous modelling results for the end of the century (Etzelmüller et al. (2011)) for some of the permafrost monitoring sites in Svalbard (Kapp Linné, Janssonhaugen and Endalen) revealed the following major effects towards 2100: 1) A significant warming (ca. +4°C) in the near-surface layers (<10m depth). 2) A varying ground temperature increase depending on the ice/water content and the present permafrost thermal state. 3) Warming rates are efficiently reduced where the temperature is close to 0°C, and where ice is present due to the consumption of latent heat for melting. 4) The median ground temperatures at the depth of zero annual amplitude (ZAA) is suggested to increase by 2–4°C through the period 2000-2100. 5) Over the same period, ALT increases at all sites. Model results show degradation of permafrost in bedrock sites at low elevations. Contrarily, in sedimentary landforms with a relatively high water/ice content, permafrost conditions continue to exist until 2100.

Recent ground thermal calculations by Instanes and Rongved (2017) for three different locations in Longyeardalen (the Svalbard Science Centre, the town center and Skjæringa) based on recent regional climate model runs using the RCP4.5 scenario suggest an increase in ALT, from about 1.5 m today to 2.5 m by the end of the century. Due to high ice content in the fluvial material and silt and clay-dominated marine sediments, warming rates

are efficiently reduced due to the consumption of latent heat for melting. By 2100, the calculations suggest that the temperature at 20 m will still be at -2 to -3°C.

In general, all modelling results are consistent, taking into account the different forcing data, geographical locations and ground properties. The limit between "permafrost remains (at least partly)" and "near-surface permafrost disappears entirely by 2100" is suggested to be somewhere between the RCP4.5 and RCP8.5 scenarios for most of the lowland landscape in western Svalbard.

7.1.5 Permafrost responses to climate changes

Although the modelling results suggest that there will still be permafrost below 5 m depth in most sites after 2100, increases in the active layer thickness and permafrost temperature, will for buildings and structures, in general, lead to strength deterioration and deformation, potential accelerated settlements and possible foundation failure (Instanes, 2003). Therefore, an evaluation of these effects must be taken into account in future planning, design, construction and maintenance of buildings and structures on Svalbard (Instanes and Rongved, 2017). For the landscape and in particular for the slopes on Svalbard the observed and projected near-surface permafrost warming and increase in active-layer thickness may in certain areas be associated with large-scale thaw settlement as ice-rich soils in the upper permafrost layer thaw. One consequence is a marked increase in slope instability (e.g. Harris et al. 2001; Haeberli et al. 2010; Chapter 7.3). While permafrost in steep bedrock slopes has not systematically been investigated in Svalbard, permafrost warming and thawing may also strongly affect rock stability and can trigger potentially hazardous rockslides (e.g. Haeberli et al. 2010; Chapter 7.3).

Recent measurements of temperatures in vertical rockwalls near Ny-Ålesund conducted from 2016-2018 (unpublished data, University of Oslo) suggest that ground temperatures in coastal cliffs can be even higher than in adjacent inland boreholes, most likely also influenced by the lack of sea ice at the

investigated sites. Such warming and thawing permafrost can affect coastal dynamics (e.g. Romanovsky et al., 2017). Along the coastal mixed cliffs at Vestpynten, close to Svalbard Airport, coastal erosion of the cliffs due to permafrost degradation have been identified as largely controlled by nivation processes (primarily erosion by meltwater from snow patches located at the lee side of the coastal cliffs) (Guégan and Christiansen 2016). Coastal erosion is largest where the coastline consists only of sediments, whereas the mixed coasts (sediment on top of bedrock) and the bedrock coasts are less exposed to coastal erosion. Coastal erosion is locally also controlled by both wave action and the duration of the sea ice cover.

7.2 Solifluction

Slowly deforming active layers moving downslope due to gravity, in the form of solifluction sheets and lobes, are widespread on the lower slopes in the Svalbard landscape (Figure 7.2.1; Harris et al., 2011; Matsuoka et al., 2004; Sørbel and Tolgensbakk, 2002). Harris et al. (2011) used several years of detailed solifluction process observations in the lower slopes of the Endalen area next to Longyearbyen to show how active layer thickening causes increased solifluction movement. Matsuoka et al. (2004) expected active layer thickening to trigger temporary, but episodic ground movements, causing extensive solifluction, in areas where the top permafrost is ice-rich. In areas with one-way freezing of the active layer, future temperature increases are seen as unlikely to significantly affect solifluction (Matsuoka, 2001) when temperature effects are considered isolated from other changing parameters, such as precipitation. However, winter warm events (including "rain-on-snow") were found to lead to increased ground temperatures in a solifluction lobe in the Endalen area down to two metres depth (Strand, 2016). Increased numbers of such warm winter precipitation events (Vikhamar-Schuler et al., 2016) might therefore affect solifluction rates. Consequently, it is important to take also solifluction processes properly into account during the design and construction phases of new infrastructure.

Figure 7.2.1 Solifluction is evident in Longyearbyen where posts formerly used as foundations of houses have tilted downslope (Photo J. Alean, Swisseduc.ch)

7.3 Avalanches and landslides

7.3.1 Classification and triggering mechanisms

Different types of snow avalanches and landslides are the dominant slope processes in cold climatic landscapes of moderate to steep terrain consisting of various types of sediments and rock types. These parts of the landscape are typically snow covered for most of the year.

Avalanches and landslides can be classified in various ways depending on both the type of movement (fall, slide, flow) and the type of material. We use here a classification based on Norem & Sandersen (2012) which differentiates processes depending on the relative proportions of rock and soil, water, snow and ice (Figure 7.3.1).

Snow avalanches are – depending on the water content of the snow – classified into dry snow avalanches, wet snow avalanches and slushflows.

As opposed to dry and wet snow avalanches, which normally occur in steep slopes, slushflows can occur on slopes from 2^0 to 20^0, i.e. they can be initiated in relatively flat terrain and can have long runouts. Landslides range from rockfalls, debris slides (coarse material), debris flows (coarse material and high water content) and earth slides (fine material) to mudflows (fine material and high water content) and quick clay slides. Another typical landslide phenomenon in arctic environments with permafrost is active layer detachment. Quick clay slides typically occur in relatively flat terrain in lower lying areas below the upper marine limit (former seabed). Such slides are not common in permafrost areas as the low temperatures in the ground give increased strength and significantly increase the remoulded shear strength. However, slides resembling quick clay phenomena can occur in the upper active layer during thawing.
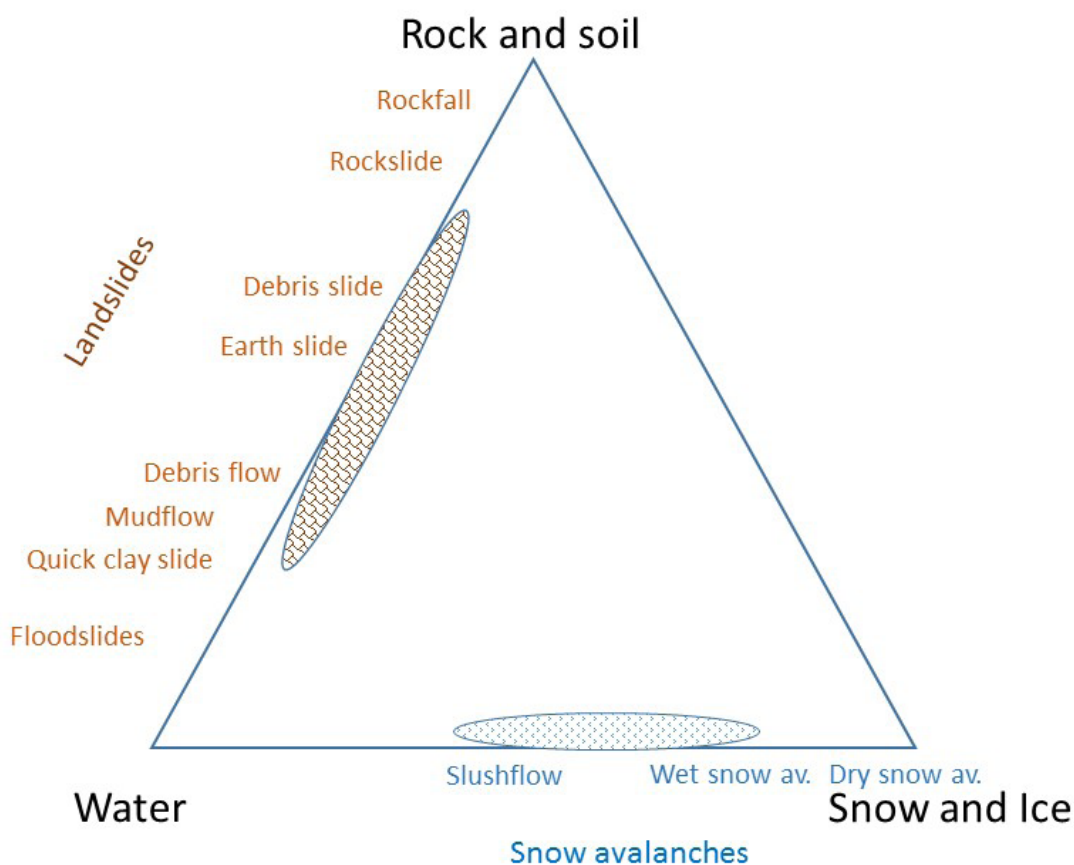
Figure 7.3.1: Classification of avalanches and landslides (Modified from Norem and Sandersen, 2012)

Snow avalanches (Figure 7.3.2) can also be classified according to their morphology/form into loose snow avalanches, slab avalanches, cornice fall avalanches and glide avalanches. Loose snow and slab avalanches both may consist of dry or wet snow. A loose snow avalanche is a mass of snow that originates at a single point on a slope and gathers more loose snow as it descends. In Svalbard, slab avalanches often form from deposited fresh snow in combination with wind (Eckerstorfer & Christiansen, 2011a). They are released when the stress of a cohesive slab of snow exceeds the strength of an underlying weak snow layer. To trigger a slab avalanche, either an additional load, such as new or wind accumulated snow or a weakening of the underlying snow, is needed. A skier, snowmobile or other mechanical loading can also trigger slab avalanches. Break-off of cornices is an additional documented threat.

Cornices form by wind blowing snow over, for example, the crest of a mountain. They are often overhanging, can break off unexpectedly and, once released, may trigger larger avalanches in the slope underneath (Hestnes & Lied 1991; Hestnes & Bakkehøi 2003; Eckerstorfer & Christiansen, 2011a; Vogel et al., 2012). The Svalbard topography, with large plateau-like mountains, provide ideal accumulation areas for wind-drifted snow, which is deposited at the edge of the plateaus as cornices. Many of the cornices are thus located above steep slopes, where secondary avalanches could be triggered by the additional load of the cornice falling or the cornices themselves may run far into valleys. The formation of cornices depends on the terrain, the quality and amount of snow in catch areas and the direction and strength of the wind fields. Glide avalanches are released after a period of gliding along

Figure 7.3.2 Avalanche at Fritham March 2015, Photo: Odd Magne Kvålshagen

the ground, typically after developing glide cracks in the release area and on ground surfaces with low friction (bare bedrock or smooth grass).

In Svalbard, small amounts of snow in combination with relatively low temperatures typically give a shallow snowpack with a high vertical temperature gradient. This combination is ideal for the development of persistent weak layers in the snowpack and, consequently, the formation of slab avalanches, which can occur when these weak layers are buried under new snow and/or under accumulating snowdrifts. Snow in Svalbard is particularly exposed to redistribution by wind because of the sparse vegetation and relatively smooth surfaces; hence, cornices and wind packed slabs form easily. In addition, occasional passages of low-pressure atmospheric systems associated with positive temperatures in the winter, heavy precipitation and high wind speeds have triggered both avalanches, slush flows and landslides (e.g. Eckerstorfer & Christiansen, 2011b).

The terms rockfall and rockslide are often used interchangeably, but can be distinguished according to size. According to NGI (2018) rockfalls consist of smaller, individual blocks (up to 100 m3), and rockslides have a larger volume (up to 100 000 m3). Both types have source areas in steep terrain, generally with a slope greater than 30⁰-40⁰. Smaller rockfalls can be triggered by freezing and thawing. Large rockslides typically result from long-term geological processes, but weather can be involved in the triggering of such events. In Svalbard, shear stress induced by ground freezing are important in splitting bedrock as ice lenses grow in fractures. Rock and stones thus undergo erosion and fall down mountainsides due to gravity as rockfalls,

Figure 7.3.3 Landslide west of Carolinedalen north of Longyearbyen, august 2016 Photo: Lufttransport

building up large colluvial fans or talus slopes (His-dal, 1998). Avalanches can also transport rocks that are plucked from bedrock free faces in their source areas (Vogel et al., 2012; Eckerstorfer et al., 2012). Deposits from avalanches, slushflows and landslides typically in the form of avalanche and debris fans provide direct evidence of such processes being active on mountainsides.

Landslides (Figure 7.3.3), primarily in the form of active layer detachment slides in sloping terrain can be triggered by heavy rain in permafrost landscapes (Christiansen et al., 2019b). Smaller more shallow landslides are also triggered by heavy rain. Perma-frost lowers the precipitation threshold for debris flow initiation, but limits debris flow volumes (de Haas et al., 2015).

Debris flows and slushflows have occurred infre-quently, but regularly, over the last 2000 years, based on evidence from lichenometry in Svalbard (André, 1990). In a new study, Berhardt et al. (2017) analysed a debris fan located close to Long-yearbyen and found that the recurrence period for debris flows is a few decades. This agrees with the expected accelerated mass wasting in an increasing-ly warmer Arctic.

7.3.2 Avalanche and landslide events

From the previous sections, we can conclude that there are "favourable" conditions for avalanches and landslides in Svalbard. In addition, increas-es in the commercial, research, educational and recreational activities during the past fifty years, particularly in the Longyearbyen area, have had an impact on peoples' exposure to natural hazards, especially to snow avalanches. Population and tourism have grown considerably since the 1960s and, consequently, the number of people involved in backcountry activities has strongly increased. Hu-man triggered slab avalanches seem to cause most fatalities among recreational backcountry skiers and snowmobilers, while naturally triggered avalanches are the main threat to infrastructure, transport routes and residential areas.

The slushflows from Vannledningsdalen in Long-yearbyen often occurring during the spring thaw are

well known (Chapter 10.3.2). In 1953, a slushflow killed three people and many were injured. Both in 1989 and 2012 slushflows damaged infrastructure. In 2012, slushflows occurred in the mid-winter after a warm spell and heavy rainfall (Hansen et al. 2014). At another location, Liedfjorden, in 1992, several persons were hit by a slushflow and one person died.

Snow avalanches are frequent and have caused sev-eral fatalities in Svalbard (Chapter 10.3.2). Many fatal avalanches have been snowmobile triggered, but in December 2015, two people died when a large slab avalanche from the ridge north of Suk-kertoppen destroyed ten houses in Longyearbyen. In 2017, another avalanche from Sukkertoppen triggered a secondary avalanche that reached the settlement. Several buildings were damaged, but there were no fatalities.

As a consequence of large rainstorms, debris flows and slides have caused damage to the local infra-structure in the lower Longyeardalen valley (in July 1972) and in Longyearbyen (October and Novem-ber 2016). The November 2016 event also triggered numerous snow avalanches, which were mapped from Sentinel-1 satellite radar images (Figure 7.3.4; https://titan.uio.no/node/2009).

7.3.3 Climate change effects

Because meteorological factors are important trig-gers for landslides and avalanches, future climate change will affect their frequency and type. As de-scribed in Chapter 4.1, the temperature in Svalbard has increased and the winters have warmed more than the summers. Precipitation trends are less clear, and this may partly be caused by an increased frac-tion of precipitation falling as rain at the observa-tion stations. In particular, wintertime rainfall events have increased (Chapter 4.3 and 4.4), and rain on snow may cause more unstable snow layers with implications for avalanches throughout the winter. Regional projections for the Nordic Arctic for the 21st century show continued increase in temperature and precipitation. They also indicate a significant enhancement of the frequency and intensity of win-ter warming events (Vikhamar-Schuler et al., 2016), with an increase in the frequency of autumn and
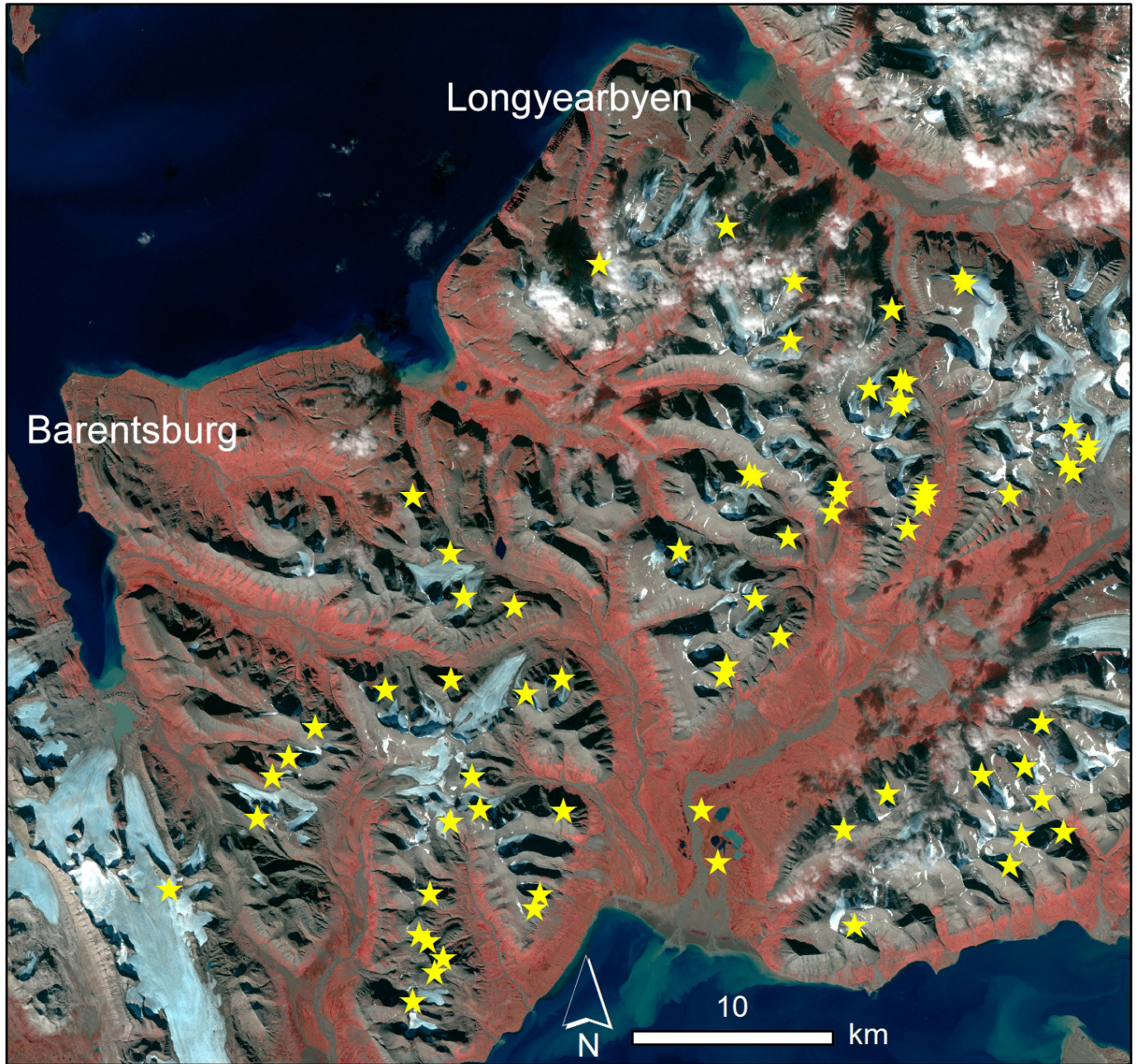
Figure 7.3.4 Snow avalanches in November 2016 (yellow stars) mapped from Sentinel-1 satellite radar images. The background is an optical satellite image from August 2016 taken by Sentinel-2. No optical satellite images are available during the winter (polar night), but radar images enable year-round mapping of avalanches and landslides. (Processing and mapping: Andreas Kääb, University of Oslo; Satellite data source: Copernicus Sentinel data 2016).

winter rainstorms. Snow conditions are described in Chapter 5.2, and show that for the period 1958-2017, snow-cover duration has decreased, whereas the maximum annual snow storage has increased. The computed future snow conditions show a continued decrease in the mean annual snow-cover duration for all the regional projections. The results for maximum annual snow storage vary in time and space and depending on emission scenario. In general, an increase is expected at higher altitudes in northwestern and eastern regions, whereas a decrease is seen at lower altitudes and in coastal areas. An exception is the high emission scenario (RCP8.5) towards the end of the century, where less snow is modelled for most of Svalbard. No significant changes in wind conditions are expected in the future, neither magnitude nor direction (Chapter 4.5).

Ongoing snow avalanche research has a focus on measurement techniques, process understanding and improved regional and local avalanche forecasting. It encompasses studies of snow accumulation, snowdrift including spatial variability of snow height and the mechanical properties of the snow pack in Svalbard. Fewer publications assess the effects of future climate change on various types of avalanches and landslides in Svalbard. Based on our understanding of processes, however, it is generally assumed that increasing temperature and precipitation, both as snow and rain, will increase the frequency of all types of avalanches and landslides in the coming decades. Given that wind direction and magnitude will undergo minor changes under a future climate (Chapter 4.5.2), the present wind controls on the location of snow avalanches will also be valid in the future.

In a changing climate where, in particular, the shoulder seasons are changing towards warmer conditions and increasing the length of the potential period for increased slope activity in the autumn, an improved understanding of slope processes is necessary for developing appropriate observation systems to assist local authorities in handling future rain- and snowstorm-geohazards in permafrost landscapes.

In a warming climate, the permafrost can warm (Chapter 7.1) and lead to a thicker active layer, both of which can cause a decrease in slope stability. Such changes cause a longer period of the year in which the ground is thawed and hence longer periods for active layer detachment sliding. It can also cause increased sliding due to the melting of ice in the top permafrost at the end of warm summers and into the autumn before ground freezing starts (Christiansen et al., 2019a). The control of permafrost on large-scale rockslides is complicated, and direct climate change effects depend on the variation in air temperature, precipitation and wind through the year (Gruber & Haeberli, 2007; Blikra & Christiansen, 2014).

The following evaluation of the effect of climate change on avalanches and landslides in Svalbard is qualitative. It is based on the climate projections described in Chapter 4.

Snow avalanches: Svalbard, with its cold, dry and windy climate has favourable conditions for dense snow packs with frequent occurrences of cornice and slab snow avalanches. It is much debated whether increasing temperatures and precipitation would lead to a more stable or less stable snowpack and, hence, to an increased or decreased probability of dry snow avalanches by the end of the century. The climate projections indicate increased precipitation. In particular, if more extreme events with heavy snowfall or heavy rain on snow occur, an increase in the occurrence of snow avalanches (including wet snow avalanches and slushflows, like in 2012) can be expected. Towards the end of the century, gradually increasing temperatures may lead to a substantially shorter snow season and reduction in the maximum annual snow amounts in particular in coastal low altitude areas (Chapter 5.2.2), and the snow line will gradually shift to higher altitudes. Over time, these factors are expected to decrease the probability of dry snow avalanches. However, the probability of wet snow avalanches and slushflows is expected to increase. Glide avalanches are not common in Svalbard in the present day climate, but may become a problem at some locations in a future warmer and wetter climate.

Rockfalls: The outermost meters of free rock faces are subject to annual freeze-thaw cycles and plucking by snow cornices, which adversely impacts rock wall stability. Smaller rockfalls are often triggered from these areas. Rising temperatures can lead to more freeze-thaw events (Chapter 4.2.3), and therefore rockfall events may increase in the future.

Rockslides: Rockslide stability is partly permafrost dependant and a warming climate may adversely affect the stability. Studies from Northern Norway (Blikra et al. 2015; Frauenfelder et al., 2018) show that increasing temperatures leading to degradation of permafrost may play an important role in the detachment of larger rockslides. There are no published studies on the effect of permafrost on rockslides in Svalbard.

Landslides: Increased air and permafrost temperatures will increase the length that the active layer will be thawed annually and the thickness of the active layer will increase. This can increase the probability of various types of landslides in the active layer. In addition, increased precipitation and extreme rainfall in sloping terrain will increase the likelihood of all types of landslides. Another very important effect is the thawing of the icy transient layer (top of the permafrost) in a future climate, in combination with strong precipitation events as rain, instead of snow, in late fall. The transient layer can be very ice-rich. It takes much energy to thaw it, and therefore it acts as a "buffer" against permafrost thaw. However, when parts of it start to thaw, the soil in these layers will have a very high water content and, consequently, the friction at the interface with the soil layers below the transient layer will decrease. An increasing frequency of strong precipitation events in the autumn, when the active layer depths are at their maximum, would then inevitably lead to a rise in landslide activity.

Quick clay: Increasing active layer depths and thawing permafrost will significantly reduce the undisturbed and remoulded soil shear strengths, which can lead to more quick clay-like slides in the future.

8 Ocean, acidification, sea ice and sea level

Knowledge about the marine climate around Svalbard is based on combinations of observations and model studies for the past, present and future climate. For the past and present, the historical climate is reconstructed from paleoclimate proxy data and instrumental records, while the future climate is based on simulations from climate models forced by known external forcing and different projections of greenhouse gas emissions.

8.1 Past, present and future climate around Svalbard

An introduction to the role of the large-scale ocean circulation for the ocean climate and sea ice variability around Svalbard was briefly given in Chapter 2 and is summarized in Figure 8.1.1.

During the past few decades, the Arctic has warmed approximately twice as rapidly as the entire Northern Hemisphere (Serreze and Barry, 2011; Francis and Vavrus, 2012; Stroeve et al., 2012). In Svalbard, the warming during winter has been particularly strong over recent decades, with an increase in winter temperature of 2– 3°C per decade at Svalbard Airport (Førland et al., 2011). The essential atmospheric processes controlling the climate in Svalbard are the large-scale transfer of heat and moisture from lower latitudes, which is strongly controlled by cyclones (Førland et al., 2011). Recent changes in these large-scale atmospheric circulation patterns have brought warm Atlantic Water from the West Spitsbergen Current onto the West Spitsbergen Shelf and further into the fjords even during winter (Cottier et al., 2007; Nilsen et al., 2008; Pavlov et al., 2013; Nilsen et al., 2016, Tverberg et al., 2018). This has halted sea ice from forming and opened up large areas of ice-free waters west and north of Svalbard (Cottier et al., 2007; Tverberg et al., 2014; Onarheim et al., 2014) with a potential impact on the Arctic ecosystem (Hegseth and Tverberg, 2013). More frequent episodes of Atlantic Water intrusion in Arctic regions support the establishment of a number of boreal species, for example, the blue mussel (Berge et al., 2005).

8.1.1 Sea-ice around Svalbard through geological time

Sea ice has been present in the Arctic Ocean at least since the mid Eocene, 47.5 million years ago, from when sea ice associated diatoms and ice rafted debris are found (Stickley et al., 2009). During the last interglacial (Eemian, ~125,000 years ago) when the Arctic was warmer than today, summer sea ice existed in the central Arctic Ocean, but sea ice was significantly reduced North of Svalbard due to inflow of Atlantic Water (Stein et al., 2017; Risebrobakken et al., 2007). During the last glacial (30,000–19,000 years ago), sea ice advanced and retreated in the Fram Strait west of Svalbard, where a perennial sea ice cover existed only from 19,000 to 17,500 years ago (Müller et al. 2009; Müller and Stein, 2014).

Around the beginning of the Holocene (~12 000–10,000 years ago), seasonal sea ice occurred west of Svalbard and the sea ice margin was likely located north of Svalbard (Müller et al. 2012, Müller and Stein, 2014). There was thus less sea ice than at preindustrial times in this region largely due to a warmer ocean (e.g. Mangerud and Svendsen, 2017). Throughout the Holocene (10,000 years ago to present), the (spring) sea ice cover gradually increased along the continental slope west of Svalbard due to a lowering of Northern Hemisphere insolation and decreasing temperatures (Müller et al. 2012). East of Svalbard, in the Barents Sea, the sea ice evolu-

tion was comparable throughout the Holocene. A reduced seasonal sea ice cover compared to present characterized the early Holocene. Sea ice increased towards the late Holocene, when the sea ice margin shifted south of Svalbard (Berben et al. 2017). In Storfjorden, near-permanent sea ice prevailed between 2800–500 years ago (Knies et al. 2017), but generally a coastal polynya with seasonally variable sea ice conditions have occurred since 6,500 years ago.

During the early Holocene, the climate of Svalbard was considerably warmer than at present. This warm period is well-documented in both terrestrial and marine geological records. The early Holocene climate was largely driven by higher summer insolation and changes in the influx of Atlantic water and feedback processes that amplified the warming in the Arctic. The mollusc fauna of Svalbard has been studied quite extensively as it contains clues to past warm climates on Svalbard. A larger number of mollusc species are found in early Holocene raised beached deposits. The majority of these species are still living along the Svalbard coast and in the fjords of Spitsbergen. However, a few, so-called thermophilic species, that are found in deposits in Svalbard are now extinct (Feyling-Hanssen, 1955). The geographical distribution of these molluscs through time provides useful information on the regional paleoclimate (Mangerud et al. 2017). The distribution of thermophilic molluscs trough time further suggest that the climate cooled somewhat after the first warm period which lasted from 11 000 to 9000 years ago. Still, between 8 200-6 000 years ago shallow water temperatures off Svalbard where about 4°C warmer than today.

Subsequently, water temperature cooled to present-day values at about 4500 years ago. Beierlein et al. (2015) reconstructed the early Holocene seasonal water temperature cycle in Dicksonfjorden based on stable oxygen isotope profiles in shells of *Arctica islandica*, another thermophilic species found in the early Holocene raised beach deposits on Svalbard. Their results suggest that the early Holocene seasonality was about 12.4 °C, which is about twice that of the modern seasonal amplitude 6°C. Interestingly, one of the previously extinct molluscs

re-appeared at the west coast of Spitsbergen in around the year 2000 suggesting that an unusually high northward mass transport of warm Atlantic water resulted in elevated sea-surface temperatures along the west coast of Svalbard at that time (Berge et al., 2005).

8.1.2 Present climate

As described in Chapter 2, the internal variability is expressed on decadal timescales in the Nordic and Barents Sea. This implies that the waters around Svalbard is governed by different, but not necessarily independent, mechanisms and processes such as the Atlantic Multidecadal Oscillation (AMO) and the North Atlantic Oscillation (NAO). This again may give rise to propagating heat and freshwater anomalies between the Atlantic and Arctic basins. On top of this natural variability comes the anthropogenic warming, which implies that future warm periods will on average be increasingly warmer and that future cold periods on average will be less cold than today.

The temperature and salinity of the inflowing waters to the Nordic Seas and to the Svalbard region have been particularly high after around 2000 (Figure 8.1.2, Onarheim et al., 2014; González-Pola et al., 2018; Tverberg et al., 2018). High recent Atlantic Water temperatures around Svalbard reflect those in the North Atlantic recorded as positive values of the Atlantic Multidecadal Oscillation (Sutton and Hodson, 2005). Over the last 100 years the wind forcing (NAO) also explains a large part of the temperature variability along the Atlantic inflow pathway (Muilwijk et al., 2018). Årthun et al. (2017) and Langehaug et al. (2018) show how anomalies from the North Atlantic propagate with the Atlantic Water into the Nordic Seas, along the Norwegian coast into the Barents Sea through the Barents Sea Opening and into the Arctic through the Fram Strait with the West Spitsbergen Current. Reduction and thinning of sea ice north and east of Svalbard in recent years is consistent with global warming and have likely lead to more wind-generated upward mixing of warm and saline Atlantic Water from about 200 m depth, preventing formation of sea ice (Ivanov et al., 2016). As this warm and saline water is cooled by the atmosphere, it gets heavier and

sinks in a convection process that brings up more Atlantic Water to the surface. In 2011, 2012 and 2013 such a process likely prevented sea ice formation during autumn and winter in large parts of the western Nansen Basin north of Svalbard. Such big anomalies in the sea ice extent create large air-sea fluxes between the relative warm ocean and the cold atmosphere during winter and have together with anomalous weather conditions (Binder et al., 2017) given many extreme high temperature events recent years. The different large-scale processes contributing to this anomalous situation is illustrated in Figure 8.1.1.

Episodes of Atlantic Water intrusion on the West Spitsbergen Shelf represent an increased oceanic heat flux into the fjord systems and toward the glaciers. Currently there is enormous interest and activity in investigating the role of ocean heat on the stability of ocean terminating glaciers (Luckman et al. 2015). Propagation of warm oceanic waters into fjords, with the potential to increase the melt rates of glaciers, has been identified as a likely mechanism leading to the acceleration, thinning, and retreat of glaciers (Straneo et al. 2010; Inall et al. 2015; Luckman et al. 2015). Recently, increased understanding of important exchange processes between the oceanic heat source in the West Spitsbergen Current and the Svalbard Shelf have been achieved. Characteristics of the water masses in the West Spitsbergen Current are transferred to the coastal shelf and fjord systems by wind generated cross-shelf exchange (Cottier et al., 2007, Inall et al., 2015, Nilsen et al., 2016, Tverberg et al., 2018). Ekman transport and pumping together with variable horizontal density gradients on the continental shelf, caused by the surface heat flux, are likely to give rise to frontal instabilities (Saloranta and Svendsen, 2001) that start a residual overturning circulation across the shelf edge front (Tverberg and Nøst, 2009).

Eddy activity along the shelf edge front is essential for residual overturning to take place (Tverberg and Nøst, 2009), and moreover, there must be some degree of topographic steering to bring the Atlantic Water from the shelf edge to the inner shelf (Nilsen et al., 2016). The continental shelf adjoining the west coast of Spitsbergen is complex, with alternating shallow banks (50–100 m depths) and deep

troughs (200–400 m depths) cutting across the shelf. Model results, compared with observations have shown that the deep Isfjorden Trough (Isfjordrenna) have a significant signature on the mean circulation (Nilsen et al., 2016) owing to the tendency to conserve potential vorticity. The Atlantic Water flooding events on the West Spitsbergen Shelf have become more frequent during the recent decades because of changes in the atmosphere pressure field and the winter cyclone tracks around Svalbard (Rogers et al., 2005; Francis and Vavrus, 2012; Barnes et al., 2014). Hence, there is a possible link between the wind-forced circulation on the West Spitsbergen Shelf (Ekman transport and pumping), the observed wintertime Atlantic Water intrusion on the West Spitsbergen Shelf and in the fjords, and the lack of sea ice around Svalbard (Nilsen et al., 2016, Muckenhuber et al., 2016, Tverberg et al., 2018).

Trends and variability of the future climate is simulated by global coupled climate models as described in Chapter 3. Arctic sea ice loss is in general strongly affected by global warming. This is also the case in the Barents Sea, which has large observed recent trends for both atmospheric and oceanic warming. Especially the northern Barents Sea has experienced a rapid climate shift and is described as the Arctic warming hotspot where the surface warming and loss of winter sea ice is the largest in the entire Arctic (Lind et al., 2018). Their results indicate that less sea ice inflow from the interior Arctic has caused a 40 % freshwater loss in the northern Barents Sea, leading to weaker stratification and increased vertical mixing with the deep Atlantic layer. More heat is then brought up from the deep Atlantic layer, resulting in a dramatically warm Arctic layer.

How well these changes in Arctic sea ice are captured by global climate models is among other things a function of northward transport of heat into the Arctic (Sandø et al., 2014b; Langehaug et al., 2018), which again is very much dependent on the horizontal grid resolution in the models. Most global models underestimate this ocean heat transport, because the topographic details and corresponding circulation is not properly resolved. The regional simulation presented below is done for the period 2006-2070 where the

focus is on the difference between two decades; the 2010s and the 2060s under a moderate global warming (RCP4.5) scenario using the best choice global coupled model available (Sandø et al. 2014a).

Figure 8.1.3 shows the simulated sea surface temperature in March around Svalbard from the first decade of the downscaled future simulation. The Atlantic Water is clearly seen as a tongue of warm water entering the western coast of Svalbard from south as the West Spitsbergen Current. West of Svalbard the Atlantic Water high temperature is gradually lost in the surface layer, but is present a long way into the Arctic deeper beneath the sea ice. Weak contours of warm Atlantic waters can also be seen at the surface as it propagates eastwards north of Svalbard in the West Nansen Basin and the Barents Sea between Svalbard and Frantz Josef Land. The observed temperatures in the northwestern parts of the Barents Sea have increased considerably since 1970, and particularly since the late 1990s. This is in part due to warming of the upstream Atlantic Water, but also to variable wind patterns and corresponding inflow of Atlantic Water from the north (Lind and Ingvaldsen, 2012). In addition, there is growing evidence for increased atmospheric heat transport by increased number of cyclones north of Svalbard (Chapter 4.5.1;Graham et al 2017), and a longer duration of cyclones in the Barents Sea (Wickstöm, 2019).

Arctic water masses dominate the banks right east of Svalbard in the Barents Sea. Here, the Atlantic Water is separated from the Arctic Water by the relative stable Arctic Front (grey line in Figure 2.2.1), which is closely linked to the bathymetry and follows the continental shelf break around the Svalbard Bank towards the Central Banks. The largest sea ice re-treat in the winter (March) is thus further east in the Barents Sea between Franz-Josef Land and Novaya Zemlya (Onarheim et al 2018).

Figure 8.1.3 shows that the modelled sea ice concentration north and east of Svalbard highly correlates with the sea surface temperature. Sea ice concentrations are highest between Edgeøya, Spitsbergen, Nordaustlandet and Kong Karl's Land, around Kvitøya, and around Franz Josef Land. Con-

centrations are smallest along the path of the warm Atlantic Water that effectively melt sea ice given sufficient vertical mixing (Peterson et al., 2017, Sirevåg and Fer, 2009).

8.1.3 Future climate in Svalbard waters

Fifty years from now, the downscaled RCP4.5 simulation shows that the surface waters around Svalbard will be about 1°C warmer (Figure 8.1.3). This is generally true for most areas that today have low concentration of sea ice, but some areas further south have a stronger warming. A few areas cool about 1°C like the outer parts of Storfjorden and Fram Strait. Consistently, simulated sea ice concentration decreases where temperature increases, mainly in the Barents Sea, and increases in the outer and western parts of Storfjorden (Figure 8.1.3). The observed temperatures at Sørøya in Figure 8.1.2 show quite strong interannual and decadal variability compared to the multidecdal trend. This is also the case for the future scenario, and the changes due to natural variability may therefore be comparable in size to the anthropogenic signal over the six decades studied here. Nevertheless, there is a big difference between these two components. While the natural variability is strong, its contributions are both positive and negative, and about zero in mean. On the other side, the anthropogenic signal is small, but always positive, and will therefore accumulate as time passes. It is therefore reason to believe that the temperatures in the Nordic and Barents Seas will continue to rise after 2070, unless the thermohaline convection and thereby the northward oceanic heat transport is reduced.

A comparison of two different CMIP3 models that were downscaled with the same regional model (ROMS) for the future emission scenario (A1B) showed relatively good agreement with respect to future temperature increase but revealed large differences with respect to changes in salinity (Sandø et al., 2014b). These dissimilarities were attributed to deviations in the respective global models and were transferred to the regional models through initial and boundary conditions. CMIP models generally differ extensively on the future changes in salinity, probably due to differences in the representation of the global hydrological cycle (Haine et al 2015).

Such large differences cannot be fixed by a regional downscaling, the ocean is too inert and the impact of the global results from the initial and boundary conditions is too large. So, despite improvements due to increased resolution in regional models, unrealistic biases in the global model projections influence the final results.

Anne Britt Sandø, Institute of Marine Research

Figure 8.1.1 Variable atmospheric forcing and oceanographic circulation contributing to changes in temperatures and sea ice extent around Svalbard.

Northern Norwegian Sea – Sorkapp Section – Atlantic Water
Data Provider: IMR – Institute of Marine Research – Norway
Reference: ICES Report on Ocean Climate
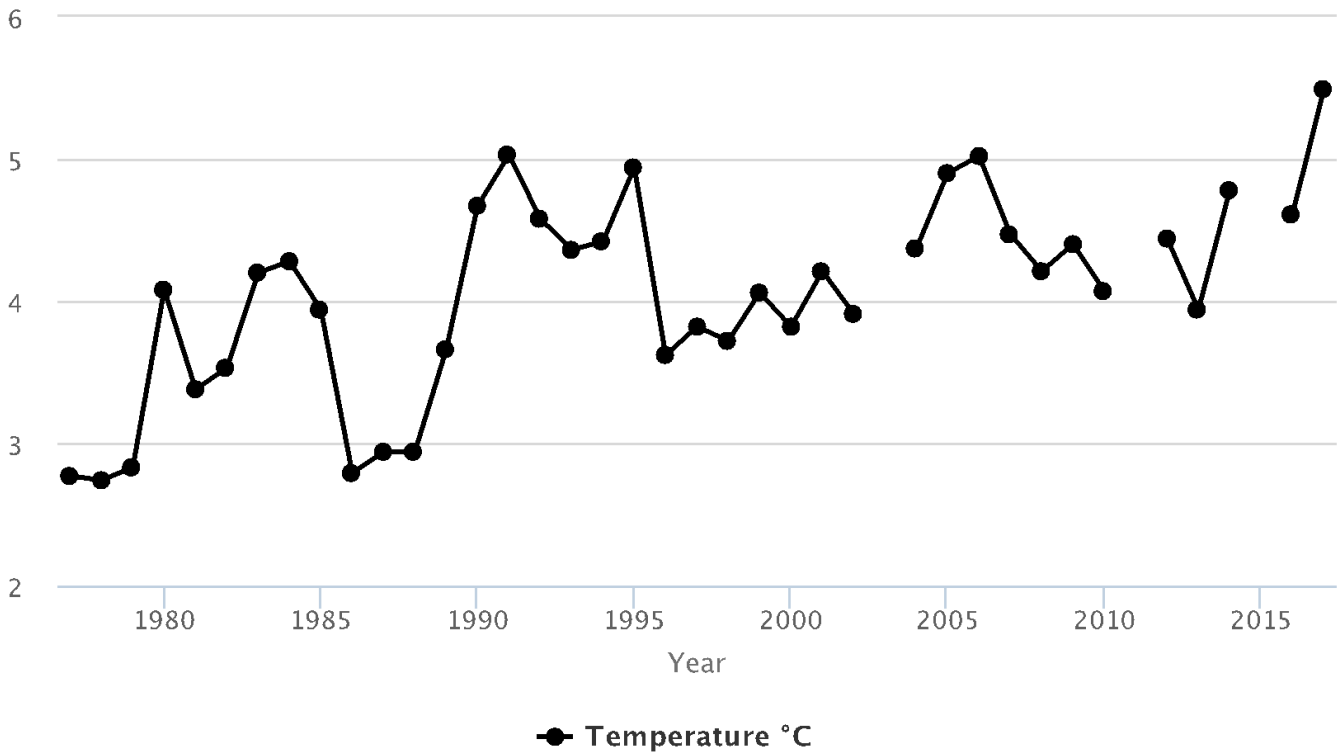
Figure 8.1.2 Sea surface temperature of Atlantic Water in the Sørkapp section in the northern Norwegian Sea (Institute of Marine Research, ICES data, www.imr.no).

8.2 Acidification

The average pH of the surface waters of the global oceans has decreased from approximately 8.2 before the onset of the industrial revolution to a present average of approximately 8.1 (Caldeira and Wickett, 2003; Orr et al., 2005). This ocean acidification is a result of the dissolution of CO_2 corresponding to approximately 1/3 of the CO_2 released to the atmosphere from combustion of fossil fuels, industrial cement production and by changes in land use (Canadell et al., 2007; Sabine et al., 2004). The surface water from the North Atlantic entering the Nordic Seas is presently equilibrated with atmospheric CO_2 and carries small or zero capacity for further uptake in the Nordic Sea region (Olsen et al., 2006). The observed pH of ocean surface waters has decreased by a rate of ~ 0.0018 year^{-1} over the last quarter century at several open-ocean time-series sites (Feely et al., 2009). Lauvset et al. (2015) report on a decrease in the surface pH in the North Atlantic subpolar seasonally biome of -0.0020 ± 0.0004 year^{-1} between 1991 and 2011 using data from SOCAT collection (www.socat.info). A time course of carbon chemistry from Ocean Weather Station Mike (OWSM, 66°N, 2°E) demonstrated an annual pH change of -0.001 pH-units year^{-1} in surface water between 2001 and 2005 (Skjelvan et al., 2008).
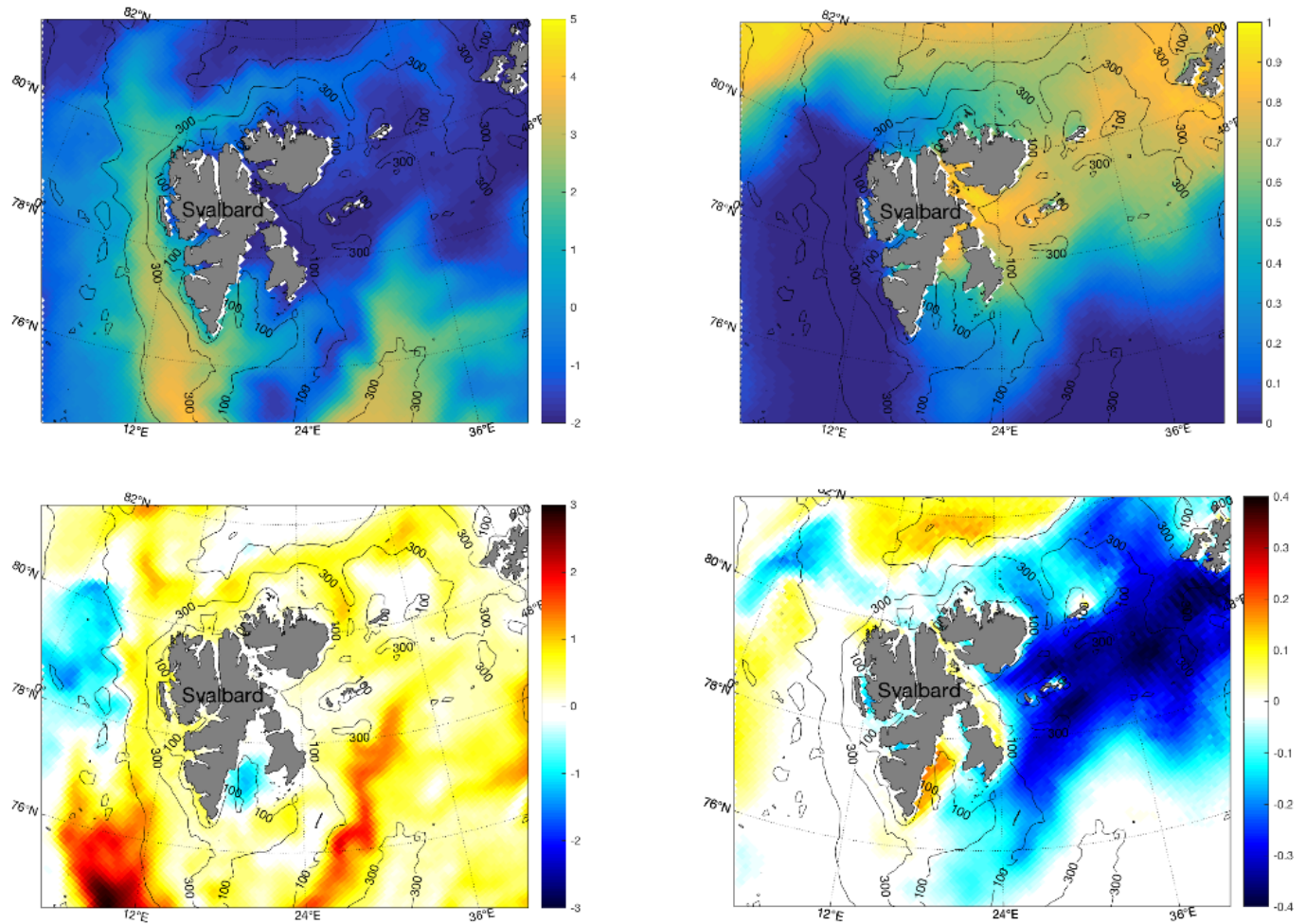
Figure 8.1.3 Simulated sea surface temperature (°C, left) and sea ice concentration (fraction, right) from March in the present climate (upper) and change in the future (lower) of the RCP4.5 scenario. The present and future periods are averages from the years 2010-19 and 2060-69, respectively.
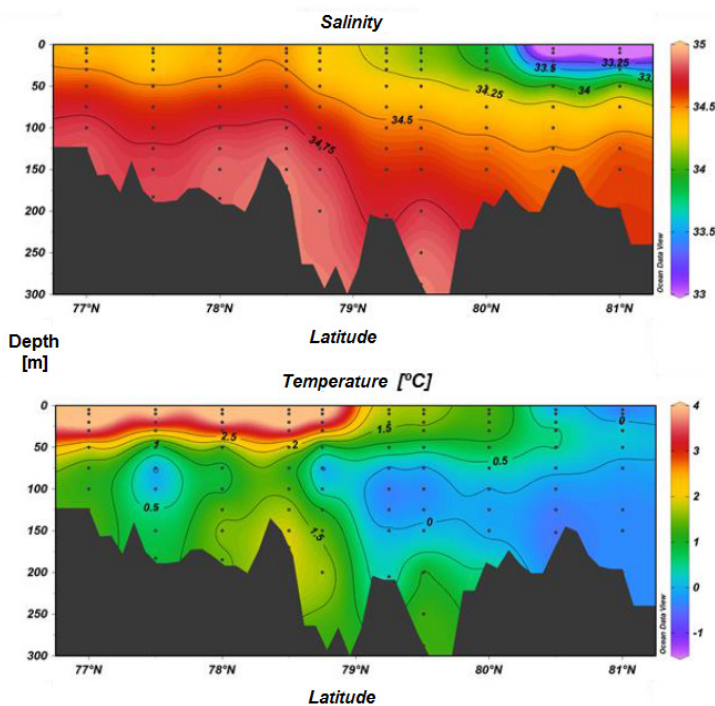
Figure 8.2.1. Salinity and temperature in section east of Svalbard (see Fig.3.3.4) August/September 2016 (From Chierici et al. 2017).
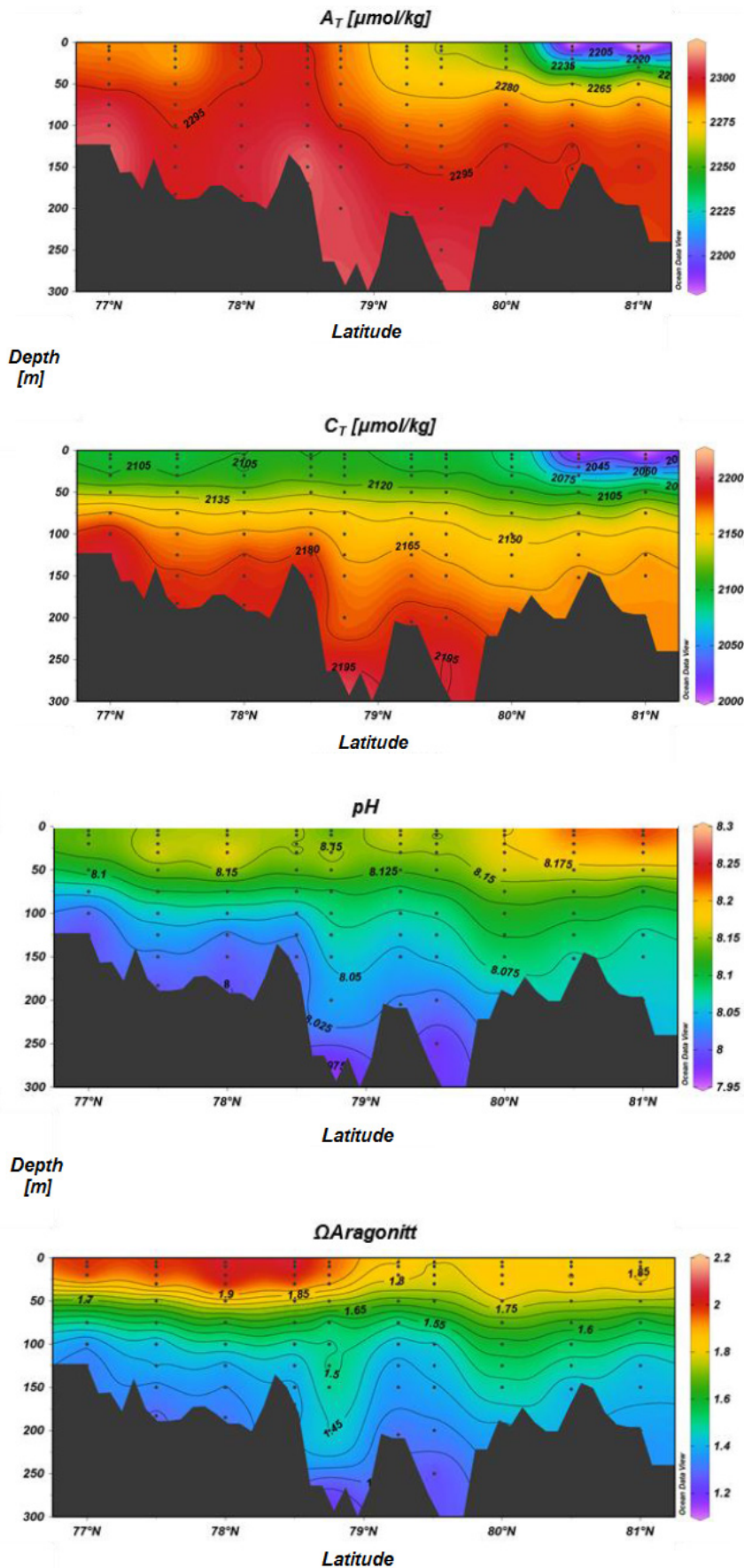
Figure 8.2.2. Alkalinity (A_T) and and total inorganic carbon (C_T) in a section (Figure 3.3.4) east of Svalbard August/September 2016 (From Chierici et al. 2017).

Figure 8.2.3. pH and aragonite saturation state (Ω_{Ar}) in section (Figure 3.3.4) east of Svalbard August/September 2016 (From Chierici et al. 2017).

8.2.1 Present ocean acidification close to Svalbard

The section east of Svalbard (Figure 3.3.4) in 2016 contains Atlantic water in the south and water from the Arctic Ocean in the north. Salinity decreases northwards throughout the water column (Figure 8.2.1). The southern part of the section carries the highest alkalinity, A_T (~2325μmol kg^{-1}) and inorganic carbon, C_T (2200 μmol kg^{-1}) as seen in Figure 8.2.2. North of 80ºN A_T and C_T is lower at all depths. The fresher and colder polar water contains less inorganic carbon than the Atlantic water. The pattern was similar in samples from 2015.

Surface pH values increase northwards and towards the bottom in the section (Figure 8.2.3). Temperature strongly influences aragonite saturation state and the highest surface values are found in the south, where pH is lower than in colder, fresher northern water. Below 100 m depth saturation state values are lower, down to 1.2 at 250 m depth. It is hypothesized that the lowest saturation states are more influenced by CO_2 from microbial degradation of organic material, than from atmospheric anthropogenic CO_2.

The water column section at 33°E (see Figure 3.3.4) shows that the water masses surrounding Svalbard have a large span of ocean carbon chemistry characteristics. There are clear differences between the water in the Arctic Ocean and the Atlantic water, and east of Svalbard there is in addition a component of recirculated Atlantic water from the Fram Strait at 100m depth between 77°N and 80°N (Figure 8.2.1). Generally fresh water from ice melting plays an important role in modifying the waters around Svalbard. This is especially prominent in the waters close to glaciers and in the fjords (Fransson et al. 2015). In addition, it should be noted that annual cycles in primary production and biological activity in general highly modify the carbon chemistry, and these fluctuations through the years will be largest in the less saline regions such as fjords surrounded by glaciers (Fransson et al. 2016). The annual cycles connected to variation in primary production rates are larger in polar waters than in temperate regions of the ocean, both because of the more extreme light/dark conditions, and the difference in buffering capacity related to alkalinity, which is lower in the Polar Ocean than in the Atlantic waters. Another important factor adding to local variability is the regional and annual variability in the presence of sea ice. Sea ice acts as a barrier for diffusion of gases between ocean and atmosphere, and the distribution of sea ice in time and space strongly influence carbon chemistry dynamics in the waters around Svalbard (Fransson et al. 2017).

8.2.2 Future acidification and primary production

To investigate the effect of further increase in atmospheric CO_2 in a future climate, numerical models have become an important tool, and using downscaled physics from a global climate model (NorESM) to force the ecosystem model NORWECOM.E2E, Skogen et al. (2018) have compared the simulated carbonate system in 2005 and 2070 under the RCP4.5 emission scenario in the Nordic and Barents seas. On average the decline in pH is around 0.12 (0.002 year^{-1}) from the first to the last decade for the whole area. Around Spitsbergen the modeled pH decline is largest to the west, and lowest north of the islands.

There are large uncertainties on the possible changes in future primary production, and no general agreement on how this will be affected both on a global and regional scale. The same simulation with NORWECOM.E2E predicts lower primary production in the Norwegian Sea, and no change in the Barents Sea, except for the ice-covered areas to the north where the primary production will increase as the ice retreats. The situation is similar for the Spitsbergen area, with a predicted decrease to the west and south and an increase in production to the east and north. Slagstad et al. (2015) predicts a general decrease in primary production in both the Barents and Nordic seas except for areas where ice retreats in 2100 under emission scenario A1B using the SINMOD model and climate forcing from MPI-ECHAM5. However, around Spitsbergen the patterns are similar to that for NORWECOM.E2E.

8.3 Sea ice

8.3.1 Introduction

Sea ice is a sensitive component of the climate system in the Arctic, where freezing, melting and motion of the sea ice is governed by thermodynamic and dynamic forcing from atmosphere and ocean. Sea ice has also important impact on the climate system through its high albedo and insulating effect, reducing the heat exchange from ocean to atmosphere. In areas where the sea ice has retreated in recent years, the albedo is reduced leading to higher absorption of solar radiation during summer . Less sea ice during winter implies that the heat flux from the ocean to the the atmosphere increases, contributing to winter atmospheric warming.

The Arctic sea ice area is characterized by a large seasonal cycle with maximum in March or April and minimum in September, but there is significant interannual variability. Systematic data collected from passive microwave data since 1979 shows a decline in the Arctic ice extent of nearly 12 % per decade for September and about 3 % per decade for March (Figure 8.3.1; se also http://osisaf.met.no/quicklooks/sie_graphs/nh/en/osisaf_nh_iceextent_seasonal.png). The most pronounced winter reduction inside the Arctic Ocean is observed in the Svalbard and Barents Sea area (Onarheim et al 2018).

The thickness of the sea ice has also decreased significantly in the last decades. The mean ice thickness in the Arctic Basin was 3.59 m in 1975, measured mainly by submarine sonar, while in 2012 the mean thickness was 1.25 m, measured by various methods (Lindsay and Schweiger, 2015). From 2000-2012 the thinning of the ice was about 0.58 m per decade. This reduction in thickness is connected to the change from predominantly multi-year ice to first-year covering the largest part of the Central Arctic Basin. In March 2016, the ice-covered area comprised of about 78 % first-year ice, while in the 1980s the firstyear ice fraction for the same month was about 55 % (Perovic et al, 2016). The observed increase of ice drift speed and increase in the length of the melt season are also connected to the thinning of the ice cover (Vaughan et al., 2013).

The ice export through the Fram Strait is an important part of the ice budget in the Arctic basin. Estimation of ice area flux from satellite data from 1979 shows that the ice export through the Fram Strait has increased by about 6% per decade. The increase is a result of faster southward ice drift due to stronger southward geostrophic winds (Figure 8.3.2) (Figure 2, Smedsrud et al., 2017).
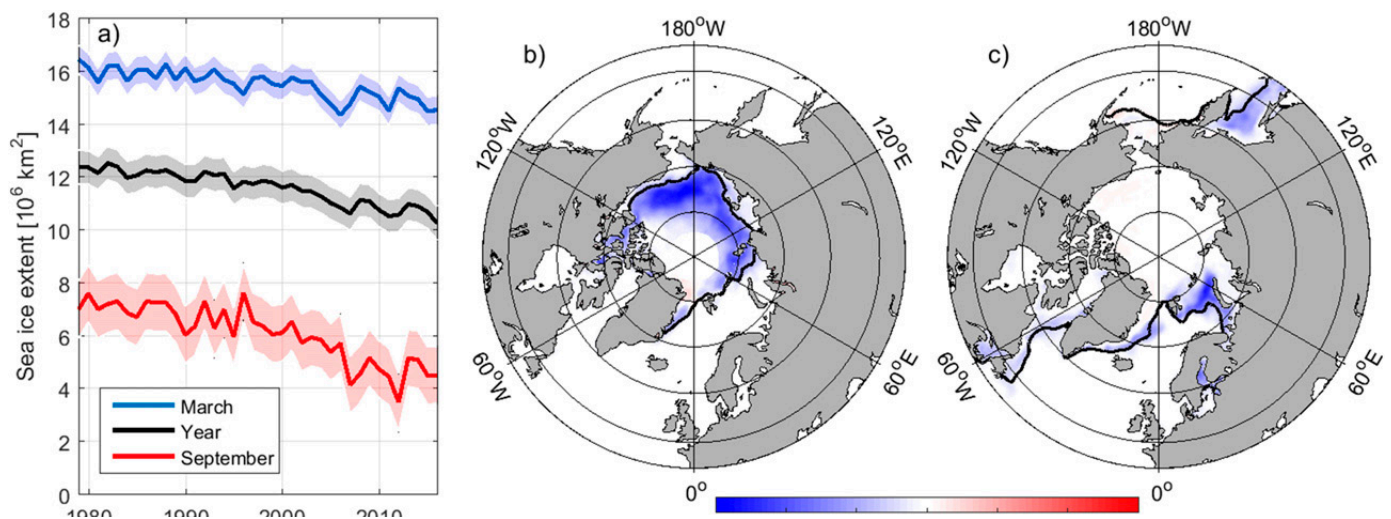
Figure 8.3.1 (a) March (blue), September (red), and annual mean (black) Northern Hemisphere sea ice extent, 1979–2016. Shaded regions indicate plus and minus one standard deviation. Linear sea ice concentration trends (% per decade) in (b) September and (c) March. (Fig 1, Onarheim et al 2018).
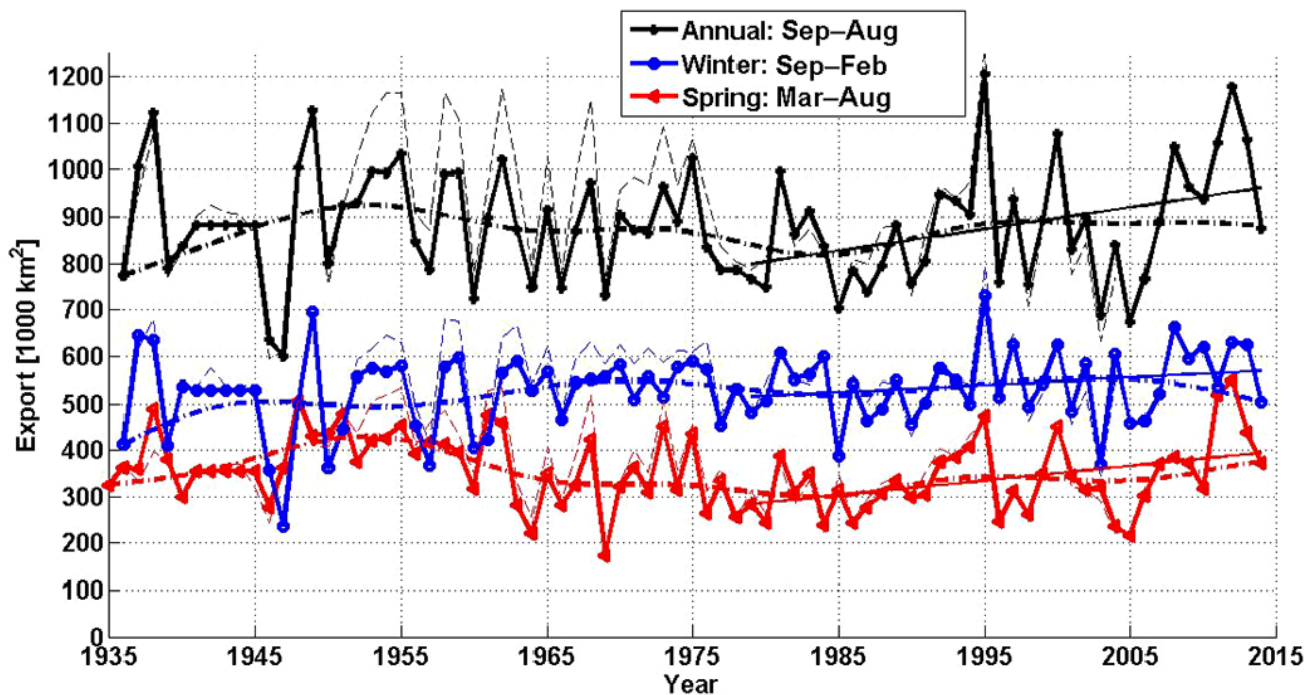
Figure 8.3.2. Southward ice area export in Fram Strait. Ice export from 1935 to 2003 is based on the relationship between observed mean sea level pressure and observed ice export by Synthetic Aperture Radar (SAR). Ice export from 2004 to 2014 is manually tracked based solely on SAR. Annual values (black) are averaged for 1 September through 31 August. Winter export is 1 September–28 February (blue) and Spring is 1 March–31 August (red). Dash-dotted lines show smoothed values, while thin dashed lines indicate uncertainties due to variations in ice concentration.

Sea ice thickness in the western Fram Strait is monitored by the Norwegian Polar Institute with upward looking sonars, installed on moorings, since the early 1990s. The measurements show that ice thickness has decreased, with a 32% reduction of old and thick ice over the period 1990-2011 (Hansen et al., 2013).

8.3.2 Trends and variability of sea ice in the Svalbard region

The large-scale trends of sea ice concentration in the Svalbard area have been documented by satellite observations over the last four decades, showing significant winter decrease (Onarheim et al., 2018). The local sea ice conditions in the fjords and coasts of Svalbard are mainly documented by in situ observations from various monitoring initiatives showing trends towards less ice extent, thinner sea ice, shorter seasons with sea ice cover, earlier onset of melt, and a reduced snow cover compared to a few decades ago. At Hopen, ice thickness monitoring started in the 1960s (Gerland et al.

2008), while other observing programmes have been ongoing for less than two decades. In some locations sea ice conditions have only been observed a few times in connection with process studies, which is not sufficient to make any statements on multiyear means and trends.

The sea ice conditions vary from region to region and from year to year. West of Svalbard, the properties of the West Spitsbergen Current play an important role for the sea ice in the western fjords. The inflow of warm Atlantic water to the fjords have strong impact on the local ice conditions. In the last decade, the fjords on the west coast have been almost ice-free in the winter (Muckenhuber et al., 2016). East of Svalbard, the East Spitsbergen Current transports Polar water and sea ice southwards, causing this region to be ice-covered most of the year. In the last decade, the whole Barents Sea, including the area east of Svalbard, has been ice-free for several months in the summer and autumn.
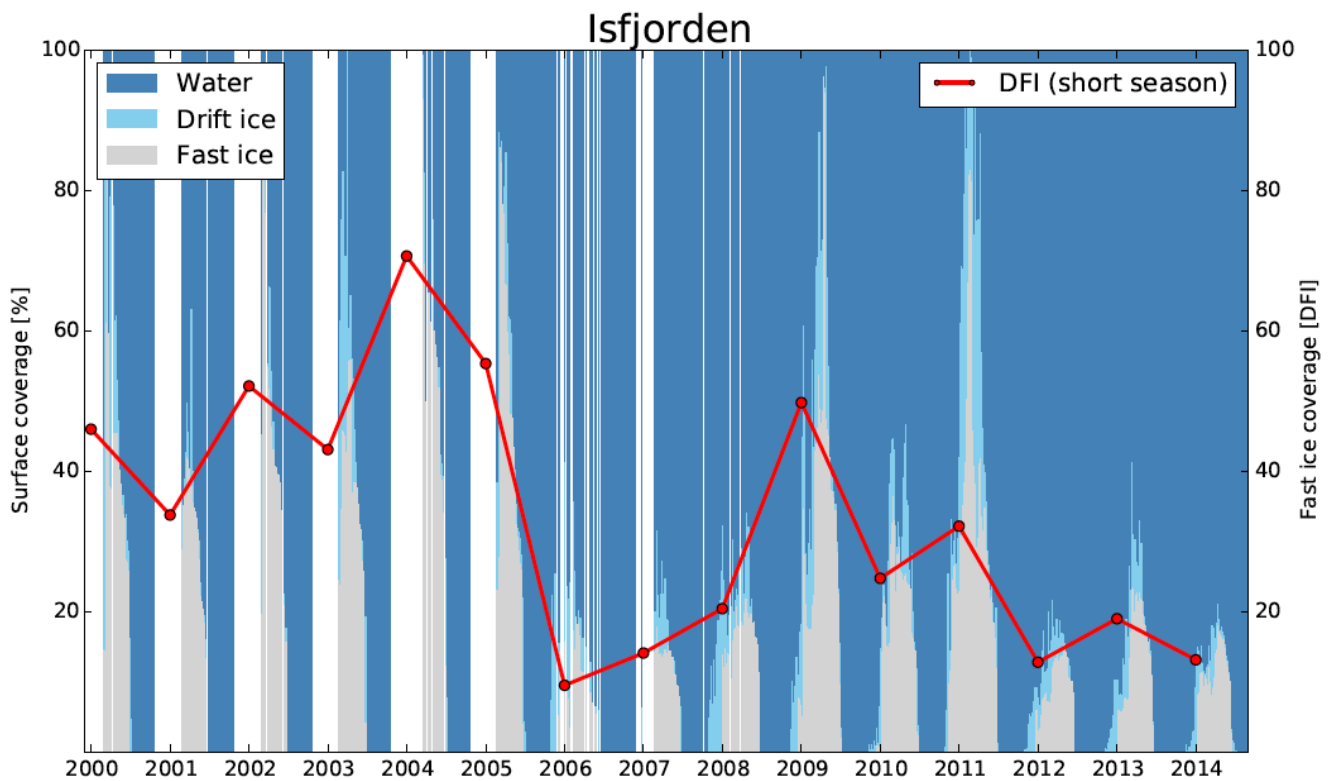
Figure 8.3.3. Surface coverage of Isfjorden between 2000 and 2014 divided into "fast ice", "drift ice", and "open water" by a sea ice expert. White gaps occur when no satellite data were
available. The red dots display the "days of fast ice" (DFI) values of the short season (from 01 March to end of ice season).

8.3.3 Sea ice in fjords on the Svalbard west coast

Muckenhuber et al. (2016) have analysed the sea ice in Isfjorden and Hornsund from 2000 to 2014 using high-resolution Synthetic Aperture Radar (SAR) and optical images. The analysis showed a significant decrease in the fast ice cover for both fjords in that period (Figure 8.3.3).

Grønfjorden is a fjord arm of the larger Isfjorden west of Barentsburg. Zhuravskiy et al. (2012) analysed long-term ice variability based on visual and instrumental observations, as well as main oceanographic and meteorological characteristics here from 1974 to 2008. The beginning of stable ice formation varied significantly from year to year, but generally occurred from mid-December to early January. Their results also indicate a tendency toward a response of landfast sea ice to a milder climate for Grønfjorden during the last decades of the 20th and the beginning of 21st century.

In Kongsfjorden north of Ny-Ålesund sea ice observations started in 2003 as a part of a long-term project at the Norwegian Polar Institute and show substantial interannual variability in fast ice thickness and extent (Gerland and Hall 2006; Gerland and Renner 2007). Observations include visual observations and quantification of sea-ice extent and in situ measurements of ice and snow thickness that are both needed for quantitative sea-ice mass-balance estimates and for characterization of the fjord ice situation.

Pavlova et al. (2019) summarize published results and present updated ice-extent and ice and snow thickness up to 2016. During this period the fast ice evolution in Kongsfjorden varied interannually with intervals (2-3 years or more) of relatively high and low sea-ice cover (Figure 8.3.4). After 2006 most years had low ice extent and shorter season of fast ice than earlier. Both fast ice and snow thickness have experienced negative trends over the
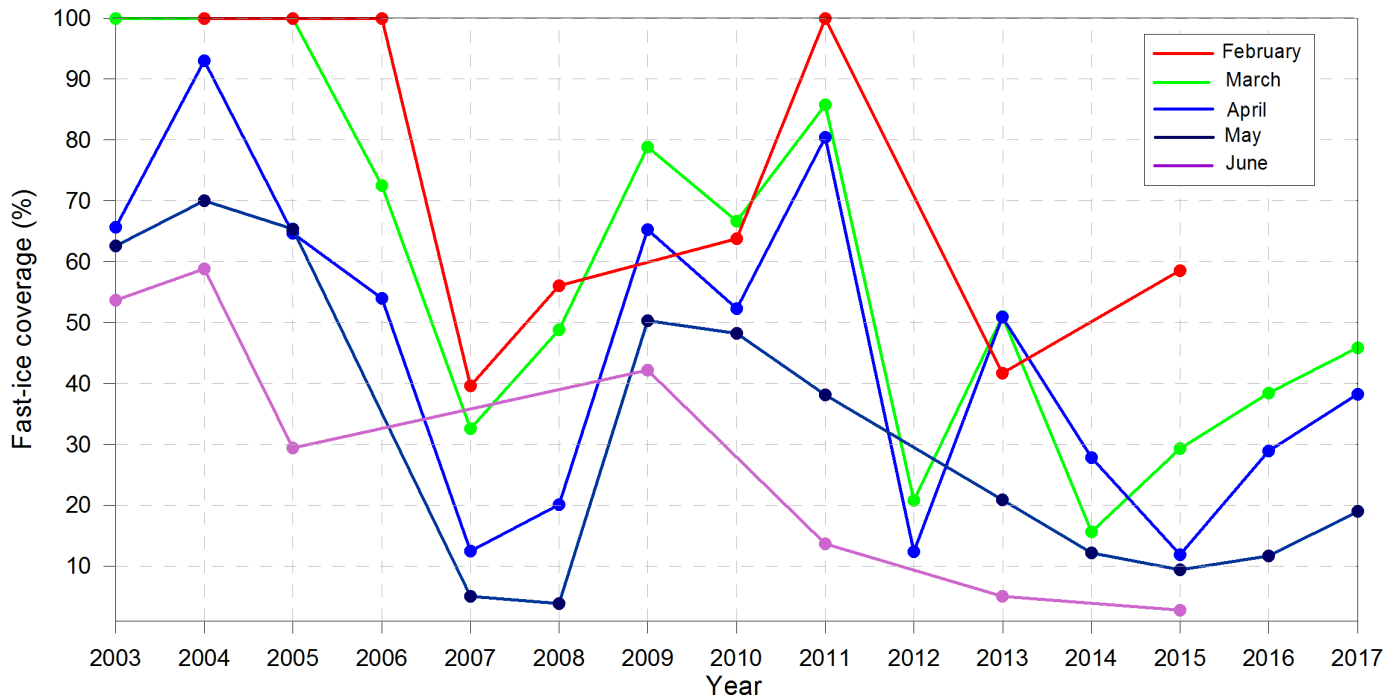
Figure 8.3.4. Maximum fast ice coverage (%) in Kongsfjorden for each month from February to June in the period of 2003-2017, modified after Pavlova et al. (2019).

observation period (1997-2016), towards thinner ice and snow cover, from levels around 70 cm in the early 2000s to 40 cm in the years around 2015, combined with substantial interannual variation. Snow contributes to the sea ice mass balance in Kongsfjorden and other Svalbard fjords (Gerland et al. 1999, Nicolaus et al. 2003, Wang et al. 2015).

Gerland and Hall (2006) compared fast ice thickness between Kongsfjorden, Van Mijenfjorden and Hornsund from thickness transects in one year. The major question addressed was how much the thickness of fast ice varied among the different fjords , and, thus, to what degree one can extend findings from one fjord to the entire western coast. The three fjords did show differences in ice thickness, although the thickness did not differ substantially among the three fjords before melt onset.

8.3.4 Sea ice north of Svalbard

Fast ice in fjords at the northern coasts of Svalbard have been less intensively observed than those in the west (see Chapter 8.3.3), but some observations have been made, mainly at Rijpfjorden at the northern part of Nordaustlandet. Wang et al. (2013) describe parts of the seasonal evolution of fast ice

at Rijpfjorden based on in situ measurements and an ice mass balance buoy frozen into the fast ice in spring 2011. Seasonal maximum mean ice thickness was observed in June with 81 cm, while snow was thickest in April with a mean of 19 cm. During spring, parts of the snow layer melted and re-froze again as sea ice (superimposed ice).

Drifting ice in and beyond the marginal ice zone (MIZ) is different from fast sea ice that remain in the same position throughout the winter. Different types of drifting ice can be observed north of Svalbard, including second and multiyear ice, and features such as surface melt ponds created by the melting of snow on top of the drifting ice during summer (e.g. Divine et al. 2015) . Ice and snow thickness levels were investigated from surveys in 2010 and 2011 (Renner et al. 2013), and during the N-ICE2015 drifts with RV Lance in 2015 (Granskog et al. 2017; Rösel et al. 2018). First-and second-year ice were observed to be thicker than the stationary fast ice on Svalbard . Modal thicknesses (the most often thickness measured) for spring sea ice have in recent years been between 1.5 and 2 m, which is less than earlier observations, while in summer modal ice thickness was observed to be

around 1 m (Renner et al. 2013, Rösel et al. 2018). Snow thickness has been observed in winter and spring to be substantial, with mean levels around 0.5 m (Rösel et al. 2018), and formation of snow ice has been observed.

8.3.5 Sea ice on the east coast of Svalbard

Storfjorden covers the southern half along the eastern side of Spitsbergen. Sea ice forms seasonally and locally here, between December and April (Skogseth et al 2004). Dependent on the atmospheric forcing, a polynya can open with a large area of open water and intense heat loss to the atmosphere, and subsequent sea ice formation. First year ice that form locally reach about 1.0 m in thickness over winter in "normal" years using 1960-1990 mean atmospheric forcing (Hendricks et al 2011). Strong winds (~ 10 m/s) from the north is the primary polynya driver, creating typical heat loss of 200-300 W/m2 in an air temperature of around -10°C. During winter, sea ice is formed inside the polynya, creating high salinity and density water that helps to ventilate the deep ocean (Skogseth et al 2004). The polynya length downwind is typically 20-80 km, and down-wind ice advection close to 0.5 m/s (Smedsrud et al 2006). When the winds are southerly the polynya closes, and the related convergence creates dynamically ridged sea ice up to 5 m in thickness (Hendricks et al 2011). The polynya activity in Storfjorden is atmospherically forced by cold northerly winds and varies annually and on shorter time scales. Storfjorden is an important location for production of Arctic dense cold-water (Skogseth at al., 2008), forming on the order of 10% of this important water mass.

Ice-thickness monitoring at the shore of Hopen in the northwestern Barents Sea shows negative trend between 1966 and 2007 (Gerland et al. 2008). This decrease in thickness is consistent with the decreasing sea ice thickness in the Arctic in general and also the decreasing extent in the Barents Sea. Gerland et al (2008) also declare that sea-ice thickness variability as a climate indicator provides more quantitative information on the state of the ice cover than solely sea ice extent.

Pavlova et al. (2014) investigated how atmospheric circulation and ocean temperature influence the inter-annual variability of sea-ice extent in the Barents Sea using sea-ice concentrations obtained from passive microwave satellite imagery, sea-surface temperatures, and NCEP-NCAR sea-level pressure data for the period 1979-2010. The results lead to the conclusion that the contributions of wind and sea-surface temperatures to the variability of sea-ice extent in the Barents Sea in winter are about equal. King et al. (2017) shows that sea ice thickness in the northwestern Barents Sea east of Svalbard can vary significantly between years. In 2003 the ice regime was dominated by sea ice forming other places and then advected into Barents Sea. Most of that ice was multiyear ice, on average 1,4 m thick. In contrast, sea ice in 2014 was seasonal ice, formed in the northwestern Barents Sea, and the average thickness was only 0,7 m. The two examples show how different sea ice characteristics can be, depending on the specific environmental conditions and forcings.

8.3.6 Future projections for sea ice in the Svalbard region

The simulated change in future sea ice concentration (Figure 8.1.3) indicate a major reduction the northern Barents Sea, a reduction in the western fjords, and a certain increase in the outer and western parts of Storfjorden. Areas with decreased sea ice concentration reflect increased sea surface temperature and vice versa.

The interannual variability of sea ice extent in the Barents Sea is largely determined by inflow of relatively warm Atlantic Water through the Barents Sea Opening (BSO) (Sandø et al., 2010; Årthun et al., 2012, Smedsrud et al, 2013, Sandø et al., 2014a, b). None of the global CMIP5 climate models are capable of simulating sufficient inflow of heat through the BSO (Sandø et al., 2014a; Langehaug et al., 2013), explaining a systematic bias for the recent Barents Sea ice loss. Because the Barents Sea also dominates the Arctic Ocean sea ice variability during winter (Onarheim et al, 2018), this missing warm Atlantic inflow has importance far beyond the region, possibly through altering the large-scale atmospheric circulation.

8.4 Sea level

Global sea level is rising owing to increasing ocean temperatures (thermal expansion) and mass loss from glaciers and the Greenland and Antarctic ice sheets (e.g. Church et al., 2013). Regional differences in sea level arise due to spatial differences in ocean density change, ocean mass redistribution and circulation, atmospheric pressure and winds, as well as changes to the gravity field. When considering sea-level changes at the coastline, vertical land motion must be taken into account. Relative sea level (RSL) is a measure of the distance of the sea surface height relative to the seafloor, i.e., the shore. For Svalbard, land motion due to Glacial Isostatic Adjustment (GIA) plays an important role in determining RSL changes. GIA is the ongoing response of the solid Earth to past and present ice mass changes

8.4.1 Paleo sea level data

During the past glacial (~20,000 years ago) many parts of the northern hemisphere, including Scandinavia, were ice covered. Global sea level was ~120 m below present-day levels (Peltier and Fairbanks, 2006). While it is well recognized that the Svalbard-Barents Sea region was covered by a major ice sheet, the configuration of the ice during the past glacial and nature of the retreat remain uncertain. This is because there is a paucity of direct marine and terrestrial evidence constraining past ice height and extent (Ingólfsson and Landvik, 2012).

Paleo data on relative sea level from Svalbard show a spatial pattern of change that largely reflects land motion over the past ~10,000 years. These data have been used to both constrain the history of the Svalbard-Barents ice sheet (e.g. Lambeck, 1996) and infer details of regional Earth structure (e.g.
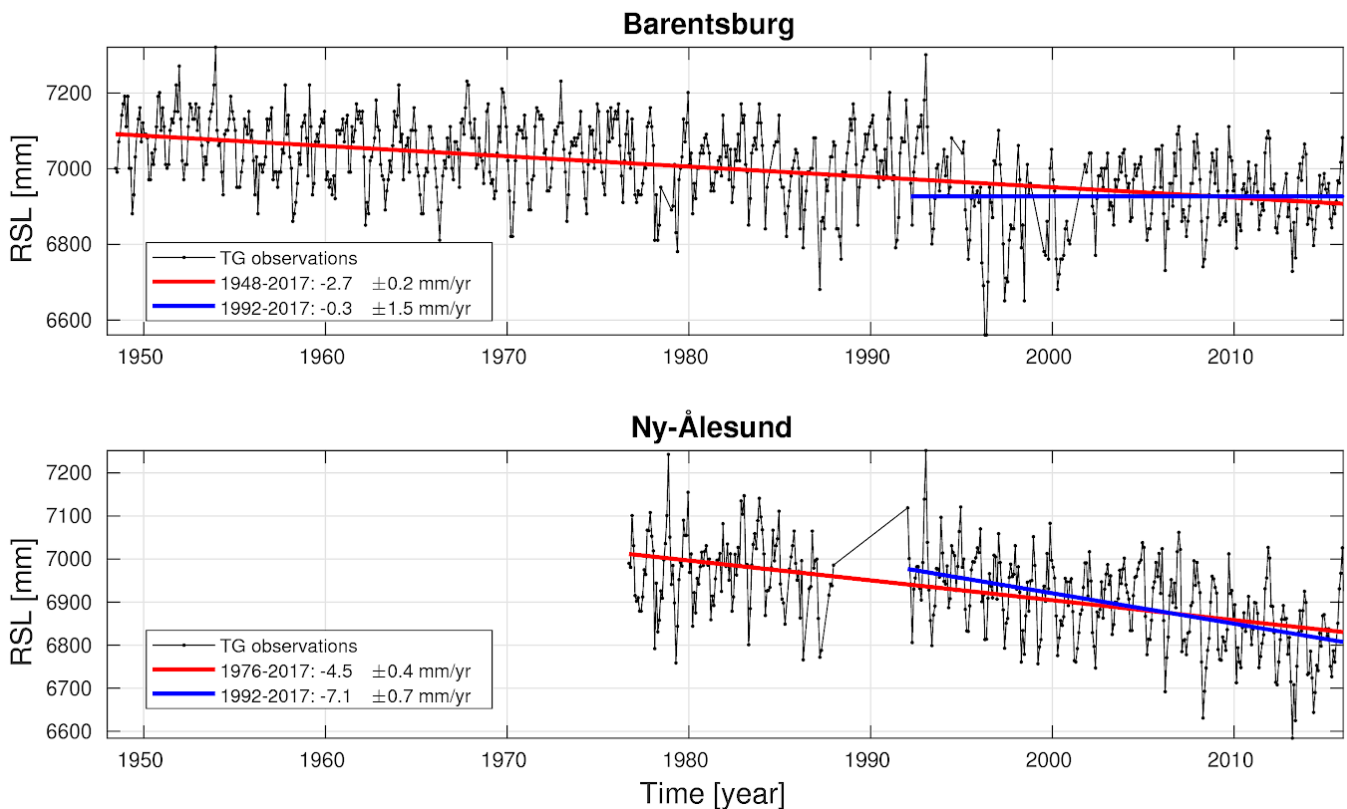
Figure 8.4.1: Relative sea level observed by the tide gauge in Barentsburg (upper panel) and Ny-Ålesund (lower panel). The black markers indicate the tide gauge observations, the red line indicate the linear trend of the entire period covered by the tide gauge observations, and the blue line the trend for the period 1992-2017.

Kaufmann and Wolf, 1996). The pattern of RSL change suggests the presence of an ice dome(s) in the northwest Barents Sea during the past glacial (see Forman et al., (2004) for a review of all the RSL data). RSL data from west Svalbard show a decrease of some tens of meters since the last glacial, while in the east RSL has fallen by >100 m. This overall fall in RSL indicates that it is vertical uplift of the Earth due to GIA that has dominated past sea-level changes across Svalbard.

8.4.2 Instrument record

For the entire tide gauge records, we calculate a trend of -2.7 ± 0.2 mm/year for Barentsburg and -4.5 ± 0.4 mm/year for Ny-Ålesund (Fig 8.4.1). The trend is significantly less than zero at both sites. For the shorter, more recent period 1992 to 2017, the rates are calculated as -0.3 ± 1.5 mm/year for Barentsburg and -7.1 ± 0.7 mm/year for Ny-Ålesund.

These results suggest that, for both stations and both study periods, the rate of vertical land uplift has been larger than the rate of sea surface height rise. If we assume that the change in sea surface height (measured in a geodetic reference frame) is similar in Barentsburg and Ny-Ålesund, the differences in rates indicate that vertical land motion at the two sites is different. Furthermore, while the rate in Ny-Ålesund for the most recent period is less than for the entire study period, the rate over the most recent period in Barentsburg is larger. This suggests that temporal variation of vertical land motion at the two sites is different and/or that the tide gauges are not connected to a stable reference benchmark.

Despite the challenges associated with its high latitude location (Chapter 3.6) there are several studies on observations of the Arctic Ocean from altimetry. Most of these studies rely on gridded multi-mission altimetry products that include the waters around Svalbard. Volkov et al. (2012) found that the sea level has risen by 0 to 2 mm/year around Svalbard for the period 1992 to 2010. They found highest rates on the west coast of Svalbard and with lower rates on the east. In Prandi et al. (2012a, 2012b), the average sea-level rise for the Arctic Ocean was estimated to 3.6 ± 1.3 mm/year (90% confidence) for the period 1993 to 2009. They also reported higher rates of sea-level rise on the west coast and, furthermore, a shift in the sea-level trend after 2003, i.e., a sea-level fall of -4.3 mm/year. This fall is supported by independent measurements of the mass and steric components of sea-level rise.

The pause in sea-level rise is also evident in a regional time series of sea-level anomalies first presented in Cheng et al. (2015). Andersen and Piccioni (2016) present an update of this series extended to 2015. The extended series shows how regional sea-level change is characterized by strong natural variability, and that the flattening in sea level in the period after 2003 is followed by sea-level rise after 2010, and a new fall after 2013. For the entire study period, Andersen and Piccioni (2016) estimate the regional trend of the Arctic Ocean to 2.2 ± 1.1 mm/year. As expected, sea-level rates estimated from altimetry are significantly larger than RSL rates from the tide gauges owing to the influence of vertical land motion.

GNSS station	Period	Uplift Rate (mm/year)
Longyearbyen	2008-2018	7.2 ± 0.6
Ny-Ålesund	1999-2018	8.0 ± 0.3
Hornsund	2009-2018	9.4 ± 0.7
Bjørnøya	2012-2018	-0.0 ± 0.6

Table 8.4.1. Observed uplift rates from permanent GNSS stations across Svalbard
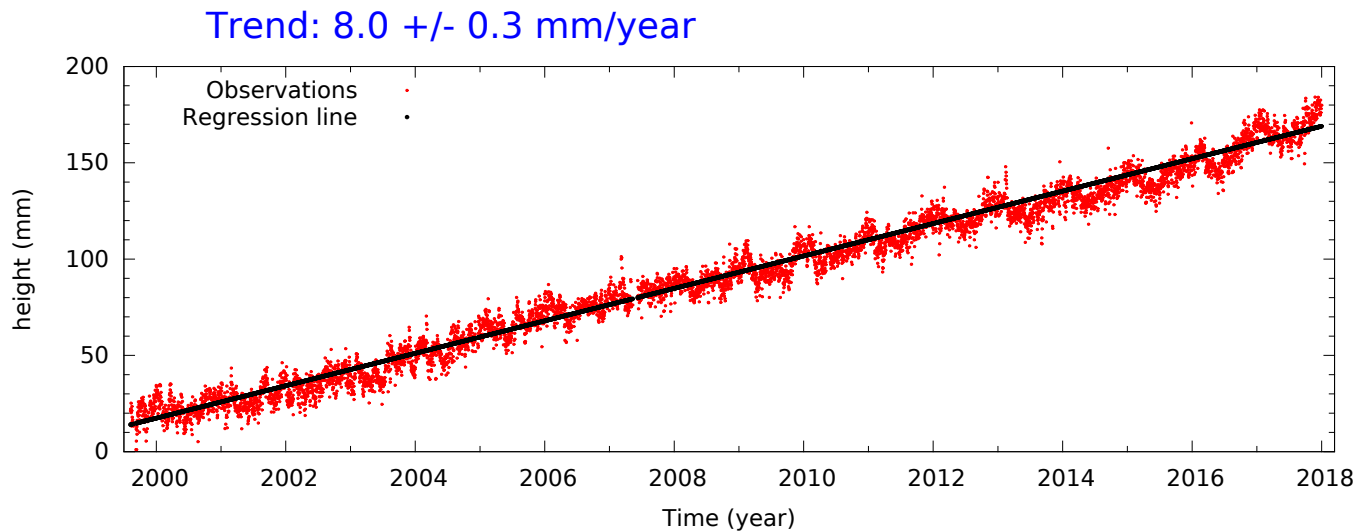
Figure 8.4.2. Observed time series of land height from the permanent GNSS station at Ny-Ålesund

The Global Navigation Satellite System (GNSS) measurements (Chapter 3.6.1) from Svalbard indicate high land uplift rates with large inter and intra annual signals (see Table 8.4.1 and Figure 8.4.2). Observed uplift rates along the west of Spitsbergen are between 7 and 10 mm/year, whereas, at the Bjørnøya station there is almost no vertical land motion and rates are not significantly different from zero. Previous work indicates that the high uplift rates are largely caused by the Earth's response to present-day glacier changes and, to a lesser extent, GIA due to past ice mass changes (e.g. Kierulf et al., 2009; Omang and Kierulf, 2011; Memin et al., 2011). However, there remain some data-model discrepancies and other geophysical processes (e.g. tectonics) might play a role here. The sparse GNSS network, with no observations in central, north, and eastern Svalbard means we only have partial understanding of land motion across the archipelago. Annual land motion variations can essentially be explained by annual mass balance changes of the nearby glaciers (Kierulf et al., 2009).

In more recent studies, there has been increased focus on identifying the individual contributions to sea-level change. Frederikse et al. (2017), for example, use the sea level equation to model regional sea-level changes for different mass contributions. Changes in the distribution of mass on the Earth's surface produce a non-uniform sea level pattern due to gravitational changes. Using data from Frederikse (pers. comm.) we estimate the following: From

1993 to 2014 the Antarctic ice sheet is estimated to have contributed ~0.25 mm/year to the RSL trend over the Svalbard region. Similarly, changes in terrestrial water storage have contributed 0.25 mm/year. Ice mass loss from the Greenland ice sheet contributed to -0.4 mm/year on the west coast of Spitsbergen and -0.2 mm/year along the eastern islands of the Svalbard archipelago over 1993 to 2014. This is due to the west–east gradient in the Greenland gravitational fingerprint. Note that as mass loss from Greenland has increased, the corresponding trends for the more recent period 2003 to 2014 are -0.6 and -0.4 mm/year over Svalbard.

The largest contribution to contemporary RSL change is from glaciers, and more specifically, the local glaciers on Svalbard. As glaciers have retreated and lost mass, their gravitational pull has been reduced and the Earth has uplifted, leading to a local RSL fall. Mass loss from Svalbard glaciers is estimated to have contributed a negative RSL trend of -4 to -8 mm/year around the margins of Svalbard over 1993 to 2014. In total, we calculate that contemporary mass changes contributed an RSL change of -8 mm/year for both Ny-Ålesund and Barentsburg over the same period.

Regional steric sea-level changes indicate a slightly negative RSL trend for the period 1993 to 2014 (Good et al., 2013). For comparison, the global mean thermal expansion trend for 1993 to 2015 is 1.1 mm/year (data from Dieng et al., 2017).

Station	20-year return height	200-year return height	1000-year return height
Ny-Ålesund	1.23 (1.16, 1.28)	1.35 (1.24, 1.41)	1.42 (1.29, 1.49)
Longyearbyen	1.33 (1.26, 1.37)	1.44 (1.34, 1.50)	1.51 (1.39, 1.58)

Table 8.4.2. Return heights for extreme high waters from Ny-Ålesund and Longyearbyen given in meters above mean sea level (1996-2014). The 5% and 95% confidence levels are given in parentheses.

8.4.3 Extreme sea level

A selection of the estimated return heights from Longyearbyen and Ny-Ålesund with corresponding confidence intervals are given in Table 8.4.2, additional return heights for other periods can be found on www.kartverket.no/sehavniva.

8.4.4 Modelled land motion as a contribution to future sea-level change

The mean Glacial Isostatic Adjustment (GIA) field in IPCC AR5 is evaluated as the mean of the ICE-5G model (Peltier, 2004) and the ANU-ICE model (Lambeck et al. (1998) and subsequent improve-ments). These GIA models are based upon global ice sheet reconstructions where the loading history of the ice sheets is essentially inferred from paleo sea level observations. The one standard error of the GIA field is taken as the difference between the separate models. Figure 8.4.3a shows the RSL change due to GIA and associated gravitational effects over the period 1986–2005 to 2081–2100. The GIA models predict continued land uplift in the Barents Sea region and, therefore, RSL is projected to fall in this area. Along the west coast of Svalbard GIA uplift rates are predicted to be stable; this area is the hinge line between vertical uplift and subsidence of the surrounding peripheral bulge.
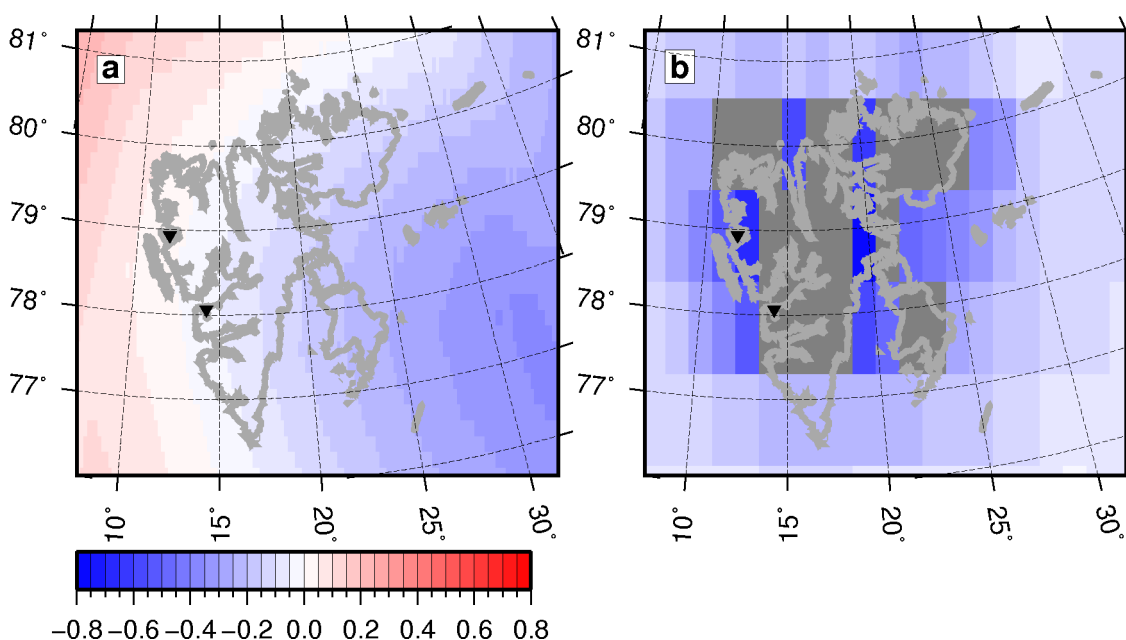
Figure 8.4.3. Relative sea-level change (m) due to GIA (panel a) and future glacier changes for RCP4.5 (panel b) over the period 1986–2005 to 2081–2100. Results are from IPCC AR5 and both show the mean field.

Figure 8.4.3b shows the glacier contribution to future RSL change over the period 1986–2005 to 2081–2100. Projected global glacier changes in IPCC AR5 and used here are based on modelled Surface Mass Balance (SMB) changes (Slangen and van de Wal, 2011; Marzeion et al., 2012; Giesen and Oerlemans, 2013; Radić et al., 2013). Svalbard is projected to have a negative SMB and, therefore, the Earth will uplift and the gravitational pull of glaciers will be reduced causing a local RSL fall.

Future RSL projections from glacier changes are given on a coarse 1 x 1 degree grid and, therefore, will not capture the sea level response at smaller scales. Observations from GNSS show that there can be large spatial variations in uplift rates owing to local glacier changes (e.g. see the results from campaign measurements across Ny-Ålesund area presented by Kierulf et al. (2009)). Furthermore, we note that the SMB glacier projections do not include any ice dynamic changes, or the response of marine-terminating glaciers to changes in oceanic conditions.

Figure 8.4.4. Projected ensemble mean relative sea-level change (m) over the period 1986–2005 to 2081–2100 and for RCP4.5.
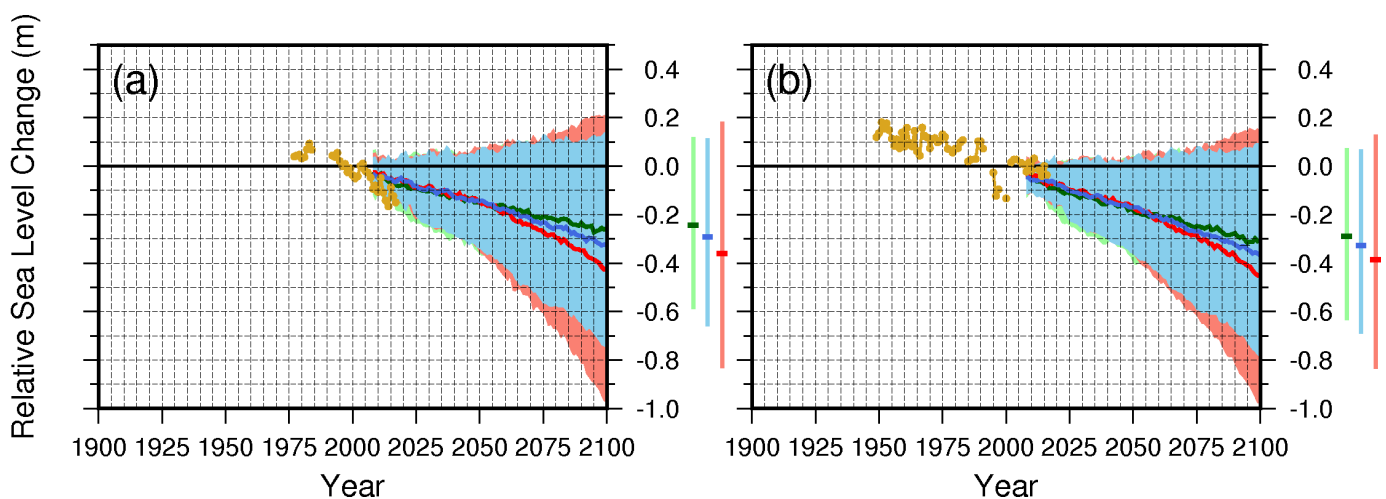
Figure 8.4.5. Relative sea-level projections for RCP2.6 (green), RCP4.5 (blue) and RCP8.5 (red) for (a) Ny-Ålesund and (b) Barentsburg. The vertical bars on the right side of the panels represent the ensemble mean and ensemble spread (5% to 95%) for RSL change for 2081–2100. Annual mean tide gauge observations are shown in yellow.

8.4.5 Projected 21st century sea level changes for Svalbard

Here we present regional sea-level projections for Svalbard using model output from the CMIP5 and for the emission scenarios RCP2.6, RCP4.5 and RCP8.5 (Figures 8.4.4 and 8.4.5). The projections are given with corresponding 5% to 95% ensemble spread, these ranges are defined as the likely ranges in IPCC AR5 (P > 66%).

The IPCC AR5 results indicate a projected RSL fall over the 21st century for all emission scenarios. The projected RSL fall is larger for scenarios with increasing greenhouse gas emissions. That is, for increasing global temperatures we see a more negative RSL change on Svalbard, which is the opposite of what we expect along the majority of the world's coastlines. This is because with increasing future warming there will be larger ice mass losses on Svalbard, which will cause larger land uplift, and a larger local RSL fall. For Longyearbyen, the ensemble mean projected RSL change is -0.39 m (ensemble spread -0.84 to 0.13 m) for RCP8.5 and over the period 1986–2005 to 2081–2100.

There are only small differences between the RCPs up until 2050 (Figure 8.4.5). Going towards 2100 the separate projections from the RCPs begin to diverge but there are still large overlaps between their respective uncertainties. In fact, inspection of the vertical bars in Figure 8.4.5 shows that differences between the ensemble means for the different RCPs are somewhat smaller than the projections ensemble spread (5% to 95%).

The largest projected contribution to RSL change on Svalbard, and largest uncertainty, is from future glaciers changes (Figure 8.4.6). As discussed, future mass loss from local glaciers will cause a local RSL fall. Other notable contributions to future RSL are from steric/dynamic sea-level changes and from ice sheet changes. Of particular concern is the contribution from Antarctica, which could potentially exceed the numbers given here, especially if a collapse of the marine portions of the ice sheet were to be triggered (e.g. DeConto and Pollard, 2016). As Svalbard sits in the near field of Greenland, projected mass loss there causes a sea-level fall owing to ice sheet's gravitational fingerprint.
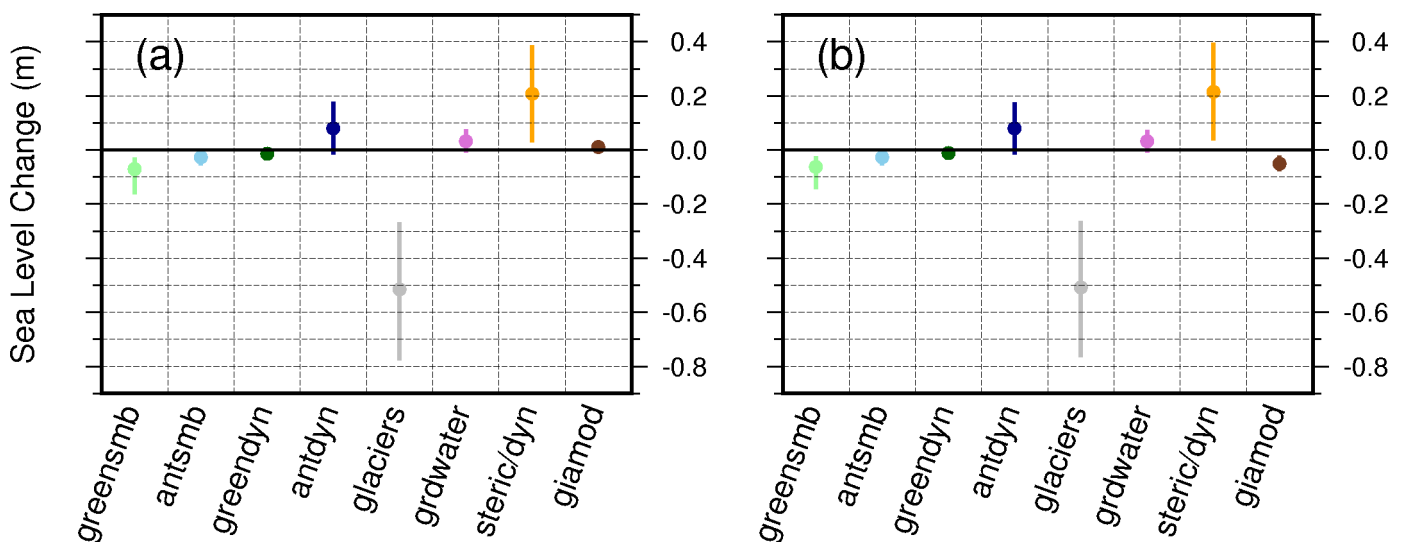
Figure 8.4.6. Contributions to projected relative sea-level change for RCP4.5 over the period 1986–2005 to 2081–2100 for (a) Ny-Ålesund (b) Barentsburg. The ensemble mean and spread (5% to 95%) are shown by the circles and vertical bars, respectively.

9. Assessment and use of projections

9.1 Uncertainties related to the climate projections

Uncertainties can be defined as incomplete knowledge because of lack of certain information or disagreement on what is known and what we have knowledge about. Many of the uncertainties in climate-change projections are different from uncertainties in weather forecasting or seasonal prediction. Weather forecasting and seasonal prediction are initial value problems where the lack of exact knowledge of the initial state of the atmosphere and ocean poses major uncertainties on the weather forecast a few days ahead. The uncertainties in climate projections that goes beyond a few decades stems from lack of complete knowledge about the boundary conditions (uncertainties related to historical and future changes in greenhouse gases, solar radiation etc.) and little from the initial conditions. Traditionally, the major uncertainties in climate projections can be categorized in three main categories:

- Incomplete knowledge related to future man made emissions
- Incomplete knowledge related to natural variations
- Model uncertainties

However, this notion has to be modified for the regions close to the marginal ice zone as biases in the initial sea ice extent can influence projections far longer than a few decades in these regions. Thus, there is an additional source of uncertainty that has to be accounted for:

- The initial state of the sea ice.

Incomplete knowledge related to future anthropogenic emissions

Uncertainties related to future anthropogenic emissions are connected to incomplete knowledge about future economic activity, demographic changes

such as population growth, future choices of energy sources, changes in energy efficiencies and other socioeconomic factors. This lack of certainty about the future translates into:

Uncertainties in greenhouse gas emissions

- This is primarily related to emissions of carbon dioxide (CO_2), methane (CH_4), dinitrogen monoxide (N_2O) and chlorofluorocarbon (CFC) gases.

Uncertainties in short lived gases and aerosols

- Uncertainties in man-made emissions from gases that are precursors to greenhouse gasses (e.g. carbon monoxide (CO) and volatile organic compounds (VOC))
- Uncertainties in man-made emissions of aerosols (small liquid droplets or solid particles that remain suspended in the air for some time) such as soot and emissions of gases that can generate aerosols such as sulphur dioxide (SO_2) and nitrogen dioxide (NO_2).

Incomplete knowledge related to natural variations

Uncertainties connected to natural variations are partly connected to the fact that the climate system is non-linear and chaotic (internal variations) and partly to lack of knowledge about natural forcings such as future changes in solar radiation and volcanic eruptions.

Uncertainties related to internal variations

- Due to the non-linear and chaotic nature of the climate system it is not possible to simulate climate change from one year to the next or from one decade to the next with the types of

models used in this report. On these timescales the non-predictable internal variations can be larger than the predictable changes that come from changes in the external climate forcings (such as changes in greenhouse gases). Internal climate variations redistribute energy between different parts of the climate system (e.g. ocean and atmosphere) or geographically which will influence the regional and global climate. Examples of this are variations in the amount of heat that is transported from the upper to the deeper ocean, natural climate oscillations such as El Nino and natural variations in the meridional transport of energy by atmosphere and ocean.

- Many of the internal variations redistribute energy from one place to another geographically without necessarily changing the global energy content and will therefore have a larger effect regionally than globally.
- Global coupled climate models simulate many of the well-known internal variations (e.g. El Nino), but as they are not predictable they will not be synchronized in time with the observed internal variability.

Incomplete knowledge connected to natural external forcings

- With the exception of the well-known 11-year cycle in solar insolation, the possibilities of predicting future changes in solar radiation are small. The same holds for the frequency and intensity of future volcanic eruptions.
- If solar variations over the next 100 years are of similar magnitude as we have seen the last 100 years, the uncertainties related to solar radiation is smaller than many of the other uncertainties listed in this chapter. This is partly true for volcanic eruptions as well, but such eruptions may have pronounced effect on climate on timescales of a few years and therefore on climatic extremes.

Model uncertainties

Model uncertainty is related to lack of knowledge about the climate system, our ability to implement our understanding into a numerical mathematical framework and limited supercomputing capabilities. One way to divide this type of uncertainty is in a parametric and structural part.

Parametric uncertainty

- Is due to uncertainty in several parameters within state of the art climate models. The most common way of spanning this type of uncertainty is to do an ensemble of simulations with the same model but different parameter settings (this is often called a Perturbed Physics Ensemble, PPE).

Structural uncertainty

- Uncertainties in the structure of the model systems. Which processes are accounted for, to what extent are they simplified, and are they based on correct knowledge? It is possible to get an estimate of this type of uncertainty by running several models with the same climate forcing (often called a Multi Model Ensemble, MME). However, this will not capture deficiencies that are shared among the models.
- Another structural uncertainty is related to processes that we are presently unaware of.
- The last part of the structural uncertainty is connected to the choice of post processing method (e.g. bias corrections etc.) for the primary climatic variables (such as temperature and precipitation) that are used as input to impact models. One example is uncertainties introduced due to distortion of the original climate change signal as a result of bias corrections.

The initial state of the sea ice

If the climate projection starts out with a too small or large sea ice extent this may influence the projections. For models having extensive ice cover, melting of the surplus ice may, through feedback mechanisms, lead to locally enhanced warming and vice versa for models starting with too small ice extent. This is discussed in some detail in Box 4.1 and how it influences the bias adjusted variables in Box 5.1.

9.2 Treatment of uncertainties in different variables

The Arctic is a region with a strong climate change signal, however it is also a region with large natural internal variations related to decadal and multidecadal variations in the large scale oceanic and atmospheric circulation (Chapter 2). These are variations that are enhanced by strong regional feedbacks (Chapter 2) and results in the Arctic being a region with a very low signal-to-noise ratio when it comes to climate change. Together with the uncertainties in the regional feedbacks this makes the Arctic a region with large uncertainty in the climate change signal. Due to the different amount of available information, uncertainty is treated differently for different climatic variables. The below sections gives a brief overview:

Uncertainties in the primary meteorological variables

Results from two possible future emission scenarios RCP4.5 (medium) and RCP8.5 (high) have been analyzed. Five regional models have been used for RCP4.5 and nine for RCP8.5. Many of them ran with the same global model as boundary condition. In the time series of temporal development, the uncertainty is illustrated by showing the ensemble median, 25th and 75th percentiles and the minimum and maximum of the ensemble. The relative low numbers of models and their dependence in terms of using either the same regional model or the same boundary conditions, implies that the uncertainties

given in the report does not span the full uncertainties as outlined in Chapter 9.1. An investigation into the spread in Arctic climate response among the different regional models participating in Arctic CORDEX can be found in Koenigk et. al. (2015). Additionally, the fine scale climate model COSMO-CLM (CCLM) has been used for the RCP8.5 scenario (Chapter 3.1.4) in order to investigate possible effects of fine scale topographical features on the climate change signal. Finally, for temperature, a suite of global models has been empirically downscaled and provide an alternative approach to running regional models (Chapter 3.1.3).

A majority of the Arctic CORDEX ensemble members have too much sea-ice in the Svalbard region in the control period, and thus are colder than the observed climate. The modelled temperature change therefore tends to be larger than it would have been for the same models under a more realistic control climate. Consequently the upper end of the uncertainty span indicated by the ensembles probably is unrealistically warm (Figure B5.1). As the amount of water vapour the atmosphere can hold before saturation depends on the temperature, models with the largest (and possibly unrealistic) future warming will tend to show the largest precipitation increase (Figure 9.2.1). Further considerations on realism in the temperature and precipitation projections for Svalbard are outlined in Box 4.1 and Box 4.2.
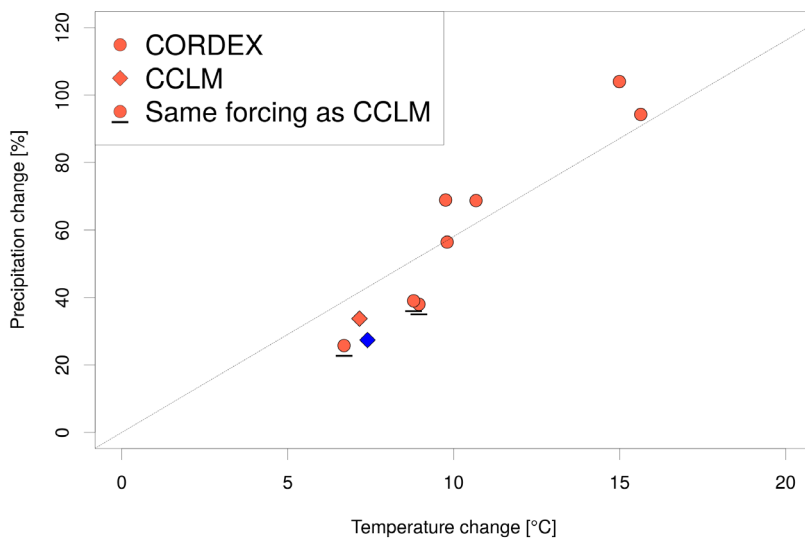
Figure 9.2.1: Temperature and precipitation changes for the Arctic CORDEX ensemble and the high resolution CCLM simulation for the end of the century with the RCP8.5 emission scenario. Regional models forced with the same global model as the high resolution CCLM are underscored. The blue diamond is the CCLM model run with coarser resolution (25*25 km^2 gridsquares instead of 2.5*2.5 km^2) to indicate the effect of resolution on the result.

Uncertainties in the oceanic variables

Due to the lack of oceanic downscaled climate scenarios, results from only one emission scenario – RCP4.5 and one model are shown in the report. Thus, there are no estimates of uncertainty linked to the hydrographic and sea ice related variables. Analysis and justification for using the NorESM as boundary condition for the regional ocean model can be found in Sandø et. al. (2014b) and Lange-haug et al. (2013).

Regional sea-level projections for Svalbard were conducted using model output from the global CMIP5 models for the emission scenarios RCP2.6, RCP4.5 and RCP8.5. The projections are given with corresponding 5% to 95% ensemble spread (for details see Chapters 8.4.4 and 8.4.5). The largest uncertainty in the estimated relative sea-level change in Svalbard is from future glaciers changes as future mass loss from local glaciers will cause a notable local relative sea-level fall which strongly depend on future glacier loss.

Uncertainties in the primary cryospheric variables

Simulations of future changes in glacier mass balance was conducted using a climatic mass balance model (Chapter 3.2.4.3) forced with near-surface climatic parameters from the fine scale climate model COSMO-CLM. The simulated mass balance represents only the climatic mass balance and neglects the ice discharge component which discharges large volumes of ice into the ocean over short periods (surges). As only one model was used to force the mass balance model there are no quantitative estimates of uncertainty. However, a discussion on the quality of the conducted simulations can be found in Chapter 3.2.4. Other cryospheric variables such as seasonal snow amounts were simulated with the hydrological model (Chapter 3.2.3) and their uncertainties are discussed in the Uncertainties in the hydrological variables section below.

Uncertainties in the bias adjusted meteorological variables

In this report the empirical quantile mapping (EQM) method used for the climate projections for Norway (Wong et al., 2016), was applied to bias-adjust temperature and precipitation with the Sval-Imp data set at 1x1 km² resolution for Svalbard (Chapter 3.1.1 and Box 5.1). Chapter 3.2.2 provides a brief description of the methodology. The bias-correction method uses the Sval-Imp data set as reality without any observational uncertainties accounted for. It bias-adjusts one meteorological variable at the time and the co-variation between different variables can be altered from the original data. As the EQM method is applied to temperature and precipitation separately and on each grid cell individually, the inter-variable, spatial and temporal dependencies are not corrected relative to the observations. It is important to bear in mind these limitations when interpreting the results of climate impact studies based on the bias-adjusted climate data. Despite its limitation, the method is capable of correcting systematic errors in the regional climate model output. However, new errors may be introduced due to the bias-adjustment (Sorteberg et al., 2014; Maraun, 2016). For the Arctic CORDEX simulations with their coarse resolution of 50x50 km², the applied re-gridding to 1x1 km² using a nearest neighbor method may have caused unexpected bias-adjustment results, especially along the coastline (see Box 5.2 for details).

Uncertainties in the hydrological variables

As described in the previous section, the bias-adjustment introduces additional uncertainty in the climate change signal that is not present in the original temperature and precipitation from the RCMs. On the other hand, the bias-adjustment reduces systematic errors in the simulation of the present day climate and is required to obtain realistic simulations of present day hydrology.

To estimate the hydrological projections, a hydrological model is applied. Only two river flow gauging stations with rather short records and difficult measurement conditions implies a poor basis for the hydrological model calibration. The parametrization of the hydrological model adds to the uncertainty (Lawrence and Haddeland, 2011). The snow model is calibrated based on observations in Norway and it is assumed that the model parameters are valid for Svalbard.

In Svalbard changes is runoff are very sensitive to the influence of temperature on glacier mass balance. The modelling results are therefore sensitive to the representation of glaciers in the model and the projected temperature changes. That permafrost and frozen ground is not included in the model, adds to the uncertainty.

Projected changes in runoff, mean annual floods and snow are shown as maps (1x1 km²), plots of the seasonal cycle, or as time series of the temporal development. The maps and the plots of the seasonal cycle do not visualize the uncertainty. In the time series of temporal development, the uncertainty is illustrated by showing the ensemble median, 25th and 75th percentiles and the minimum and maximum of the ensemble. The very large spread in

the modelling results illustrates the uncertainty. In particular the bias adjusted temperature for some of the ensemble members leads to unrealistically high future temperatures resulting in extreme runoff increases and an extreme reduction in maximum annual snow amounts and snow cover duration. There is consistency, however in the direction of change.

Because of the high uncertainty in the hydrological modelling results, expected changes in flood magnitudes are only estimated for the mean annual flood and not for more extreme floods with higher return levels.
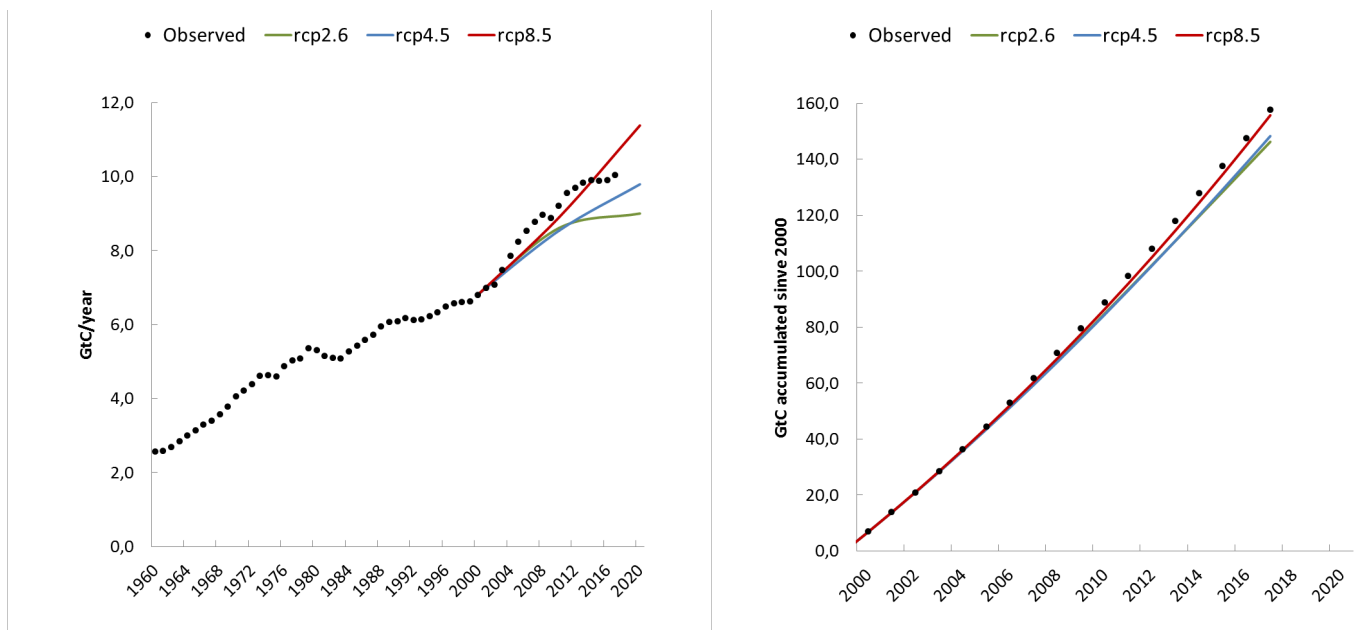
Figure 9.3.1: a) Global emissions of CO2 (from fossil fuel and cement production) given in billion tons of carbon per year from 1959 to 2017 (dots) and the three emission scenarios RCP2.6 (green), RCP4.5 (blue) and RCP8.5 (red) from 2000 to 2020. b) Accumulated emissions of CO2 over the 17 years the emission scenarios have existed. Observationally based data taken from the Global Carbon Budget project (Le Quéré et al 2018).

9.3 Recommendations

Future emissions of greenhouse gases and aerosols are to a large extent a political and societal question. It is too early to judge which of the emission scenarios are the most realistic. Since the base year for the RCP emission scenarios 18 years ago, the real accumulated greenhouse gas emissions are higher than all three scenarios (Figure 9.3.1), but this may change as a consequence of the political commitment embedded in the Paris agreement.

Recommendation on which emission scenarios and which model estimates to use cannot be generalized. It depends on the purpose of the investigation and the questions posed.

The Arctic CORDEX ensemble medians in this report may act as a first guideline for assessing the strength of climate change in Svalbard. However, it is important to keep in mind that both the fine-scale CCLM projections and the excessive sea ice found in some of the Arctic CORDEX simulations indi-

cate that some of the Arctic CORDEX simulations may give too high estimates for future temperature increase (Box 4.1). This translates into large changes in the variables derived from air temperature as well as precipitation (Box 4.2) and hydrological changes (Box 5.1).

For impact and risk analysis we emphasize methods that take into account both the large uncertainty in the climate change signal as well as the large natural internal variability in the Artic climate. This is of particular importance when dealing with low probability-high impact events.

We strongly recommend the users of information in this report to contact the institutions that have contributed to the analysis and assessment of the results that will be used. This may help in the interpretations of the results and to gain information on new knowledge.

10. Longyearbyen

Longyearbyen, the administrative centre of the Svalbard archipelago, is located in the deeply eroded Longyeardalen valley, with extensive mountain plateaus on both sides (Figure 10.1, Figure 10.3.1). Longyearelva, a braided river system draining two glaciers, runs down the central axis of Longyeardalen. Due to a lack of more suitable sites, most infrastructure in Longyeardalen is confined to areas where potentially hazardous processes, such as avalanches, slushflows, debris flows, rockfalls, solifluction and floods, can impact buildings and infrastructure (Hestnes et al., 2016). In addition, the permafrost in Longyeardalen is ice-rich, with frost-susceptible marine sediments, which must be taken into account in design, construction and maintenance of buildings and structures (Instanes and Rongved, 2017).

During the first 50 years of Longyearbyen's history beginning in the early 1900s, houses were built

Figure 10.1 Longyearbyen located in lower Longyeardalen, with extensive plateaus on both sides, and with the glaciers Larsbreen and Longyearbreen in the end of the valley, 1 May 2016. Photo: Hanne H. Christiansen

on locations close to the workplace in the mines. Longyearbyen then gradually expanded from the western side of the valley Longyeardalen, to the Longyearelva river mouth and further to the eastern side of the valley. The settlement on the western side of the valley built prior to the Second World War was almost completely destroyed in an attack by the German Navy on the 8th of August 1943. Nybyen, was built after the war, followed by further building at Haugen, and in approximately1970, the settlement Lia on the eastern side of the valley was established. The buildings at Blåmyra came in 1985, and following this, Longyearbyen expanded towards the valley Gruvedalen and the flood plain. In 1989, the process of splitting the coal mining company Store Norske Spitsbergen Kulkompani AS into three separate entities, including community administration and business development as independent organisations, was initiated. This led to a change in

the settlement from a pure 'company town' to an open community. The town has grown further in subsequent years, and several buildings and other infrastructure are found in hazard-prone areas. The river Longyearelva is continuously managed so that it runs in a single channel to gain space for settlement in the valley bottom, where most of the recent housing development has taken place. As of 2018, river management measures are taken primarily to prevent the river from eroding the river bed so as to secure the flood plain and allow for further development. Other areas of recent expansion include the harbour area and the area called Gruvedalen. Since 1990, the population in Longyearbyen has grown from approximately 1000 to well above 2000 in 2018 (https://www.ssb.no/en/befsvalbard/; https://snl.no/Longyearbyen).
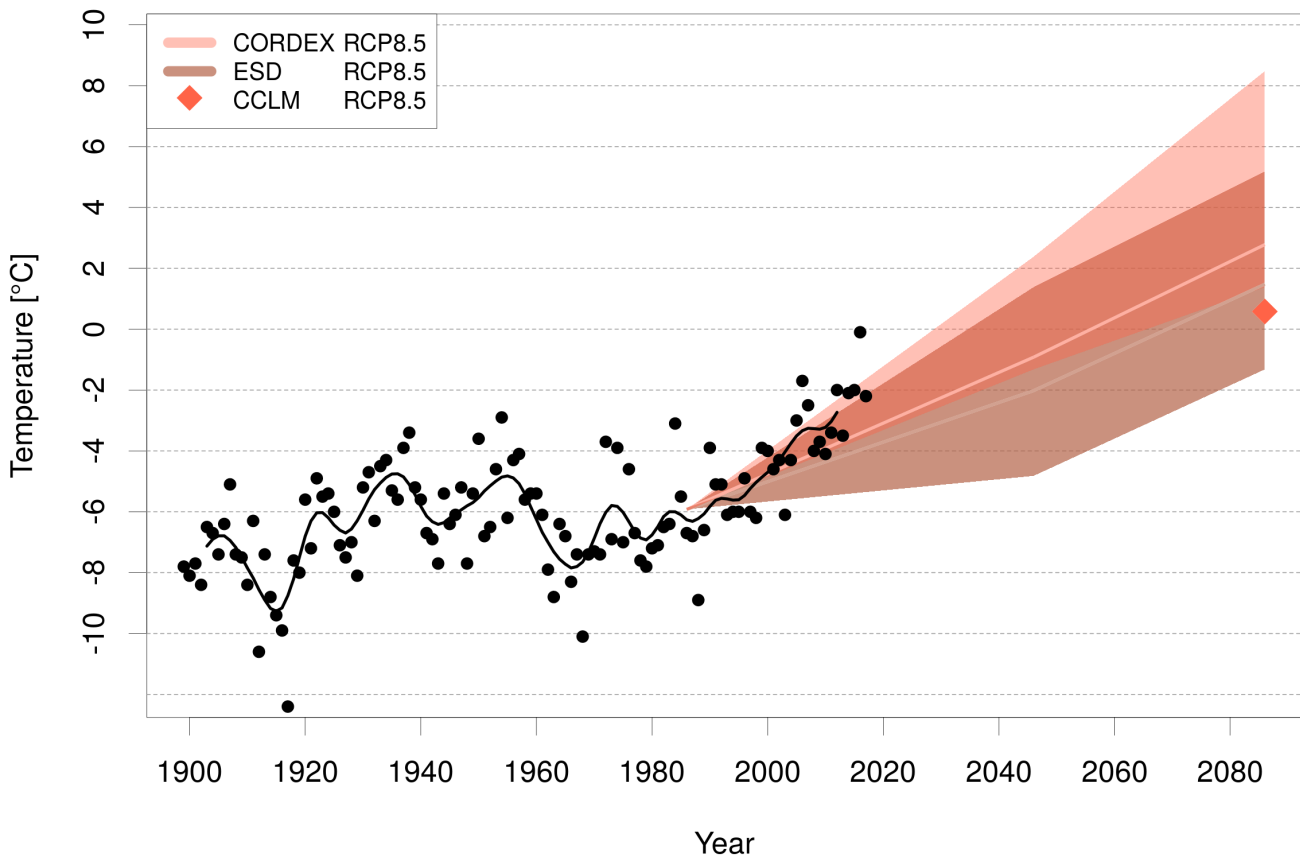
Figure 10.1.1 Annual mean temperature for Svalbard Airport/Longyearbyen [°C]. The points and black curve show single years and smoothed decadal variability based on observations from 1900 to 2017. Future projections are given for RCP8.5. ESD projections are based on 81 CMIP5 models. RCM projections are based on the 8 Arctic CORDEX simulations. Changes are projected to the periods 2031-2060 and 2071-2100. Median, "high" and "low" projections are shown. A diamond indicates the result for the CCLM RCP8.5 projection towards the end of the century.

10.1 Atmosphere

10.1.1 Temperature

The annual mean temperature at Svalbard Airport/Longyearbyen during the period 1971-2000 was approximately -6 °C. Under the emission scenario RCP8.5, the median values for the ensembles from Empirical-Statistical Downscaling (ESD) and regional climate models (Arctic CORDEX) suggest a warming of respectively 7.4 and 8.7 °C during the 21st century, while the fine-scale CCLM-model projects a warming of 6.5 °C (Figure 10.1.1 and Table 10.1.1). This means that according to these median projections, the annual mean temperature for Svalbard Airport/Longyearbyen will increase to above 0 °C at the end of the century.

For the emission scenario RCP4.5, the projected (ensemble median) warming from ESD and Arctic CORDEX are respectively 4.6 and 6.2 °C (not shown). The CCLM projection, which is used to project changes in temperature-based indices, is thus close to the low RCP8.5 projection (Figure 10.1.1) and the medium RCP4.5 projection. This also holds for seasonal temperatures (Figure 10.1.2).

The average number of days per year with a mean temperature above 5 °C ("growing days") was 40 in the control period 1971-2000, and more than 90% of them occurred during summer (Table 10.1.1). The CCLM and the Arctic CORDEX median suggest that the number of growing days increases by a factor of 2 to 3. The CCLM indicates that half the increase will occur in the summer, and the other half will be distributed between the spring and the autumn.

The average number of days per year with an average temperature below 0 °C ("frost days") was approximately 240 in the control period, including more than 90% of the winter- and spring-days as well as 2 of 3 days in the autumn (Table 10.1.1). The CCLM and the Arctic CORDEX median indicate a reduction of around 95 and 135 days, respectively. According to the CCLM, there will be a substantial reduction in frost days during the winter, though the largest reduction is expected in the spring and the autumn.
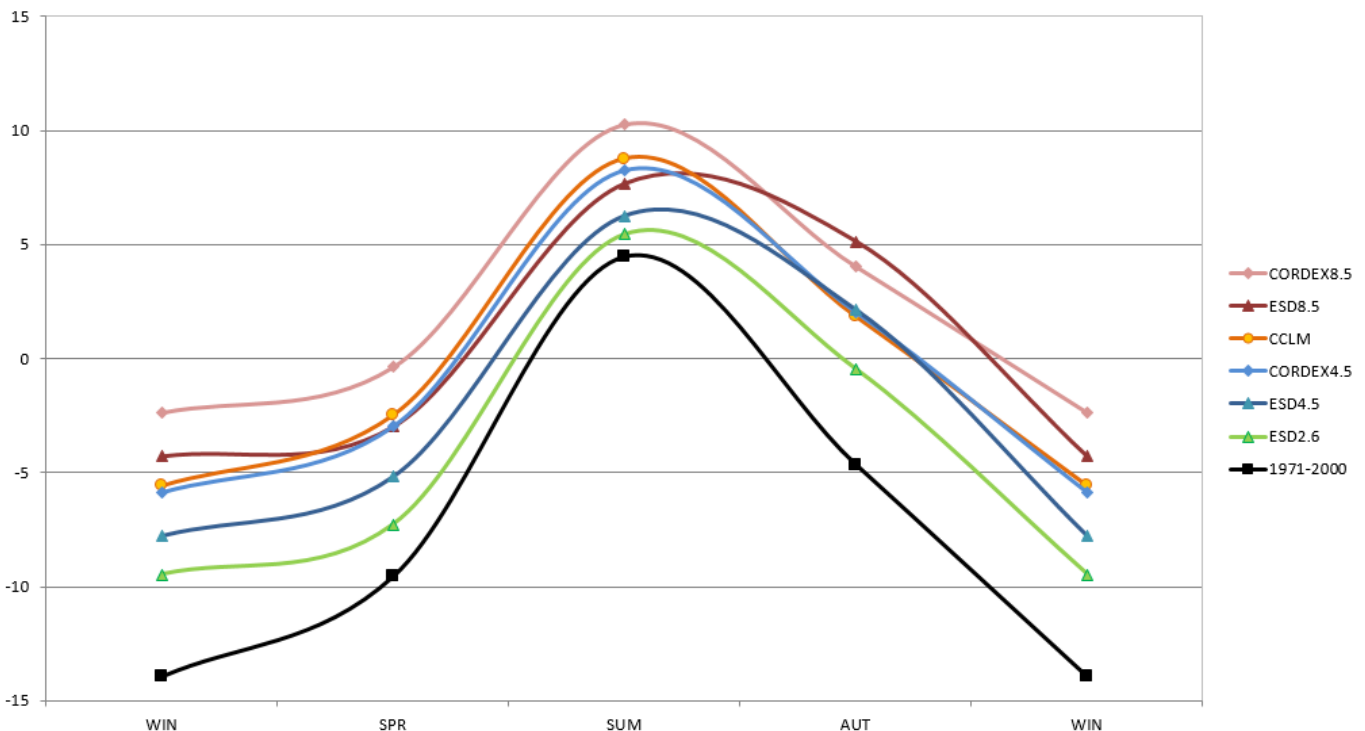
Figure 10.1.2 Observed present and projected future seasonal temperature cycle at Svalbard Airport/Longyearbyen [ºC]. Winter (Dec-Jan-Feb), spring (Mar-Apr-May), summer (Jun-Jul-Aug) and autumn (Sep-Oct-Nov) temperatures for the period 1971-2000 (black curve) are based on observations. Projections for the period 2071-2100: Arctic CORDEX median simulation under emission scenario RCP4.5 (light blue) and RCP8.5 (pink); ESD median simulations under RCP2.6 (green), RCP4.5 (dark blue) and RCP8.5 (red); CCLM RCP8.5 projection (yellow) .

The average number of days per year with maximum temperature above and minimum temperature below 0 °C ("zero crossings") was 60 in the control period. Zero crossings occurred in all seasons, but most frequently in the spring and autumn (Table 10.1.1). CCLM and the Arctic CORDEX median suggest a small increase in the number of such days. According to CCLM, there will be a reduction in zero crossings in the summer and an increase in the winter.

10.1.2 Precipitation

The mean annual precipitation measured in the Longyearbyen area is about 200 mm (Table 10.1.1); i.e. lower than the driest areas on the Norwegian mainland. The precipitation in Longyearbyen is also less than half the values measured at Barentsburg, Isfjord Radio and Ny-Ålesund (Table 4.3.1); discharge measurements from De Geerdalen (Chapter 10.2.1) and those modelled from the Sval-Imp dataset (Chapter 3.1.1, Vikhamar-Schuler et al., 2019). The precipitation measurements are hampered by undercatch in the gauges (Chapter 3.1.1), but the main reason why the Longyearbyen values are lower than the surroundings, is probably that Longyearbyen lies in a "rain shadow" on the leeward side of the mountain ranges. The historical variability of annual precipitation is shown in Figure 10.1.3. The observed annual precipitation has increased by approximately 4% per decade since measurements started in 1912, and the largest increase is found for the summer and autumn (Table 4.3.2). As stated in Chapter 4.3.2 the trends in the measured precipitation may be influenced by reduced undercatch because of an increasing fraction of the precipitation as rain.

a)

Element		Observed 1971-2000			
	ANN	DJF	MAM	JJA	SON
Mean air temperature (°C)	-5.9	-13.9	-9.6	4.5	-4.7
No. of Growing days	40	0	0	38	3
No. of Frost days	241	87	84	5	64
No. of Zero-crossing days	60	9	18	9	23
Mean precipitation (mm)	196	41	52	52	51

b)

Element		Changes to 2071-2100. CCLM (Arctic CORDEX)			
	ANN	DJF	MAM	JJA	SON
Air temperature change (°C)	+6.5 (+8.7)	+8.2 (+11.6)	+7.1 (+9.2)	+4.3 (+5.8)	+6.5 (+8.7)
Growing days, change	+73 (+121)	1	14	38	20
Frost days, change	-96 (-133)	-18	-35	-2	-40
Zero-crossing days, change	+9 (+2)	13	4	-7	-1
Precipitation change (%)	+19 (+39)	+21 (+26)	+29 (+36)	+6 (+37)	+21 (+40)

Table 10.1.1 a) Present climatology for Svalbard Airport/Longyearbyen and b) Projected changes from 1971-2000 to 2071-2100 under emission scenario RCP8.5. The projections are based on CCLM-simulations; median values from Arctic CORDEX are given in parenthesis.

Climate simulations show that both the annual and seasonal precipitation are estimated to increase in the future. For the RCP8.5 emission scenario, the median projection for the Arctic CORDEX ensemble gives an increase in annual precipitation of about 40% towards the end of the century, and for the CCLM the increase is approximately 20% (Table 10.1.1 and Figure 10.1.3). The CCLM projection indicates that the largest precipitation increase (around 30%) occurs in the spring and the lowest (around 5%) in the summer, while the median Arctic CORDEX results show an increase of 35-40% for the spring, summer and autumn and around 25% for the winter season. For emission scenario RCP4.5 the median increase for annual precipitation in the Arctic CORDEX ensemble is approximately 30%.

Precipitation intensities are usually rather low in Longyearbyen: Daily precipitation exceeding 1 mm occurs on average 50 days/year and exceeding 5 mm just 8 days/year (Isaksen et al., 2017). Despite the majority of low intensities, events with high rainfalls are not unusual. The highest observed daily rainfall at Svalbard Airport is 43 mm, and rainfalls exceeding 25 mm have a return period of around 10 years (Table 4.4.1).

The CCLM simulations for future heavy rainfalls indicate an increase of 20% for low return periods and 35% for the 100-year return period (Table 4.4.2). In recent years there has been a clear tendency for more precipitation as rain in the winter months (Figure 4.3.4). During the winter months, up to a threefold increase in the number of mild weather episodes with rain is calculated, as compared to the current situation (Isaksen et al., 2017).
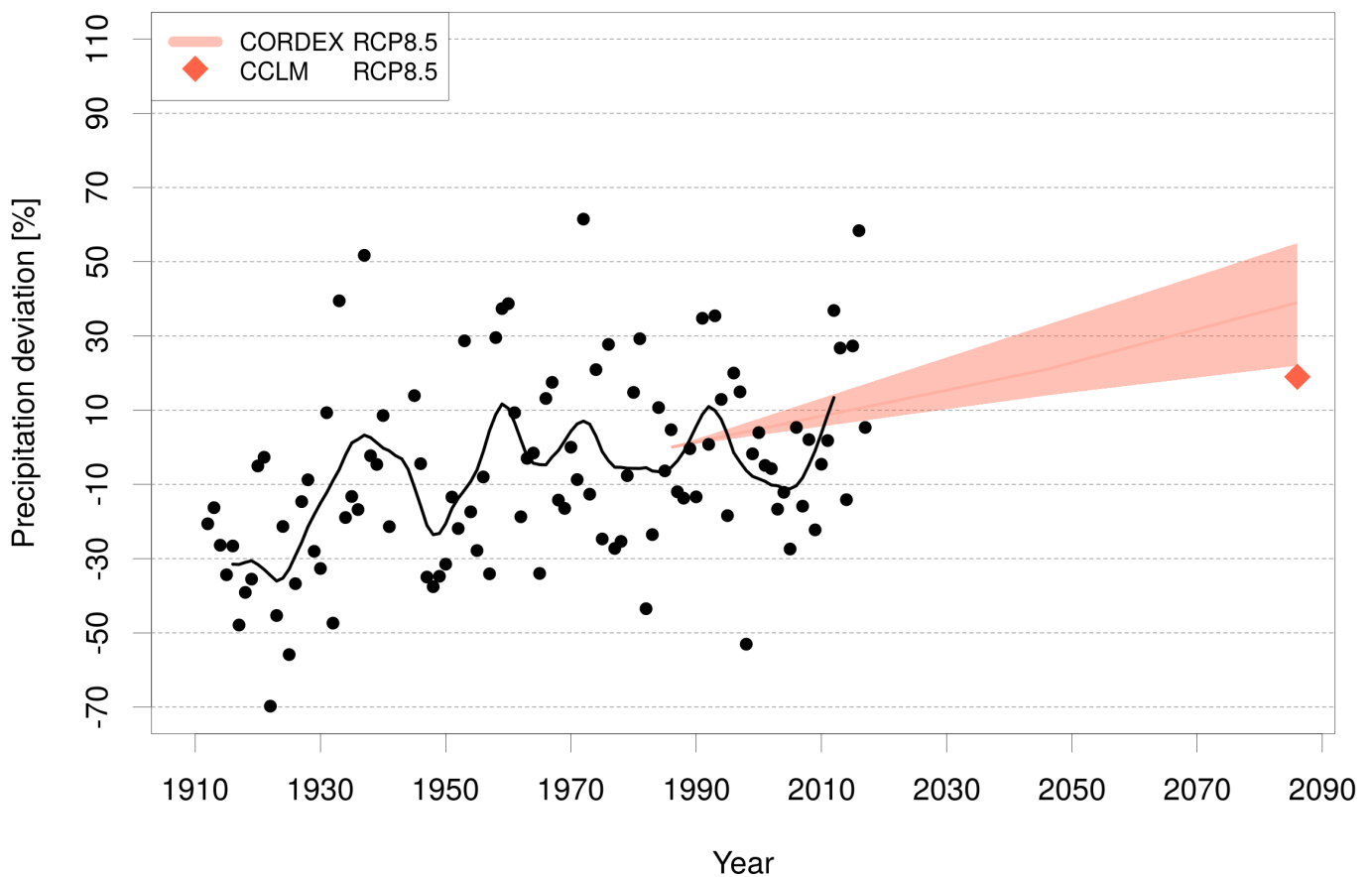
Figure 10.1.3 Annual mean precipitation for Svalbard Airport as a deviation [%] from the reference period 1971-2000. The points and black curve show single year and smoothed decadal variability based on observations from 1912 to 2017. Future projections are given for Arctic CORDEX and COSMO-CLM (CCLM) projections under emission scenario RCP8.5

10.1.3 Wind

At Svalbard Airport, the wind blows with force "strong breeze" (6 Beaufort) or more on 60 days a year on average and with highest frequencies in the winter (DJF). In the most recent 40 years, there has been a slight decline in the frequency of strong winds at Svalbard Airport (Isaksen et al., 2017). The dominant wind direction at Svalbard Airport is southeast, and this is particularly prominent (i.e. occurs more than 50% of the time) in the winter period November – April.

The CCLM simulations indicate that the dominant wind direction in the Isfjorden area remains fairly unchanged towards the end of the century. However, a slight decrease in wind speed is simulated for Isfjorden sea areas, as is a slight increase for mountain areas east of Longyearbyen. More information about present and future local wind conditions is presented in Dobler (2019).

10.2 Hydrology, snow and glaciers

10.2.1 River flow

Discharge measurements from De Geerdalen, approximately 20 km away from the river Longyearelva catchment, were used to set up a hydrological model for the river Longyearelva. The Longyearelva catchment is rather small, approximately 23 km^2, with approximately 30% covered by glaciers (Stenius, 2016). The river drains into Isfjorden, and the highest altitudes are more than 1000 m a.s.l. The modelled and observed runoff in the Longyearbyen area is more than twice the observed precipitation (Chapter 10.1.2). One reason for the high runoff values relative to precipitation is likely glacier melt, as the mass balance of the glaciers in the catchment has been negative for the previous 30-40 years (Chapter 10.2.4). Other contributing factors are undercatch of precipitation, and that the location of
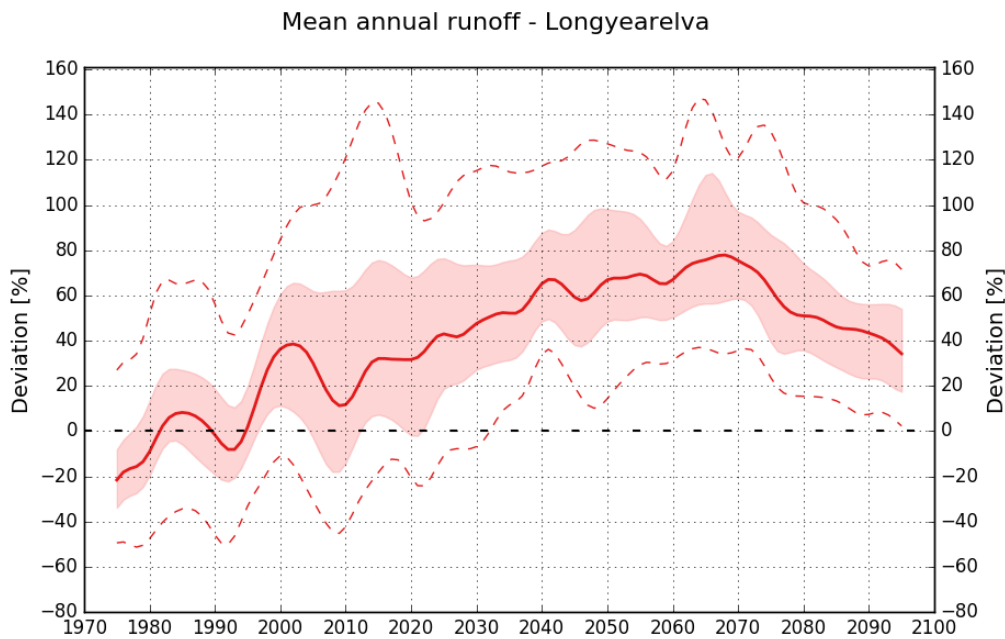
Figure 10.2.1. Mean annual runoff for the river Longyearelva, simulated using the HBV-model forced with downscaled and bias-adjusted Arctic CORDEX data, for the high emission scenario, RCP8.5. The solid red line shows the ensemble median of eight models; the pink band outlines the 25th and 75th percentiles, whereas the dotted lines indicate the minimum and maximum. Runoff values are given as a deviation (%) from the reference period 1971–2000. The low-pass filtered series are smoothed by Gaussian weighting coefficients and show variability on a decadal time scale.

precipitation stations (i.e., in low-laying areas) does not represent the precipitation amounts at higher elevations (Chapter 4.3.1; Killingtveit et al., 2003). Continued warming under the medium emission scenario (RCP4.5, not shown) and the high emission scenario (RCP8.5) leads to an increase in runoff towards the middle of the century, and a weaker increase towards the end of the century (Figure 10.2.1). The increase until approximately 2070 is caused by a combination of increased precipitation and glacier melt. After this, much of the glacier volume has melted and the contribution from glacier melt to the river Longyearelva is reduced. As discussed in Chapter 5, glacier melt is likely overestimated by the hydrological model, giving an increase in runoff which is both too rapid and too large, and a maximum runoff which occurs possibly too early in the 21st century.

The projected seasonal cycle of runoff shows an increase in the peak flow towards the middle of the century, mainly due to more efficient glacier melt and snowmelt (Figure 10.2.2). Because of increasing temperature, the snowmelt will start somewhat earlier during the year, and the autumn and winter runoff will increase slightly towards the end of the century, snowmelt starts much earlier and the peak runoff occurs one month earlier than in the present day climate. Because of reduced glacier volumes, glacier melt contributes less to the peak flow. Higher winter runoff is expected and, in particular, the late summer and autumn runoff increases because of increased precipitation and high temperatures causing glacier melt. These results are highly uncertain due to limited observational data, uncertainties in projected temperature and precipitation (Box 4.1 and 5.1), limited information about the glacier geometry and volume in the current climate and a too crude representation of the glaciers in the hydrological model.

Seasonal runoff distribution, Longyearelva
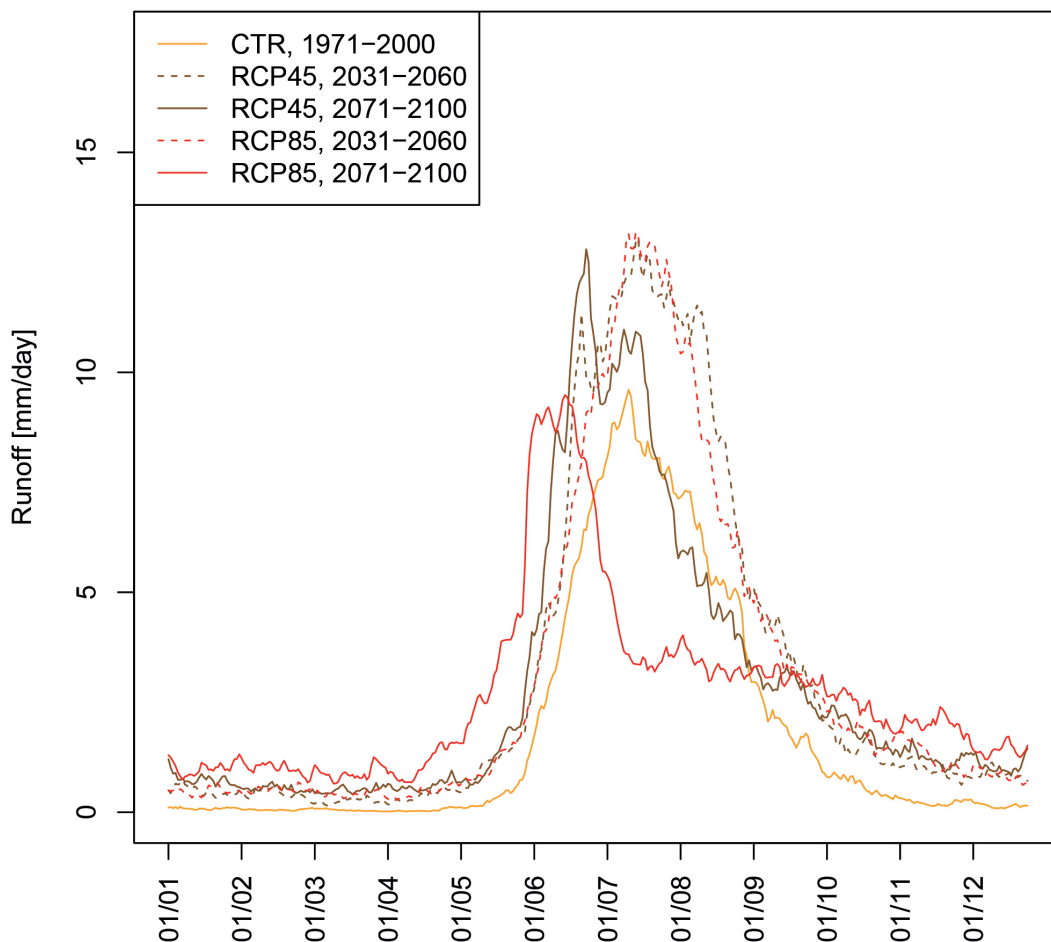
Figure 10.2.2. Modelled seasonal distribution of the Longyearelva runoff for the periods 1971–2000, 2031–2060 and 2071–2100.

10.2.2 Floods

A flood estimation is available for Longyearelva (Stenius, 2016), based, amongst other things, on the available discharge measurements from the river Bayelva (near Ny-Ålesund) and De Geerdalen. As described in Chapter 3.2 and Chapter 5.1.1, the records are short, constrained to the period June to September/October, and the observations are very uncertain. The majority of floods are observed during the snowmelt period in June and July, but floods caused by a combination of glacier melt and rain in August, September and October also occur, as do the winter floods generated by rainfall, e.g. in December 2015/January 2016.

Projected floods in a warmer climate can be assessed by looking at the modelled changes in the mean annual flood for the river Longyearelva. The mean annual flood in Longyearelva is expected to increase as long as the contribution from glacier melt increases. The contribution from snowmelt will gradually decrease as snow amounts are reduced, whereas increases in events with extreme rainfall can increase the frequency and magnitude of rain-dominated floods.

The development of the mean annual flood under RCP8.5 is shown in Figure 10.2.3 for Longyearelva. Similar to the mean annual runoff, the mean annual flood increases towards the middle of the century due to increased glacier melt and increased rainfall.
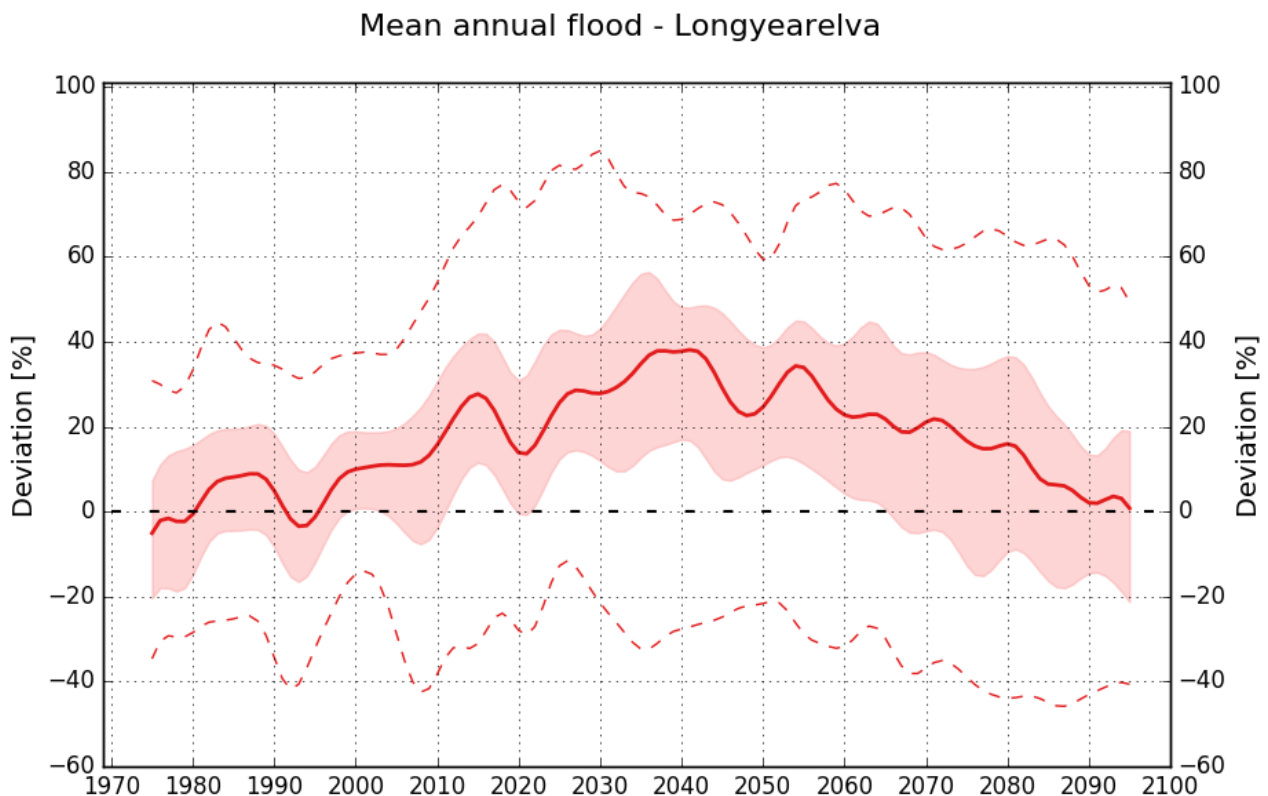
Figure 10.2.3. Mean annual flood for the river Longyearelva, simulated using the HBV-model forced with downscaled and bias-adjusted Arctic CORDEX data for the high emission scenario RCP8.5. The solid red line shows the ensemble median of eight models; the pink band outlines the 25th and 75th percentiles, whereas the dotted lines indicate the minimum and maximum. Flood values are given as deviation (%) from the reference period 1971–2000. The low-pass filtered series are smoothed by Gaussian weighting coefficients, and show variability on a decadal time scale.

10.2.3 Snow

The number of days with snow cover on the ground at low altitudes in and around Longyearbyen has decreased since the 1970s (Figure 10.2.4, Svalbard Airport) and will continue to decrease under both emission scenarios (Table 10.2.1). Even at higher altitudes (e.g. Platåberget 445 m a.s.l.), a reduction in the number of days with snow cover is projected when comparing the reference period 1971-2000 with the median scenario for both RCP4.5 and RCP8.5 for the future periods 2031-2060 and 2071-2100. For the RCP8.5 median projection, the reduction is almost six months at Svalbard Airport and three and a half months at Platåberget. The more moderate COS-MO-CLM (CCLM) projection also shows a reduction of the snow cover season of almost four months towards the end of the century.

Note that the criteria for snow cover in the model estimates is snow water equivalent larger than 20 mm (i.e. around 20 cm dry snow), while the observed snow cover just indicates that more than half the ground is covered by snow. The main reason why Table 10.2.1 despite the stronger snow cover criteria still shows a longer snow season than Figure 10.2.4 is that the precipitation (and thus also snow) is over-estimated in the model results (Chapter 5.2.1).

The maximum annual snow storage will also decrease as temperature and the fraction of precipitation as rain increases. The modelled annual maximum snow storage for Longyearbyen and Platåberget are given in Table 10.2.2 The modelled gradual reduction in maximum annual snow storage can be seen in Figure 10.2.5. The fastest reduction takes place under RCP8.5. It should be noted that
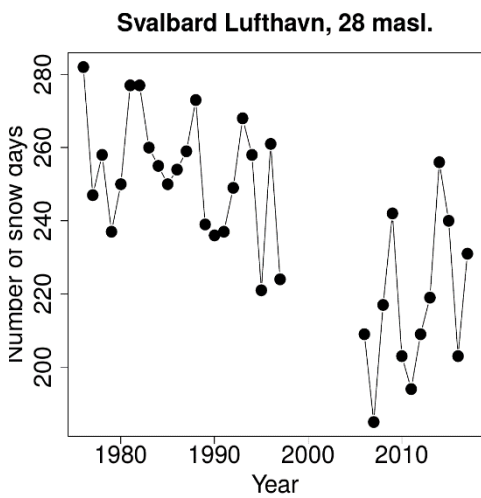
Figure 10.2.4 Snow cover duration observed at Svalbard Airport, 28 m a.s.l. (Plot generated based on data from http://www.mosj.no/en/climate/land/duration-snow-cover.html.)

1971-2000 (Sval-Imp)		From 1971-2000 to 2031-2060	From 1971-2000 to 2071-2100
284 days	Arctic CORDEX RCP4.5	*-80 days*	*-128 days*
		-53 days	**-76 days**
328 days	Arctic CORDEX RCP8.5	*-90 days*	*-177 days*
		-55 days	**-108 days**
	COSMO-CLM RCP8.5	-	*-118 days*
			-113 days

Table 10.2.1 Modelled reduction of snow cover duration in the Longyearbyen area, 2 m a.s.l. and Platåberget, 445, m a.s.l. using different models. (Number of days per year with more than 20 mm snow water equivalent are shown as 30-year mean values.) *Italic: Longyearbyen*, **Bold: Platåberget.**

1971-2000		From 1971-2000 to 2031-2060	From 1971-2000 to 2071-2100
336 mm **494 mm** *(Sval-Imp)*	*Arctic CORDEX median, RCP4.5*	*-48%* **(-15%)**	*-66%* **(-22%)**
	Arctic CORDEX median, RCP8.5	*-48%* **(-19%)**	*-90%* **(-67%)**
	COSMO-CLM RCP8.5	-	*-69%* **(-66%)**

Table 10.2.2 Modelled maximum annual snow storage in the Longyearbyen area, 2 m a.s.l. and Platåberget 445 m a.s.l. Historic period: mm snow water equivalent. Future periods: relative change (%) shown as 30-year mean values. *Italic: Longyearbyen*, **Bold: Platåberget.**

for Platåberget under RCP4.5, the reduction is not large. It should also be noted that the interannual and decadal variability can be large, and in the near future, years with larger than average snow amounts can be expected even at lower altitudes.

10.2.4 Glaciers

Central Spitsbergen is the least glaciated region of Svalbard (Nuth et al, 2013). Only ~30% of its land area is covered by glaciers (Figure 10.2.6), due to the lower precipitation in the interior, compared with the coastal areas. The glaciers near Longyearbyen are in general higher in the terrain than those along the western coast, and largely comprise valley glaciers. Similarly to glacier all around Svalbard, glacier area has been decreasing with time (Figure 10.2.6).

Only one glacier near Longyearbyen has had mass balance measurements of any duration: Bogerbreen (Figure 10.2.6) was measured by Soviet Union scientists from 1975-1985, and by University of Oslo, UNIS and NPI for three years in the early 2000s (Neumann, 2006; J. Kohler, unpublished data) (Figure 10.2.7). The mean net balance of all measurements is -0.5 m w.eq. year[-1], roughly the same as the long-term average for the small valley glaciers Austre Brøggerbreen and Midtre Lovénbreen near Ny-Ålesund, even though the latter are at lower elevations. A regression of the balance terms between the Austre Brøggerbreen and Bogerbreen allows

an estimation of the long-term net balance of the former. The trend is negative, but not statistically significant, as for the Austre Brøggerbreen record. The mean equilibrium line altitude (ELA) for the 2000s measurements was 824 m a.s.l. No ELA was available for the older Soviet-era measurements.

The long-term outlook for these glaciers is the same as elsewhere in Svalbard (Chapter 6), namely they are expected to lose mass at an increasing rate. Using the future simulations presented in Chapter 6, we extracted grid points for the Longyearbreen area to calculate the change in mass balance between the two time periods 1970-2000 and 2070-2100. There is no clear pattern to the change as a function of elevation, meaning that the mass balance gradient remains close to that of the present, but the step change is significant at 1.8 m w.eq. year[-1], and the simulated future ELA is significantly higher than the present (around 825 m a.s.l. for Bogerbreen) at 1400 m a.s.l. Since this is much higher than the highest elevations of the glaciers in the area, we can expect a rapid wasting away of these glaciers.

10.2.5 Erosion and sediment transport

In its natural state, the entire length of the river Longyearelva from the glaciers to the sea was a braided river system. Along with the development of Longyearbyen, roads, bridges and housing have confined the river. Channel stability has been maintained by removing the flood deposits by bulldozers.
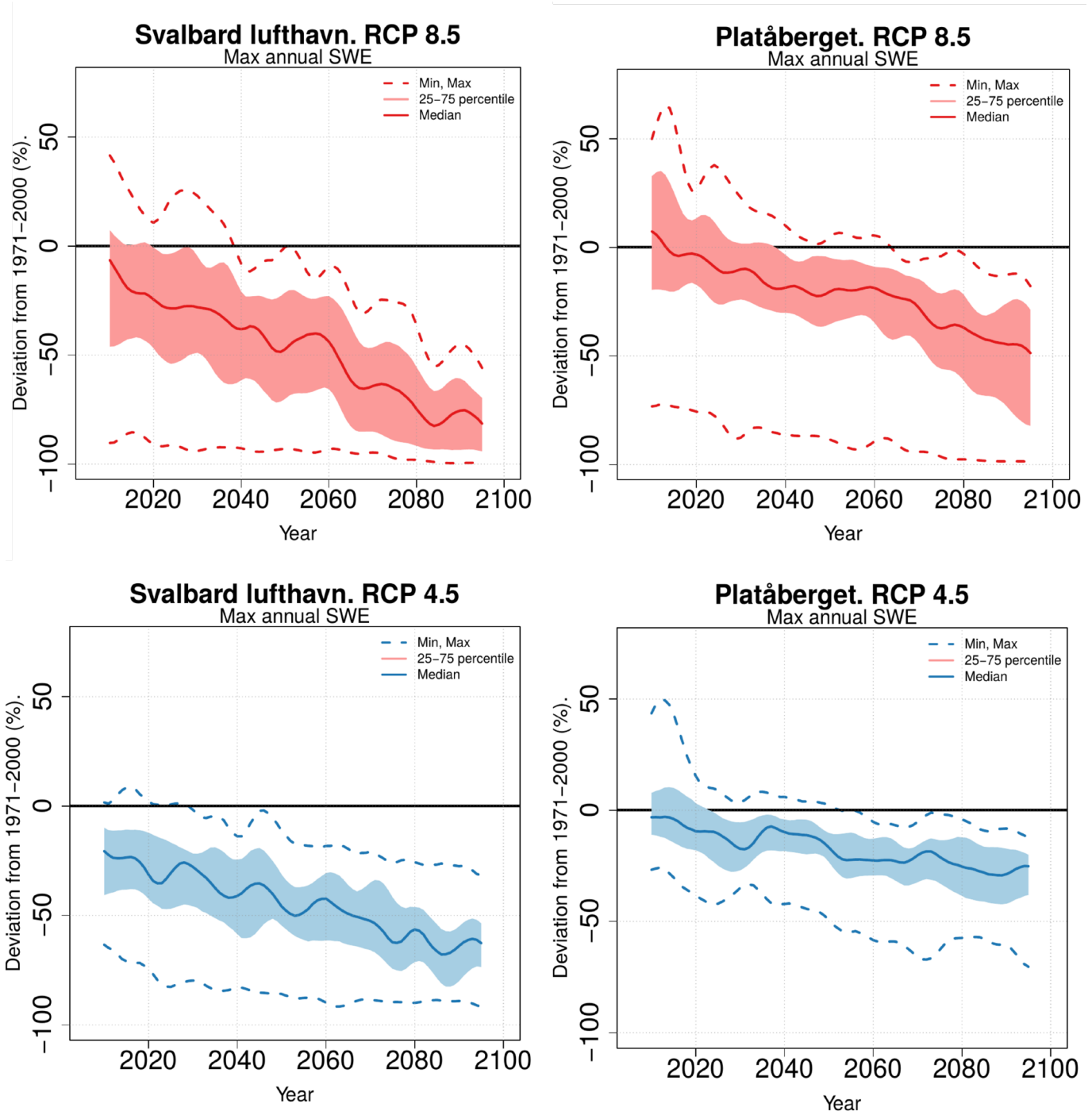
Figure 10.2.5 Maximum annual snow storage (deviation from 1971-2000, %) at the valley bottom (Svalbard Airport, left) and at the mountain plateau area (Platåberget, right). Simulations show the ensemble median, 25-75 percentiles (shaded area), minimum and maximum from the snow model run with the bias-adjusted Arctic CORDEX projections RCP4.5 (upper panel) and RCP 8.5 (lower panel). The time series are derived from the nearest 1 by 1 km^2 grid-cell to the weather station locations.
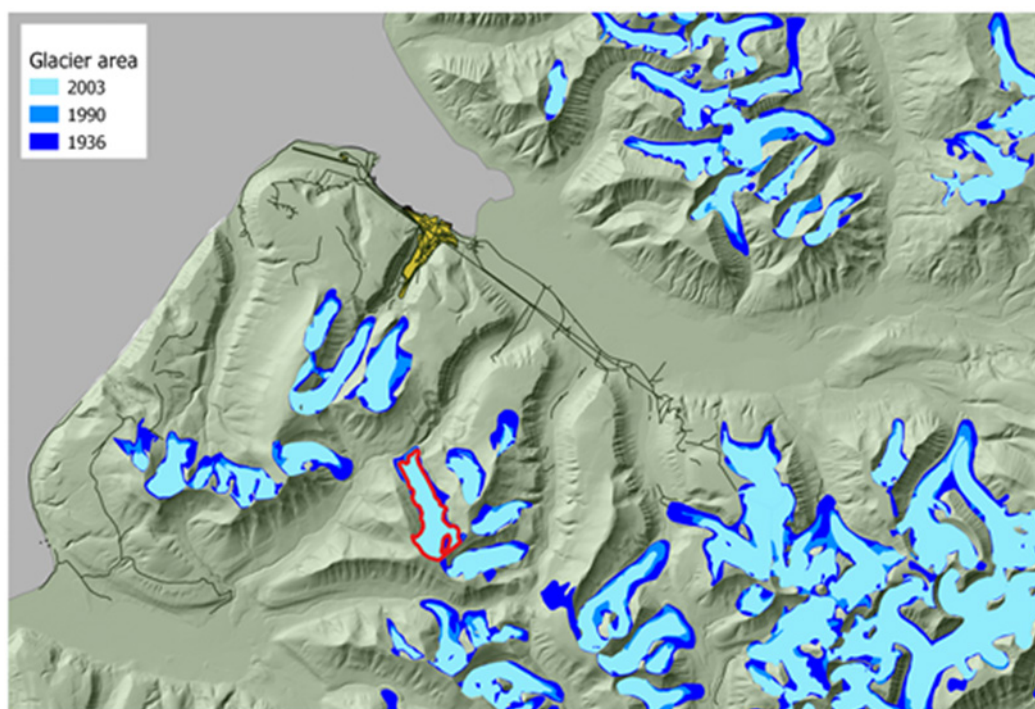
Figure 10.2.6 Glaciers near Longyearyen, with Bogerbreen outlined in red.

$$y = -0.01x + 10.29$$
$$R^2 = 0.05$$
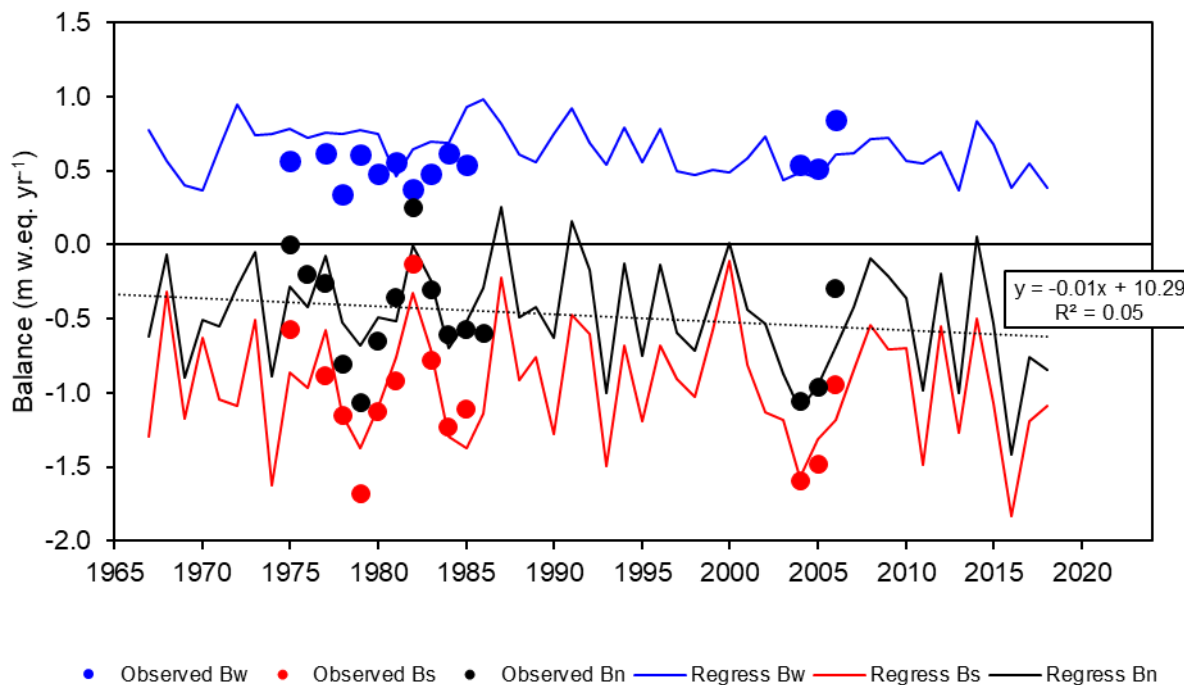
Figure 10.2.7 Winter, summer and net balance for Bogerbreen, near Longearbyen. Blue lines show the total accumulation on the glacier during the winter, converted to an area average thickness of water (metres of water equivalent, m w.eq.); red lines similarly show the net melt over the summer, while black lines are the sum of the two, or the total mass gained or lost through the glacier surface processes over the year. The observations (symbols) are extended by performing a linear fit of the Bogerbreen to the long-term Austre Brøggerbreen record. The trend is shown for the regressed net balance.

To secure areas of the floodplain for construction of houses and further erosion protection, a sedimentation dam will be built. It is anticipated that climate change with increasing temperatures, glacier melt and heavy rainfall will lead to increased river flows and floods. This will increase the intensity of erosion and the sediment transport and thus sedimentation that are delivered from the sources. Erosion of the moraines of the Larsbreen appear to be an important sediment source that will be subject to a future increase. The presence of permafrost limits the erosion. However, as the temperature of the active layer rises, more sediments are available for transport (Etzelmuller and Frauenfelder, 2009).

10.3 Permafrost, landslides and avalanches

10.3.1 Permafrost and solifluction

Relatively warm permafrost occur in the Longyearbyen area, which is especially sensitive to warming. The permafrost temperature records nearby Longyearbyen generally show a continuous temperature increase in the upper 10-20 m of the ground the last 20 years. Since 2008-2009 ground temperatures have increased with rates between 0.06°C and 0.15°C per year at 10 m depth (Chapter 7.1).

Recent permafrost modelling by Instanes and Rongved (2017) for three different locations in Longyeardalen (the Svalbard Science Centre, the town centre and Skjæringa) based on recent regional climate model runs using the RCP4.5 scenario suggest an increase in the active-layer thickness, from about 1.5 m today to 2.5 m by the end of the century. Using the RCP8.5 scenario to simulate the ground temperatures in the upper 10 m in Longyearbyen suggest a substantial thickening of the active layer and an increase in permafrost temperatures at 5 m and 10 m depth that will be close to 0 °C before the end of the present century (Chapter 7.1). Due to high ice content in the fluvial material and silt and clay-dominated marine sediments in Longyeardalen, warming rates are efficiently reduced due to the consumption of latent heat for melting of ice. However, as warmer permafrost is more deformable

than cold permafrost, this will cause increases in creep rates of existing foundations such as piles and footings (Instanes, 2003) and a speed up of slope processes controlled by permafrost such as rock glacier deformation and solifluction.

Solifluction is a slope process primarily occurring in the lower slopes of the valley Longyeardalen that will also be affected by climate change. Permafrost warming and increase in active-layer thickness in the higher rock and debris slopes around Longyearbyen may also lead to increased instability, manifested as an increased number and magnitude of rock falls, debris flows, and related phenomena. This needs to be considered when planning and building new infrastructure (Chapter 7.2).

10.3.2 Avalanches and landslides

Evidence of avalanches and landslides are seen in the landscape in and around Longyearbyen. Examples are larger rocks from rockfalls in the valley bottom of Longyeardalen and debris flow tracks with levees on the mountain slopes. Avalanches and debris flows occur on all mountainsides. Snow avalanche release in Longyearbyen is primarily a consequence of drifting snow, embedded weak layers and cornice collapses triggering also larger slab avalanches (Chapter 7.3). Hestnes et al. (2016) give an overview of avalanches and landslides that have caused damages to infrastructure and buildings, as well as fatalities and injuries.

More sediment delivery to the main river may cause aggradation, channel changes and lateral activity in the area upstream from the sedimentation dam. Debris slides and debris flows need special attention as they may deliver large amounts of material to the channel system during single events. To assess the volumes involved and the possible aggradation at the glacier outwash fans that may trigger channel changes, monitoring in the upper part of the catchment, e.g. using red laser scans (Bogen et al., 2016), is a possibility.

Snow avalanches have caused a number of fatalities. The first known fatalities concern two teenagers, who were killed by an avalanche on Longyearbreen during Easter 1978. Since February 2001 seven additional fatalities and numerous accidents due to avalanches have occurred in Longyearbyen, or in the general vicinity of Longyearbyen: two snowmobilers were caught by an avalanche in February 2001 (Fardalen); further accidents happened in April 2004 (Mälardalen), March 2009 (Hiorthfjellet) and January 2015 (Fardalen), all involving snowmobile-triggered avalanches. In December 2015, two people died when a large slab avalanche from the ridge north of Sukkertoppen destroyed ten houses in Longyearbyen. In February 2017, another slab avalanche released from the top of the mountain Sukkertoppen, triggering a secondary avalanche that reached the settlement. Several buildings were damaged, but luckily, this time with no fatalities. These accidents have led to a higher focus on a safe infrastructure, especially restructuring of the housing areas, building avalanche protective measures and focussing on avalanche observations, prediction, preparedness, mitigation, education and research.

A detailed mapping of avalanches between 2006 and 2009 according to type can be seen in Figure 10.3.1 (Eckerstorfer and Christiansen, 2011c), illustrating avalanche activity on the most used snowmobile track "Little Round" close to Longyearbyen. Almost 50% of 423 avalanches were cornice fall avalanches due to the plateau mountain topography and prevailing south-easterly winds (Chapter 10.1.3). Slab avalanches were also frequent (~30%). Most avalanches were released in spring after low-pressure systems with rising temperatures, high wind speeds and precipitation reaching Svalbard. Hancock et al. (2018) found strong easterly winds and moderate to heavy snowfall as precursors to the two devastating naturally triggered avalanches on the west-facing slope of Sukkertoppen in 2015 and 2017.

Due to favourable topographic and climatic conditions, the valley Vannledningsdalen in Longyearbyen (Figure 10.3.2) has a history of slushflows, often occurring during the spring thaw. In the summer of 1953, for example, a slushflow occurred on
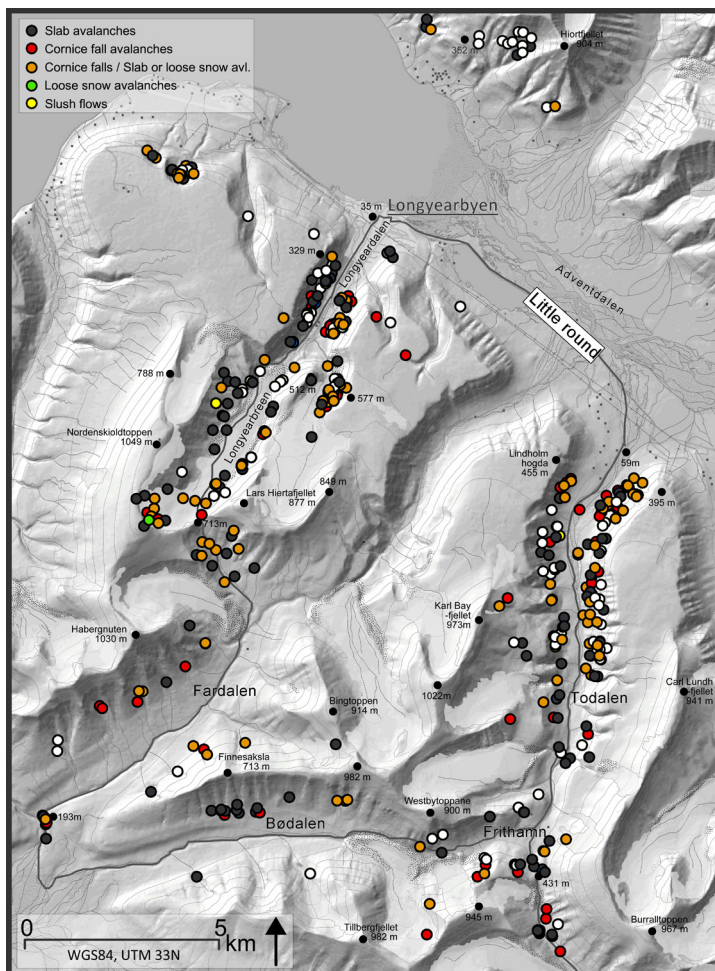
Figure 10.3.1 The furthest runout distance of all 423 avalanches indicated by points along "The Little Round" snowmobile track for the period 2006 to 2009. The colour of the points distinguishes avalanche types. (Reprinted from Eckerstorfer and Christiansen, 2011c; reproduced by permission of Elsevier)

the large depositional fan called the Haugen area of Longyearbyen at the mouth of Vannledningsdalen, destroying several houses, killing three people and injuring another 30 (Ramsli, 1953). Following this event, protective measures were built and routines were established for drainage measures prior to snowmelt. The routines were not followed in 1989, resulting in a slushflow from Vannledningsdalen, which hit the Haugen area again on 14 June, damaging one house and destroying the main water and heating pipes. In the midwinter of 2012, another slushflow caused by a rain-on-snow event destroyed the pedestrian bridge across the river from Vannledningsdalen (Hansen et al. 2014). Smaller slushflows have also reached the new harbour-area and have been observed from Larsbreen and Tverrdalen following rain events. Hestnes et al. (2016) state that slushflows from Larsbreen may reach Nybyen.

Rockfalls from steep cliffs and protruding rock noses along the plateau edges are frequent, but have so far only led to damages of infrastructure. Debris flows and slides have also caused damage to infrastructure in Longyearbyen. In July 1972, 80 debris flows and slides caused damage to the local infrastructure in the lower Longyeardalen valley when approximately 30 mm of rain fell in the Longyearbyen area in 12 hours (Larsson, 1982). Two relatively large rainstorms reached Svalbard in October and November 2016, triggering 26 larger hillslope mass movements mapped in the areas just around Longyearbyen. The events are described in detail by Christiansen et al. (2019b). The majority of slope mass movement occurred during the October rainstorm (e.g. Figure 10.3.3), which had the lowest rain intensity, with only in total around 20 mm of rain recorded. The November rainstorm had much more rain, around 75 mm (recorded by a mini-logger in

Figure 10.3.2 The valley Vannledningsdalen and the Haugen fan with protective measures, 18 August 2012. Note the summer-firn, a result of considerable snow accumulation. Photo: Hanne H. Christiansen

Longyearbyen), and with a much higher intensity. This storm, however, led to only very limited slope mass movement locally in the Longyearbyen area. During the October storm, the still unfrozen active layer likely became rapidly water saturated with no percolation beyond the permafrost table. As thaw was near the annual maximum, the melting of ice lenses at the top of the permafrost likely contributed to increased pore water pressure at the active layer/permafrost interface, contributing to the initiation of many slope failures. In contrast, before the second storm, the upper active layer had frozen, impeding infiltration of rainfall and thus limiting slope failures despite much more precipitation.

The projected changes in climate with increasing temperatures and precipitation, although there are only insignificant changes in wind conditions, may increase the frequency of all types of avalanches and landslides that already occur in the Longyearbyen area (Chapter 7.3.3). Climate change and increased uncertainty were addressed as one of the main challenges for avalanche forecasting and risk management in Longyearbyen in the evaluation report after the February 2017 event (Landrø et al., 2017). Indeed, avalanche accidents and avalanche related problems, along with increased backcountry activities, led to the establishment of a regional avalanche warning region, Nordenskjöld Land. Since February 2016 the Norwegian Avalanche Warning Service at the Norwegian Water Resources and Energy Directorate (NVE, Varsom.no) has issued regional avalanche warnings. After the fatal avalanche in December 2015, local avalanche danger warnings for avalanche paths threatening houses in Longyearbyen were also issued by NVE. In addition, protection measures to prevent avalanches from hitting buildings have been built after 2015. This

Figure 10.3.3 Slope failures at the Longyearbyen cemetery 16 October 2016 causing a slump and associated debris flow crossing the road. Photo: Hanne H. Christiansen.

includes snow fences, supporting structures and a smaller melt water drainage. After the avalanche event in 2017, new hazard maps were made for the area exposed to avalanches from the west-facing slopes of Sukkertoppen and further protection measures are recommended (Hoseth et al., 2018; Gundersen et al., 2018). Regarding the slushflows

in Vannledningsdalen, a warmer and wetter climate may lead to such slides in the mid-winter without the possibility for prior draining measures. Hence, further protective measures are considered also in Vannledningsdalen.

10.4 Ocean

Atlantic Water (AW) from the West Spitsbergen Current can reach the upper shelf along western Spitsbergen and eventually flood into the fjords (Nilsen et al., 2008; 2016). These warm water intrusions have a strong effect on the seasonal sea ice cover inside the fjords. A distinct shift to a lower sea ice cover occurred in 2006, as seen from remote sensing data from 2000 to 2014 (Muckenhuber et al., 2016). Before 2006 the mean was 50 days of land-fast ice for Isfjorden, while after 2006 the mean dropped to 22 (Figure 8.3.4). These observations also show that Isfjorden had two periods with relatively high sea ice cover (2000–2005 and 2009–2011) and two periods with relatively low sea ice cover (2006–2008 and 2012–2014). All periods last 3 years or more, which suggests the involvement of an oceanic mechanism because the atmospheric

conditions vary on shorter time scales. However, wind forcing on the West Spitsbergen Shelf on timescales from days to months is one of the mechanisms starting a circulation of warm AW towards the fjords (Cottier et al., 2007; Nilsen et al., 2016). Ongoing hydrographic measurement programs and the construction of longer time series (e.g. Pavlov et al., 2013; Tverberg et al., 2018) show that the fjords along west Spitsbergen shifted from an Arctic state to a more Atlantic state after the winter 2006 (Cottier et al., 2007). This has large implications for the local climate and the winter air temperatures in Longyearbyen and other settlements along the west coast of Svalbard.

Figure 10.4.1 shows the simulated winter sea surface temperature and ice concentration today and
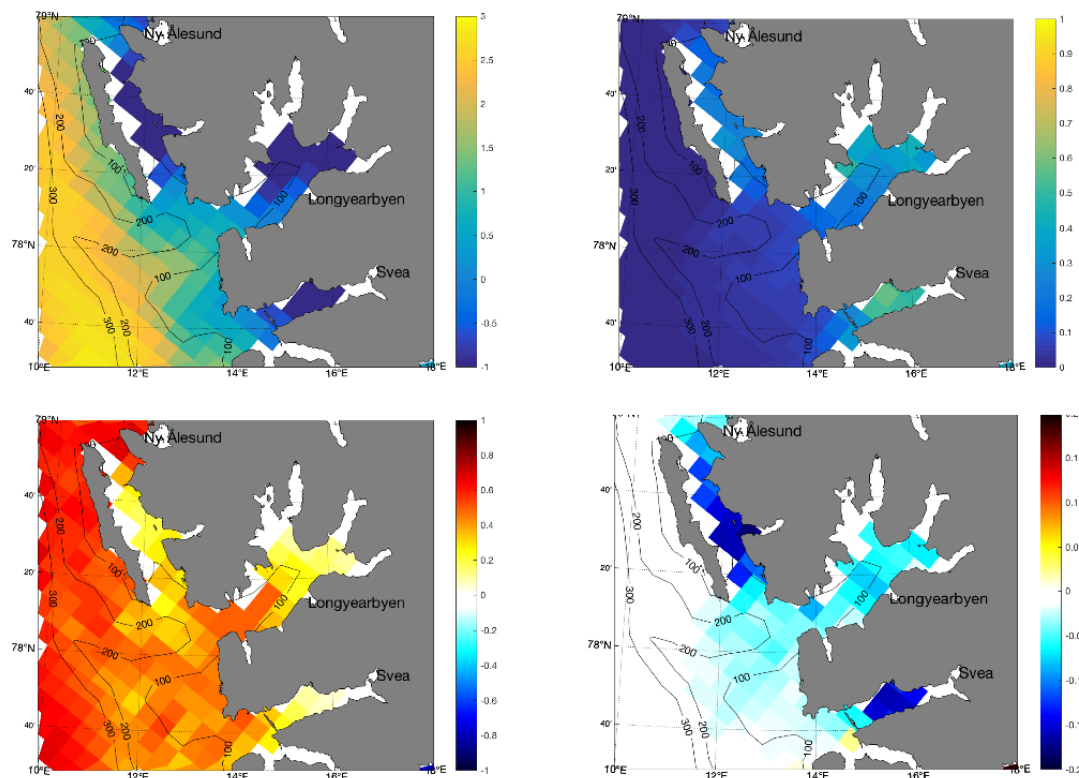
Figure 10.4.1 Simulated sea surface temperature (°C, left) and sea ice concentration (fraction, right) around Isfjorden on the west coast of Svalbard. Fields shown are monthly means for March in the present climate (upper, 2010-2019) and the future change (lower, 2060-2069 - 2010-2019) of the RCP4.5 scenario.

change into the future in different fjords close to Longyearbyen. In general, temperatures will rise and sea ice diminish. The temperatures in the fjords are much lower than in the ocean outside which is strongly influenced by AW. The change in future sea surface temperature appears most affected along the AW path and where it penetrates into the fjords (Figure 10.4.1 lower left). Ice concentrations are generally higher inside the sheltered fjords that have longer pathways for the AW flow. The largest sea ice loss, of about 20%, occurs in Van Mijen-fjorden outside Svea and in Forlandsundet between Isfjorden and Ny Ålesund, but there is also a clear loss of sea ice inside Isfjorden itself.

Sea level rise is a large-scale phenomenon; hence, the assessment in Chapter 8.4 is representative for Longyearbyen. Any spatial differences between

Ny-Ålesund, Barentsburg, and Longyearbyen would have to come from land uplift. The land uplift due to Glacial Isostatic Adjustment is similar to Barentsburg (Figure 8.4.3a). Differences that are more detailed would have to come from individual glacier mass changes, for which projections are currently not available. Existing AR5 projections of surface mass balance show no spatial difference between these locations (Figure 8.4.3b). For Longyearbyen, the ensemble mean projected relative sea level change is -0.39 m (ensemble spread -0.84 to 0.13 m) for RCP8.5 and over the period from 1986–2005 to 2081–2100, i.e. the sea level will sink. Differences between emission scenarios are minute and far smaller than the ensemble spreads (Figure 8.4.5).

10.5 Synthesis

The projections show that the temperature and precipitation in Longyearbyen will increase towards the end of the century. Under the emission scenario RCP8.5 the median value indicates that the annual temperature will increase by 8.5 °C and the CCLM indicates an increase of 6.5°C; - i.e. the annual mean temperature for Longyearbyen will increase to above 0 °C. The winter temperatures will increase more than the summer temperatures. The median RCP8.5 projection indicates an increase of 40% in the annual precipitation, whereas the CCLM projection indicates an increase of 20%. In addition, the frequency and intensity of heavy rainfall events will increase. The wind simulations for a future climate do not indicate significant changes, either in magnitude or in direction.

These changes will intensify glacier melt, and river flow including floods will likely increase, although the results concerning floods are very uncertain. The percentage of the catchment area covered by glaciers is decisive for the changes in river flow. The seasonal distribution of runoff will change with

an earlier snowmelt and higher winter and autumn runoff. Increases in rain, glacier melt and river flows will increase erosion and sediment transport. The number of days with snow cover will continue to decrease and even the moderate CCLM-projection shows a reduction of the snow cover season of almost four months towards the end of the century.

The projected changes in climate with increasing temperatures and precipitation, and increasing permafrost temperatures, will likely increase the frequency of all types of avalanches and landslides that already occur in the Longyearbyen area.

In the ocean, the temperatures will rise, the sea ice will diminish, and the sea-level will most likely sink.

References

Aarnes OJ, O Breivik, M Reistad (2012). Wave Extremes in the Northeast Atlantic, *J Climate*, 25, pp 1529-1543, doi:10/bvbr7k

Aarnes OJ, M Reistad, O Breivik, E Bitner-Gregersen, LI Eide, O Gramstad, AK Magnusson, B Natvig, E Vanem (2017). Projected changes in significant wave height towards the end of the 21st century: Northeast Atlantic, *J Geophys Res: Oceans,* 122, pp 3394-3403, doi:10.1002/2016JC012521

Aas K, T Dunse, E Collier, T Schuler, T Berntsen, J Kohler and B Luks (2016). The climatic mass balance of Svalbard glaciers: a 10-year simulation with a coupled atmosphere-glacier mass balance model. *The Cryosphere*, 1089–1104.

ACIA (2005). Arctic Climate Impact Assessment. *CambridgeUniversity Press*, 1042p. (Available at http://www.amap.no/acia/)

AMAP, 2017. Snow, Water, Ice and Permafrost in the Arctic (SWIPA) (2017). *Arctic Monitoring and Assessment Programme* (AMAP), Oslo, Norway. xiv + 269 pp

Andersen OB and G Piccioni (2016). Recent Arctic Sea Level Variations from Satellites, *Frontiers in Marine Science*, 3:76. doi: 10.3389/fmars.2016.00076.

André M-F (1990) Frequency of debris flows and slush avalanches in Spitsbergen: a tentative evaluation from lichenometry, *Polish Polar Research*, 11 (3-4), 345-363

Barnes EA, E Dunn-Sigoin, G Masato and T Woolling (2014). Exploring recent trends in Northern Hemisphere blocking. *Geophys. Res. Lett.*, 41, 638–644, doi:10.1002/2013GL058745.

Barsch D, M Gude, R Mausbacker, G Schukraft and A Schulte. (1994). Recent fluvial sediment budgets in glacial and periglacial environments, NW Spitsbergen. *Zeitschrift fűr Geomorphologie* N.F. suppl.bd 97,111-122

Beierlein L, O Salvigsen, BR Schone, A Mackensen, and T Brey (2015). The seasonal water temperature cycle in the Arctic Dicksonfjord (Svalbard) during the Holocene Climate Optimum derived from subfossil *Arctica islandica* shells. *The Holocene*, 25(8), 1197–1207. http://doi.org/10.1177/0959683615580861

Beldring,S, K Engeland, LA Roald, NR Sælthun and A Voksø (2003). Estimation of parameters in a distributed precipitation-runoff model for Norway. *Hydrology and Earth System Sciences*, 7, 304-316.

Benestad RE (2001). A Comparison between Two Empirical Downscaling Strategies. *Int. J. Climatol.*, 21, 1645–1668.

Benestad RE (2003). What can present climate models tell us about climate change? *Climatic Change* Vol 59, 311-332.

Benestad RE, KM Parding, K Isaksen and A Mezghani (2016). Climate change and projections for the Barents region: what is expected to change and what will stay the same? Environmental Research Letters, 11(5): 054017, doi:10.1088/1748-9326/11/5/054017.

Bengtsson L, VA Semenov and OM Johannessen (2004). The early twentieth-century warming in the Arctic – a possible mechanism. *J. Clim.,* 17, 4045-4057

Bentsen M et al. (2013). The Norwegian Earth System Model, NorESM1-M—Part 1: Description and basic evaluation of the physical climate, *Geosci. Model Dev.*, 6(3), 687–720, doi:10.5194/gmd-6-687-2013.

Berben SMP, K Husum, A Navarro-Rodriguez, ST Belt and S Aagaard-Sørensen (2017). Semi-quantitative reconstruction of early to late Holocene spring and summer sea ice conditions in the northern Barents Sea. *Journal of Quaternary Science,* 32(5), 587–603. doi: 10.1016/j.marmicro.2012.10.001.

Berge J, G Johnsen, F Nilsen, B Gulliksen and D Slagstad (2005). Ocean temperature oscillations enable reappearance of blue mussels Mytilus edulis in Svalbard after 1000 yr absence, *Marine Ecology Progress* Series, 303, 167-175.

Bergström S (1995). The HBV-model. In: Singh, V.P. (Ed.), Computer Models of Watershed Hydrology. *Water Resources Publications*, Highlands Ranch, 443-476.

Berhardt H, D Reiss, E Hauber, H Hiesinger and A Johnsson (2017). Short debris flow recurrence periods for a Svalbard debris fan: Possible implications for earth and Mars. *Lunar and Planetary Science*, XLVIII (Conference proceedings), 1132.pdf

Binder H, M Boettcher, CM Grams, H Joos, S Pfahl and H Wernli (2017). Exceptional air mass transport and dynamical drivers of an extreme wintertime Arctic warm event. Geophys. Res.Lett., 44, 12,028–12,036. https://doi.org/10.1002/2017GL075841

Bintanja R and O Andry (2017). Towards a rain-dominated Arctic. *Nature Climate Change* 7: 263-267

Błaszczyk M, J Jania and JO Hagen (2009). Tidewater glaciers of Svalbard: Recent changes and estimates of calving fluxes. *Polish Polar Research*, 30(2), 85-142.

Blikra LH and HH Christiansen (2014). A field-based model of permafrost-controlled rockslide deformation in northern Norway. *Geomorphology*, 208, 34-49 http://dx.doi.org/10.1016/j.geomorph.2013.11.014

Blikra LH, HH Christiansen, L Kristensen and M Lovisolo (2015). Characterization, Geometry, Temporal Evolution and Controlling Mechanisms of the Jettan Rock-Slide, Northern Norway. In: Lollino G. et al. (eds) *Engineering Geology for Society and Territory* 2, 273-278

Blindheim J, V Borovkov, B Hansen, SA Malmberg, WR Turrell and S Østerhus (2000). Upper layer cooling and freshening in the Norwegian Sea in relation to atmospheric forcing, *Deep-Sea Research I,* 47, 655-680.

Bogen J and TE Bønsnes (2003). Erosion and sediment transport in high Arctic rivers, *Svalbard Polar Research* 22 (2) 175-189

Bogen J, TE Bønsnes, AM Moquet-Stenback, M Xu and MC Elster (2016). Gudbrandsdalslågen. Sedimentkilder og sedimenttransport som bakgrunn for tiltak i forvaltningsplanen. *NVE-rapport* Nr. 89-2016, pp 145

Boike J, I Juszak, S Lange, S Chadburn, E Burke, PP Overduin, K Roth, O Ippisch, N Bornemann, L Stern, I Gouttevin, E Hauber and S Westermann (2018). A 20-year record (1998–2017) of permafrost, active layer and meteorological conditions at a high Arctic permafrost research site (Bayelva, Spitsbergen), *Earth Syst. Sci. Data,* 10, 355-390, https://doi.org/10.5194/essd-10-355-2018.

Breili K, MJR Simpson and JEØ Nilsen (2017). Observed Sea-Level Changes along the Norwegian Coast, *J. Mar. Sci. Eng.*, 5(29), doi:10.3390/jmse5030029.

Breivik O, OJ Aarnes, J-R Bidlot, A Carrasco and O Sætra (2013). Wave Extremes in the Northeast Atlantic from Ensemble Forecasts, *J Climate*, 26, pp 7525-7540, doi:10/mpf

Brown R, D Vikhamar-Schuler, O Bulygina, C Derksen, K Luojus, L Mudryk, L Wang and D Yang (2017). Arctic terrestrial snow cover. Chapter 3 in: *Snow, Water, Ice and Permafrost in the Arctic (SWIPA)* 2017, pp. 25-64, Arctic Monitoring and Assessment Programme (AMAP), Oslo, Norway.

Bruland O and JO Hagen (2002): Glacial mass balance of Austre Brøggerbreen (Spitsbergen), 1971–1999, modelled with a precipitation-run-off model. *Polar Research* 21 (1), 109–121. DOI: 10.3402/polar.v21i1.6477

Burton DJ, JA Dowdeswell, KA Hogan and R Noormets (2016). Marginal fluctuations of a Svalbard surge-type tidewater glacier, Blomstrandbreen, since the Little Ice Age: a record of three surges. *Arctic, Antarctic, and Alpine Research,* 48(2), 411–426. doi: 10.1657/AAAR0014-094

Caldeira K and M Wickett (2003). Anthropogenic carbon and ocean ph. *Nature* 425 (6956),365.

Canadell J, C Quere, M Raupach, C Field, E Buitenhuis, P Ciais, T Conway, N Gillett, R Houghton and G Marland (2007). Contributions to accelerating atmospheric CO2 growth from economic activity, carbon intensity, and efficiency of natural sinks. *Proc. Natl. Acad. Sci*. U. S. A. 104 (47), 18866–18870.

Cao Y, S Liang, X Chen, T He, D Wang and X Cheng (2017). Enhanced wintertime greenhouse effect reinforcing Arctic amplification and initial sea-ice melting. *Scientific Reports*, Vol. 7, Article number: 8462.

Cheng Y, O Andersen and P Knudsen (2015). An Improved 20-Year Arctic Ocean Altimetric Sea Level Data Record, *Marine Geodesy*, 38:2, 146-162, doi: 10.1080/01490419.2014.954087

Chierici M, I Skjelvan, M Norli, E Jones, KY Børsheim, HH Lauvset, H Lødemel, K Sørensen, AL King, T Johannessen (2017). Overvåking av havsuring i norske farvann. *Rapport, Miljødirektoratet,* M-776. In Norwegian with summaries in English.

Christiansen HH, B Etzelmüller, K Isaksen, H Juliussen, H Farbrot, O Humlum, M Johansson, T Ingeman-Nielsen, L Kristensen, J Hjort, P Holmlund, ABK Sannel, C Sigsgaard, HJ Åkerman, N Foged, LH Blikra, MA Pernosky and R Ødegård (2010). The thermal state of permafrost in the Nordic area during the International Polar Year. *Permafrost and Periglacial Processes*, 21:156-181.

Christiansen HH, GL Gilbert, N Demidov, M Guglielmin, K Isaksen, M Osuch and J Boike (2019a). Permafrost thermal snapshot and active-layer thickness in Svalbard 2016-2017, 18 p. First *SIOS SESS report*: https://sios-svalbard.org/SESS_Issue1

Christiansen HH, M Eckerstorfer, W Farnsworth, GL Gilbert, H Hancock, O Humlum, A Prokop, SM Strandand HB O'Neill (2019b). The influence of ground freezing on slope stability during autumn rainstorms in the Longyearbyen area, central Svalbard. (in prep)

Church JA, PU Clark, A Cazenave, JM Gregory, S Jevrejeva, A Levermann, MA Merrifield, GA Milne, RS Nerem, RPD Nunn et al. (2013). Sea level change. In *Climate Change 2013*: The Physical Science Basis. Contribution of Working Group I to the *Fifth Assessment Report of the Intergovernmental Panel on Climate Change*; Stocker TF, Din, G-K Plattner, M Tignor, SK Allen, J Boschung, A Nauels, Y Xia, VBex and PM Midgley (Eds.); Cambridge University Press: Cambridge, UK; New York, NY, USA, 2013.

Collier E, T Mölg, F Maussion, D Scherer, C Mayer and ABG Bush (2013). High-resolution interactive modelling of the mountain glacier–atmosphere interface: an application over the Karakoram. *The Cryosphere*, 7, 779–795, doi:10.5194/tc-7-779- 2013

Collier E, F Maussion, LI Nicholson, T Mölg, WW Immerzeel and ABG Bush (2015). Impact of debris cover on glacier ablation and atmosphere–glacier feedbacks in the Karakoram. *The Cryosphere* 9, 1617–1632, doi:10.5194/tc-9-1617-2015.

Cottier F, F Nilsen, ME Inall, S Gerland, V Tverberg and H Svendsen (2007). Wintertime warming of an Arctic shelf in response to large-scale atmospheric circulation, *Geophys. Res. Lett*., 34, L10607, doi:10.1029/2007GL029948.

Dahlke S and M Maturilli (2017). Contribution of Atmospheric Advection to the Amplified Winter Warming in the Arctic North Atlantic Region. *Advances in Meteorology,* vol. 2017, Article ID 4928620, 8 pages, 2017. https://doi.org/10.1155/2017/4928620.

Day JJ, JL Bamber, PJ Valdes and J Kohler (2012). The impact of a seasonally ice free Arctic Ocean on the temperature, precipitation and surface mass balance of Svalbard. *The Cryosphere*, 6, 35-50. doi:10.5194/tc-6-35-2012, 2012.

DeConto RM and D Pollard (2016) Contribution of Antarctica to past and future sea-level rise. *Nature,* 531, 591–597.

de Haas T, MG Kleinhaus, PE Carbonneau, L Rubensdotter and E Hauber (2015). Surface morphology of fans in the high-Arctic periglacial environment of Svalbard: Controls and processes. *Earth-Science Reviews* 146, 163-182

Deser C, A Phillips, V Bourdette et al. (2012). *Clim Dyn* 38: 527. https://doi.org/10.1007/s00382-010-0977-x

De Wet G, NL Balascio, WJ D'Andrea, J Bakke, RS Bradley and B Perren (2017. Holocene glacier activity reconstructed from proglacial lake Gjøavatnet on Amsterdamøya, NW Svalbard. *Quaternary Science Reviews*.

Dieng HB, A Cazenave, B Meyssignac and M Ablain (2017). New estimate of the current rate of sea level rise from a sea level budget approach. *Geophysical Research Letters* 44 (8), doi.org/10.1002/2017GL073308

Divine DV, MA Granskog, SR Hudson, CA Pedersen, TI Karlsen, SA Divina and S Gerland (2015). Regional melt pond fraction and albedo of thin Arctic first-year drift ice in late summer. *The Cryosphere*, 9, 255–268, 2015. www.the-cryosphere.net/9/255/2015/doi:10.5194/tc-9-255-2015

Dobler A (2019). Convection permitting climate simulations for Svalbard - Background-report for Climate in Svalbard 2100. *NCCS-Report 2/2019* (www.klimaservicesenter.no).

Dobler A, E J Førland and K Isaksen (2019). Present and future heavy rainfall statistics for Svalbard - Background-report for Climate in Svalbard 2100. *NCCS-Report 3/2019* (www.klimaservicesenter.no).

Dunse T, T Schellenberger, JO Hagen, A Kääb, TV Schuler and CH Reijmer (2015). Glacier-surge mechanisms promoted by a hydro-thermodynamic feedback to summer melt. *The Cryosphere*, 9, 197-215.

Eckerstorfer M and HH Christiansen (2011a). Relating meteorological variables to the natural slab avalanche regime in High Arctic Svalbard. *Cold Reg. Sci. Technol*. 69, 184-193 doi:10.1016/j.coldregions.2011.08.008

Eckerstorfer M, HH Christiansen (2011b). Meteorology, Topography and Snowpack Conditions causing Two Extreme Mid Winter Slush and Wet Slab Avalanche Periods in High Arctic Maritime Svalbard. *Permafrost and Periglacial Processes*, 23 (1), 15-25

Eckerstorfer M and HH Christiansen (2011c). Topographical and meteorological control on snow avalanching in the Longyearbyen area, central Svalbard 2006-2009, *Geomorphology,* 134, 186196, doi:10.1016/j.geomorph.2011.07.001

Eckerstorfer M, HH Christiansen, S Vogel and L Rubensdotter (2012). Seasonal cornice dynamics controlling backwall rock debris plucking at Gruvefjellet, central Svalbard. *Earth Surface Processes and Landforms*. 38 (5), 466-476 DOI: 10.1002/esp.3292

Eldevik T, B Risebrobakken, AE Bjune et al. (2014). A brief history of climate – the northern seas from Last Glacial Maximum to global warming. *Quat. Sci. Rev.*, 106, 225–246.

Elverhøy A, JI Svendsen, A Solheim, ES Andersen, J Milliman, J Mangerud, M Hald and R LeB Hooke (1995). Late Quaternary sediment yield from the High Arctic Svalbard Area. *Journal of Geology* 103,1,1-17

Esau I and S Zilitinkevich (2010). On the role of the planetary boundary layer depth in the climate system. *Adv. Sci. Res*., 4, 63–69, 2010. doi:10.5194/asr-4-63-2010

Etzelmuller B and R Frauenfelder (2009). Factors Controlling the Distribution of Mountain Permafrost in The Northern Hemisphere and Their Influence on Sediment transfer. *Arctic Antarctic and Alpine Research*, 41 (1),48-58

Etzelmüller B, TV Schuler, K Isaksen, HH Christiansen, H Farbrot and R Benestad (2011). Modeling the temperature evolution of Svalbard permafrost during the 20th and 21st century, *The Cryosphere*, 5, 67-79, https://doi.org/10.5194/tc-5-67-2011

Farnsworth WR, Ó Ingólfsson R Noormets, L Allaart, H Alexanderson, M Henriksen and A Schomacker (2017). Dynamic Holocene glacial history of St. Jonsfjorden, Svalbard. *Boreas* 46, 585-603.

Farrell W E and J A Clark (1976). On postglacial sea level, *Geophys. J. Int*., 46(3), 647–667, doi:10.1111/j.1365-246X.1976.tb01252.x.

Feely R, S Doney and S R Cooley (2009). Ocean acidification. present conditions and future changes in a high CO 2 world. *Oceanography* 22 (4), 36–47.

Feldhoff JH, S Lange ,J Volkholz, JF Donges, J Kurths and FW Gerstengarbe (2015). Complex networks for climate model evaluation with application to statistical versus dynamical modeling of South American climate. *Climate Dynamics*, 44(5-6), pp.1567-1581, doi: 10.1007/s00382-014-2182-9.

Feldl N, BT Anderson and S Bordoni (2017). Atmospheric Eddies Mediate Lapse Rate Feedback and Arctic Amplification. *J. Climate*, 30, 9213–9224, https://doi.org/10.1175/JCLI-D-16-0706.1

Feyling-Hanssen RW (1955) .Stratigraphy of the marine Late- Pleistocene of Billefjorden, Vestspitsbergen. *Norsk Polarinstitutts Skrifter* 107: 1–226.

Fiddes J and S Gruber (2014). TopoSCALE v.1.0: downscaling gridded climate data in complex terrain, *Geosci. Model Dev*., 7, 387-405, https://doi.org/10.5194/gmd-7-387-2014, 2014

Forman SL, DJ Lubinski, Ó Ingólfsson, JJ Zeeberg, JA Snyder, MJ Siegert and GG Matishov (2004). A review of postglacial emergence on Svalbard, Franz Josef Land and Novaya Zemlya, northern Eurasia. *Quaternary Science Reviews,* 23, 1391-1434.

Francis JA and SJ Vavru (2012). Evidence linking arctic amplification to extreme weather in mid-latitudes. *Geophys. Res. Lett*., 39, L06801, doi:10.1029/2012GL051000.

Fransson A, M Chierici, D Nomura, MA Granskog, S Kristiansen, T Martma and G Nehrke (2015). Effect of glacial drainage water on the CO_2 system and ocean acidification state in an Arctic tidewater-glacier fjord during two contrasting years. *Journal of Geophysical Research-Oceans*, 120(4): 2413-2429.

Franssona A, M Chierici, H Hop, HS Findlay, S Kristiansen and A Wold (2016). Late winter-to-summer change in ocean acidification state in Kongsfjorden, with implications for calcifying organisms. *Polar Biology:* 39(10): 1841-1857.

Fransson A, M Chierici, I Skjelvan, A Olsen, P Assmy, AK Peterson, G Spreen and B Ward (2017). Effects of sea-ice and biogeochemical processes and storms on under-ice water fCO(2) during the winter-spring transition in the high Arctic Ocean: Implications for sea-air CO_2 fluxes. *Journal of Geophysical Research-Oceans,* 122(7): 5566-5587.

Frauenfelder R, K Isaksen, J Nötzli and MJ Lato (2018). Ground thermal and geomechanical conditions in a permafrost-affected high-latitude rockslide site (Polvartinden, Northern Norway), *The Cryosphere,* 12, 1531–1550 https://doi.org/10.5194/tc-12-1531-2018.

Frederikse T, K Simon, CA Katsman and R Riva (2017). The sea-level budget along the Northwest Atlantic coast: GIA, mass changes, and large-scale ocean dynamics, *J. Geophys. Res. Oceans*, 122, doi:10.1002/2017JC012699.

Fredrikse T (2018). Personal communication with J.E.Ø. Nilsen (NERSC/IMR).

French HM (2018). The Periglacial Environment, Fourth Edition. *John Wiley and Sons*, Ltd., Chichester, UK (2018) (515 pp).

Früh B, A Will and CL Castro (2016). Recent developments in Regional Climate Modelling with COSMO-CLM. *Meteorologische Zeitschrift*, pp.119-120.

Førland EJ, I Hanssen-Bauer and PØ Nordli (1997a). Orographic precipitation at the glacier Austre Brøggerbreen, Svalbard. *Klima 02/97*, Norwegian Meteorological Institute, Oslo.

Førland EJ, I Hanssen-Bauer and PØ Nordli (1997b). Climate statistics and long-term series of temperature and precipitation at Svalbard and Jan Mayen. *Klima* 21/97, Norwegian Meteorological Institute, Oslo.

Førland EJ and I Hanssen-Bauer (2000). Increased precipitation in the Norwegian Arctic: True or false? *Climatic Change*, 46, 485-509.

Førland EJ, TE Skaugen, RE Benestad, I Hanssen-Bauer and OE Tveito (2004). Variations in Thermal Growing, Heating, and Freezing Indices in the Nordic Arctic, 1900-2050. Arctic, *Antarctic and Alpine Research*, Vol.36, No.3, 346-355

Førland EJ, RE Benestad, F Flatøy, I Hanssen-Bauer, JE Haugen, KI saksen, A Sorteberg and B Ådlandsvik (2009). Climate development in North Norway and the Svalbard region during 1900-2100. *Norwegian Polar Institute, Report series* no. 128.

Førland E J, RE Benestad, I Hanssen-Bauer, JE Haugen and TE Skaugen (2011). Temperature and Precipitation Development at Svalbard 1900–2100, *Adv. Meteor.*, 2011, 1–14, doi:10.1155/2011/893790.

Gardner AS, G Moholdt, JG Cogley, B Wouters, AA Arendt, J Wahr, E Berthier, R Hock, WT Pfeffer, G Kaser, SRM Ligtenberg, T Bolch, MJ Sharp, JO Hagen, MR van den Broeke and F Paul (2013). A reconciled estimate of glacier contributions to sea level rise: 2003 to 2009. *Science* 340(6134), 852-7. doi:10.1126/science.1234532.

Gatto, LW (1995). Soil Freeze-Thaw Effects on Bank Erodibility and Stability, *Special Report 95-24, US Army, Corps of Engineers,* CRREL,17pp

Gerland S, J-G Winther, JB Ørbæk and B Ivanov (1999). Physical properties, spectral reflectance and thickness development of first year fast-ice in Kongsfjorden, Svalbard; *Polar Research*, Vol. 18 (2), pp. 275-282.

Gerland S and R Hall (2006). Variability of fast-ice thickness in Spitsbergen fjords. *Ann Glaciol* 44:231-239

Gerland S and AHH Renner (2007). Sea-ice mass balance monitoring in an Arctic fjord. *Ann Glaciol* 46:435-442

Gerland S, AHH Renner, F Godtliebsen, D Divine and TB Løyning (2008). Decrease of sea ice thickness at Hopen, Barents Sea, during 1966–2007. *Geophys Res Lett* 35, L06501, doi:10.1029/2007GL032716

Giesen RH and J Oerlemans (2013). Climate-model induced differences in the 21st century global and regional glacier contributions to sea-level rise. *Clim. Dyn*.,41, 3283–3300.

Giorgetta MA, J Jungclaus, CH Reick, S Legutke, J Bader, M Böttinger, V Brovkin, T Crueger, M Esch, K Fieg and K Glushak (2013). Climate and carbon cycle changes from 1850 to 2100 in MPI☐ESM simulations for the Coupled Model Intercomparison Project phase 5. *Journal of Advances in Modeling Earth Systems*, 5(3), pp.572-597, doi: 10.1002/jame.20038.

Giorgi F, C Torma, E Coppola, N Ban, C Schär and S Somot (2016). Enhanced summer convective rainfall at Alpine high elevations in response to climate warming, *Nature Geoscience,* 9, 584–589.

Gjelten HM, Ø Nordli, K Isaksen, EJ Førland, PN Sviashchennikov, P Wyszynski, UV Prokhorova, R Przybylak, BV Ivanov and AV Urazgildeeva (2016). Air temperature variations and gradients along the coast and fjords of western Spitsbergen, Polar Research, 35(1), doi: 10.3402/polar.v35.29878

González-Pola C, KMH Larsen, P Fratantoni, A Beszczynska-Möller and SL Hughes (Eds). (2018). ICES Report on Ocean Climate 2016. *ICES Cooperative Research Report* No. 339. 110 pp.

Good SA, MJ Martin and NA Rayner (2013). EN4: Quality controlled ocean temperature and salinity profiles and monthly objective analyses with uncertainty estimates, *J. Geophys. Res. Oceans*, 118, 6704–6716, doi:10.1002/2013JC009067

Graham RM, L Cohen, AA Petty, LN Boisvert, A Rinke, SR Hudson, M Nicolaus and MA Granskog (2017). Increasing frequency and duration of Arctic winter warming events, *Geophys. Res. Lett.*, 44, 6974–6983, doi:10.1002/2017GL073395.

Granskog MA, A Rösel, PA Dodd, D Divine, S Gerland, T Martma and MJ Leng (2017). Snow contribution to first-year and second-year Arctic sea ice mass balance north of Svalbard. *Journal of Geophysical Research - Oceans*. 122, doi:10.1002/2016JC012398. N-ICE2015 special issue.

Graversen RG, PL Langen and T Mauritsen (2014). Polar amplification in CCSM4: Contributions from the lapse rate and surface albedo feedbacks. *J. Climate,* 27, 4433–4450,

Groisman PY, EG Bogdanova, VA Alexeev, JE Cherry and ON Bulygina (2014). Impact of snowfall measurement deficincies on quantificationof precipitation and its trends over Northern Eurasia. *Ice and Snow*, 2, 29-43.

Groisman PY, ON Bulygina, X Yin, RS Vose, SK Gulev, I Hanssen-Bauer and EJ Førland (2016). Recent changes in the frequency of freezing precipitation in North America and Northern Eurasia. *Environ. Res. Lett.* 9 (11), doi:10.1088/1748-9326/9/11/114021. Available from: https://www.researchgate.net/publication/301578742

Gruber S and W Haeberli (2007). Permafrost in steep bedrock slopes and its temperature-related destabilization following climate change*, J. Geophys. Res.,* 112, F02S18, 1-10

Gudmundsson L, JB Bremnes, JE Haugen and T Engen-Skaugen (2012). Technical Note: Downscaling RCM precipitation to the station scale using statistical transformations - a comparison of methods. *HESS,* 16, 3383-3390, DOI: 10.5194/hess-16-3383-2012

Guégan EBM and HH Christiansen (2017). Seasonal Arctic Coastal Bluff Dynamics in Adventfjorden, Svalbard. *Permafrost and Periglac. Process*., 28: 18–31. doi: 10.1002/ppp.1891.

Gundersen J, OA Mikkelsen, I Johnsen and RU Nikolaisen (2018). Skredrapport Sukkertoppen –Dimensjonerende skred fra Sukkertoppen og faresoner. *NVE-Rapport* Nr. 80-2018

Haeberli W, J Noetzli, L Arenson, R Delaloye, I Gärtner-Roer, S Gruber, K Isaksen, C Kneisel, M Krautblatter and M Phillips (2010). Mountain permafrost: development and challenges of a young research field. *Journal of Glaciology* 56, No. 200: 1043–1058. doi:10.3189/002214311796406121

Hagen JO and A Sætrang (1991). Radio-echo soundings of sub-polar glaciers with low-frequency radar. *Polar Research* 9, 99-107

Hagen JO, O Liestøl, E Roland and T Jørgensen (1993). Glacier atlas of Svalbard and Jan Mayen, *Norwegian Polar Institute*, Oslo.

Hagen JO, J Kohler, K Melvold and J-G Winther (2003). Glaciers in Svalbard: mass balance, runoff and freshwater flux. *Polar Research* 22 (2), 145-159.

Haagmans VJT (2018). Long-term hydrological response predictions of two High-Arctic catchments under the influence of climate change. *Bachelor thesis, Aachen University*, Germany

Haine TWN, B Curry, R Gerdes, E Hansen, M Karcher, C Lee, B Rudels, G Spreen, L de Steur, KD Stewart and R Woodgate (2015). Arctic freshwater export: Status, mechanisms, and prospects*, Global and Planetary Change* 125 (2015) 13–35.

Haldorsen S and M Heim (1999). An artic groundwater system and its dependence upon climatic change: An example from Svalbard. *Permafrost and Periglacial Processes* 10,137-149.

Hancock H, A Prokop, M Eckerstorfer and J Hendrikx (2018). Combining high spatial resolution snow mapping and meteorological analyses to improve forecasting of destructive avalanches in Longyearbyen, Svalbard. *Cold Regions Science and Technology*, 154, 120-132

Hansen E, S Gerland, MA Granskog, O Pavlova, AHH Renner, J Haapala, TB Løyning and M Tschudi (2013). Thinning of Arctic sea ice observed in Fram Strait: 1990–2011, *J. Geophys. Res. Oceans*, 118, 5202–5221, doi:10.1002/jgrc.20393.

Hansen BB, K Isaksen, RE Benestad, J Kohler, ÅØ Pedersen, L E Loe, SJ Coulson, JO Larsen and Ø Varpe (2014). Warmer and wetter winters: characteristics and implications of an extreme weather event in the High Arctic, *Env. Res. Lett.*, 9(11), 114021, doi:10.1088/1748-9326/9/11/114021.

Hanssen-Bauer I (2002). Temperature and precipitation at Svalbard 1900-2050: Measurements and scenarios. *Polar Record,* 38 (206), 225-232

Hanssen-Bauer I and EJ Førland (1998). Long-term trends in temperature and precipitation in the Norwegian Arctic: Can they be explained by changes in the atmospheric circulation patterns. *Climate Research*, 10, 143-153

Hanssen-Bauer I, EJ Førland, I Haddeland, H Hisdal, S Mayer, A Nesje, JEØ Nilsen, S Sandven, AB Sandø, A Sorteberg and B Ådlandsvik (2015). Klima i Norge 2100 – Kunnskapsgrunnlag for Klimatilpasning, oppdatert i 2015. *NCCS report* no. 2/2015 (www.klimaservicesenter.no)

Hanssen-Bauer I, EJ Førland, H Hisdal and S Mayer (2017). Climate in Norway 2100 – a knowledge base for climate adaptation. *NCCS Report* no. 1/2017 (www.klimaservicesenter.no)

Harris C, MCR Davies and B Etzelmüller (2001). The assessment of potential geotechnical hazards associated with mountain permafrost in a warming global climate, *Permafrost Periglacial Proc.,* 12, 145–156.

Harris C, M Kern-Luetschg, HH Christiansen and F Smith (2011). The Role of Interannual Climate Variability in Controlling Solifluction Processes, Endalen, Svalbard. *Permafrost and Periglacial Processes*, 22 (3), 239-253 doi: 10.1002/ppp.727

Hasselmann K, TP Barnett, E Bouws, H Carlson, DE Cartwright, K Enke, JA Ewing, H Gienapp, DE Hasselmann, P Kruseman, A Meerburg, P Muller, DJ Olbers, K Richter, W Sell and H Walden (1973). Measurements of wind-wave growth and swell decay during the Joint North Sea Wave Project (JONSWAP), *Deutsch Hydrogr Z*, A8(12), pp 1-95

Hátún H, AB Sandø, H Drange, B Hansen and H Valdimarsson (2005). Influence of the Atlantic Subpolar Gyre on the Thermohaline Circulation. *Science*, 309: 1841–1844.

Hegseth EN and V Tverberg (2013). Effect of Atlantic water inflow on the timing of the phytoplankton spring bloom in a high arctic fjord (Kongsfjorden, Svalbard). *J. Mar. Syst.,* 113– 114, 94–105, doi:10.1016/j.jmarsys.2013.01.003.

Hendricks S, S Gerland, LH Smedsrud, C Haas, A Pfaffhuber and F Nilsen (2011). Sea-ice thickness variability in Storfjorden, Svalbard. *Annals of Glaciology* 52 61-68, (57).

Henriksen M, H Alexanderson, JY Landvik,H Linge and G Peterson (2014). Dynamics and retreat of the Late Weichselian Kongsfjorden ice stream, NW Svalbard. *Quaternary Science Reviews* 92, 235-245

Herring T, R King and S McClusky (2011). Introduction to GAMIT/GLOBK release 10.4, *Tech. Rep., Mass Inst. of Technol.*, Cambridge, U.K.

Hestnes E and K Lied (1991). Vurdering av tiltak mot snøskred, sørpeskred og drivsnø i Longyearbyen. (Evaluation of mitigative measures against avalanches, slushflows and drifting snow in Longyearbyen.) *NGI-Rapport* 904025-1, pp. 61

Hestnes E and S Bakkehøi (2003). Nybyen, Longyearbyen. Skredfarevurdering. (Nybyen, Longyearbyen. Hazard evaluation.) *NGI-Rapport* 20031134-1, pp. 21

Hestnes E, S Bakkehøi and C Jaedicke (2016). Longyearbyen, Svalbard - Vulnerability and risk management of an arctic settlement under changing climate - a challenge to authorities and experts. *Proceedings of the International Snow Science Workshop* 2016, Breckenridge, Colorado, 363-370

Hisdal V (1998). Svalbard Nature and History, Polarhåndbok No. 12, *Norwegian Polar Institute*, pp. 123

Hodgkins R, R Cooper, J Wadham and M Tranter (2003). Suspended sediment fluxes in a high-Arctic glacierised catchment: implications for fluvial sediment storage, *Sedimentary Geology* 162, 105–117

Hodson AJ and RI Fergusson (1999). Fluvial suspended sediment transport from cold and warm-based glaciers in Svalbard. *Earth Surface Processes and Landforms* 24, 957-974.

Holgate SJ, A Matthews, PL Woodworth, LJ Rickards,ME Tamisiea, E Bradshaw, PR Foden, KM Gordon, S Jevrejeva and J Pugh (2013). New Data Systems and Products at the Permanent Service for Mean Sea Level, *Journal of Coastal Research,* 29(3), 493504, doi:10.2112/JCOASTRES-D-12-00175.1.

Hoseth KA, I Johnsen and J Gundersen (2018). Konseptstudie. Sikringstiltak Sukkertoppen og Vannledningsdalen. *NVE-Rapport* Nr. 78-2018

Humlum O, B Elberling, A Hormes, K Fjordheim, OH Hansen and I Heinemeier (2005). Late-Holocene glacier growth in Svalbard, documented by subglacial relict vegetation and living soil microbes. *The Holocene* 15, 396-407.

Humlum O, A Instanes and JL Sollid (2003). Permafrost in Svalbard: A review of research history, climatic background and engineering challenges. *Polar Research* Vol.22, No2.

Husebye S, J Bogen, AK Helgestad and LE Petterson (1993). Environmental impacts of road construction between Longyearbyen and Svea: runoff, erosion and landscape. *NVE-Publikasjon* Nr. 19/1993, 40 p. PDF: http://publikasjoner.nve.no/publikasjon/1993/publikasjon1993_19.pdf

Huss M, G Jouvet, D Farinotti and A Bauder (2010). Future high-mountain hydrology: a new parameterization of glacier retreat. *Hydrol. Earth Syst. Sci.* ,14, 815–829. http://dx.doi.org/10.5194/hess-14-815-2010.

Inall ME, F Nilsen, FR Cottier and R Daae (2015). Shelf/fjord exchange driven by coastal-trapped waves in the Arctic, *J. Geophys. Res. Oceans*, 120, doi:10.1002/2015JC011277.

Ingvaldsen RB, L Asplin and H Loeng. (2004). Velocity field of the western entrance to the Barents Sea, *J. Geophys. Res.*, 109, C03021, doi:10.1029/2003JC001811.

Ingólfsson Ó and JY Landvik (2012). The Svalbard-Barents ice-sheet – Historical, current and future perspectices, *Quaternary Science Reviews,* 64, 33-60.

Instanes A (2003). Climate change and possible impact on Arctic infrastructure. In M. Phillips et al. (eds.): *Proceedings 8th International Permafrost Conference*, Zürich, Switzerland. Vol. 1. Pp. 461–466. Lisse, The Netherlands: Balkema Publishers.

Instanes A and JL Rongved (2017). Forventede klimaendringers påvirkning på byggegrunn i Longyearbyen-området. Delrapport 2 i oppdraget «Bygging og forvaltning på Svalbard i et langsiktig Klimaperspektiv». *Statsbygg Rapport* nr. IAS2171-1. 36 pp.

IPCC (2013). Climate Change 2013: The Physical Science Basis. Contribution of Working Group I to the Fifth Assessment Report of the Intergovernmental Panel on Climate Change [TF Stocker, D Qin, G-K Plattner, M Tignor, SK Allen, J Boschung, A Nauels, Y Xia, V Bex and PM Midgley (eds.)]. *Cambridge University Press*, Cambridge, United Kingdom and New York, NY, USA, 1535 pp, doi:10.1017/CBO9781107415324.

Isaksen K, P Holmlund, JL Sollid and C Harris (2001). Three deep alpine-permafrost boreholes in Svalbard and Scandinavia. *Permafrost and Periglacial Processes* 12: 13–25. doi:10.1002/ppp.380

Isaksen K, JL Sollid, P Holmlund and C Harris, (2007). Recent warming of mountain permafrost in Svalbard and Scandinavia. *Journal of Geophysical Research*, 112:F02S04, doi:10.1029/2006JF000522.

Isaksen K, PØ Nordli, EJ Førland, E Łupikasza, S Eastwood and T Niedźwiedź (2016). Recent warming on Spitsbergen—Influence of atmospheric circulation and sea ice cover. *Journal of Geophysical Research: Atmospheres*, 121, 11913–11931. https://doi.org/10.1002/2016JD025606.

Isaksen K, EJ Førland, A Dobler, R Benestad, JE Haugen and A Mezghani (2017). Klimascenarioer for Longyearbyen-området, Svalbard. *MET Norway Report* 14/2017. (In Norwegian)

Ivanov V, VA Alexeev, NV Koldunov, I Repina, AB Sandø, LH Smedsrud and A Smirnov (2016). Arctic Ocean heat impact on regional ice decay – a suggested positive Feedback, *J. Phys. Oceanogr.*, doi:10.1175/JPO-D-15-0144.1

Jacob T, J Wahr, WT Pfeffer and S Swenson (2012). Recent contributions of glaciers and ice caps to sea level rise. *Nature* 482, 514. doi:10.1038/nature10847

James T, T Murray, N Barrand, H Sykes and A Fox (2012). Observations of enhanced thinning in the upper reaches of Svalbard glaciers. *The Cryosphere*, 1369–1381.

Jania J and M Pulina (1994). Polish hydrological studies in Spitsbergen, Svalbard: a review of some results. In: Sand, K., Killingtveit, Å. (Eds.): Proceedings of the 10th International Northern Research Basins Symposium and Workshop, Spitsbergen, Norway. *SINTEF Report* 22 A96415, Trondheim,47–76.

Jordan P and O Slaymaker (1991). Holocene Sediment Production in Lillooet River Basin, British Colombia: A Sediment Budget Approach. *Géogr. Phys. Quat.*, 45 (1991), pp. 45-57

Kanevskiy M, Y Shur, J Strauss, T Jorgenson, D Fortier, E Stephani and A Vasiliev (2016). Patterns and rates of riverbank erosion involving ice-rich permafrost (yedoma) in northern Alaska. *Geomorphology*, Volume 253:370-384

Karlén, W (1981). Lacustrine Sediment Studies. A technique to obtain a continuous record of Holocene glacier variations. *Geografiska Annaler. Series A. Physical Geography*, 273-281.

Kaser G, J Cogley, M Dyurgerov, M Meier and A Ohmura (2006). Mass balance of glaciers and ice caps: Consensus estimates for 1961–2004. *Geophysical Research Letters*, 33(19), L19501.

Kaufmann G. and D Wolf (1996). Deglacial land emergence and lateral upper-mantle heterogeneity in the Svalbard Archipelago-11. Extended results for high-resolution load models, *Geophys. J. Int*. 127, 125-140.

Kierulf HP, B Pettersen, D McMillan and P Willis (2009). The kinematics of Ny☐Ålesund from space geodetic data, *J. Geodyn.*, 48, 37–46, doi:10.1016/j.jog.2009.05.002.

Kierulf HP, H Steffen, MJR Simpson, M Lidberg, P Wu and H Wang (2014). A GPS velocity field for Fennos-candia and a consistent comparison to glacial isostatic adjustment models, *J. Geophys. Res. Solid Earth*, 119, doi:10.1002/2013JB010889.

Killingtveit Å, L-E Pettersson and K Sand (2003). Water balance investigations in Svalbard. *Polar Research,* 22 (2), 161-174.

King J, G Spreen, S Gerland, C Haas, S Hendricks, L Kaleschke and C Wang (2017). Sea-Ice Thickness from field measurements in the north-western Barents Sea. *Journal of Geophysical Research - Oceans*. DOI 10.1002/2016JC012199.

Knies J, I Pathirana, P Cabedo-Sanz, A Banica, K Fabian, TL Rasmussen, M Forwick and ST Belt (2017). Sea-ice dynamics in an Arctic coastal polynya during the past 6500 years. *Arktos*, 3(1), 1–15, doi: 10.1016/j.dsr.2011.06.001.

König M, C Nuth, J Kohler, G Moholdt and R Pettersen (2014). A digital glacier database for Svalbard. Book chapter in *Global Land Ice Measurements from Space* J.S. Kargel G.J. Leonard, M.P. Bishop, A. Kääb & B.H. Raup (Editors). Springer-Verlag Berlin Heidelberg

Koenigk T, A Devasthale and KG Karlsson (2014). Summer sea ice albedo in the Arctic in CMIP5 models. *Atmospheric Chemistry and Physics*, 14, 1987-1998.

Koenigk T, P Berg and R Döscher (2015). Arctic climate change in an ensemble of regional CORDEX simulations. *Polar Research*, 34, 24603, doi: 10.3402/polar.v34.24603.

Kohler J, TD James, T Murray, C Nuth, O Brandt, NE Barrand, HF Aas and A Luckman (2007). Acceleration in thinning rate of western Svalbard glaciers. *Geophysical Research Letters* 34, L18502, doi:10.1029/2007GL030681.

Kohnemann SHE, G Heinemann, DH Bromwich and O Gutjahr (2017). Extreme warming in the Kara Sea and Barents Sea during the winter period 2000–16. *J. Climate*, 30, 8913–8927, https://doi.org/10.1175/JCLI-D-16-0693.1. Link, Google Scholar

Korablev A et al. (2014). Climatological Atlas of the Nordic Seas and Northern North Atlantic. D. Seidov, A. R. Parsons, Eds., *NOAA Atlas NESDIS,* 77, 122 pp. dataset doi: 10.7289/V54B2Z78.

Kostrzewski A, A Kanecki, J Kapuschinski, R Klimczak, A Stach and Z Zwolinski (1989). The dynamics and rate of denudation of glaciated and non-glaciated catchments in central Spitsbergen, *Polish Polar Res.* 10(3), 317-367

Krawczyk WE and J Opolka-Gadek (1994). Suspended sediment concentrations in the Werenskiold glacier drainage basin in 1986. *XXI Polar Symposium*, Warzawa 1994, 215-224.

Krigstrøm A (1962). Geomorphological studies of sandar plains and their geomorphological significance. *Geogr. Ann.* 44, 328– 346

Lambeck K (1996). Limits on the areal extent of the Barents Sea ice sheet in Late Weichselian time. *Global and Planetary Change* 12, 41-51.

Lambeck K, C Smither and P Johnston (1998). Sea-level change, glacial rebound and mantle viscosity for northern Europe. *Geophys. J. Int*., 134, 102–144.

Landrø M, O-A Mikkelsen and C Jaedicke (2017). Gjennomgang og evaluering av skredhendelsen i Longyearbyen 21.02.2017. *NVE-Rapport* Nr. 31-2017

Landvik JY, EJ Brook, L Gualtieri, H Linge, Raisbeck, O Salvigsen and F Yiou (2013). 10Be exposure age constraints on the Late Weichselian ice-sheet geometry and dynamics in inter-ice-stream areas, western Svalbard. *Boreas* 42, 43-56.

Langehaug HR, I Medhaug, T Eldevik and OH Otterå (2012). Arctic/Atlantic exchanges via the subpolar gyre. *J.Clim.* 25: 2421–2439.

Langehaug HR, F Geyer, LH Smedsrud and Y Gao (2013). Arctic sea ice decline and ice export in the CMIP5 historical simulations, *Ocean. Modell.*, 71, 114–126.

Langehaug H, AB Sandø, M Årthun and M Ilicak (2018). Variability along the Atlantic water pathway in the forced Norwegian Earth System Mode, *Climate Dynamics*. https://doi.org/10.1007/s00382-018-4184-5.

Larsson S (1982). Geomorphological effects on the slopes of Longyear Valley, Spitsbergen, after a heavy rain-storm in July 1972. *Geogr. Ann.* 64A (3-4), 105-125

Lauvset S, N Gruber, P Landschutzer, A Olsen and J Tjiputra (2015). Trends and drivers in global surface ocean pH over the past 3 decades. *Biogeosciences* 12, 1285–1298

Lawrence D and I Haddeland (2011). Uncertainty in hydrological modelling of climate change impacts in four Norwegian catchments, *Hydrology Research*, 42, 457-471, doi:10.2166/nh.2011.010

Lepkowska E and L Stachnik (2018). Article Which Drivers Control the Suspended Sediment Flux in a High Arctic Glacierized Basin (Werenskioldbreen, Spitsbergen), *Water,* 10, 1408; doi:10.3390/w10101408

Le Quéré et al. (2018). Global Carbon Budget 2017. *Earth Syst. Sci. Data*, 10, 405–448, 2018 https://doi.org/10.5194/essd-10-405-2018

Li H, S Beldring, C-Y Xu, M Huss, K Melvold and SK Jain (2015). Integrating a glacier retreat model into a hydrological model – Case studies of three glacierised catchments in Norway and Himalayan region, Journal of Hydrology, 527, 656-667. http://dx.doi.org/10.1016/j.jhydrol.2015.05.017.

Liestøl O (1975). Setevatnet, a glacier dammed lake in Spitsbergen. *Norsk Polarinst. Årbok,* 1975, 31-35.

Liestøl O (1977). Pingos, spings, and permafrost in Spitsbergen. *Norsk Polarinstitutt Skrifter,* 141.

Lind S and RB Ingvaldsen (2012). Variability and impacts of Atlantic Water entering the Barents Sea from the north, *Deep Sea Res.*, Part I, 62, 70–88, doi:10.1016/j.dsr.2011.12.007.

Lind S, RB Ingvaldsen and T Furevik (2018). Arctic warming hotspot in the northern Barents Sea linked to declining sea ice import, *Nature Climate Change*. https://doi.org/10.1038/s41558-018-0205-y

Lindbäck K, J Kohler, R Pettersson, C Nuth, K Langley, A Messerli, D Vallot, K Matsuoka and O Brandt (2018). Subglacial topography, ice thickness, and bathymetry of Kongsfjorden, northwestern Svalbard. *Earth System Science Data*, 10:1769–1781. doi: 10.5194/essd-10-1769-2018.

Lindsay R and A Schweiger (2015). Arctic sea ice thickness loss determined using subsurface, aircraft, and satellite observations. *The Cryosphere,* 9, 269–283. www.the-cryosphere.net/9/269/2015/, doi:10.5194/tc-9-269-

Luckman A, DI Benn, F Cottier, S Bevan, F Nilsen and M Inall (2015). Calving rates at tidewater glaciers vary strongly with ocean temperature. *Nature Communications*. doi 10.1038/ncomms9566.

Lutz J and FW Gerstengarbe (2015). Improving seasonal matching in the STARS model by adaptation of the resampling technique. *Theoretical and Applied Climatology*, 120(3-4), pp.751-760, doi:10.1007/s00704-014-1205-0.

Lydersen C, P Assmy, S Falk-Petersen, J Kohler, KM Kovacs, M Reigstad, H Steen, H Strøm, A Sundfjord, Ø Varpe, W Walczowski, JM Weslawski, M Zajaczkowski (2014). The importance of tidewater glaciers for marine mammals and seabirds in Svalbard, Norway, *J. Mar. Syst*. 129, 452–471.

Mangerud J, JP Briner, T Goslar and J-I Svendsen (2017). The Bølling-age Blomvåg Beds, western Norway: implications for the Older Dryas glacial re-advance and the age of the deglaciation. *Boreas.* 46: 162-184. doi: 10.1111/bor.12208

Mangerud J and JI Svendsen (2017). The Holocene Thermal Maximum around Svalbard, Arctic North Atlantic; molluscs show early and exceptional warmth, *The Holocene*, 1-19.

Maraun D (2016). Bias Correcting Climate Change Simulations – a Critical Review. *Curr Clim Change* Rep 2: 211-220, https://doi.org/10.1007/s40641-016-0050-x

Marzeion B, AH Jarosch and M Hofer (2012). Past and future sea-level changes from the surface mass balance of glaciers. *Cryosphere*, 6, 1295–1322.

Matsuo K and K Heki (2013). Current ice loss in small glacier systems of the Arctic islands (Iceland, Svalbard, and the Russian High Arctic) from satellite gravimetry. *Terr. Atmos. Ocean. Sci*., 24(4), Part I, 657-670. doi:10.3319/TAO.2013.02.22.01

Matsuoka N (2001). Solifluction rates, processes and landforms: a global review. *Earth-Science Reviews* 35, 107-134

Matsuoka N, S-I Sawaguchi and K Yoshikawa (2004). Present-Day Periglacial Environments in Central Spitsbergen, Svalbard. *Geographical Review of Japan*, 77 (5) 276-300

Matsuoka N, HH Christiansen and T Watanabe (2018). Ice –wedge polygon dynamics in Svalbard: Lessons from a decade of automated multi-sensor monitoring *Permafrost and Periglacial Processes* vol 29, Issue 3.

Maturilli M and M Kayser (2017). Arctic warming, moisture increase and circulation changes observed in the Ny-Ålesund homogenized radiosonde record. *Theor Appl Climato,*130:1–17. DOI 10.1007/s00704-016-1864-0

McKinney W, J Perktold and S Seabold (2011). Time Series Analysis in Python with statsmodels, in P*roceedings of the 10th Python in Science Conference,* edited by S. van der Walt & J. Millman, pp. 96102.

Mc Namara JP and DL Kane (2009). The impact of a shrinking cryosphere on the form of arctic alluvial channels. *Hydrological processes* 23,159-168

Meehl GA, C Covey, T Delworth,M Latif, B McAvaney, JFB Mitchell, RJ Stouffer and KE Taylor (2007). The WCRP CMIP3 multimodel dataset – A new era in climate change research, *B. Am. Meteorol. Soc.,* 88, 1383, doi:10.1175/Bams-88-9-1383.

Mémin A, Y Rogister, J Hinderer, OC. Omang and B Luck (2011). Secular gravity variation at Svalbard (Norway) from ground observations and GRACE satellite data, *Geophys. J. Int.,* 184(3), 1119–1130, doi:10.1111/j.1365-246X.2010.04922.x.

Miller GH, JY Landvik, SJ Lehman and JR Southon (2017). Episodic Neoglacial snowline descent and glacier expansion on Svalbard reconstructed from the 14C ages of ice-entombed plants. *Quaternary Science Reviews* 155, 67-78.

Moholdt G, C Nuth, JO Hagen and J Kohler (2010). Recent elevation changes of Svalbard glaciers derived from ICESat laser altimetry. *Remote Sensing Env*, 114(11), 2756-2767. doi:10.1016/j.rse.2010.06.008.

Moore GWK, A Schweiger, J Zhang and M Steele (2018). Collapse of the 2017 winter Beaufort High: A response to thinning sea ice? *Geophys. Res. Lett*., 45, 2860-2869. https://doi.org/10.1002/2017GL076446

Mork KA, Ø Skagseth, V Ivshin, V Ozhigin, SL Hughes and H Valdimarsson (2014). Advective and atmospheric forced changes in heat and fresh water content in the Norwegian Sea, 1951–2010. *Geophysical Research Letters,* 41: 6221–6228.

Muckenhuber S, F Nilsen, A Korosov and S Sandven (2016). Sea ice cover in Isfjorden and Hornsund, Svalbard (2000–2014) from remote sensing data, *Cryosphere*, 10(1), 149–158, doi:10.5194/tc-10-149-2016.

Muilwijk M, LH Smedsrud, M Ilicak and H Drange (2018). Atlantic Water heat transport variability in the 20th century Arctic Ocean from a global ocean model and observations. *J. Geophys. Res.- Oceans.* (In review)

Müller J, G Massé, R Stein and ST Belt (2009). Variability of sea-ice conditions in the Fram Strait over the past 30,000 years. *Nature Geoscience,* 2(11), 772–776. doi: 10.1038/ngeo665.

Müller J, K Werner, R Stein, K Fahl, M Moros and E Jansen (2012). Holocene cooling culminates in sea ice soscillations in Fram Strait, *Quaternary Science Reviews*, 47, 1-14.

Müller J and R Stein (2014). High-resolution record of late glacial and deglacial sea ice changes in Fram Strait corroborates ice–ocean interactions during abrupt climate shifts: *Earth and Planetary Science Letters,* 403, 446–455. doi: 10.1016/j.epsl.2014.07.016.

Mölg T, NJ Cullen, DR Hardy, G Kaser and L Klok (2008). Mass balance of a slope glacier on Kilimanjaro and its sensitivity to climate*, Int. J. Climatol*., 28, 881–892.

Mölg T, NJ Cullen, DR Hardy, M Winkler and G Kaser (2009). Quantifying Climate Change in the Tropical Midtroposphere over East Africa from Glacier Shrinkage on Kilimanjaro, *J. Clim*., 22, 4162–4181

Mölg T and G Kaser (2011). A new approach to resolving climate-cryosphere relations: Downscaling climate dynamics to glacier-scale mass and energy balance without statistical scale linking, *J. Geophys. Res.*, 116, D16101, doi:10.1029/2011JD015669.

Möller M and J Kohler (2018). Differing Climatic Mass Balance Evolution Across Svalbard Glacier Regions Over 1900–2010. *Frontiers in Earth Science* 6(128) 1--18. doi:10.3389/feart.2018.00128. ISSN: 2296-6463

Möller M, F Obleitner, CH Reijmer, VA Pohjola, P Głowacki and J Kohler (2016). Adjustment of regional climate model output for modeling the climatic mass balance of all glaciers on Svalbard, *J. Geophys. Res. Atmos*. 121(10), 5411-5429. doi:10.1002/2015JD024380

Möller M, F Navarro and A Martín-Español (2016). Monte Carlo modelling projects the loss of most land-terminating glaciers on Svalbard in the 21st century under RCP8.5 forcing. *Environ. Res. Lett*. 11:094006. doi: 10.1088/1748-9326/11/9/094006

Neumann U (2006). Climate - glacier links on Bogerbreen, Svalbard : Glacier mass balance investigations in central Spitsbergen 2004 / 2005. *Master-thesis, Dept. Geosciences, Univ. Oslo,* Norway. http://urn.nb.no/URN:N-BN:no-14313

NGI (2018) https://www.ngi.no/eng/Services/Technical-expertise-A-Z/Rock-slides

Nicolaus M, C Haas and J Bareiss (2003). Observations of superimposed ice formation at melt-onset on fast ice on Kongsfjorden, Svalbard. *Physics and Chemistry of the Earth* 28, 1241-1248.

Nilsen F, F Cottier, R Skogseth and S Mattsson (2008). Fjord-shelf exchanges controlled by ice and brine production: The interannual variation of Atlantic Water in Isfjorden, Svalbard, *Continental Shelf Research*, 28, doi:10.1016/j.csr.2008.04.015, 1838-1853.

Nilsen F, R Skogseth, J Vaardal-Lunde and M Inall (2016). A Simple Shelf Circulation Model - Intrusion of Atlantic Water on the West Spitsbergen Shelf, *J. Physical Oceanography*, 46, 1209-1230, DOI: 10.1175/JPO-D-15-0058.1.

Nordli Ø, I Hanssen-Bauer and EJ Førland (1996). Homogeneity analyses of temperature and precipitation series from Svalbard and Jan Mayen. *Klima 16/96*. Norwegian Meteorological Institute report series.

Nordli Ø, R Przybylak, AEJ Ogilvie and K Isaksen (2014). Long-term temperature trends and variability on Spitsbergen: the extended Svalbard Airport temperature series 1898-2012. *Polar Research*, 33, doi: 10.3402/polar.v33.21349.

Norem H and F Sandersen (2012). Flom- og sørpeskred. Høringsutgave av veileder. *Statens Vegvesen rapporter* Nr. 73, pp. 102

Norges vassdrags- og energidirektorat (NVE) (2016). Skredfarekartlegging i utvalgte områder på Svalbard. Red. Maria Hannus. *NVE-Rapport* nr 91-2016. ISBN 978-82-410-1544-1.

Nuth C, G Moholdt, J Kohler, JO Hagen and A Kääb (2010). Svalbard glacier elevation changes and contribution to sea level rise. *J. Geophys. Res*., 115, F01008. doi:10.1029/2008JF001223

Nuth C, J Kohler, M König, A von Deschwanden, JO Hagen, A Kääb, G Moholdt and R Pettersson (2013). Decadal changes from a multi-temporal glacier inventory of Svalbard. *The Cryosphere* 7, 1–19. doi:10.5194/tc-7-1-2013

Næss A and O Gaidai (2009). Estimation of extreme values from sampled time series, *Structural Safety,* 31(4), 325-334, doi: 10.1016/j.strusafe.2008.06.021

Obu J, S Westermann, A Bartsch et al. (2019). Northern Hemisphere permafrost map 2000-2016 based on TTOP modelling at 1 km scale, *Earth Science Reviews*.

Olsen A, A Omar, R Bellerby, T Johannessen, U Ninnemann, K Brown, K Olsson, J Olafsson, G Nondal, C Kivimäe, S Kringstad, C Neill and S Olafsdottir (2006). Magnitude and origin of the anthropogenic CO_2 increase and 13C suess effect in the Nordic seas since 1981. *Glob. Biogeochem. Cycles* 20 (GB3027).

Omang OCD and HP Kierulf (2011). Past and present-day ice mass variation on Svalbard revealed by superconducting gravimeter and GPS measurements, *Geophys. Res. Lett.,* 38, L22304, doi:10.1029/2011GL049266.

Onarheim IH, LH Smedsrud, RB Ingvaldsen and F Nilsen (2014). Loss of sea ice during winter north of Svalbard. *Tellus A*, 66, 23933.

Onarheim IH, T Eldevik, LH Smedsrud and JC Stroeve (2018). Seasonal and Regional Manifestation of Arctic Sea Ice Loss. *J. Climate*, Vol 31, 49-17-4932, DOI: 10.1175/JCLI-D-17-0427.1

Orlowsky B, F-W Gerstengarbe and P Werner (2008). A resampling scheme for regional climate simulations and its performance compared to a dynamical RCM. *Theor. Appl. Climatol.*, 92(3), 209-223. doi: 10.1007/s00704-007-0352-y.

Orr J, V Fabry, O Aumont, L Bopp, S Doney, RAG Feely,N, Gruber, A Ishida, F Joos, R Key, K Lindsay, E Maier-Reimer, R Matear, P Monfray, A Mouchet, R Najjar, G-K Plattner, K Rodgers, CL Sabine, J Sarmiento, R Schlitzer, R Slater. Systems 131 (2014) 10–20 Totterdell I, M-F Weirig, Y Yamanaka and A Yool (2005). Anthropogenic ocean acidification over the twentyfirst century and its impact on calcifying organisms. *Nature* 437, 681–686.

Orvik KA, Ø Skagseth and M Mork (2001). Atlantic inflow to the Nordic Seas: current structure and volume fluxes from moored current meters, VM-ADCP and SeaSoar-CTD observations, 1995-1999, *Deep-Sea Research I*, 48, 937-957.

Pavlov AK, V Tverberg, BV Ivanov, F Nilsen, S Falk-Petersen and M Granskog (2013). Warming of Atlantic water in two West Spitsbergen fjords over the last century (1912-2009), *Polar Research*, 32(1). 11206, http://dx.doi.org/10.3402/polar.v32i0.11206.

Pavlova O, V Pavlov and S Gerland (2014). The impact of winds and sea surface temperatures on the Barents Sea ice extent, a statistical approach. *J Mar Sys* 130:248–255, http://dx.doi.org/10.1016/j.jmarsys.2013.02.011

Pavlova O, S Gerland and H Hop (2019). Changes in sea-ice extent and thickness in Kongsfjorden, Svalbard (2003-2016). In: Hop H, Wiencke C (eds) The ecosystem of Kongsfjorden, Svalbard. *Advances in Polar Ecology* 2, Springer Verlag (in press)

Peeters B, ÅØ Pedersen, LE Loe, K Isaksen, V Veiberg, A Stien, J Kohler, J-C Gallet, R Aanes and BB Hansen (2018). *Environmental Research Letters* 1748-9326. URL: http://iopscience.iop.org/10.1088/1748-9326/aaefb3

Peltier WR (2004). Global glacial isostasy and the surface of the ice-age earth: The ICE-5G (VM2) model and GRACE. *Annu. Rev. Earth Planet. Sci.*, 32, 111–149.

Peltier WR and RG Fairbanks (2006). Global glacial ice volume and Last Glacial Maximum duration from an extended Barbados sea level record. *Quaternary Science Reviews* 25, 3322.

Perovich, D, W Meier, M Tschudi, S Farrell, S Gerland, S Hendricks, T Krumpen, T and C Haas (2016): Sea ice. In: Arctic Report Card 2016. http://www.arctic.noaa.gov/Report-Card.

Peterson AK, I Fer, MG McPhee and A Randelhoff (2017). Turbulent heat and momentum fluxes in the upper ocean under Arctic sea ice, *J. Geophys. Res. Oceans*, 122, 1439–1456, doi:10.1002/2016JC012283.

Petterson L-E (1994). The hydrological regime of Spitsbergen, Svalbard. In: Sand, K., Killingtveit, Å. (Eds.): Proceedings of the 10th International Northern Research Basins Symposium and Workshop, Spitsbergen, Norway. *SINTEF Report 22* A96415, Trondheim, 95–107.

Pithan F and T Mauritsen (2014). Arctic amplification dominated by temperature feedbacks in contemporary climate models. *Nature Geoscience*, DOI: 10.1038/NGEO2071

Polyakov IV, RV Bekryaev, GV Alekseev, US Bhatt, RL Colony, MA Johnson, AP Maskshtas and D Walsh (2003). Variability and trends of air temperature and pressure in the maritime Arctic 1875-2000. *J. Clim.,* 16, 2067-2077

Polyakov IV, AV Pnyushkov, MB Alkire, IM Ashik, TM Baumann, EC Carmack, I Goszczko, J Guthrie, VV Ivanov, T Kanzow, R Krishfield, R Kwok, A Sundfjord, J Morison, R Rember and A Yulin (2017). Greater role for Atlantic inflows on sea-ice loss in the Eurasian Basin of the Arctic Ocean. *Science.* 10.1126/science.aai8204

Prandi P, M Ablain, A Caxenave and N Picot (2012a). A New Estimation of Mean Sea Level in the Arctic Ocean from Satellite Altimetry, *Marin Geodesy*, 35(S1), 61-91, doi: 10.1080/01490419.2012.718222.

Prandi P, M Ablain, A Cazenave and N Picot (2012b). Sea level variability in the Arctic Ocean observed by satellite altimetry, *Ocean Science Discussions*, 9, 2375-2401, doi: 10.5194/osd-9-2375-2012.

Prein AF, W Langhans, G Fosser, A Ferrone, N Ban, K Goergen, M Keller, M Tölle, O Gutjahr, F Feser and E Brisson (2015). A review on regional convection permitting climate modelling: Demonstrations, prospects, and challenges. *Reviews of Geophysics*, 53(2), pp. 323-361, doi: 10.1002/2014RG000475.

Przybylak R and R Maszewski (2012). Atmospheric circulation and dynamic conditions. In Topoclimatic Diverisity in Forlandsundet Region (NWSpitsbergen) in *Global Warming Conditions,* Przybylak R, Araźny A, Kejna M (eds). Oficyna Wydaw. "Turpress": Toruń; 27–51.

Radić V, A Bliss, AD Beedlow, R Hock, E Miles and JG Cogley (2013). Regional and global projections of the 21st century glacier mass changes in response to climate scenarios from global climate models. *Clim. Dyn.*, doi:10.1007/s00382-013-1719-7.

Ramsli G (1953) Skredet i Vannledningsdalen, Longyearbyen 11. juni 1953. (The slushflow in Vannledningsdalen, Longyearbyen 11 June 1953.) *Notat, Statens Naturskadefond*, pp. 3

Ravndal OR and B Sande (2016). Ekstremverdianalyse av vannstandsdata langs norskekysten, *Technical report of the Norwegian Mapping Authority*, NDDF 16-1.

Rayner NA, DE Parker, EB Horton, CK Folland, LV Alexander, DP Rowell, EC Kent and A Kaplan (2003). Global analyzes of sea surface temperature, sea ice, and night marine air temperature since the late nineteenth century. *J. Geophys. Res.,* 108(D14), 4407, doi: 10.1029/2002JD002670.

Reistad M, O Breivik, H Haakenstad, OJ Aarnes, BR Furevik and J-R Bidlot (2011). A high-resolution hindcast of wind and waves for the North Sea, the Norwegian Sea, and the Barents Sea, *J Geophys Res*, 116, p 18, doi:10/fmnr2m

Renner AHH, S Hendricks, S Gerland, J Beckers, C Haas and T Krumpen (2013). Large-scale ice thickness distribution of first-year sea ice in spring and summer north of Svalbard. *Annals of Glaciology* 54(62), 13-18, doi:10.3189/2012AoG62A146.

Reusche M, K Winsor, AE Carlson, SA Marcott, DH Rood, A Novak, S Roof, M Retelle, A Werner and M Caffee (2014). 10Be surface exposure ages on the late-Pleistocene and Holocene history of Linnébreen on Svalbard. *Quaternary Science Reviews* 89, 5-12.

Rinke A, M Maturilli, RM Graham, H Matthes, D Handorf, L Cohen, SR Hudson and JC Moore (2017). Extreme cyclone events in the Arctic: Wintertime variability and trends. *Environ. Res. Lett*. 12, 094006

Risebrobakken B, T Dokken, OH Otterå, E Jansen, YQ Gao and H Drange (2007). Inception of the Northern European ice sheet due to contrasting ocean and insolation forcing, *Quaternary Research*, 67, 128-135, 2007.

Riser S, H Freeland, D Roemmich, S Wijffels, A Troisi, M Belbéoch, D Gilbert, J Xu, S Pouliquen, A Thresher, P-Y Le Traon, G Maze, B Klein, M. Ravichandran, F Grant, P-M Poulain, T Suga, B Lim, A Sterl, P Sutton, K-A Mork, P Vélez-Belchí, I Ansorge, B King, J Turton, M Baringer and S Jayne (2016). Fifteen years of ocean observations with the global Argo array, *Nature Clim. Change,* 6,145–153.

Rogers JC, L Yang and L Li (2005). The role of Fram Strait winter cyclones on sea ice flux and on Spitsbergen air temperatures. *Geophys. Res. Lett*., 32, L06709, doi:10.1029/2004GL022262.

Romanovsky VE, S Smith and HH Christiansen (2010) . Permafrost thermal state in the polar Northern Hemisphere during the international polar year 2007–2009: a synthesis. *Permafrost Periglac. Process*., 21, 106-116.

Romanovsky V, K Isaksen, D Drozdov, O Anisimov, A Instanes, M Leibman, AD McGuire, N Shiklomanov, S Smith and D Walker (2017). Changing permafrost and its impacts. In: Snow, Water, Ice and Permafrost in the Arctic (SWIPA) 2017. pp. 65-102. *Arctic Monitoring and Assessment Programme (AMAP)*, Oslo, Norway.

Rösel A, P Itkin, J King, D Divine, C Wang, MA Granskog, T Krumpen and S Gerland (2018). Winter and spring development of sea-ice and snow thickness distributions north of Svalbard observed during N-ICE2015. *Journal of Geophysical Research – Oceans* (special issue N-ICE2015), DOI 10.1002/2017JC012865

Røthe TO, J Bakke, K Vasskog, M Gjerde, WJ D'Andrea RS Bradley (2015). Arctic Holocene glacier fluctuations reconstructed from lake sediments at Mitrahalvøya, Spitsbergen. *Quaternary Science Reviews 109*, 111-125.

Røthe TO, J Bakke, EW Støren and RS Bradley (2018). Reconstructing Holocene glacier and climate fluctuations from lake sediments in Vårfluesjøen, northern Spitsbergen. *Frontiers in Earth Science* 6.

Sabine C, R Feely, N Gruber, R Key, K Lee, J Bullister, R Wanninkhof, C Wong, D Wallace, B Tilbrook, F Millero, T-H Peng, A Kozyr, T Ono and A Rios (2004). The oceanic sink for anthropogenic CO 2. *Science* 305 (5682), 367–371.

Saloranta TM (2016). Operational snow mapping with simplified data assimilation using the seNorge snow model, Journal of Hydrology, 538, 314-325, https://doi.org/10.1016/j.jhydrol.2016.03.061.

Saloranta TM and H Svendsen (2001). Across the Arctic front west of Spitsbergen: High-resolution CTD sections from 1998–2000. *Polar Res.,* 20, 177–184, doi:10.1111/ j.1751-8369.2001.tb00054.x.

Sand K, J-G Winther, D Maréchal, O Bruland and K Melvold (2003). Regional variations of snow accumulation on Spitsbergen, Svalbard, 1997–99. *Nordic Hydrology,* 34, 17–32.

Sandø AB, JEØ Nilsen, Y Gao and K Lohmann (2010). Importance of heat transport and local air-sea heat fluxes for the Barents Sea climate variability, *J. Geoph. Res. Oceans*, 115, C07013, doi:10.1029/2009JC005884.

Sandø AB, JEØ Nilsen and T Eldevik (2012). Mechanisms behind the Nordic Seas-North-Atlantic exchanges. *J. Geoph. Res.,* 117.

Sandø AB, Y Gao and HR Langehaug (2014a). Relation between ocean heat transports, sea ice processes and Arctic sea ice variability in NorESM1-M simulations, *J. Geophys. Res*. *Oceans*, 119, 2095-2108, doi: 10.1002/2013JC009435.

Sandø AB, A Melsom and WP Budgell (2014b). Downscaling IPCC control run and future scenario with focus on the Barents Sea, *Ocean Dynamics*, doi:10.1007/s10236-014-0731-8.

Schuler TV, P Crochet, R Hock, M Jackson, I Barstad and T Jóhannesson (2008). Distribution of snow accumulation on Svartisen ice cap, Norway, assessed by a model of orographic precipitation. *Hydrol. Proc*., 22, 3998–4008

Schuler TV (2018). Svalbard impact assessment forcing dataset, version 1 [Data set]. Norstore. *Department of Geosciences, University of Oslo* https://doi.org/10.11582/2018.00

Screen JA and I Simmonds (2010). Increasing fall⬜winter energy loss from the Arctic Ocean and its role in Arctic temperature amplification, *Geophys. Res. Lett*., Vol. 37, L16707.

Serreze MC and RG Barry (2011). Processes and impacts of Arctic amplification: A research synthesis, *Global and Planetary Change* 77 (2011) 85–96

Serreze MC, AD Crawford and AP Barrett (2015). Extreme daily precipitation events at Spitsbergne, and Arctic Island. *Int. J. Climatol* . DOI: 10.1002/joc.4308

Shchepetkin AF and JC McWilliams (2005). The regional oceanic modelling system (ROMS): a split-explicit, free-surface, topography-following-coordinate oceanic model. *Ocean Modelling* 9:347–404.

Shiklomanov NI, DA Streletskiy and FE Nelson (2012). Northern Hemisphere component of the global Circumpolar Active LayerMonitoring (CALM) Program. In: Hinkel KM, ed. Proceedings of the 10th International Conference on Permafrost, vol. 1. Salekhard: *The Northern Publisher Salekhard*, 377–382.

Sidorchuk A and B Matveev (1994). Channel processes and erosion rates in the rivers of the Yamal Peninsula in Western Siberia, *IAHS publ.* no.224

Sirevaag A and I Fer (2009). Early spring oceanic heat fluxes and mixing observed from drift stations north of Svalbard. *J. Phys. Oceanogr.,* 39, 3049–3069, doi:10.1175/2009JPO4172.1.

Skjelvan I, E Falck, F Rey and S Kringstad (2008). Inorganic carbon time series at Ocean Weather Station M in the Norwegian Sea. *Biogeosciences* 5, 549–560.

Skjong M, A Naess and OEB Næss (2013). Statistics of Extreme Sea Levels for Locations along the Norwegian Coast, *Journal of Coastal Research*, 29(5), 1029 – 1048, https://doi.org/10.2112/JCOASTRES-D-12-00208.1.

Skogen MD, SS Hjøllo, AB Sandø and J Tjiputra (2018). Future ecosystem changes in the Northeast Atlantic: A comparison study between a global and regional models. Accepted for publication in *ICES J. Mar. Sci*.

Skogseth R, PM Haugan and J Haarpaintner (2004). Ice and brine production in Storfjorden from four winters of satellite and in situ observations and modeling, *J. Geophys. Res.,*109, C10008, doi:10.1029/2004JC002384.

Skogseth R, LH Smedsrud, F Nilsen and I Fer (2008). Observations of hydrography and downflow of brine-enriched shelf water in the Storfjorden polynya, Svalbard, *J. Geophys. Res.,*113, 08049,doi:10.1029/2007JC004452.

Skogseth R, MG McPhee, F Nilsen and LH Smedsrud (2013). Creation and tidal advection of a cold salinity front in Storfjorden: 1. Polynya dynamics, *J. Geophys. Res. Oceans*, 118, doi:10.1002/jgrc.20231.

Slagstad D, P Wassmann and I Ellingsen (2015). Physical constrains and productivity in the future Arctic Ocean. *Front. Mar. Sci*. 2 (85).

Slangen ABA and RSW van de Wal (2011). An assessment of uncertainties in using volume-area modelling for computing the twenty-first century glacier contribution to sea-level change. *Cryosphere*, 5, 673–686.

Smedsrud LH, P Budgell, AD Jenkins and B Ådlandsvik (2006). Fine-scale sea-ice modelling of the Storfjorden polynya, Svalbard, *Annals of Glaciology* 44.

Smedsrud LH, I Esau, R Ingvaldsen, T Eldevik, P Haugan, C Li, V Lien, A Olsen, A Omar, O Otterå, B Risebrobakken, AB Sandø, V Semenov and S Sorokina (2013). The role of the Barents Sea in the Arctic climate system, *Review of Geophysics,* 51, 415–449, doi:10.1002/rog.20017.

Smedsrud LH, MH Halvorsen, JC Stroeve, R Zhang and K Kloster (2017). Fram Strait sea ice export variability and September Arctic sea ice extent over the last 80 years, *The Cryosphere,* 11, 65–79, www.the-cryosphere.net doi:10.5194/tc-11-65-2017.

Smith SL, VE Romanovsky, AG Lewkowicz, CR Burn, M Allard, GD Clow, K Yoshikawa and J Throop (2010). Thermal state of permafrost in North America - A contribution to the International Polar Year. *Permafrost and Periglacial Processes,* 21:117-135.

Smith RB and I Barstad (2004). A linear theory of orographic precipitation. *J. Atmos. Sci.,* 61, 1377–1391.

Snyder J, A Werner and G Miller (2000). Holocene cirque glacier activity in western Spitsbergen, Svalbard: sediment records from proglacial Linnévatnet. *The Holocene* 10, 555-563.

Sorteberg A, I Haddeland, JE Haugen, S Sobolowski and WK Wong (2014). Evaluation of distribution mapping based bias correction methods. *NCCS-report* no. 1/2014 (www.klimaservicesenter.no)

Stein R, K Fahl, P Giertz, F Niessen and G Lohmann (2017). Arctic Ocean sea ice cover during the penultimate glacial and the last interglacial, *Nature Communication*, 8:373, doi:10.1038/s41467-017-00552-1

Stenius S (2016). Flomberegning for Longyearelva, Spitsbergen, Svalbard (400). *NVE-Oppdragsrapport* A 7:2016. http://publikasjoner.nve.no/oppdragsrapportA/2016/oppdragsrapportA2016_07.pdf

Stickley et al. (2009). Evidence for middle Eocene Arctic sea ice from diatoms and ice-rafted debris, *Nature*, 460, doi:10.1038/nature08163

Strand SM (2016). Ground temperature response to winter warm events in Svalbard - A periglacial landform comparison. MSc-thesis, *Department of Geosciences, University of Oslo,* pp. 89

Straneo F, GS Hamilton, DA Sutherland, LA Stearns, F Davidson, MO Hammill, GB Stenson and A Rosing-Asvid (2010). Rapid circulation of warm subtropical waters in a major glacial fjord in East Greenland *Nature Geoscience*, 3:182-186. doi.org/10.1038/ngeo764.

Stroeve JC, MC Serreze, MM Holland, JE Kay J Malanik and AP Barret (2012). The Arctic's rapidly shrinking sea ice cover: a research synthesis. *Climate Change,* 110, 1005-1027. doi:10.1007/s10584-011-0101-1.

Sund M (2008). Polar hydrology. Norwegian Water Resources and Energy Directorate's work in Svalbard. *NVE-Report* No. 2/2008,

Sund M, TR Lauksnes and T Eiken. (2014). Surge dynamics in the Nathorstbreen glacier system, Svalbard. *The Cryosphere*, 8, 623-638

Sutton RT and DLR Hodson (2005). Atlantic Ocean Forcing of North American and European Summer Climate, *Science,* 309(5731), 115–118, doi:10.1126/science.1109496.

Svendsen JI and J Mangerud (1997). Holocene glacial and climatic variations on Spitsbergen, Svalbard. *The Holocene* 7, 45-57.

Sørbel L and J Tolgensbakk (2002). Ice-wedge polygons and solifluction in the Adventdalen area, Spitsbergen, Svalbard, *Norsk Geografisk Tidsskrift*. 56 (2), 62-66, DOI: 10.1080/002919502760056369

Tapley BD, S Bettadpur, M Watkins and C Reigber (2004). The gravity recovery and climate experiment: Mission overview and early results. *Geophysical Research Letters* 31(9), doi: 10.1029/2004GL019920

Taylor KE, RJ Stouffer and GA Meehl (2012). An Overview of CMIP5 and the Experiment Design. *Bulletin of the American Meteorological Society*, 93, 485–498.

Thomson J and WE Rogers (2014). Swell and sea in the emerging Arctic Ocean*, Geophys Res Lett*, 41(9), pp 3136-3140, doi:10.1002/2014GL059983

Tverberg V and OA Nøst (2009). Eddy overturning across a shelf edge front. *J. Geophys. Res.,* 114, C04024, doi:10.1029/ 2008JC005106.

Tverberg V, OA Nøst, C Lydersen and KM Kovacs (2014). Winter sea ice melting in the Atlantic water subduction area, Svalbard Norway. *J. Geophys. Res. Oceans*, 119, 5945–5967, doi:10.1002/ 2014JC010013.

Tverberg V, R Skogseth, F Cottier, A Sundfjord, W Walczowski, M Inall, E Falck, O Pavlova and F Nilsen (2018). The Kongsfjorden transect: seasonal and inter-annual variability in hydrography. In: Hop, H., Wiencke, C. (Eds.), The Ecosystem of Kongsfjorden, Svalbard. Vol. 2 of *Advances in Polar Ecology*. Springer, ISBN 978-3-319-46425-1.

Van der Bilt WGM, J Bakke, K Vasskog, WJ D'Andrea, RS Bradley and S Ólafsdóttir (2015). Reconstruction of glacier variability from lake sediments reveals dynamic Holocene climate in Svalbard. *Quaternary Science Reviews* 126, 201-218.

Van der Bilt WGM, WJ D`Andrea, J Bakke, N Balascio, JP Werner, M Gjerde and R Bradley (2016). Alkenone-based reconstructions reveal four-phase Holocene temperature evolution for High Arctic Svalbard. *Quaternary Science Reviews* 183, 204-213. doi: 10.1016/j.quascirev.2016.10.006.

Van Pelt WJJ, J Oerlemans, CH Reijmer, VA Pohjola, R Pettersson and JH van Angelen (2012). Simulating melt, runoff and refreezing on Nordenskiöldbreen, Svalbard, using a coupled snow and energy balance model. *The Cryosphere*, 6, 641-659. doi:10.5194/tc-6-641-2012

Van Pelt WJJ, J Kohler, GE Liston, JO Hagen, B Luks, CH Reijmer and VA Pohjola (2016). Multidecadal climate and seasonal snow conditions in Svalbard, *J. Geophys. Res. Earth Surf*., 121, doi:10.1002/2016JF003999.

Vaughan DG, JC Comiso, I Allison, J Carrasco, G Kaser, R Kwok, P Mote, T Murray, F Paul, J Ren, E Rignot, O Solomina, K Steffen and T Zhang (2013). Observations: Cryosphere. In: *Climate Change 2013: The Physical Science Basis.* Contribution of Working Group I to the Fifth Assessment Report of the Intergovernmental Panel on Climate Change [Stocker, T.F., D. Qin, G.-K.

Vikhamar-Schuler D, K Isaksen, JE Haugen, H Tømmervik, B Luks, TV Schuler and JW Bjerke (2016). Changes in Winter Warming Events in the Nordic Arctic Region, *Journal of Climate*, 29(17), 6223–6244, doi:10.1175/JCLI-D-15-0763.1.

Vikhamar-Schuler D, EJ Førland, J Lutz and HM Gjelten (2019). Evaluation of downscaled reanalysis and observations for Svalbard - Background-report for Climate in Svalbard 2100. *NCCS-report* 4/2019 (www.klimaservicesenter.no).

Vogel S, M Eckerstorfer and HH Christiansen (2012). Cornice dynamics and meteorological control at Gruvefjellet, Central Svalbard. *The Cryosphere*, 6, 157-171

Volkov DL and M-I Pujol (2012). Quality assessment of a satellite altimetry data product in the Nordic, Barents, and Kara seas, *Journal of Geophysical Research*, 117, C03025, doi:10.1029/2011JC007557.

Walczowski W and J Piechura (2011). Influence of the West Spitsbergen Current on the local climate. *Int. J. Climatol.* 31: 1088–1093, DOI: 10.1002/joc.2338.

Wang C, L Shi, S Gerland, MA Granskog, AHH Renner, Z Li, E Hansen and T Martma (2013). Spring sea ice evolution in Rijpfjorden (80°N), Svalbard, from in situ measurements and Ice Mass Balance Buoy (IMB) data. *Annals of Glaciology* 54 (62). 253-260.

Wang C, B Cheng, K Wang, S Gerland and O Pavlova (2015). Modelling snow ice and superimposed ice formation on landfast sea ice. *Polar Research*, 34, 20828, http://dx.doi.org/10.3402/polar.v34.20828.

Wanner H, J Beer, J Bütikofer, TJ Crowley, U Cubasch, J Flückiger, H Goosse, M Grosjean, F Joos and JO Kaplan (2008). Mid-to Late Holocene climate change: an overview. *Quaternary Science Reviews* 27, 1791-1828.

Werner A (1993). Holocene moraine chronology, Spitsbergen, Svalbard: lichenometric evidence for multiple Neoglacial advances in the Arctic. *The Holocene,* 3, 128-137.

Werner K, J Müller, K Husum, RF Spielhagen, ES Kandiano and L Polyak (2015). Holocene sea subsurface and surface water masses in the Fram Strait–Comparisons of temperature and sea-ice reconstructions. *Quaternary Science Reviews* 147, 194-209. Doi: 10.1016/j.quascirev.2015.09.007

Westermann S, TV Schuler, K Gisnås and B Etzelmüller (2013). Transient thermal modeling of permafrost conditions in Southern Norway. *The Cryosphere*, 7(2), p.719.

Westermann S, M Langer, J Boike, M Heikenfeld, M Peter, B Etzelmüller and G Krinner (2016). Simulating the thermal regime and thaw processes of ice-rich permafrost ground with the land-surface model CryoGrid 3. *Geoscientific Model Development*, 9(2), p.523.

Wickström S, OM Jonassen, P Uotila and T Vihma (2019). 1979-2016 Trends in Cyclone Activity in The European Arctic (in progress).

Willis MJ, W Zheng, WJ Durkin, M Pritchard, JM Ramage, JA Dowdeswell, TJ Benham, RP Bassford, LA Stearns, AF Glazovsky, YY Macheret and CC Porter (2018). Massive destabilization of an Arctic ice cap. *Earth and Planetary Science Letters*, 502, doi: 10.1016/j.epsl.2018.08.049.

Wong WK, I Haddeland, D Lawrence and S Beldring (2016). Gridded 1 x 1 km climate and hydrological projections for Norway. *NVE Report* No. 59/2016, ISBN: 978-82-410-1512-0, http://data.nve.no/report/climate_hydrological_projections_Norway.pdf

Wouters B, D Chambers and EJO Schrama (2008). GRACE observes small-scale mass loss in Greenland. *Geophys. Res. Letters* 35(20), L20501, doi:10.1029/2008GL034816.

Yang D, D Kane, Z Zhang, D Legates and B Goodison (2005). Bias-corrections of long-term (1973-2004) daily precipitation data over the northern regions., *Geophysical Research Letters,* 32. doi:10.1029/2005GL024057

Zhang Y, H Renssen and H Seppä (2016). Effects of melting ice sheets and orbital forcing on the early Holocene warming in the extratropical Northern Hemisphere. *Climate of the Past* 12, 1119-1135.

Zhu X, W Wang and K Fraedrich (2013). Future climate in the Tibetan Plateau from a statistical regional climate model. *J.Clim.* 26(24), pp. 10125–10138, doi: 10.1175/JCLI-D-13-00187.1.

Zhuravskiy D, B Ivanov and A Pavlov (2012). Ice conditions at Grønfjorden Bay, Svalbard, from 1974 to 2008. *Polar Geogr* 35:169-17

Østby TI, TV Schuler, JO Hagen, R Hock, J Kohler and CH Reijmer (2017). Diagnosing the decline in climatic mass balance of glaciers in Svalbard over 1957\0232014, *The Cryosphere*, 11, 191-215, doi:10.5194/tc-11-191-2017.

Årthun M, T Eldevik, LH Smedsrud, Ø Skagseth and R Ingvaldsen (2012). Quantifying the influence of Atlantic heat on Barents Sea ice variability and retreat, *Journal of Climate* 25 (13), 4736-4743

Årthun M, T Eldevik , E Viste , H Drange, T Furevik , HL Johnson and NS Keenlyside (2017). Skillful prediction of northern climate provided by the ocean, *Nature Communications,* DOI: 10.1038/ncomms15875.

APPENDIX

A1: Climate model results applied for the atmospheric projections in this report

Table A1.1 The following ArcticCORDEX runs (available on the Earth System Grid Federation) were applied for calculating the RCM-based projections of temperature and precipitation. The MPI-ESM-LR (r1i1p1) is also applied for the COSMO projections. Symbols - and YES denote non-available and available simulations, respectively.

GCM (run)	RIP	RCM	HIST (1971-2000)	RCP2.6	RCP4.5	RCP8.5
CCCma-CanESM2 (1)	r1i1p1	SMHI-RCA4	YES	-	YES	YES
ICHEC-EC-EARTH (2)	r12i1p1	SMHI-RCA4-SN	YES	-	-	YES
		SMHI-RCA4	YES	-	YES	YES
ICHEC-EC-EARTH (1)	r3i1p1	DMI-HIRHAM5	YES	-	YES	YES
MPI-M-MPI-ESM-LR (3)	r1i1p1	MGO-RRCM	YES	-	-	YES
		SMHI-RCA4-SN	YES	-	-	YES
		SMHI-RCA4	YES	-	YES	YES
NCC-NorESM1-M (1)	r1i1p1	SMHI-RCA4	YES	-	YES	YES

Table A1.2 All available CMIP5 runs used for statistical downscaling. An overview over available projections assuming the RCP2.6, RCP4.5, and RCP8.5 emission scenarios is given here. Value between brackets show the total number of simulations in each of the cases. Simulations shown in red are left out in the "selected" ensemble in Table A.2.2 and A.2.3.

Institute ID	Climate Model ID	RIP	Realization		RCP2.6 (65)	RCP4.5 (108)	RCP8.5 (81)	Selected
CSIRO-BOM (2)	ACCESS1-0 (1)	r1i1p1	1	-	YES	YES	YES
	ACCESS1-3 (1)	r1i1p1	1	-	YES	YES	YES
BCC (1)	bcc-csm1-1 (1)	r1i1p1	1	YES	YES	YES	YES
	bcc-csm1-1-m (1)	r1i1p1	1	YES	YES	-	YES
BNU (1)	BNU-ESM (1)	r1i1p1	1	YES	YES	YES	YES
CCCma (5)	CanESM2 (5)	r1i1p1	1	YES	YES	YES	YES
		r2i1p1	2	YES	YES	YES	YES
		r3i1p1	3	YES	YES	YES	YES
		r4i1p1	4	YES	YES	YES	YES
		r5i1p1	5	YES	YES	YES	YES

NCAR (6)	CCSM4 (6)	r1i1p1	1	YES	YES	YES	YES
		r2i1p1	2	YES	YES	YES	YES
		r3i1p1	3	YES	YES	YES	YES
		r4i1p1	4	YES	YES	YES	YES
		r5i1p1	5	YES	YES	YES	YES
		r6i1p1	6	YES	YES	YES	YES
NSF-DOE-NCAR (4)	CESM1-BGC (1)	r1i1p1	1		YES	YES	YES
	CESM1-CAM5 (3)	r1i1p1	1	YES	YES	YES	YES
		r2i1p1	2	YES	YES	YES	YES
		r3i1p1	3	YES	YES		YES
CMCC (2)	CMCC-CM (1)	r1i1p1	1	-	YES	YES	YES
	CMCC-CMS (1)	r1i1p1	1	-	YES	YES	YES
CNRM-CERFACS (5)	CNRM-CM5 (5)	r1i1p1	1	YES	YES	YES	YES
		r2i1p1	2	-	-	YES	YES
		r3i1p1	3	-	-	YES	YES
		r4i1p1	4	-	-	YES	YES
		r5i1p1	5	-	-	YES	YES
CSIRO-QCCCE	CSIRO-Mk3-6-0 (10)	r1i1p1	1	YES	YES	YES	YES
		r2i1p1	2	YES	YES	YES	YES
		r3i1p1	3	YES	YES	YES	YES
		r4i1p1	4	YES	YES	YES	YES
		r5i1p1	5	YES	YES	YES	YES
		r6i1p1	6	YES	YES	YES	YES
		r7i1p1	7	YES	YES	YES	YES
		r8i1p1	8	YES	YES	YES	YES
		r9i1p1	9	YES	YES	YES	YES
		r10i1p1	10	YES	YES	YES	YES
ICHEC (9)	EC-EARTH (9)	r1i1p1	1	-	YES	YES	YES
		r2i1p1	2	-	YES	YES	YES
		r3i1p1	3	-	YES	-	YES
		r6i1p1	6	-	YES	-	YES
		r8i1p1	8	YES	YES	YES	YES
		r9i1p1	9	-	YES	YES	YES
		r11i1p1	11	-	-	YES	YES
		r12i1p1	12	YES	YES	YES	YES
		r13i1p1	13	-	-	YES	YES
LASG-CESS (3)	FGOALS_g2 (1)	r1i1p1	1	YES	YES	YES	YES
FIO (3)	FIO-ESM (3)	r1i1p1	1	YES	YES	YES	YES
		r2i1p1	2	YES	YES	YES	YES
		r3i1p1	3	YES	YES	YES	YES

NOAA GFDL (3)	GFDL-CM3 (1)	r1i1p1	1	YES	YES	YES	YES
	GFDL-ESM2G (1)	r1i1p1	1	YES	YES	YES	YES
	GFDL-ESM2M (1)	r1i1p1	1	YES	YES	YES	YES
NASA-GISS (34)	GISS-E2-H (15)	r1i1p1	1	YES	YES	YES	-
		r2i1p1	2	-	YES	YES	-
		r3i1p1	3	-	YES	YES	-
		r4i1p1	4	-	YES	-	-
		r5i1p1	5	-	YES	-	-
		r1i1p2	1	YES	YES	YES	-
		r2i1p2	2	-	YES	YES	-
		r3i1p2	3	-	YES	YES	-
		r4i1p2	4	-	YES	-	-
		r5i1p2	5	-	YES	-	-
		r1i1p3	1	YES	YES	-	-
		r2i1p3	2	-	YES	-	-
		r3i1p3	3	-	YES	-	-
		r4i1p3	4	-	YES	-	-
		r5i1p3	5	-	YES	-	-
	GISS-E2-H-CC (1)	r1i1p1	1	-	YES	-	-
	GISS-E2-R (15)	r1i1p1	1	YES	YES	-	-
		r2i1p1	2	-	YES	-	-
		r3i1p1	3	-	YES	-	-
		r4i1p1	4	-	YES	-	-
		r5i1p1	5	-	YES	-	-
		r1i1p1	6	-	YES	-	-
		r1i1p2	1	YES	YES	-	-
		r2i1p2	2	-	YES	-	-
		r3i1p2	3	-	YES	-	-
		r4i1p2	4	-	YES	-	-
		r5i1p2	5	-	YES	-	-
		r1i1p3	1	YES	YES	-	-
		r2i1p3	2	-	YES	-	-
		r3i1p3	3	-	YES	-	-
		r4i1p3	4	-	YES	-	-
		r5i1p3	5	-	YES	-	-
		r6i1p3	6	-	YES	-	-
	GISS-E2-R-CC (1)	r1i1p1	1	-	YES	-	-
NIMR-KMA (1)	HadGEM2-AO (1)		1	YES	YES	YES	YES

MOHC (5)	HadGEM2-CC (1)	r1i1p1	1		YES	YES	YES
	HadGEM2-ES (4)	r1i1p1	1	YES	YES	YES	YES
		r2i1p1	2	YES	YES	YES	YES
		r3i1p1	3	YES	YES	YES	YES
		r4i1p1	4	YES	YES	YES	YES
INM (1)	inmcm4 (1)		1	-	YES	YES	YES
IPSL (6)	IPSL-CM5A-LR (4)	r1i1p1	1	YES	YES	YES	YES
		r2i1p1	2	YES	YES	YES	YES
		r3i1p1	3	YES	YES	YES	YES
		r4i1p1	4	YES	YES	YES	YES
	IPSL-CM5A-MR (1)	r1i1p1	1	YES	YES	YES	YES
	IPSL-CM5B-LR (1)	r1i1p1	1	-	YES	YES	YES
MIROC (5)	MIROC5 (3)	r1i1p1	1	YES	YES	YES	YES
		r2i1p1	2	YES	YES	YES	YES
		r3i1p1	3	YES	YES	YES	YES
	MIROC-ESM (1)	r1i1p1	1	YES	YES	YES	YES
	MIROC-ESM-CHEM (1)	r1i1p1	1	YES	YES	YES	YES
MPI-M (6)	MPI-ESM-LR (3)	r1i1p1	1	YES	YES	YES	YES
		r2i1p1	2	YES	YES	YES	YES
		r3i1p1	3	YES	YES	YES	YES
	MPI-ESM-MR (3)	r1i1p1	1	YES	YES	YES	YES
		r2i1p1	2	-	YES	-	YES
		r3i1p1	3	-	YES	-	YES
MRI	MRI-CGCM3 (1)	r1i1p1	1	YES	YES	YES	YES
NCC	NorESM1-M (1)	r1i1p1	1	YES	YES	YES	YES
NCC	NorESM1-ME (1)	r1i1p1	1	YES	YES	YES	YES

A2: Climate projections for temperature

Table A.2.1 Annual and seasonal temperature changes calculated from RCM under the emission scenarios RCP4.5 and RCP8.5 for the middle and the end of the century

Temp. change [°C]	1971-2000 to 2031-2060						1971-2000 to 2071-2100						
	RCP4.5			RCP8.5			RCP4.5			RCP8.5			
	Med	Low	High	Med	Low	High	Med	Low	High	Med	Low	High	CCLM
Svalbard land area													
Annual	4.9	4.3	7.1	5.5	4.4	8.7	6.9	4.9	9.4	9.8	6.7	15.6	7.2
DJF	7.1	5.7	10.3	7.9	6.8	13.3	10.3	6.8	13.2	14.4	10.6	21.9	9.1
MAM	4.4	3.1	6.9	4.9	4	7.7	6.5	4.1	8.4	9.2	7.7	16.1	7.2
JJA	2.3	1.6	3.6	3.1	1.2	3.9	3.3	2.3	4.7	5.8	2	8.4	4.9
SON	5.5	5.3	8.2	6.5	4.5	10.2	8.2	6	11.4	10.3	6.5	16.2	7.4
Northeast Svalbard area													
Annual	5.3	4.5	7.3	5.9	4.4	9	7.4	5.2	9.7	10.5	7	16.4	7.6
DJF	7.2	6.2	10.6	8.8	7.1	13.8	11.1	7.3	13.8	16.1	11.1	23.5	10.2
MAM	4.6	3	6.9	4.9	3.9	7.8	6.8	4.1	8.5	9.8	7.8	16.7	7.5
JJA	2.3	1.5	3.5	3	1.1	3.8	3	2.3	4.6	5.8	1.9	8.4	4.9
SON	6.1	5.9	8.8	7.1	4.9	11	9	6.7	12.1	11.2	7.1	17.3	8
Northwest Svalbard area													
Annual	4.5	4	6.4	4.9	4.3	8	6.2	4.5	8.8	8.9	6.6	14.9	6.7
DJF	6.5	4.9	9.1	6.8	6	12.1	8.4	5.9	11.8	12.1	10	20.4	8
MAM	4.1	2.9	6.6	4.7	3.9	7.5	6.2	3.9	8	8.7	7.8	15.7	6.8
JJA	2.4	1.5	3.7	3.1	1.5	3.9	3.2	2.3	4.8	6	2.3	8.2	5
SON	4.9	4.7	7.4	6	4.3	9.4	7.1	5.4	10.8	9.6	6.2	15.8	6.8
South Svalbard area													
Annual	4.4	3.9	7.5	5	4.1	8.8	6.1	4.5	9.3	8.7	6.1	14.3	6.4
DJF	7.1	5.2	11	7	6.1	13	9.1	6.3	13	11.8	9.7	19.2	7.5
MAM	4.3	3.7	7.2	4.8	4.1	8.1	6.3	4.2	8.7	8.7	7.4	15.1	6.6
JJA	3.1	1.7	4.1	3.3	1.3	5.2	4.3	2.3	5.5	5.8	1.9	9.1	5
SON	4.6	4.2	7.6	5.3	3.8	9.1	6.5	4.6	9.8	8.5	5.5	13.7	6.4
Longyearbyen grid-point													
Annual	4.6	4	7.1	5	4.6	8.3	6.3	4.4	8.9	8.7	7.3	14.4	6.5
DJF	6.4	5	9.8	6.9	5.9	12	8.1	6	11.9	11.6	9.8	18.9	8.2
MAM	4.4	3.5	7.3	5	4.2	8.1	6.6	4.4	8.6	9.2	8.2	15.9	7.1
JJA	2.8	2.4	3.7	3.2	2.7	4.4	3.8	2.8	5.1	5.8	4.3	8.7	4.3
SON	4.8	4.3	7.7	5.5	4.4	9	6.7	4.6	10.1	8.7	6.2	14.1	6.5

Table A.2.2 ESD changes of annual and seasonal temperatures over all regions and Longyearbyen by **2071-2100 assuming the RCP2.6, RCP4.5 and RCP8.5** emission scenarios respectively. Displayed values show the medium, low (5%), and high (95%) percentiles of absolute changes with regards to 1971-2000. Results obtained when using the MPI-ESM-LR, all, selected (skipping the red model runs in Table A.1.2), and common global climate models to downscale temperature are also shown in the table for comparison with the CCLM simulation (Table A.2.1. Last column)

	RCP26	Temperature changes by 2071-2100								
Models	MPI-ESM-LR	All models			Selected models			Common models		
Perc. Name		Med	Low	High	Med	Low	High	Med	Low	High
Perc. Value		50%	5%	95%	50%	5%	95%	50%	Min.	Max.
Svalbard-land area										
Annual	4	3.8	0.6	6.5	3.9	-0.5	6.6	4	3.8	4.3
DJF	5.3	5.8	-0.4	10.8	6.2	-2.6	10.9	5.3	4.9	7.4
MAM	4.5	3.2	0.5	5.4	3.2	-0.3	5.5	3.6	3	4.5
JJA	1.6	1.4	-0.3	3.2	1.5	-0.6	3.3	1.6	1	1.9
SON	4.8	4.8	0.6	8	4.6	-0.2	7.8	4.8	4.6	5.4
Svalbard/East										
Annual	4.3	3.9	0.7	6.8	4	-0.3	6.8	4.3	4	4.8
DJF	5.6	5.9	-0.1	11.8	6.2	-2.2	11.9	5.6	5.2	8.7
MAM	4.8	3.4	0.8	5.8	3.5	0.1	5.8	3.7	3.3	4.8
JJA	1.6	1.3	-0.3	3.4	1.4	-0.5	3.5	1.6	0.9	2
SON	5.2	4.9	0.8	7.8	4.9	0	7.7	5.2	4.9	5.7
Svalbard/North-West										
Annual	3.5	3.4	0.1	6.3	3.5	-1	6.4	3.5	3.2	3.6
DJF	4.7	5	-1.2	9.8	5.1	-3.4	9.9	4.7	3.8	5.7
MAM	3.7	2.9	-0.1	5.6	2.9	-1.1	5.7	3.3	2.1	3.7
JJA	1.4	1.4	-0.3	3	1.5	-0.5	3.1	1.4	0.9	1.7
SON	4.4	4.6	0.2	8.3	4.4	-0.6	8	4.4	4.4	5.2
Svalbard/South										
Annual	3.9	3.8	0.5	6.3	3.8	-0.6	6.4	3.8	3.6	3.9
DJF	5.1	6.1	-0.5	10.7	6.4	-2.6	11	5.1	5.1	7
MAM	4.9	3.4	0.3	5.5	3.4	-0.9	5.5	3.6	2.9	4.9
JJA	1.6	1.6	-0.5	3.4	1.6	-0.8	3.4	1.6	1.3	1.7
SON	4	4.3	0.6	7.8	4	-0.2	7.7	4	3.9	4.8
Svalbard/ Airport										
Annual	3.1	3	0.3	5	3.1	-0.3	5.1	3.1	2.7	3.5
DJF	4	4.5	-2.1	8	4.6	-1.6	8.1	4	3.3	5.8
MAM	3.2	2.3	-1.4	5.5	2.3	-2.1	5.5	3	1.7	3.2
JJA	1	1	-0.3	2.3	1.1	-0.4	2.3	1	0.9	1.3
SON	4.1	4.2	0.8	7.4	4.1	0.1	7.4	4.1	3.3	5.5

	RCP45		Temperature changes by 2071-2100								
Models	MPI-ESM-LR		All models			Selected models			Common models		
Perc. Name	-	Med	Low	High	Med	Low	High	Med	Low	High
Perc. Value	-	50%	5%	95%	50%	5%	95%	50%	Min.	Max.
Svalbard-land area										
Annual	4.7	6.2	3.6	10	6.2	3.5	9.5	6.2	4.7	8.2
DJF	6.5	9.9	4.4	16.6	9.9	4.1	16.2	8.5	6.5	12.7
MAM	4.6	5.7	2.8	9.6	5.6	2.7	9.1	5.7	4.6	6.5
JJA	2	2.4	0.2	4.8	2.5	0.6	4.8	2.8	2	3.8
SON	5.7	7.1	4.1	11.2	7	3.9	10.1	7.2	5.7	10.7
Svalbard/East										
Annual	5	6.3	3.6	10.1	6.3	3.5	10	6.7	5	8.8
DJF	6.9	9.8	4.1	17.6	9.7	3.7	16.8	9.6	6.9	13.4
MAM	4.8	5.8	2.6	9.7	5.8	2.6	9.5	6	4.8	7
JJA	2.1	2.3	0.2	5	2.3	0.6	5	2.9	2.1	3.8
SON	6.1	7.3	4.1	11.2	7.2	4	10.4	7.7	6.1	11.5
Svalbard/North-West										
Annual	4.2	5.9	3.1	9.2	5.8	3	8.9	5.4	4.2	7.4
DJF	5.6	8.5	3.6	14.6	8.2	3.5	13	6.5	5.6	10.9
MAM	4	5.3	2.4	10.3	5.3	2.4	9.2	5	4	5.7
JJA	1.8	2.3	0.3	4.6	2.4	0.5	4.6	2.7	1.8	3.9
SON	5.3	7.3	3.8	11.3	7	3.7	10.1	7	5.3	10.2
Svalbard/South										
Annual	4.5	6.3	3.2	10.4	6.4	3.2	9.8	5.7	4.5	7.7
DJF	6.3	10.1	4.3	17.6	10	4.1	17.5	7.7	6.3	12.5
MAM	4.7	5.7	2.9	10	5.6	2.8	9.6	5.5	4.7	5.8
JJA	2	2.7	0.1	4.9	2.7	0.5	4.9	2.8	2	3.5
SON	4.9	6.7	3.6	10.4	6.6	3.5	9.3	6.3	4.9	9.2
Svalbard/ Airport										
Annual	3.7	4.6	2.2	7.7	4.6	2.4	7.4	4.4	3.6	7.4
DJF	5.1	6.2	-1.9	12.7	6.3	-1.8	12.5	5.5	3.4	11.4
MAM	3.2	4.4	1.1	8.4	4.4	1.1	8.4	4.1	3.2	6.2
JJA	1.5	1.8	0.5	3.8	1.8	0.6	3.9	2.1	1.5	2.6
SON	5.1	6.8	3.6	10.1	6.7	3.6	9.5	6.5	5.1	9.7

Models	**RCP85** MPI-ESM-LR	Temperature changes by 2071-2100								
		All models			Selected models			Common models		
Perc. Name	-	Med	Low	High	Med	Low	High	Med	Low	High
Perc. Value	-	50%	5%	95%	50%	5%	95%	50%	Min.	Max.
Svalbard-land area										
Annual	8.4	9.5	6.4	13.3	9.3	6.4	13.2	8.8	8.4	11.6
DJF	12.8	15.1	9	23.9	15	8.5	23.1	14	12.6	18.5
MAM	8.3	8.3	5.1	12.6	8.2	5	12.5	8.5	7.3	9.3
JJA	3.9	4.2	1.5	7.2	4.4	1.5	7.3	4.1	3.8	6.6
SON	8.8	10	7	15.6	9.8	6.9	14.9	9.5	7.8	13.2
Svalbard/East										
Annual	9	10	6.7	13.8	9.9	6.7	13.6	9.4	9	12.2
DJF	13.9	16.3	9.2	25	16.2	8.9	23.8	15.5	13.5	19.8
MAM	8.9	8.6	5.2	12.9	8.5	5.1	12.6	8.9	7.6	9.9
JJA	4.1	4.2	1.2	7.4	4.5	1.7	7.5	4.3	3.8	6.6
SON	9.2	10.4	7.3	15.8	10	7.1	15.3	10	7.9	13.8
Svalbard/North-West										
Annual	7.7	9	5.7	13.1	8.6	5.6	12.7	7.9	7.6	10.7
DJF	11.2	13.6	6.7	21.6	13.1	6.2	20.3	11.3	10.2	16.1
MAM	7.1	7.4	3.7	12.1	7.2	3.7	11.8	7.3	6.6	7.9
JJA	4	4	1.6	7.1	4.2	1.7	7.1	4	3.7	6.9
SON	8.4	10.1	7	16.3	9.7	6.9	14.9	9.2	8.3	12.9
Svalbard/South										
Annual	7.8	9.4	6.3	13.3	9.2	6.1	13.1	8.4	7.7	10.9
DJF	11.7	15	8.3	23.2	14.7	8.1	23.1	12.9	11.7	17.3
MAM	8	8.1	5.2	13.1	8.1	5.1	12.7	8.3	7.2	9.4
JJA	3.4	4.4	1.4	6.9	4.6	1.3	7.1	3.7	3.4	6.2
SON	8	9.3	6.4	15	8.9	6.3	13.6	8.6	6.8	12
Svalbard/ Airport										
Annual	6.4	7.4	4.6	11.1	7.3	4.3	11.1	6.8	6.1	9.5
DJF	9.4	9.7	2.6	18	9.8	2.6	18.1	10	8.8	13.5
MAM	6.2	6.6	3	11.5	6.3	2.9	11.3	6.4	5	8.9
JJA	2.1	3.2	1.5	5.5	3.3	1.5	5.5	3.2	2.1	5
SON	7.8	9.8	5.7	14.7	9.4	5.6	14.2	8.5	5.5	12.5

Table A.2.3 ESD changes of annual and seasonal temperatures over all regions and Longyearbyen by **2031-2060 assuming the RCP2.6, RCP4.5 and RCP8.5** emission scenarios respectively. Displayed values show the medium, low (5%), and high (95%) percentiles of absolute changes with regards to 1971-2000. Results obtained when using the MPI-ESM-LR, all, selected (skipping the red model runs in Table A.1.2), and common global climate models to downscale temperature are also shown in the table for comparison with the CCLM simulation (Table A.2.1. Last column)

Models	RCP26 MPI-ESM-LR	Temperature changes by 2031-2060								
		All models			Selected models			Common models		
Perc. Name		Med	Low	High	Med	Low	High	Med	Low	High
Perc. Value		50%	5%	95%	50%	5%	95%	50%	Min.	Max.
Svalbard-land area										
Annual	3.6	3.6	1.4	5.2	3.6	1.1	5.2	3.6	3.6	4.3
DJF	5.4	5.3	-0.1	8.9	5.3	-0.9	8.9	5.4	4.3	6.9
MAM	3.1	3	1.3	5.1	3	1	5.1	3.1	3	3.9
JJA	1.4	1.3	0.2	2.4	1.3	0.1	2.5	1.4	1.1	1.5
SON	4.6	4.1	1.6	6.4	4	1.5	6.1	4.6	4.3	5.2
Svalbard/East										
Annual	3.8	3.5	1.5	5.7	3.5	1.2	5.7	3.8	3.8	4.6
DJF	5.7	5.4	0.3	9.6	5.5	-0.5	9.7	5.7	4.5	7.3
MAM	3.2	3.2	1.1	5	3.2	0.8	5	3.3	3.2	4.1
JJA	1.4	1.2	0.2	2.5	1.3	0.1	2.5	1.4	1.1	1.7
SON	5	4.3	1.7	6.4	4.3	1.6	6	5	4.5	5.7
Svalbard/North-West										
Annual	3.2	3.2	1	5.3	3.2	0.7	5.1	3.2	3	3.7
DJF	5	4.5	-0.9	8.9	4.3	-1.5	7.5	5	3.3	5.6
MAM	2.5	2.6	0.8	5.2	2.6	0.5	5.4	2.5	2.2	3.5
JJA	1.3	1.3	0.3	2.2	1.3	0.2	2.2	1.3	1.1	1.4
SON	4.3	4.2	1.3	6.6	4.1	1.1	6.4	4.3	4.2	4.9
Svalbard/South										
Annual	3.5	3.4	1.1	5.6	3.4	0.7	5.6	3.5	3.1	4.2
DJF	5.2	5.2	-0.5	8.8	5.2	-1.3	8.9	5.2	4.4	7.3
MAM	3.4	2.9	1.1	5.1	2.9	0.8	5.1	3.4	2.9	3.8
JJA	1.5	1.4	0.1	2.5	1.4	0.1	2.5	1.5	1.4	1.5
SON	4	3.8	1.6	6	3.7	1.4	5.9	4	3.6	4.4
Svalbard/ Airport										
Annual	2.9	2.7	0.7	4.1	2.7	0.7	4.1	2.9	2.2	3.9
DJF	4.3	3.3	-2.1	6.6	3.6	-1.9	6.6	4.3	2.8	6.4
MAM	2.1	2.1	0	4.2	2.1	-0.1	4.2	2.1	1.3	3.9
JJA	0.9	0.9	0.1	1.8	0.9	0.1	1.8	0.9	0.9	1.2
SON	4.2	3.9	1.9	6.1	3.9	1.7	5.9	4.2	3	4.7

Models	RCP45 MPI-ESM-LR	Temperature changes by 2031-2060								
		All models			Selected models			Common models		
Perc. Name	-	Med	Low	High	Med	Low	High	Med	Low	High
Perc. Value	-	50%	5%	95%	50%	5%	95%	50%	Min.	Max.
Svalbard-land area										
Annual	3.8	4.5	2	6.9	4.5	1.8	6.8	4.4	3.8	5.8
DJF	5.3	7	1.5	11.7	6.9	0.9	11.2	5.9	5.3	8.7
MAM	3.9	3.8	1.3	7.3	3.7	1.2	7	4.2	3.9	4.3
JJA	1.6	1.6	0.2	2.8	1.7	0.4	2.7	1.8	1.6	2.3
SON	4.5	5.4	2.9	8.1	5.3	2.8	7.9	5.6	4.5	7.9
Svalbard/East										
Annual	4	4.6	2.2	6.9	4.6	2	6.7	4.8	4	6.2
DJF	5.6	7.2	1.8	12.4	7.1	1.2	12.1	6.6	5.6	9.2
MAM	4.1	3.8	1.5	7.2	3.7	1.4	7.2	4.4	4.1	4.6
JJA	1.6	1.6	0.2	2.7	1.6	0.5	2.7	1.9	1.6	2.3
SON	4.9	5.5	3	8.3	5.4	2.9	8	6	4.9	8.5
Svalbard/North-West										
Annual	3.5	4.2	1.6	6.6	4.2	1.4	6.4	3.8	3.5	5.1
DJF	4.6	5.5	0.5	10.1	5.5	0.4	9.9	5	3.8	7.3
MAM	3.5	3.6	0.9	7.3	3.6	0.9	7.2	3.6	3.3	3.8
JJA	1.6	1.7	0.2	2.8	1.7	0.6	2.8	1.8	1.4	2.5
SON	4.2	5.3	2.6	8.6	5.3	2.5	8.2	5.4	4.2	7.2
Svalbard/South										
Annual	3.6	4.5	1.8	7.7	4.5	1.5	7.2	4	3.6	5.5
DJF	5.1	7.2	1.8	13.1	7.2	1	13	5.9	4	8.7
MAM	3.8	4	1.2	7.7	3.9	1.1	7.2	4	3.8	4.3
JJA	1.6	1.8	0.1	2.9	1.9	0.4	2.9	1.9	1.6	2.5
SON	3.8	5.1	2.6	8.1	4.8	2.4	7.2	4.9	3.8	6.8
Svalbard/ Airport										
Annual	3.3	3.5	1	5.4	3.5	1.1	5.4	3.5	2.2	5.4
DJF	4.8	4.8	-1.3	9.2	4.8	-1.2	9	4.9	1	8.6
MAM	3	3	-0.6	5.5	2.9	-0.9	5.3	3.1	2.1	4.6
JJA	1.1	1.2	0.1	2.1	1.3	0.1	2.1	1.3	1.1	1.7
SON	4.2	5	2.5	7.7	5	2.8	7.2	5	4.2	7

	RCP85		Temperature changes by 2031-2060							
Models	MPI-ESM-LR		All models			Selected Models			Common models	
Perc. Name	-	Med	Low	High	Med	Low	High	Med	Low	High
Perc. Value	-	50%	5%	95%	50%	5%	95%	50%	Min.	Max.
Svalbard-land area										
Annual	4.9	5.1	2.2	8.4	5.1	1.9	8.2	5.2	4.8	6.6
DJF	8.1	8	1.4	13.2	7.8	1.3	13	8.1	7.6	10.7
MAM	4.1	4.3	1.4	7.8	4.1	1.2	7.8	4.6	4.1	5.8
JJA	1.7	1.9	0.5	3.7	2	0.4	3.7	2.1	1.7	2.8
SON	5.8	5.9	2.9	10.3	5.8	2.8	10.1	6.5	4.7	8.2
Svalbard/East										
Annual	5.3	5.3	2.5	8.8	5.3	2.1	8.2	5.5	5.3	7.2
DJF	8.6	8.5	1.5	13.6	8.4	1.5	13.4	8.9	8.1	11.6
MAM	4.4	4.5	1.9	7.9	4.4	1.6	7.8	4.8	4.4	6.3
JJA	1.8	1.9	0.5	3.6	2	0.5	3.7	2.2	1.8	2.8
SON	6.2	6.2	2.9	10.6	6.2	2.9	10.5	7	5	8.7
Svalbard/North-West										
Annual	4.5	4.6	1.6	7.7	4.4	1.4	7.6	4.6	4	5.8
DJF	7.1	7	1.1	11.8	6.5	0.7	10.8	7.1	5.7	8.8
MAM	3.6	3.9	0.7	7.3	3.6	0.5	6.9	3.9	3.3	4.9
JJA	1.7	1.9	0.5	3.5	2	0.5	3.6	2	1.7	2.9
SON	5.5	5.8	2.8	10.4	5.5	2.6	10.2	6	4.9	7.7
Svalbard/South										
Annual	4.6	4.8	1.8	8.6	4.8	1.6	8.4	5	4.2	6.2
DJF	7.6	7.8	1.6	14.7	7.8	1.4	14.5	7.7	6.7	9.9
MAM	4	4.3	1	8	4	1	7.8	4.5	4	5.6
JJA	1.6	2.1	0.2	3.7	2.1	0.2	3.9	2	1.6	3.1
SON	5	5.4	2.6	9.7	5.2	2.4	9.1	5.6	3.9	7.1
Svalbard/ Airport										
Annual	3.9	3.9	1.1	7.3	3.9	1.1	7.1	4.2	3.1	5.8
DJF	7	5.6	-0.7	10.5	5.7	-0.7	10.7	7	4.9	9.1
MAM	3.2	3.5	-0.1	6.9	3.4	-0.1	6.7	3.9	1.7	5.6
JJA	0.5	1.5	0.2	2.6	1.5	0.1	2.6	1.5	0.5	2.4
SON	5	5.5	2.6	9.8	5.3	2.8	9.6	5.7	3.3	7.4

A3: Climate projections for precipitation

Table A3.1 RCM rel. precipitation changes, near and far future, rcp4.5 & rcp8.5, annual and seasonal, all regions + Longyearbyen, med/low/hi CORDEX +, CCLM

Precip. change [%]	1971-2000 to 2031-2060						1971-2000 to 2071-2100						
	RCP4.5			RCP8.5			RCP4.5			RCP8.5			
	Med	Low	High	Med	Low	High	Med	Low	High	Med	Low	High	CCLM
Svalbard land area													
Annual	27	20	44	33	16	49	43	22	53	63	27	106	34
DJF	33	15	62	40	19	72	49	22	73	78	22	147	39
MAM	30	16	44	34	12	44	44	14	47	55	22	110	40
JJA	21	13	25	26	8	35	26	22	32	48	29	67	16
SON	26	25	44	35	15	53	46	27	66	59	30	110	40
Northeast Svalbard area													
Annual	29	19	46	37	20	54	49	23	57	70	36	112	44
DJF	36	14	69	43	24	83	54	21	84	90	33	162	52
MAM	31	15	43	37	13	44	46	18	49	62	28	112	51
JJA	22	13	25	27	8	36	27	23	33	48	30	74	23
SON	29	25	48	38	22	56	55	27	70	66	39	115	50
Northwest Svalbard area													
Annual	26	22	41	30	10	45	41	23	56	61	18	116	24
DJF	32	21	52	39	10	57	44	28	76	78	8	157	32
MAM	26	17	48	28	12	47	40	11	45	51	12	123	25
JJA	20	13	27	24	9	32	26	21	35	50	29	56	6
SON	28	25	44	35	7	54	50	30	71	59	21	128	33
South Svalbard area													
Annual	25	17	40	24	13	41	32	17	41	39	13	78	17
DJF	27	9	54	26	14	55	41	17	52	43	6	94	13
MAM	29	13	42	31	6	43	38	7	45	40	18	88	27
JJA	21	12	32	25	8	38	25	23	29	41	13	63	10
SON	22	14	36	25	5	45	32	17	48	33	6	79	20
Longyearbyen grid-point													
Annual	22	14	32	21	14	33	29	14	30	39	22	55	19
DJF	19	3	31	20	10	29	21	10	28	26	7	49	21
MAM	31	9	45	27	-3	39	31	-2	41	36	19	66	29
JJA	21	18	39	26	8	39	29	23	39	37	17	70	6
SON	20	10	29	24	4	40	20	5	38	40	-3	68	21

Authors

Contributors	Affiliation(s)	Responsibilities
EDITORS:		
Hanssen-Bauer, Inger	MET Norway, KSS	Coordinating editor; Editor Ch. 1 and 4; Lead: Ch. 4.1, 4.2, 10.1; Contrib. author: Ch. 3.1, 4.3, 4.4, 4.5 and 9
Førland, Eirik	MET Norway, KSS	Editor Summary; Lead: Ch. 4.3, 4.4, 4.5; Contrib. author: Ch. 2, 3, 4, 9, 10.1
Hisdal, Hege	NVE, KSS	Editor Ch. 5, 7, 10; Lead: Ch. 7.3, 10.3.2,10.5; Contrib. author: Ch. 3.2, 5, 9, 10.2.1, 10.2.2, 10.2.3
Mayer, Stephanie	NORCE, Bjerknes Centre, KSS	Editor Ch. 3; Lead author: Ch. 3.1; Contrib. author: Ch. 4, 9 and 10.1
Sandø, Anne Britt	IMR, Bjerknes Centre	Editor Ch. 8; Lead author: Ch. 2.2, 3.5, 8.1, 8.2 and 10.4; Contrib. author: Ch. 9
Sorteberg, Asgeir	UiB, Bjerknes Centre	Editor Ch. 2 and 9; Contributing author: Ch. 4
AUTHORS:		
Adakudlu, Muralidhar	NORCE, Bjerknes Centre	Contrib. author Ch. 3.1, 4.1 and 4.2
Andersen, Jess	NVE	Contrib. author Ch. 5.2
Bakke, Jostein	UiB, Bjerknes Centre	Contrib. author Ch. 6
Beldring, Stein	NVE, KSS	Responsible for hydrological modelling; Lead author 3.2; Contrib. author Ch. 5.1
Benestad, Rasmus	MET Norway	Contrib. author 3.1
Bilt, Willem van der	UiB, Bjerknes Centre	Lead author 6.1
Bogen, Jim	NVE	Lead author Ch. 5.3, 10.2.5; Contrib. author Ch.3.2
Borstad, Christian	UNIS	Contrib. author Ch. 6
Breili, Kristian	Kartverket	Contrib. author Ch. 8.4
Breivik, Øyvind	MET Norway, UiB	Contrib. author Ch. 4.5
Børsheim, Knut Yngve	IMR, Bjerknes Centre	Contrib. author Ch. 8
Christiansen, Hanne H.	UNIS	Lead author Ch. 7.2; Contrib. author Ch. 7.1, 7.3, 10.3
Dobler, Andreas	MET Norway	Responsible for the CCLM modelling; Contrib. author Ch. 3.1, 4.1, 4.2, 4.3, 4.4, 4.5,10.1, Appendix
Engeset, Rune	NVE	Contrib. author Ch. 7.3 and 10.3.2
Frauenfelder, Regula	NGI	Contrib. author Ch. 7.2, 7.3 and 10.3.2
Gerland, Sebastian	NP	Contrib. author Ch. 8.3
Gjelten, Herdis Motrøen	MET Norway	Contrib. author Ch. 4.1 and 4.3

Gundersen, Jeanette	NVE	Contrib. author Ch. 7.3 and 10.3.2
Isaksen, Ketil	MET Norway, KSS	Lead author 3.4, 7.1, 10.3.1; Contrib. author Ch. 4; Internal review
Jaedicke, Christian	NGI	Contrib. author Ch. 7.3, 10.3.2
Kierulf, Halfdan	Kartverket	Contrib. author Ch. 8.4
Kohler, Jack	NPI	Lead author Ch. 6 and Ch. 10.2.4; Contrib. author Ch. 9
Li, Hong	NVE, KSS	Hydrological modelling; Contrib. author Ch. 5.1
Lutz, Julia	MET Norway, KSS	Contrib. author Ch. 3.1, 4.1, 4.2, 4.3, 4.4, 4.5
Melvold, Kjetil	NVE, KSS	Contrib. author, Ch. 5
Mezghani, Abdelkader	MET Norway, KSS	Responsible for ESD modelling; Contrib. author Ch. 3.1, 4.1, Appendix
Nilsen, Frank	UNIS, UiB	Contrib. author Ch. 2.2, 3.5, 8.1, 8.2, 9 and 10.4
Nilsen, Irene Brox	NVE, KSS	Lead author Ch. 5.1, 10.2.1, 10.2.2; Contrib. author Ch. 3.2
Nilsen, Jan Even Øie	IMR, NERSC, Bjerknes Centre	Contrib. author Ch. 3.4, 8.4, 10.4
Pavlova, Olga	NPI	Contrib. author Ch. 8.3
Ravndal, Oda	Kartverket	Contrib. author Ch. 8.4
Risebrobakken, Bjørg	NORCE, Bjerknes Centre	Contrib. author Ch. 8.1
Saloranta, Tuomo	NVE	Contrib. author Ch. 3.2, 5.2
Sandven, Stein	NERSC, UNIS, Bjerknes Centre	Lead author Ch. 8.3; Contrib. author Ch. 3.5 and 9
Schuler, Thomas Vikhamar	UiO, UNIS	Responsible for glacier modelling; Contributing author Ch. 3.3, 6, 10.2.4
Simpson, Matthew	Statens kartverk	Lead author Ch. 3.4, 8.4; Contrib. author Ch.9, 10.4
Skogen, Morten	IMR, Bjerknes Centre	Contrib. author, Ch. 8.1 and 8.2
Smedsrud, Lars Henrik	UiB, UNIS, Bjerknes Centre	Contrib. author Ch. 2.2, 3.5, 8.1, 8.2, 8.3 and 10.4
Sund, Monica	NVE	Contrib. author Ch. 7.3 and 10.3.2
Vikhamar-Schuler, Dagrun	MET Norway, NVE, KSS	Responsible for snow modelling; Lead author Ch. 5.2, 10.2.3; Contrib. author Ch. 3.2
Westermann, Sebastian	UiO	Responsible for permafrost modelling; Contrib. author Ch. 7.1
Wong, Wai Kwok	NVE, KSS	Responsible for bias adjustment; Contrib. author Ch. 3.2, 5.1

Photo, visual elements: Ketil Isaksen